

Adsorption and Thin-Film Adhesion on Single-Crystalline Surfaces: Enthalpies, Entropies, and Kinetic Prefactors for Surface Reactions

Jason R. V. Sellers

A dissertation
submitted in partial fulfillment of the
requirements for the degree of

Doctor of Philosophy

University of Washington
2013

Reading Committee:
Charles T. Campbell, Chair
Munira Khalil
David J. Masiello

Program Authorized to Offer Degree:
Chemistry

©Copyright 2013
Jason R. V. Sellers

Abstract

Adsorption and Thin-Film Adhesion on Single-Crystalline Surfaces: Enthalpies, Entropies, and Kinetic Prefactors for Surface Reactions

Jason R. V. Sellers

Chair of the Supervisory Committee:
Professor Charles T. Campbell
Chemistry

Chemical bonding at solid surfaces and interfaces is influential in a wide range of important technological applications including catalysis, fuel cells, batteries, chemical sensors, and device fabrication for microelectronics, computers, solar cells, and all variety of coatings. Adsorption and adhesion energetics are key elements in understanding interfacial properties, and these properties can be used to develop functional industrial materials. First, the properties of single-crystalline oxide surfaces are reviewed in detail, particularly in regards to the adsorption energetics of these surfaces. This includes the largest collection of experimental adsorption data on single-crystalline oxide surfaces ever presented, from which trends in the thermodynamic properties of adsorbates are revealed which greatly expand our understanding of the physical processes occurring on these surfaces. Among these trends is the discovery that the entropy of adsorbed molecules tracks their gas-phase entropy, retaining $\sim 2/3$ of that entropy upon adsorption. This allows for a method of predicting not only entropies of adsorption, but also the kinetic prefactors associated with many classes of elementary surface reactions. These estimations of desorption prefactors are then used to improve calculations of adsorption energies from temperature programmed desorption (TPD) measurements for many systems.

Metal adsorption on oxide surfaces and the strength of the binding at metal / oxide interfaces are then discussed. The motivation here is to understand oxide-supported transition metal nanoparticles such as those used in industrial heterogeneous catalysis. For metal atom

adsorption, adsorption energetics and adhesion energies are directly related to the energy of the adsorbed atoms, which define their stability, sintering rates, and reactivity, and which are found to vary with both the size of the nanoparticle and the nature of the oxide support. The experimental techniques necessary for obtaining these values, as well as the data analysis involved, is explained, and in several cases improved upon. In particular, a new single crystal adsorption calorimeter capable of making the first direct measurements of adsorption energies for metals with high bulk cohesive energies has recently been completed.

These studies greatly expand upon the understanding of and ability to measure the thermodynamic properties associated with adsorption on single-crystalline surfaces.

Table of Contents

Abstract	iii
List of Tables	ix
List of Figures	xi
Acknowledgments.....	xviii
Chapter 1: Introduction.....	1
1.1: Background.....	1
1.2: Experimental Techniques for Measuring Adsorption Thermodynamics	4
1.2.1: Equilibrium Adsorption Isotherms	5
1.2.2: Temperature Programmed Desorption	6
1.2.3: Single Crystal Adsorption Calorimetry	8
1.3: Theoretical Methods for Calculating Adsorption Energetics	9
1.4: Overview of This Dissertation	10
Chapter 2: Enthalpies and Entropies of Adsorption on Well-Defined Oxide Surfaces: Experimental Measurements.....	14
2.1: Introduction	14
2.2: Experimental Methods for Measuring Adsorption Energies and Entropies on Single Crystals	18
2.2.1: Single Crystal Adsorption Calorimetry (SCAC)	18
2.2.2: Equilibrium Adsorption Isotherms (EAI): Enthalpies <i>and</i> Entropies of Adsorption	20
2.2.3: Temperature Programmed Desorption (TPD): Activation Energies and Prefactors for Desorption	23
2.3: Intact Molecular Adsorption and Noble Gas Adsorption on MgO(100).....	26
2.3.1: Entropies of Adsorption on MgO(100) and Other Surfaces: Correlation with Gas-Phase Entropies.....	28
2.3.2: Predicting Desorption Prefactors using this Adsorption Entropy Correlation	34

2.3.3: Trends in Adsorption Enthalpies on MgO(100).....	36
2.4: Intact Molecular Adsorption on Oxide Single Crystal Surfaces: Adsorption Enthalpies from TPD Studies of Desorption Energies.....	38
2.4.1: CO	47
2.4.2: Alkanes	47
2.4.3: Water	48
2.4.4: Alcohols	49
2.4.5: Comparison to Adsorption Calorimetry on Powdered Oxides	52
2.5: Reversible Dissociative Adsorption on Oxides: Adsorption Enthalpies by TPD	53
2.6: Metal Atom Adsorption on Oxide Surfaces and Metal / Oxide Interfacial Adhesion.....	56
2.6.1: Predicting when the Adsorbing Metal Will Reduce the Underlying Oxide.....	57
2.6.2: Metal / oxide Adhesion Energies and Wetting of Oxide Surfaces by Metal Films.....	59
2.6.3: Relating Metal Atom Adsorption Energies with Metal / Oxide Adhesion Energies and Sublimation Energies of the Bulk Metal	61
2.6.4: SCAC Studies of Metal Adsorption Enthalpies on Single Crystal Oxide Surfaces	63
2.6.4.1: Adsorption Enthalpies of Different Metal Atoms on Defective MgO(100).....	63
2.6.4.2: Silver Atom Adsorption Enthalpies on Different Oxide Surfaces	72
2.6.5: TPD studies of Metal Atom Adsorption Enthalpies on Oxides	78
2.6.5.1: TPD studies of the Adsorption of Late Transition Metals and Noble Metals	80
2.6.5.2: TPD studies of the Adsorption of Alkali Metals.....	84
2.7: Figures	86

Chapter 3: The Entropies of Adsorbed Molecules.....	102
3.1: Introduction	102
3.2: Experimental and Theoretical Methods.....	104
3.3: Results.....	107
3.4: Discussion.....	111
3.5: Figures	118
Chapter 4: Kinetic Prefactors of Reactions on Solid Surfaces.....	120
4.1: Introduction	121
4.2: Entropies of Adsorbed Molecules	122
4.3: Prefactors for Desorption	123
4.4: Why Do Adsorbates Have Such Large Entropies?	128
4.5: Estimating Prefactors for Other Elementary Surface Reactions	134
4.5.1: Adsorbate Diffusion	134
4.5.2: Adsorbate Dissociation.....	136
4.5.3: Association of Two Adsorbates	138
4.6: Dealing with Mechanistic Complexity: When an Adsorbate Must Assume Some Special Minority Structure Before Producing the Transition State	140
4.7: Statistical Models for Adsorbates: 2D Ideal Gas, 2D Lattice Gas, and 2D Crystals	141
4.8: Figures	146
Chapter 5: Anchored Metal Nanoparticles: Effects of Support and Size on Their Energy, Sintering Resistance and Reactivity.....	150
5.1: Introduction	151
5.2: The Chemical Potential of Metal Atoms in Anchored Nanoparticles.....	153
5.3: How Metal / Oxide Adhesion Energies Depend on the Metal and the Oxide.....	154
5.4: The chemical potential of metal atoms in nanoparticles increases quickly with decreasing particle size below 6 nm, but less quickly on “strong” supports.....	168

5.5: Increasing the chemical potential of surface metal atoms by decreasing particle size or anchoring them to a “weaker” support increases the strength with which they bond adsorbed catalytic intermediates.....	173
5.6: Figures.....	179
Chapter 6: Adsorption Calorimetry during Metal Vapor Deposition on Single Crystal Surfaces: Increased Flux, Reduced Optical Radiation, and Real-Time Flux and Reflectivity Measurements	182
6.1: Introduction	183
6.2: Experimental Details.....	186
6.3: Real-time Flux Determination in the Metal Atom Beam.....	192
6.4: Optical Radiation from the Metal Atom Beam	194
6.5: Real-time <i>In-situ</i> Relative Diffuse Optical Reflectivity Determination	198
6.6: Absolute accuracy of Heats of Adsorption for Metals on Single-Crystalline Supports from SCAC.....	200
6.7: Example Application of New Calorimeter: Cu Adsorption on CeO _{1.95} (111) and MgO(100) Surfaces	202
6.8: Figures.....	203
Chapter 7: Conclusions	209
References.....	214
Curriculum Vitae.....	231

List of Tables

Table 2.1. Enthalpies and entropies of molecular adsorption on MgO(100) determined by equilibrium adsorption isotherms in a temperature range with the specified average temperature. When a range of enthalpy or entropy values are given, the arrow indicates that this is the direction of increasing coverage.....	27
Table 2.2. Adsorption enthalpies and entropies for molecularly adsorbed species on MgO(100) determined by TPD, showing also the peak temperature and heating rate. Prefactor and enthalpy values in bold were determined in the original paper by careful analysis of the TPD data, so the resulting adsorbate's entropy at T_p determined from this prefactor using Eq. (2.11) are also in bold. The remaining prefactor, enthalpy and entropy values not in bold were estimated using Eqs. (2.16), (2.6) and (2.11), respectively. The entries in bold under "Adsorption site" are as reported in the original paper. Those not in bold are based on our tentative assignments as justified in Section 4. When a range of T_p and enthalpy values are given, the arrow indicates that this is the direction of increasing coverage.....	29
Table 2.3: Adsorption enthalpies and entropies for molecularly adsorbed species on oxide surfaces determined by TPD, showing also the peak temperature and heating rate. Prefactor and enthalpy values in bold were determined in the original paper by careful analysis of the TPD data, so the resulting adsorbate's entropy at T_p determined from this prefactor using Eq. (2.11) are also in bold. The remaining prefactor, enthalpy and entropy values not in bold were estimated using Eqs. (2.16), (2.6) and (2.11), respectively. The entries in bold under "Adsorption site" are as reported in the original paper. Those not in bold are based on our tentative assignments as justified in the text. When a range of T_p and enthalpy values are given, the arrow indicates that this is the direction of increasing coverage.	39
Table 2.4. Adsorption enthalpies for dissociatively adsorbed molecules on oxide surfaces, based on TPD analysis of peaks for their associative desorption. Prefactor and enthalpy values in bold were determined in the original paper by careful analysis of the TPD data. The remaining prefactors not in bold were assumed to be 10^{17} s^{-1} as justified in the text, and the corresponding enthalpies were estimated using Eqs. (2.6) and (2.3). For all these species, the sticking probabilities are large enough to analyze TPD assuming negligible activation energy for dissociative adsorption.	55
Table 2.5: Comparison of the initial heats of adsorption (ΔH_{ad}^0) measured calorimetrically for selected metals on MgO(100) at 300 K with values for the adsorption energy of isolated metal atoms on the most stable sites where they can adsorb on terraces, steps and kinks calculated with DFT slab models at 0 K. Included are also the measured initial sticking probability (S_0) and the heat of sublimation of the bulk metal (ΔH_{sub} , from ¹). Light grey spheres represent oxygen atoms, black magnesium, and light blue adsorbed metal atoms. Reprinted with permission from Reference ² . Copyright 2009 Elsevier.	64

Table 2.6. The calorimetrically-measured adhesion energies of Ag nanoparticles to MgO(100), two reduced CeO _{2-x} (111) surfaces and Fe ₃ O ₄ (111), and the initial heats of Ag adsorption ($\Delta H_{ad,init}^0$) for the first pulse (~0.03 monolayer) of Ag gas at 300 K. Also listed are the Ag particle size and Ag coverage used to get the adhesion energy. The adhesion energy for Ag on Ag (i.e., twice the surface energy of bulk solid Ag) is given for comparison.	76
Table 2.7: Adsorption enthalpies for metal atoms adsorbed on oxide surfaces, listing the parameters in Eq. (2.28) used to fit the coverage dependence. Desorption energies at each initial coverage were determined by Redhead analysis of the TPD data in the citations listed, using T_p and the prefactor estimated using Eq. (2.16) (also listed for the range of T_p values analyzed). Also listed are the bulk metal's sublimation enthalpy and surface energy from the literature, and the metal /oxide adhesion energy and contact angle determined from these using Eqs. (2.30-2.32).....	79
Table 3.1. Adsorbate and gas-phase entropies determined by EAI and by using the prefactors determined from TPD data analysis as described in the text, taken from Reference ³	104
Table 3.2. Parameters for best linear fits to subsets of the data in Fig. 3.2 corresponding to different materials' surfaces.....	110
Table 4.1. Experimentally measured prefactors for desorption of strongly adsorbed small adsorbates and comparison to the predictions of Eq. (4.9).....	133
Table 5.1: Adhesion energies of metals on oxide surfaces measured by sessile drop / contact angle techniques for the liquid metal drops (top section) and by the shape of the particle for solid metals (bottom section). All data are from Ref. ⁴ , but the values marked with an asterisk have been recalculated based on newer values for the surface energies of the pure metals reported in Ref. ⁵ . Metals are ordered by their bulk heat of sublimation ($\Delta H_{sub,M}$) divided by the area per metal atom ($\Omega_M^{2/3}$). Also listed is the heat of formation of the bulk oxide support (per mole of oxygen atoms), $\Delta H_{f,OxSup}$	156
Table 5.2: Adhesion energies of solid metals measured on clean oxide surfaces under ultrahigh vacuum conditions. Methods used are based either on the particle shape (HRTEM and GISAXS) or on the integral heat of adsorption of metal vapor at multilayer coverage (SCAC and TPD). All data are from the citations listed, but the values marked with an asterisk have been recalculated based on newer values for the surface energies of the pure metals reported in Ref. ⁵ . Also listed is the heat of formation of the most stable bulk oxide of that metal (per mole of metal atoms), $\Delta H_{f,MOx}$. Metals are ordered by their bulk heat of sublimation divided by the area per metal atom. (Table 5.1 lists these values.).....	159

List of Figures

- Figure 2.1.** Schematic of the single crystal adsorption calorimeter developed by the group of Sir David King. Pulses of a molecular beam impinge on the clean surface of a very thin single crystal, held in ultrahigh vacuum. The transient temperature rise is measured by infrared optical pyrometry of the back of the crystal. The heat signal associated with this temperature rise was calibrated using pulses of light of known power from a He-Ne laser, which are directed down the molecular beam path. Reprinted with permission from Reference ⁶. Copyright 1996 Elsevier. 86
- Figure 2.2.** Typical equilibrium adsorption isotherm (EAI) data, in this case volumetric measurements of Kr adsorption on MgO(100) smoke. Isotherm temperatures (in K): (a) 66.76, (b) 67.82, (c) 69.10, (d) 70.97, (e) 72.56, (f) 75.21, (g) 77.47, (h) 78.97, (i) 80.28, (j) 81.59, (k) 83.16, (l) 84.52, (m) 85.87, (n) 87.56, (o) 90.88, (p) 95.21, and (q) 98.66 K. The Kr pressure ($P_{\theta,eq}$) at the adsorbed volume in the middle of the first large vertical riser (i.e., at $\theta_{eq} = \frac{1}{2}$ ML coverage) was used to determine the enthalpy and entropy of the first monolayer from a plot of $\ln(P_{\theta,eq}/P^0)$ versus $1/T$, as described in the text. Dashed lines indicate estimated phase boundaries. Reprinted with permission from Reference ⁷. Copyright 1984 American Physical Society..... 87
- Figure 2.3.** Typical TPD data for butane on MgO(100) at a heating rate of 0.6 K/s for 16 initial coverages in the range of 0–1.76 ML: 0.00, 0.10, 0.19, 0.28, 0.42, 0.51, 0.66, 0.76, 0.88, 1.05, 1.13, 1.21, 1.31, 1.38, 1.52, and 1.76 ML. Two desorption peaks are resolved, multilayer (99 K) and first-layer (110 K) desorption, as well as a high-temperature tail on the first-layer peak due to desorption from defect sites on the surface (mainly step edges). Reprinted with permission from Reference ⁸. Copyright 2005 American Institute of Physics..... 87
- Figure 2.4.** Plot of the standard entropies of adsorbates ($S_{ad}^0 = S_{gas}^0 + \Delta S_{ad}^0$) on MgO(100) smoke determined by equilibrium adsorption isotherms (EAI) plotted versus the standard entropy of the gas phase species at the same temperature from Table 2.1. The standard entropies of these same and other adsorbates determined using desorption prefactors and peak temperatures from TPD data together with Eq. (2.11) are also included from Table 2.2. The agreement with EAI results proves the accuracy of this method. The best linear fit to these data is also shown, along with the standard deviation (σ) of the adsorbate entropies from this line. Reprinted with permission from Reference ⁹. Copyright 2012 American Chemical Society..... 88
- Figure 2.5.** Plot of the standard entropies of adsorbates (S_{ad}^0) on several surfaces plotted versus the standard entropy of the gas phase species at the same temperature. Data for MgO(100) and other oxides are from Tables 2.1 through 2.3. Entropies for linear alkanes on Pt(111) and graphite(0001) were calculated using Eq. (2.11) with experimental prefactors and peak temperatures reported in ⁶⁷. The best-fit line is also shown. Adapted with permission from Reference ⁹. Copyright 2012 American Chemical Society. 89

Figure 2.6. Prefactors for the desorption of molecularly adsorbed species as predicted from the gas-phase entropies using Eq. (2.16) (which was derived from the linear relationship in Fig. 2.5 using transition state theory) plotted versus the experimentally measured prefactors. Data are mostly for molecules on oxide single crystals from Table 2.3, but also shown are data for *n*-alkanes on graphite(0001) and Pt(111), from ¹⁰. The line shows the expectation based on Eq. (2.16), which the data fit with a standard deviation in $\log(\nu / s^{-1})$ of 0.86. Reprinted with permission from Reference ⁹. Copyright 2012 American Chemical Society..... 90

Figure 2.7. Heats of adsorption for noble gases on MgO(100) determined by EAI versus atomic number. Data from Reference ⁷, and also listed in Table 2.1. Reprinted with permission from Reference ³. Copyright 2013 American Chemical Society..... 91

Figure 2.8. Heats of adsorption determined by TPD for linear alkanes on MgO(100), graphite(0001) and Pt(111), all at ½ ML coverage plotted versus alkane chain length, from Reference ¹⁰. Also plotted are adsorption enthalpies for alkanes on PdO(101) from TPD (Table 2.3) and on MgO(100) smoke determined by EAI at full, saturated ML coverage (Table 2.1). For comparison, the bulk vaporization enthalpies of pure liquid alkanes at their normal boiling point are also shown, from Reference ¹. Reprinted with permission from Reference ³. Copyright 2013 American Chemical Society..... 92

Figure 2.9. Heats of adsorption for linear alcohols on rutile TiO₂(110) near saturation coverage (determined by TPD, see Table 2.3) plotted versus the number of carbon atoms in the alcohol molecule. Data for both the Ti sites and O sites are shown. For comparison, the bulk vaporization enthalpies of the pure liquid alcohols are also shown, from Reference ¹. Reprinted with permission from Reference ³. Copyright 2013 American Chemical Society..... 93

Figure 2.10. Example heats of adsorption versus coverage data for metals on single crystal oxides as measured by SCAC at 300 K. Data are shown for: Pb, Ag and Ca on MgO(100) as well as Ag on CeO₂(111) (with 5% oxygen vacancies in XPS probe depth). Data from References ¹¹⁻¹⁴; where these original papers show data to higher coverages. One monolayer here is defined as the number of oxygen ions per unit area in the topmost atomic plane ($1.12 \times 10^{15} \text{ cm}^{-2}$ for MgO(100) and $7.9 \times 10^{14} \text{ cm}^{-2}$ for CeO₂(111)). Solid horizontal lines mark the bulk heats of sublimation from the literature. Reprinted with permission from Reference ³. Copyright 2013 American Chemical Society. 94

Figure 2.11. Heat of adsorption of Pb onto Pb nanoparticles on MgO(100) versus average Pb particle radius. Also shown is the Gibbs-Thomson model of Eq. (2.26), which assumes that the surface energy is the bulk value, independent of particle size. This is seen to fit the experimental data very poorly at small radii. In contrast, the modified bond additivity (MBA) model, which is also shown (see details in text), is a much better estimate for the experimental data. Adapted with permission from Reference ¹⁵. Copyright 2002 American Association for the Advancement of Science..... 95

Figure 2.12. The heat of Ag atom adsorption during experiments where Ag is vapor deposited onto oxide surfaces at 300 K where Ag atoms transiently adsorb on clean parts of the oxide surface but quickly diffuses across the surface and add to growing Ag particles on the surface. Plotted here is the measured heat of Ag atom adsorption versus the Ag particle diameter to which it adds (i.e., the average Ag particle size at the Ag coverage corresponding to that heat value). Data are shown for four different surfaces: Fe₃O₄(111) thin film and two CeO₂(111) thin films with different extents of surface reduction ($x = \sim 0.1$ and 0.2 in CeO_{2-x}), all grown on Pt(111) to 4 or 5 nm thickness, and a 4 nm thick MgO(100) film grown on Mo(100). The data for Fe₃O₄(111) are from Reference ¹⁶ and those for CeO₂(111) and MgO(100) are from Reference ¹⁷. Adapted with permission from Reference ¹⁶. Copyright 2011 Royal Society of Chemistry. 96

Figure 2.13. An STM image of Ag nanoparticles grown on the same type of CeO₂(111) film on Pt(111) as in Fig. 2.12 (here only 2.6 nm thick). Reprinted with permission from Reference ¹⁸. Copyright 2012 American Chemical Society. 97

Figure 2.14. Partial molar enthalpy of Ag atoms in Ag nanoparticles (i.e., the enthalpy of the last Ag atom to be added to the particle (relative to bulk solid Ag) versus the average Ag particle size for Ag adsorption on different oxide surfaces. These enthalpies were taken from the data in Fig. 2.12. Copyright 2013 American Chemical Society. 98

Figure 2.15. TPD spectra from different Au coverages adsorbed on a 2.5 nm thick SiO₂ film on Mo(110). Reprinted with permission from Reference ¹⁹. Copyright 2001 Elsevier. The insert shows the heat of adsorption as a function of initial Au coverage determined from the peak temperatures as described in the text, and, for comparison, as determined by the original authors by fitting the leading edge of each TPD spectrum to the Arrhenius law. We present several reasons in the text why such an analysis leads to very large errors at low coverage. Reprinted with permission from Reference ³. Copyright 2013 American Chemical Society. 99

Figure 2.16. Comparison of heats of adsorption for Cu (upper curves) and Ag (lower curves) on alumina determined from TPD data by simple first-order Redhead analysis assuming a prefactor for desorption based on Eq. (2.16) using the entropy correlation of Eq. (13), which gives a prefactor of $\sim 10^{15} \text{ s}^{-1}$. Also shown for comparison are the results by leading-edge analysis as reported by the original authors. The Cu data are for an ordered Al₂O₃ film grown on Mo(110) whose hexagonal LEED pattern was attributed to either α -Al₂O₃(0001) or γ -Al₂O₃(111) ²⁰. The Ag data are from a bulk sapphire α -Al₂O₃(11-20) surface and a thin Al₂O₃ film grown on Re(0001) (also to either α -Al₂O₃(0001) or γ -Al₂O₃(111)), from References ²¹ and ²², respectively. The lowest-coverage heat of adsorption for Ag by the leading-edge analysis gave a prefactor of only $\sim 10^5 \text{ s}^{-1}$, which is clearly many orders of magnitude too low. The text argues that the results from our Redhead analysis are much more accurate. Also shown are best fits of Eq. (28) to these data analyzed by this preferred method. Reprinted with permission from Reference ³. Copyright 2013 American Chemical Society. 100

Figure 2.17. TPD curves for Cs desorption from TiO₂(110) after adsorption at ~230 K to increasing initial coverages of Cs. The completion of a monolayer is easily identified by the appearance of the sharp multilayer peak at ~ 300 K. Coverages below 0.4 ML are so strongly bound that they do not desorb by the highest TPD temperature. The heating rate was ~5 K/s. Reprinted with permission from Reference ²³. Copyright 1997 American Physical Society..... 101

Figure 3.1. Plot of the standard entropies of molecular adsorbates ($S_{ad}^0 = S_{gas}^0 + \Delta S_{ad}^0$) on MgO(100) determined by EAI and TPD, from ³, plotted versus the standard entropy of the gas-phase molecule at the same temperature minus the entropy for one degree of translational freedom. Reprinted with permission from Reference ⁹. Copyright 2012 American Chemical Society..... 118

Figure 3.2. Plot of the standard entropies of molecular adsorbates (S_{ad}^0) on several surfaces plotted versus the standard entropy of the gas-phase molecule at the same temperature. Data for MgO(100) and other oxides are from ³. Entropies for linear alkanes on Pt(111) and graphite(0001) calculated using Eq. (3.5) with experimental prefactors reported in ^{10, 24, 25}. (Since the prefactor was shown to be constant between C₁₂ and C₂₄ ²⁵, we used the C₁₂ prefactor value for C₁₄ and C₁₆.) The best linear fits to the data for molecules smaller and larger than 35 atoms are also shown. For comparison, the standard entropies of bulk 3D liquids at the normal boiling point (as estimated by Trouton's Rule) are also shown. Reprinted with permission from Reference ⁹. Copyright 2012 American Chemical Society.... 119

Figure 4.1. An illustration of the effects of a lattice mismatch of 4% between an adsorbate and an underlying support for a 40 kJ/mol hypothetical diffusion barrier across the surface. (a) This leads to an increase in the energy of 14.5 kJ/mol per atom with the central atom at the most ideal binding site. (b) When the central atom is translated to its least ideal binding site, this energy increases by only 11 kJ/mol per atom, so that the barrier for diffusion is just 28% of the single atom diffusion barrier. This logic could also be applied to explain why large polyatomic adsorbates whose atom-to-atom spacing does not match the substrate have low diffusion barriers. 146

Figure 4.2. Bottom axis: The classic hindered rotor: Potential energy versus rotational angle for the rotation of one methyl group about the C–C axis in gas-phase ethane. From McQuarrie ²⁶. The same form of potential applies to helicopter-type rotations of an adsorbate. Top axis: Potential energy versus distance along the surface (x) for the diffusion of an adsorbate, where a = site-to-site separation. Reprinted with permission from Reference ²⁷. Copyright 2013 de Gruyter..... 147

Figure 4.3. Prefactors for the desorption of adsorbed species as predicted using Eq. (4.9) plotted versus the experimentally measured prefactors. The line shows the expectation based on Eq. (4.9). Most of the data points were already shown in Fig. 2.6, but the new points (red squares) are for more strongly bound adsorbates (see Table 4.1 for details). Reprinted with permission from Reference ²⁷. Copyright 2013 de Gruyter. 148

Figure 4.4. Schematic representation showing how entropy is lost in the transition state for the dissociation of an adsorbate, in this example for an adsorbed methoxy on a metal surface losing a methyl H to form adsorbed -OCH₂ plus -H. The reactant has two relatively free rotations, but those motions are lost as the methyl starts to form its own bond to the metal in the transition state. Reprinted with permission from Reference ²⁷. Copyright 2013 de Gruyter. 149

Figure 5.1: Adhesion energies of different metals on α -Al₂O₃(0001) plotted versus (a) the surface energy of the metal and (b) the bulk metal's sublimation enthalpy per atom ($\Delta H_{\text{sub,M}}/N_A$) divided by the area per metal atom ($\Omega_M^{2/3}$). Black points are based on measurements of particle shapes for molten metal drops (round) and solid particles (squares) without verification of surface cleanliness, from Table 5.1. Lines through the subsets of data are the best linear fits. Reprinted with permission from Reference ²⁸. Copyright 2013 Royal Society of Chemistry..... 177

Figure 5.2. Adhesion energies of different metals on clean MgO(100) measured in ultrahigh vacuum (from Table 5.2) plotted versus the bulk metal's value of $[\Delta H_{\text{sub,M}}/N_A]/\Omega_M^{2/3}$ (a) and versus $[(\Delta H_{\text{sub,M}} - \Delta H_{\text{f,MOx}})/N_A]/\Omega_M^{2/3}$, where $\Delta H_{\text{f,MOx}}$ is the standard heat of formation of the most stable bulk oxide of that metal (per mole of metal atoms) (b). The best-fit lines are also shown. Different symbols correspond to different measurement methods. Reprinted with permission from Reference ²⁸. Copyright 2013 Royal Society of Chemistry..... 178

Figure 5.3: Adhesion energies of the same metal (normalized to $2\gamma_M$) on different oxide supports plotted versus the heat of formation of the oxide support per mole of oxygen ($\Delta H_{\text{f,OxSup}}$). Different colors of points and lines are for different metals. Black points are for liquid Ni, Fe and Co droplets on oxide surfaces whose cleanliness was not proven, from Table 5.1. These metals are grouped together since they have very similar sublimation energies (and thus appear at nearly the same place on the x-axis of Fig. 5.1). Colored points are for solid metals collected on clean oxide surfaces in UHV, from Table 5.2. Lines through the subsets of data are the best linear fits. Reprinted with permission from Reference ²⁸. Copyright 2013 Royal Society of Chemistry. 179

Figure 5.4. Example heats of adsorption versus coverage data for metals on single-crystal oxides as measured by calorimetry at 300 K. Data are shown for: Pb, Ag and Cu on MgO(100) and Ag on CeO₂(111) (with 5% oxygen vacancies in XPS probe depth). Data from References ^{11, 12, 14, 29}. One ML equals the number of oxygen ions per unit area in the topmost atomic plane ($1.12 \times 10^{15} \text{ cm}^{-2}$ for MgO(100) and $7.9 \times 10^{14} \text{ cm}^{-2}$ for CeO₂(111)). Horizontal lines mark the bulk heats of sublimation of the metal adsorbate. Reprinted with permission from Reference ²⁸. Copyright 2013 Royal Society of Chemistry. 180

Figure 5.5. The chemical potential of Ag atoms in Ag nanoparticles on different oxide surfaces versus the average Ag particle size. The chemical potential here is estimated by the difference in magnitude between the bulk heat of sublimation of the metal and its differential heat of adsorption on particles of that size (using the data in Fig. 2.12), and neglects entropy differences. Reprinted with permission from Reference ²⁸. Copyright 2013 Royal Society of Chemistry. 181

Figure 6.1. A schematic of the calorimeter, which uses an e-beam evaporator and a chopper to create a pulsed atomic beam of gaseous metal atoms (copper colored in the figure) which impinges upon the surface of a single crystalline sample. The transient heat input due to the adsorption of each gas pulse is detected by a flexible pyroelectric PVDF ribbon that is gently pressed against the back of the single crystal. As shown, this ribbon is mounted in the shape of an arch on the “cal head”, which can be translated to bring the ribbon into contact with the single crystal, or removed for crystal cleaning and surface analysis. The single crystal is mounted to a platen, which sits on a fork on a thermal reservoir during calorimetry but is moved for surface analysis. Also illustrated are the components for the real-time flux and relative reflectivity measurements. Not to scale. Reprinted with permission from Reference ³⁰. Copyright 2013 American Institute of Physics. 203

Figure 6.2. (a) Plot of the flux from the electron beam evaporator running at constant emission current vs. time at both the sample position QCM and the off-axis monitor QCM. Measured flux data are plotted as points, while the calculated flux at the sample position is plotted as a continuous red line. Also plotted is the ratio between the two fluxes, which is fit to the linear dashed line as a function of time. The flux ratio is used to calculate the flux at the sample position based on the flux at the monitor QCM. (b) Similar data for a control run where the flux was collected with a QCM located at the sample position throughout the entire experiment. This shows that the changing flux ratio is well approximated as changing linearly with time. The dashed line showing the best linear fit to the flux ratio is essentially hidden within the scatter of the data. Reprinted with permission from Reference ³⁰. Copyright 2013 American Institute of Physics. 204

Figure 6.3. Calorimetry heat pulses as detected via SCAC from Cu adsorbing onto ~17 ML of Cu on ~1 μm single crystals at 300 K, where the Cu vapor was generated by: (a) the Knudsen cell used in our earlier calorimeter ³¹, and (b) and (c) the e-beam evaporator of this new instrument. The solid black lines are calorimetry data from Cu atom pulses, the solid blue lines are the heat due to optical radiation from the hot metal source (measured through the BaF₂ window at the end of the experiment) and the dashed red lines are the heat signal due only to Cu adsorption, as determined by the difference in the two solid curves. These signals are for (a) 0.014 ML pulses of Cu from the Knudsen cell used in our earlier calorimeter ³¹ onto ~17 ML Cu on Mo(100) (pre-coated with 4 nm of MgO(100), which only slightly changes the reflectivity ²⁹), (b) 0.014 ML pulses of Cu from the e-beam evaporator onto ~17 ML of Cu on Pt(111), and (c) 0.056 ML pulses of Cu from the e-beam evaporator onto ~17 ML of Cu on Pt(111). The differences in line shapes arise from differing time constants for the high-pass filters and differences in the quality of the thermal contact between the sample and detector. Curves were smoothed with a low-pass filter.

One ML is defined as the Cu(111) surface atom density, 1.77×10^{15} atoms/cm². Reprinted with permission from Reference ³⁰. Copyright 2013 American Institute of Physics 205

Figure 6.4. A sample run demonstrating the *in-situ* relative diffuse optical reflectivity measurement. Every third pulse from the metal atom beam line is replaced with a pulse from a HeNe laser at a 45° angle of incidence. The black portion of the curve is the response to heat deposition from the atomic beam line, while the red portions are the heat response from the laser. In this manner the absorbance of the sample at 633 nm can be monitored throughout the experiment so that the reflectivity of the sample can be accurately determined at all coverages. Heat pulses from the atomic beam were simulated with a laser directed down the atomic beam path in this example. Reprinted with permission from Reference ³⁰. Copyright 2013 American Institute of Physics..... 206

Figure 6.5. Heat of adsorption versus coverage for 100 pulses of Cu (each pulse containing 0.017 ML) onto a Cu multilayer on Pt(111) at 300 K. The data in the figure have been normalized so that their average value equals the literature value for the enthalpy of sublimation of bulk Cu solid at 300 K (337.4 kJ/mol¹, shown as the solid red line), to remove a small error in absolute calibration. The pulse-to-pulse standard deviation is 0.83 kJ/mol. One ML is defined as the Cu(111) surface atom density, 1.77×10^{15} atoms/cm². Reprinted with permission from Reference ³⁰. Copyright 2013 American Institute of Physics..... 207

Figure 6.6. Heat of adsorption versus coverage for Cu on MgO(100) ²⁹ (blue circles) and CeO_{1.95}(111) ³² (red squares) at 300 K. The dashed black line is the heat of sublimation of bulk Cu solid at 300 K (337.4 kJ/mol¹). One ML is defined as the Cu(111) surface atom density, 1.77×10^{15} atoms/cm²..... 208

Acknowledgements

Financial support for this work was provided by the U.S. Department of Energy-Office of Basic Energy Sciences under grant no. DE-FG02-96ER14630 and the National Science Foundation under grant no. CHE-1010287.

First and foremost, I would like to thank Dr. Charles T. Campbell for his insight, dedication, and support throughout my graduate studies. The original designs for the new instrument were the work of Dr. Jason Farmer, who taught me everything I know about instrument design and construction. The initial calibration and tuning of the calorimeter would never have been accomplished in such a timely manner without the tireless work of Trevor James, and the first meaningful experimental results from that project are attributed to him and Stephanie Hemmingson. The Campbell group as a whole has been a terrific place to do my graduate work thanks to group members such as James Sharp, James Lownsbury, Trent Silbaugh, Eric Karp, Chris Wolcott, Matt Crowe, Isabel Green, Wanda Lew, Ole Lytken, Jack Baricuatro, Daniel Mazur, Hans-Jörg Drescher and all of the others who have come and gone in my time here.

Dr. Markus Raschke was also instrumental in my development as a scientist, as were my colleagues and friends from his group at the University of Washington: Catalin Neacsu, Alex Anderson, Friedrich Kirschner, Sam Berweger, Andy Jones, and Rob Olmon. I would also like to thank Jim Gladden, Lon Buck, Roy Olund, and Bill Beaty in the UW Chemistry electronics shop and Brian Holm, John Heutnik, and Ed McArthur in the UW Chemistry machine shop for their help and expertise throughout the years.

Among my earlier scientific influences, I would like to thank Dr. John Cooper at Old Dominion University, and Dr. Jay Parker and Deborah Foy at Morphix Technologies for showing me what it takes to excel as a scientist. I'd also like to offer a special thank you to Chris Deloglos, my chemistry teacher at First Colonial High School, whose class originally inspired me to pursue a career in this field.

In addition, I would like to thank my family and friends on both coasts. These include Jimmie and Jeanette Sellers, Jake Sellers, Joyce Sellers, Esther Tate, Patricia Canciglia, the extended Sellers and Zipparro families, Erica McGillivray, Steve Stone, Lewis Johnson, Matt Green, Eric Newton, Michael Newton, Jim and Ann Newton, Brian Roskovitch, John Mintz, Amber Hoback, Kimberly Nixon, Winston Zeddemore Sellers-McGillivray, Cassidy Sellers, and many others. I could not have done this without all of you.

This dissertation is dedicated to the memories of Ralph Waldo Sellers, Vincent John Zipparro, Gwendolyn Zipparro, and Wayne Morris Watson.

Chapter 1

Introduction

1.1: Background

Chemical bonding at solid surface and interfaces is crucial for a wide range of important technologies, including catalysis, fuel cells, batteries, chemical sensors and the fabrication of countless devices such as microelectronics, computers, solar cells and all variety of coatings. Wolfgang Pauli was famously quoted as having said that “God made the bulk; the surface was invented by the devil” when discussing the relative complexity of the two forms of matter. This is due to the fact that the physical properties of an atom are directly influenced by its chemical environment. In the bulk, the uniform surrounding of the atoms provides a relatively simplistic system. When looking at an atom on a surface, however, its physical properties are controlled not only by the bulk with which it is still connected, but also by the medium that extends beyond it. This drastically increases the complexity of the system being observed, and therefore increases the difficulty in characterizing and defining its physical properties.

But if one wants to approach an understanding of the functional use of a solid material, the physical properties of the surface are extremely important. The surface, or more directly the interface between two substances, is where many useful functions of a solid material will take place. Optical properties, thermodynamic stability, and electronic properties are all directly tied to the interfacial energy of the material, which is in turn controlled by the environment at the interface. The physical processes underlying adsorption and adhesion on solid surfaces have therefore been the subject of intense scientific interest for many decades.

The chemistry of adsorption, metal nanoparticle growth, and adhesion on oxide surfaces will be a major focus of this dissertation. Oxide surfaces play a central role in many current technologies, and promise to play an ever-increasing role in future technologies. Oxides are commonly used as reactive substrates or supports in catalytic and electrocatalytic materials, and are also central ingredients in photocatalysts, photoelectrocatalysts, transparent electrodes for photovoltaics, solid electrolytes, superconductors, microelectronics, computer chips, protective coatings, windows, optics, batteries, piezoelectrics, pyroelectrics, and ceramics, just to name a few current fields of interest. When compared to metal surfaces, however, much less is understood about the chemistry of oxide surfaces³³.

Most realistic surfaces such as those used in industrial applications consist of multifaceted surfaces whose complex properties largely influence their interaction with adsorbates. Adsorbates can not only bind to differently faceted terraces and their defects, but the domain boundaries between the facets also provide unique sites at which binding can occur. Experimental results from such systems are often so complex that it is impossible to gain any significant insight into the physical processes at play. It is therefore useful to reduce these surfaces to model single crystals³⁴. On a single-crystalline surface, the exact arrangement of the atoms and the available binding sites for adsorbates are well known, making the data much more easily interpretable.

However, even for these simplified surfaces, the strength of the interaction between an adsorbate and a single-crystalline oxide support is often unknown. In order to properly understand the strength of these interfacial interactions, it is important to be able to define the basic thermodynamic properties of the adsorbates, which differ from their bulk or gas-phase properties. The enthalpies (H_{ad}) and entropies (S_{ad}) of the adsorbates define their relative

thermodynamic stability, and the changes in these two properties upon adsorption from the gas phase (ΔH_{ad} and ΔS_{ad} , respectively) can be used to determine how strongly they are bound to a surface³³. The relationship of the enthalpies of adsorption to the integrated heat of adsorption (q_{ad}), the change in internal energy of adsorption (ΔH_{ad}), and the adsorption energy (E_{ad}), is defined by the equation

$$q_{\text{ad}} = -\Delta H_{\text{ad}}^0 = -\Delta U_{\text{ad}}^0 + RT = E_{\text{ad}} + RT, \quad (1.1)$$

for a given temperature (T), where the superscript 0 denotes the values at the standard pressure of 1 bar. These terms are often used interchangeably in the literature since the RT correction only amounts to ~ 2.5 kJ/mol at room temperature, which is usually within the uncertainty of the experimental techniques.

In interface formation by thin film growth, physical properties that describe the strength of the interactions between two disparate materials, such as systems' adhesion energy, are related to the adsorption energetics³³. The energy released upon adsorption provides essential information about the thermodynamic properties that impact interface formation and thin film growth, and trends in these properties can provide insight into reactions at solid surfaces as well as the reactivities of adsorbed nanoparticles.

Unfortunately, for many adsorbate / support systems these basic properties have not been measured, and these data for adsorbates on oxide supports in particular are very scarce³. With oxide supports, a particular problem has been the difficulty of preparing well-ordered single-crystalline surfaces of oxides, and the fact that even once prepared they are often not electrically conductive enough to be amenable to many of the techniques for surface characterization. Fortunately, the past decade has seen the development of many new sample preparation

techniques for oxide surfaces that have overcome these problems ³⁵, allowing for experiments that can characterize adsorption and surface reactions on a variety of well-defined oxide surfaces.

Of particular interest, oxides are often used industrially as supports for nanoparticulate catalysts due to their stability, relative inexpensiveness, and high surface areas ³⁶. These properties are particularly important in heterogeneous catalysts such as those used in many important applications including fuel production, pollution reduction, and chemical mass-production ^{37, 38}. Among the most promising catalysts are those consisting of late transition metal nanoparticles on high surface area oxide supports ^{39, 40}. The large surface / bulk ratio in nanoparticles makes them ideal for creating the most reactive area with the least amount of material, which is particularly important in commercial applications where the cost of these catalytically active metals is a major factor. Nanoparticles also exhibit quantum confinement effects which have been shown to generate catalytic properties in metals such as Au that are relatively inert in the bulk ⁴¹. The size of these particles can be tuned to affect their catalytic properties and selectivity ^{42, 43}. At small particle sizes, the nanoparticle's properties depend on the nature of the surface upon which they are supported, and it has also been shown that the interaction between an adsorbed nanoparticle and the substrate can have a large effect on the catalytic activity and selectivity of the adsorbed nanoparticles ⁴².

1.2: Experimental Techniques for Measuring Adsorption Thermodynamics

In order to be able to gain insight into trends in the strength of interfacial interactions, it is important to have data from experiments which are performed under conditions in which the surface to be studied can be prepared and maintained for the time of the measurement in an atomically clean state, and where its cleanliness can be verified with a variety of surface analysis

techniques. Ultrahigh vacuum (UHV) is ideal for these purposes⁴⁴. Techniques for measuring adsorption energetics on single-crystalline oxide surfaces in UHV include equilibrium adsorption isotherms (EAI), temperature programmed desorption (TPD), and single crystal adsorption calorimetry (SCAC).

1.2.1: Equilibrium Adsorption Isotherms (EAI)

Equilibrium adsorption isotherms use the relationship between adsorbate coverage, equilibrium vapor pressure, and sample temperature to obtain thermodynamic information from the system. In a typical EAI experiment, a sample at constant temperature is exposed to increasing back pressures of a gas while monitoring the amount that adsorbs to the surface. A series of these experiments over a reasonably narrow range of sample temperatures can be used to produce a curve of vapor pressure versus $1/T$, with a slope equal to $\Delta H_{\text{ad}}^0/R$ and a y -intercept equal to $-\Delta S_{\text{ad}}^0/R$ (where both values correspond to a specific coverage and 1 bar pressure), where R is the ideal gas constant^{7, 45}. The measurements are fairly straightforward, with the ability to extract both enthalpies and entropies of adsorption directly, but do require that the adsorption \rightleftharpoons desorption process is reversible.

Historically, EAI is the only experimental method for which entropies of adsorption have accurately been extracted. However, this technique has not been widely applied with single-crystalline oxide surfaces. The only EAI studies of adsorption on single-crystalline oxide surfaces that have been reported in the literature were performed with small molecules on nanocubic MgO(100) smoke^{7, 45, 46}, so the available data is very limited.

1.2.2: Temperature Programmed Desorption (TPD)

Temperature programmed desorption, also referred to as thermal desorption spectroscopy (TDS), is much less direct and requires some explanation and interpretation of the measured TPD spectra in order to extract enthalpies of adsorption. In a typical TPD experiment, an adsorbate pre-covered surface is heated incrementally while monitoring for desorbing molecules. The temperature at which the adsorbates in the first monolayer desorb can be used to analyze the strength of a specific adsorbate–surface bond⁴⁷. Since the physical process being observed is the desorption of pre-adsorbed molecules, in the best case TPD only provides an accurate activation energy for desorption, E_d . This can only be equated with the adsorption energy, E_{ad} , when both the adsorption \rightleftharpoons desorption process is reversible and the activation energy for adsorption is negligible. The high temperatures often required in TPD of adsorbed metals is particularly problematic in that supported atoms can sinter or diffuse into the support at temperatures below that at which desorption occurs^{15, 48}.

To extract E_d from TPD experiments, the surface species are usually assumed to be in equilibrium, in which case the desorption rate is a single-valued function of coverage (θ) and temperature (T): $r(\theta, T)$. For cases of reversible molecular adsorption \rightleftharpoons desorption, where it is reasonable to assume that desorption is a first-order process, the Polanyi-Wigner equation gives:

$$r(\theta, T) = -d\theta/dt = \nu \exp(-E_d(\theta)/RT) \theta, \quad (1.2)$$

where ν is the pre-exponential factor, which is typically assumed to be constant over all coverages and temperatures, $E_d(\theta)$ is the coverage-dependent desorption activation energy, and R is the ideal gas constant. This adsorption energy changes with coverage because various adsorption sites (e.g. defects, terrace sites, etc.) have different strengths of interaction, and interactions between the adsorbates change with the average adsorbate-adsorbate distance, so E_d

is certainly expected to vary with coverage. By mathematical inversion of the rate data, the value of $E_d(\theta)$ can be obtained from the Polanyi-Wigner equation if ν is known⁴⁹:

$$E_d(\theta) = -RT \ln[(-d\theta/dt)/(\nu\theta)]. \quad (1.3)$$

Typically, one treats ν as a variational parameter to optimize the fit between experimental and simulated TPD spectra, thus finding the prefactor that best matches the kinetics of the desorption process^{8,24}. The value of the prefactor can be used to estimate the adsorption entropy, since the transition state for desorption is very similar to the gas.

One can also extract E_d using the first-order Redhead equation, which relates the temperature at which the desorption rate maximizes (T_p) to E_d , the heating rate (β) and ν ⁴⁷:

$$E_d/(RT_p^2) = (\nu/\beta) \exp[-E_d/(RT_p)]. \quad (1.4)$$

The most common practice has been to simply use Eq. (1.4) and an assumed value for ν , which gives reasonable accuracy if the value of ν is approximately correct. A factor of 10 error in ν corresponds to an error of only $\sim 2.3RT_p$ in E_d , which is only 6 kJ/mol, or $\sim 7\%$, for $T_p = 300$ K and $\nu = 10^{15} \text{ s}^{-1}$.

Until recently there has been no method for extracting reliable information on the entropy of adsorbates from TPD measurements. In Chapter 3 a recently developed method is described for determining entropies from TPD that works well in cases where the sticking probability for that gas is near unity⁹. There have also been relatively few TPD experiments for metal adsorbates on single-crystalline oxide supports, and for these strongly bound adsorbates adsorption energies for the smallest particles from TPD have often been misinterpreted. A new method for extracting more reliable metal atom adsorption energies vs. coverage from TPD experiments is presented in Chapter 2.

1.2.3: Single Crystal Adsorption Calorimetry (SCAC)

The Campbell group has pioneered the development of UHV adsorption microcalorimetric techniques that make it possible to directly measure adsorption energies for a large variety of systems^{31, 50-52}. A thin polyvinylidene fluoride (PVDF) ribbon serves as the heat detecting element of the calorimeters. The 9 μm thick ribbon consists of amorphous PVDF in which poled β -PVDF crystals, which are both piezoelectric and pyroelectric, have been embedded. When brought into gentle mechanical contact with the back of a sample, the pyroelectric properties of β -PVDF respond to a slight increase in temperature with a measurable change in the face-to-face voltage of the ribbon.

The samples are typically 1 μm thick metal single crystals. For studies on oxide surfaces, ~ 4 nm single-crystalline oxide thin films are grown *in-situ* on the metal surface, which is made possible by the removable nature of the heat detector. The metal atom beam is chopped into pulses, with the spatial distribution defined by a series of apertures. When heat is deposited on the face of a 1 μm crystal, $\sim 10\%$ of the energy is transferred to the ribbon. The intimate thermal contact between the sample and the ribbon allows for the heat released from the adsorption events to be detected almost instantaneously. With this setup, adsorption energies are determined to within 3% in most cases and with a point-to-point standard deviation of only 0.6 kJ/mol when depositing 2% of a monolayer per pulse⁵¹. In this manner heats of adsorption are determined by directly monitoring the adsorption process, so the results are unambiguous.

The details of this technique are discussed in greater detail in Chapter 6, where an improvement in SCAC design is described that allows for measurements of adsorption energetics using metals that have high enthalpies of vaporization, such as Pt, Pd, Rh, Ni, and Au, for which direct measurement of heats of adsorption and adhesion energies were previously not possible³⁰.

It has also been shown recently that adsorption energetics can be extracted from SCAC measurements using adsorbates which transiently adsorb to the single-crystalline surfaces, for which their surface residence time at a given temperature (or desorption rate constant) can also be extracted⁵³. In Chapter 3, it is shown that these values can be analyzed to determine adsorbate entropies for species with sticking probabilities near unity.

1.3: Theoretical Methods for Calculating Adsorption Energetics

Accompanying the rapid developments in the experimental study of adsorption on oxide surfaces mentioned above, there also has been a dramatic increase in efforts to understand the surface reactivity of oxides and trends in their surface reactivity at the electronic-structure level, through computational quantum mechanical approaches. Approaches using density functional theory (DFT), with the generalized gradient approximation (GGA) and periodic boundary conditions, which have proven so effective in explaining and even predicting the reactivity of metal surfaces⁵⁴⁻⁶⁰, have been shown to have greater limitations when applied to oxide surfaces⁶¹⁻⁶³. An improved version, "DFT+U", cures some of the problems by introducing the U parameter in the Hamiltonian to localize the d- or f-electrons. This U can be chosen to give a better fit than GGA-DFT to some reaction energies⁶⁴. GGA+U is now the most widely used methodology, but it still has limitations in energy accuracy. Due to the greater challenges presented by oxide surfaces, there are currently many efforts worldwide to improve such computational methodology for applications in oxide surface chemistry, for example through use of hybrid functionals, which is a much more computationally intensive alternative.

Currently, the main experimental benchmarks that are used for validating these new theoretical approaches are bulk properties like the heats of oxide formation, band gaps, lattice

parameters, phonon spectra, etc. Experience with metal surfaces has proven that to achieve the most effective theoretical codes, they must also be validated against experimental measurements of surface properties, namely enthalpies of adsorption, surface reaction energies, and adsorbate geometries for well-defined adsorbates at well-defined surface sites. Such measurements are only possible using single-crystalline surfaces.

Therefore, experimental analyses of adsorption energetics are necessary for understanding the properties of adsorbed materials. For metal adsorption, the physical behavior of the adsorbates, such as dispersion, particle size, sintering, and sub-surface diffusion, are all directly related to the bond energy between the metal and its support². The strength and nature of these interactions also affects the way these nanoparticles bind small molecules, thereby influencing their catalytic properties⁶⁵.

1.4: Overview of This Dissertation

In order to gain a greater insight into trends in adsorption energetics for adsorbates on oxide surfaces, it is useful to look at experimental measurements of adsorption energetics for a wide range of adsorbates on single-crystalline oxide surfaces. In Chapter 2, all of the current experimental thermodynamic data for small molecule and metal adsorption on single-crystalline oxide surfaces are presented. While still limited, this large set of data can be used to draw some broad conclusions about periodic trends in adsorption on oxide surfaces.

The collection of data in Chapter 2 also allows for the chance to look at periodic trends in the basic thermodynamic properties of adsorbed molecules. Among the observations was the discovery of a correlation between the entropy of an adsorbed molecule and the gas phase entropy of that same molecule at the same temperature. This is presented in detail in Chapter 3.

Surface chemists usually think about adsorbate entropies in terms of the two limiting cases that have been discussed in statistical thermodynamics texts: the 2D lattice gas model and the 2D ideal gas model ⁶⁶. In calculating rate constants for surface reactions based on quantum mechanical calculations (mainly DFT) of reactant and transition state energies, surface chemists almost exclusively rely on harmonic transition state theory approaches, which assume that each adsorbate is a localized oscillator with only vibrational modes ⁶⁶. Vibrations generally have very low entropy compared to translations and rotations of their gas-phase analogues. From the data collected in Chapter 2, it is seen that these common approximations greatly underestimate the entropies of adsorbed molecules even when they are held together in islands by attractive interactions. Instead, their entropies are almost 2/3 of the entropy of their gas-phase analogue ⁹ (at temperatures high enough to measure desorption rates or adsorption \rightleftharpoons desorption equilibria), suggesting that all components of motions in two out of the three dimensions are nearly as labile as in the gas phase.

It is well established that one must know the enthalpies and entropies of the reactants if one is to develop systematic theories that can predict equilibrium constants and rate constants for chemical reactions of any type. It is further shown that the correlation described in Chapter 3 between the entropies of adsorbed and gas-phase molecules can be quite useful in predicting rate constants for adsorbed molecules. Chapter 4 describes in detail the application of this powerful tool for estimating entropies of adsorption in improving estimates of desorption prefactors for TPD ²⁷. Much of the TPD literature in which adsorption energies have been reported uses calculations that rely upon assumed pre-exponential factors for desorption ³. In these cases, reevaluation of the adsorption energies using instead values for ν estimated from the correlation in Chapter 3 provides more reliable estimates for adsorption energies of molecularly adsorbed

species. Chapter 4 goes on to describe how these adsorbate entropies can also be used to estimate the other main classes of adsorbate reactions: dissociation, association and diffusion.

The studies presented in Chapters 2 through 4 provide further insight into the behavior of adsorbed molecules. In Chapter 5, the ramifications of these properties are discussed in relation to metal atoms and metal nanoparticles adsorbed on oxide surfaces²⁸. Metal-doped oxide surfaces and late transition metal nanoparticles supported on oxide surfaces form the basis for many important industrial catalysts used in energy and environmental technology. The energy, or chemical potential, of the metal atoms in a nanoparticle vary with both the size of the nanoparticle and the nature of the surface on which it is supported. When the chemical potential of the metal atoms in a nanoparticle is larger, so is the drive for those particles to sinter. Since the chemical potential increases with decreasing particle size below 6 nm, this explains the tendency for highly disperse nanoparticles to deactivate under realistic conditions. However, the high chemical potential of these smallest nanoparticles also results in an increase in the strength of the bonds they can form to small molecules, so it is intimately related to their reactivity. Chapter 5 presents the first ranking of small selection of oxide supports by the strength of the bonds they form with metal nanoparticles, which is the first step in developing a systematic method for designing the most efficient catalysts.

As can be seen in Chapter 5, experimental studies characterizing adsorption energetics for metal adsorbates on oxide surfaces are still very limited. If progress is to be made in understanding trends in adsorption on oxide surfaces, it is therefore necessary to further improve the techniques with which these data are acquired. Chapter 6 reports on the design, construction, and experimental details of a new SCAC which modifies the Campbell group's established UHV adsorption microcalorimetric techniques in order to directly measure adsorption energetics for a

wider range of metals on well-defined oxide surfaces of relevance to industrial oxide-supported metal catalyst systems³⁰. Specifically, the instrument's metal atom beam source has been improved so that it is now capable of producing a pulsed atomic beam with lower vapor pressure metals (Pt, Pd, Rh, Ni, Au, etc.), allowing for the measurement of heats of adsorption for these industrially and scientifically important transition metal catalysts. This was accomplished by replacing the Knudsen cell type metal vapor source with an electron beam evaporator, which localizes the heat input to the surface of the metal melt and produces much less optical radiation, thereby increasing the signal/noise of the calorimetry measurements. This improvement will allow for experiments that can clarify the interfacial bonding strengths of a wide variety of metal / support systems.

Chapter 2

Enthalpies and Entropies of Adsorption on Well-Defined Oxide Surfaces: Experimental Measurements

2.1: Introduction

The chemistry of oxide surfaces plays a central role in many current technologies, and promises to play an ever-increasing role in future technologies. In addition to their importance in catalytic and electrocatalytic materials, oxides are central ingredients in photocatalysts, photoelectrocatalysts, transparent electrodes for photovoltaics, solid electrolytes, superconductors, microelectronics, computer chips, protective coatings, windows, optics, batteries, piezoelectrics, pyroelectrics, and ceramics, just to name a few. When compared to metal surfaces, however, much less is understood about the chemistry of oxide surfaces. This is mainly related to the greater difficulty of preparing well-ordered single crystalline surfaces of oxides, and the fact that even once prepared they are often not electrically conductive enough to be amenable to many of the techniques for surface characterization. However, the past decade has seen the development of many new sample preparation techniques for oxide surfaces that overcame these problems, and consequently an explosion of experimental results characterizing adsorption and surface reactions on well-defined oxide surfaces, where the nature of the surface sites involved is well known.

Here we review what has been learned about the enthalpies and entropies of adsorption reactions on well-defined oxide surfaces from experimental measurements. In discussing well-defined oxide surfaces here, we refer to studies on ordered surfaces of bulk single crystal oxides and single-facet nanomaterials, and of ordered thin films of oxides that have been grown epitaxially on the surfaces of bulk single crystals of metals. We will refer to these collectively as

“single-crystalline oxide surfaces” below. Since adsorption energies on thin-film oxides have been shown to be strengthened by interactions with the underlying metal when the oxide film is 1 nm thick or thinner, we limit this review to include only those cases where the oxide films are thicker than 1 nm. Trends in experimental adsorption energies and entropies are revealed and discussed. These energies and entropies will serve as important experimental benchmarks to guide the currently intense worldwide efforts to improve theoretical methods, like density functional theory (DFT) with periodic boundary conditions, with respect to their accuracy at predicting the relative energies of adsorbates on oxide surfaces.

Accompanying the rapid developments in the experimental study of adsorption on oxide surfaces mentioned above, there also has been a dramatic increase in efforts to understand the surface reactivity of oxides and trends in their surface reactivity at the electronic-structure level, through computational quantum mechanical approaches. Approaches using density functional theory, with the generalized gradient approximation (GGA-DFT) and periodic boundary conditions, which have proven so effective in explaining and even predicting the reactivity of metal surfaces⁵⁴⁻⁶⁰, have been shown to have greater limitations when applied to oxide surfaces⁶¹⁻⁶³. An improved version, "DFT+U", cures some of the problems by introducing the U parameter in the Hamiltonian to localize the d- or f-electrons. This U can be chosen to give a better fit than GGA-DFT to some reaction energies⁶³. GGA+U is now the most widely used methodology, but it still has limitations in energy accuracy. Due to the greater challenges presented by oxide surfaces, there are currently many efforts worldwide to improve such computational methodology for applications in oxide surface chemistry, for example through use of hybrid functionals, which is a much more computationally intensive alternative.

Currently, the main experimental benchmarks that are used for validating these new theoretical approaches are bulk properties like the heats of oxide formation, band gaps, lattice parameters, phonon spectra, etc. Experience with metal surfaces has proven that to achieve the most effective theoretical codes, they must also be validated against experimental measurements of surface properties, namely adsorption energies, surface reaction energies, and adsorbate geometries for well-defined adsorbates at well-defined surface sites. Such measurements are only possible using single crystalline surfaces. Currently, there is no easily accessible source for adsorption energies of well-defined adsorbates at well-defined sites on single crystalline oxide surfaces. This review presents by far the most extensive compilation of such energies yet available. In many cases, these energies have been extracted directly from the source literature, but in many cases the data in the source literature were treated here with kinetic and thermodynamic models to provide reliable estimates of the adsorption energies and metal / oxide adhesion for vapor-deposited metal films.

Adsorption energies on single-crystalline oxide surfaces have been measured by single crystal adsorption calorimetry (SCAC); equilibrium adsorption isotherms (EAI); and temperature programmed desorption (TPD), also referred to as thermal desorption spectroscopy (TDS). The SCAC measurements provide these energies very directly, so they are unambiguous. Equilibrium adsorption isotherms are also relatively straightforward, but do require that the adsorption \rightleftharpoons desorption process is reversible.

On the other hand, TPD is much less direct and requires some explanation and, for many of the cases here, our own interpretation of the measured TPD spectra to extract adsorption energies. In the best case, TPD only provides an accurate activation energy for desorption, E_d . This can only be equated with the adsorption energy when both the adsorption \rightleftharpoons desorption

process is reversible and the activation energy for adsorption is negligible. We will limit ourselves to such cases here. Also, many of the papers used here for extracting adsorption energies in such cases have already reported such estimates of adsorption energies, but only by assuming a pre-exponential factor for desorption, ν . In these cases, and when the adsorbate is molecularly adsorbed, we will reevaluate the adsorption energies using instead values for ν estimated from a recently discovered correlation between the pre-exponential factor for desorption and the entropy of the gas phase product ⁹, which applies only to reversible molecular adsorption \rightleftharpoons desorption where the activation energy for adsorption is negligible. This new approach provides more reliable estimates for adsorption energies of molecularly adsorbed species.

In some cases of dissociative adsorption and associative recombination in desorption, the criteria also hold that adsorption \rightleftharpoons desorption is reversible and the activation energy for adsorption is negligible. We will also estimate adsorption energies from TPD data for these cases, using instead estimates for the pre-exponential factor determined in similar cases from detailed kinetic analyses of the TPD peak line shapes versus coverage. Unfortunately, there are few cases of this type. There are no other cases where we know the adsorption energy associated with molecular fragments on single crystal oxide surfaces by either EAI or direct calorimetric measurements. These must await SCAC measurements, which we have recently initiated for studying dissociative adsorption on single crystal oxide surfaces.

2.2: Experimental Methods for Measuring Adsorption Energies and Entropies on Single Crystals

2.2.1: Single Crystal Adsorption Calorimetry (SCAC)

Calorimetric measurements of heats of adsorption of gases on high surface area metal films were being performed already in the 1950s (⁶⁷⁻⁶⁹ and refs. therein). However, on such complex surfaces, it is generally not clear what are the structures or even the chemical formulas of the adsorbates being formed upon gas adsorption. Single crystals provide much simpler surfaces which offer tremendous advantages for determining the chemical formulas and geometric structures of the adsorbates formed upon gas adsorption. Adsorption microcalorimetry thus became much more powerful when methods were developed which allowed it to be done on such single crystal surfaces by measuring the tiny temperature increase associated with exothermic gas adsorption.

Masel's group published a description of the first apparatus that could measure heats of adsorption on single crystal surfaces ⁷⁰. The precision of that method for heat detection, based on a thermistor, was problematic and not further applied. The real breakthrough came with an apparatus developed by David King's group, who named the measurement of heats of adsorption on single crystal surfaces "single crystal adsorption calorimetry," or SCAC for short. Their apparatus, shown schematically in Fig. 2.1, detects the transient temperature rise of a single crystal (proportional to the heat of reaction) upon adsorption of gas pulses from a molecular beam onto surface using infrared optical pyrometry ^{6, 71-77}. This method is sensitive enough to detect the heat of adsorption of gas pulses containing only ~5% of a monolayer of adsorbate, thus allowing measurements of the heat of adsorption versus coverage. However, since the heat signal in that method varies as T^3 , where T is the sample temperature, it is not sensitive enough

for measurements on samples well below room temperature. King's group subsequently developed a method that works at very low temperatures wherein the single crystal is fused to a pyroelectric crystal (lithium tantalate)⁷⁸, but this has not been further applied since it does not allow most samples to be annealed to high enough temperature to obtain a well ordered surface.

Most recently, our group has developed^{31, 79-81} and further perfected^{50, 51, 82, 83} a heat detection method for SCAC based on gently touching a soft pyroelectric polymer ribbon against the back surface of the single crystal sample during calorimetry measurements, and removing it during sample cleaning and annealing. This heat detection method has proven to have much, much higher sensitivity. It is now routinely applicable at cryogenic conditions^{51, 84-86}. Precision is high, with a pulse-to-pulse standard deviation as good as 1.3 kJ/mol from 100 K to 300 K when using gas pulses that contain only 1.5×10^{13} molecules per cm^2 (1% of a monolayer)⁵¹. The pulse-to-pulse standard deviation mentioned above sets the detection limit at ~ 5 kJ/mol. This heat detection method has the added advantage that it can use much thicker single crystals⁸², which are easier to obtain, clean and maintain. The absolute accuracy of this type of calorimeter depends on the accuracy of its calibration, but also the accuracy of measuring the absolute beam flux and area, and the sticking probability. When applying it to measure the energy of metal vapor adsorption, where the high-coverage limit should equal the literature value for the bulk heat of sublimation, we generally found the agreement to be within 3% (based on the average of several runs). Most of those measurements will be reviewed below. Our more recent low-temperature measurements with molecules which form multilayers, whose heat can also be compared to the bulk sublimation energy, also gave absolute accuracies better than 3%⁸⁵. The re-adsorption of gases in the molecular beam that do not stick upon first hitting the sample makes a negligible contribution to the heat for all the systems we have studied, and will generally be the

case when the sticking probability is higher than 0.3 and the gases are well pumped. Also, we have never noticed any contamination on the front face of the sample from the ribbon touching the back of the sample.

In SCAC, one derives the differential heat of adsorption (q_{ad}) from the measured heat (q_{cal}) using^{31, 50}:

$$q_{\text{ad}} = -\Delta H_{\text{ad}}^0 = -\Delta U_{\text{ad}}^0 + RT_{\text{sample}} = q_{\text{cal}} - 4/2 RT_{\text{source}} + 5/2 RT_{\text{sample}}, \quad (2.1)$$

where ΔH_{ad}^0 is the standard enthalpy change for the adsorption reaction (gas \rightarrow adsorbed, with gas and solid both at the temperature of the single crystal, T_{sample}), R is the universal gas constant, and T_{source} is the temperature of the effusive molecular beam source. The heat of adsorption as defined here is identical to the isosteric heat of adsorption. The superscripts 0 here on ΔH_{ad}^0 and ΔU_{ad}^0 refer to their values at the standard pressure of 1 bar. Both ΔU_{ad}^0 and ΔH_{ad}^0 are always negative numbers, so ΔU_{ad}^0 is always smaller in absolute value than ΔH_{ad}^0 .

Methods for and results from SCAC have been reviewed several times previously^{2, 52, 87-89}.

2.2.2: Equilibrium Adsorption Isotherms (EAI): Enthalpies *and* Entropies of Adsorption

The use of equilibrium adsorption isotherms to determine the enthalpy change upon adsorption of a gas (ΔH_{ad}) is analogous to making a Clausius-Clapeyron plot to determine the enthalpy of vaporization (ΔH_{vap}). In the latter, the equilibrium vapor pressure above a liquid ($P_{\text{vap,eq}}$) is measured versus temperature (T). The plot of $\ln(P_{\text{vap,eq}}/P^0)$ versus $1/T$ over a reasonably narrow range of T gives a straight line with slope equal to $-\Delta H_{\text{vap}}^0/R$ (where P^0 is the standard pressure of 1 bar and R is the gas constant) and a y-intercept equal to $\Delta S_{\text{vap}}^0/R$, where ΔS_{vap} is the entropy of vaporization. The superscripts 0 here on ΔH_{vap}^0 and ΔS_{vap}^0 refer to their

values at the standard pressure of 1 bar. Their values correspond to the average temperature in the range over which this straight line is fitted to the data. Similarly, to determine an adsorption enthalpy, the equilibrium vapor pressure ($P_{\theta,\text{eq}}$) above an adlayer at fixed coverage (θ) is measured versus temperature (T). The plot of $\ln(P_{\theta,\text{eq}}/P^0)$ versus $1/T$ over a reasonably narrow range of T gives a slope equal to $\Delta H_{\text{ad}}^0/R$ and a y-intercept equal to $-\Delta S_{\text{ad}}^0/R$, where both values correspond to that specific coverage and 1 bar pressure. The change of signs here is due to reversing the reaction direction from vaporization to condensation. The coverage dependence can be determined by repeating the measurements and data analysis at a different coverage. Coverage can be measured by any of a variety of probes. We will cite here examples where it was measured on flat single crystals by LEED and helium atom scattering for the purposes of EAI measurements.

The simplest way to generate the needed data ($P_{\theta,\text{eq}}$ versus T at several fixed coverages) is to perform an isotherm, starting with a clean surface in a fixed volume, and then introducing more and more gas in fixed increments, allowing the system to come to equilibrium at the same constant temperature after each incremental dose. The pressure ($P_{\theta,\text{eq}}$) and coverage (θ) are measured at each increment and plotted as θ versus $P_{\theta,\text{eq}}$. After plotting a series of these isotherms, a horizontal cut at any constant θ gives the needed $P_{\theta,\text{eq}}$ versus T data points^{7,45}.

Starting already before 1978, a group at the University of Washington made the first quantitative measurements of adsorption enthalpies on any oxide single crystal surfaces using EAI measurements on “MgO(100) smoke”^{7,45}. This special MgO powder was produced by burning Mg filaments as done in early camera flash bulbs. This results in a powder with relatively large specific area which, upon examination by electron microscopy, proved to consist primarily of single-crystal nanocubes of MgO (with sizes from 20 to 200 nm) with only the (100)

surface exposed except at the edges ⁷. The advantage of such a single-facet powder (which we will refer to here as “MgO(100) smoke”) compared to a flat crystal is that the surface coverage can be measured with much simpler equipment. Thus, the equilibrium coverage was measured by simple volumetric measurements of the amount of gas consumed by adsorption (i.e., by monitoring the decrease in pressure compared to that for the same number of moles of gas introduced into the same volume in the absence of any adsorbent).

An advantage of EAI measurements is that they also provide the entropy of adsorption. To our knowledge, the only cases where this entropy has actually been determined in this way for any single crystal oxide surface are about a dozen examples using MgO(100) smoke, which we will discuss in detail. The entropy of adsorption is important since it can be combined with the enthalpy to provide the equilibrium constant for adsorption, K_{eq} , and its temperature dependence:

$$\ln K_{\text{eq}} = \Delta S_{\text{ad}}^0/R - \Delta H_{\text{ad}}^0/(RT). \quad (2.2)$$

As we discuss below, the entropy of adsorption is also needed to calculate the rate constant for reactions of the adsorbate using transition state theory. We apply it below to do just that, specifically in predicting pre-exponential factors for desorption from entropy trends.

This MgO(100) smoke was also used by that same group for calorimetric measurements of the heat capacity of He adlayers on MgO(100) back in 1985 ⁴⁶, which to our knowledge was the only calorimetric measurement ever reported for the heat capacity of any adlayer on any single crystal surface, until our recent report for adsorbed water on Pt(111) ⁸⁵. Interestingly, while that same calorimeter could have been used to determine adsorption energies on MgO(100) smoke, it was not applied for that purpose.

2.2.3: Temperature Programmed Desorption (TPD): Activation Energies and Prefactors for Desorption

In TPD, a sample with pre-adsorbed species is heated in ultrahigh vacuum, typically at a constant heating rate between 0.1 and 100 K/s, while monitoring the rate of appearance of gases emitted by the surface⁴⁷. The rate of appearance of gases is typically monitored using a mass spectrometer. A typical example of TPD, measuring the rate of butane desorption from MgO(100) after different initial doses⁸, is shown in Fig. 2.3.

Methods for improving mass spectrometric measurements of desorption rates for TPD have been discussed⁹⁰. Frequently the ionization source of the mass spectrometer or its entrance aperture is located in line-of-sight, near and normal to the surface to enhance the signal of the desorbing species being monitored. In well-pumped systems this has the advantages that (1) the signal from the front surface of the sample is greatly enhanced compared to its back and edges, and (2) the signal for a given species is directly proportional to the flux of desorbing molecules (provided the common assumptions hold that all the molecules desorb with the same velocity distribution and that their internal energy distribution does not change, or at least that the changes in this distribution do not affect the ionization probability). It is necessary for kinetic analyses to be able to relate the measured signal (flux) at any time, t , to the total instantaneous desorption rate, $r(t)$.

Commonly, it is assumed that this total desorption rate is directly proportional to the instantaneous mass spectrometer signal for a given species, but this is not true for such line-of-sight measurements if the angular distribution of desorbing molecules changes. To minimize the error when the desorption angular distribution changes, the mass spectrometer can be placed so that the measured flux is at the so-called magic angle ($\sim 38^\circ$ from the surface normal)⁹¹. If the signal is sufficient, it is better to instead monitor the non-line-of-site increase in the background

pressure of the desorbing gas, which is proportional to the total desorption rate for well-pumped systems even when the velocity and angular distributions of the desorbing gas change with temperature.

Once desorption rate data versus temperature and coverage of the type shown in Fig. 2.3 are obtained, one analyzes it to determine the activation energy for desorption, E_d . There are many methods that have been used to do this. A useful comparison on these methods and their accuracy in extracting E_d and other kinetic parameters has been published⁹². That report shows that some methods are much more accurate than others. When the adsorption \rightleftharpoons desorption process is reversible and the activation energy for adsorption is negligible, E_d can be related to enthalpy of adsorption, ΔH_{ad}^0 , by adding $\frac{1}{2} RT$:

$$q_{ad} = -\Delta H_{ad}^0 = E_d + \frac{1}{2} RT, \quad (2.3)$$

where R is the gas constant and T is the average sample temperature where the desorption rates were measured⁸⁷. When the sticking probability for adsorption is near unity, as is usually the case for simple molecular adsorption, it is safe to assume that the activation energy for adsorption is negligible.

To extract E_d , the surface species are always assumed to be in equilibrium, in which case the desorption rate is a single-valued function of coverage and temperature: $r(\theta, T)$. We next describe our recommended method for extracting E_d for the case of most importance here: reversible molecular adsorption / desorption, where it is reasonable to assume that desorption is a first-order process, in which case the Polanyi-Wigner equation gives:

$$r(\theta, T) = -d\theta/dt = \nu \exp(-E_d(\theta)/RT) \theta, \quad (2.4)$$

where ν is the pre-exponential factor, which we typically assume does not vary with coverage or temperature, and $E_d(\theta)$ is the coverage-dependent desorption activation energy. This adsorption

energy changes with coverage because various adsorption sites (e.g. defects, terrace sites, etc.) have different strengths of interaction, and interactions between the adsorbates change with the average adsorbate-adsorbate distance, so E_d is certainly expected to vary with coverage. By mathematical inversion of the rate data, the value of $E_d(\theta)$ can be obtained from the Polanyi-Wigner equation if ν is known ⁴⁹:

$$E_d(\theta) = -RT \ln[(-d\theta/dt)/(\nu\theta)]. \quad (2.5)$$

Typically, one treats ν as a variational parameter to optimize the fit between experimental and simulated TPDs, thus finding the prefactor that best matches the kinetics of the desorption process. This was the method used for alkanes on MgO(100) ^{8,24}. As to be discussed below, the value of the prefactor can be used to estimate the adsorption entropy, since the transition state for desorption is very similar to the gas.

One can also extract E_d using the first-order Redhead equation, which relates the temperature at which the desorption rate maximizes (T_p) to E_d , the heating rate (β) and ν ⁴⁷:

$$E_d/(RT_p^2) = (\nu/\beta) \exp[-E_d/(RT_p)]. \quad (2.6)$$

The most common practice is to simply use Eq. (2.6) and an assumed value for ν , which gives reasonable accuracy if the value of ν is approximately correct. A factor of 10 error in ν corresponds to an error of only $\sim 2.3RT_p$ in E_d , which is only 6 kJ/mol, or $\sim 7\%$, for $T_p = 300$ K and $\nu = 10^{15} \text{ s}^{-1}$. We review below our recent discovery of a new method for estimating this prefactor ⁹, which gives values with a standard deviation in $\log(\nu/\text{s}^{-1})$ of only 0.86 from a tabulation of 24 measured prefactors. We apply this below in Eq. (2.6) to estimate E_d for many systems.

Whenever molecular adsorption / desorption is not completely reversible such that partial dissociation competes with desorption, it leads to complexity that invalidates the above analyses.

A creative way to circumvent that problem whenever that dissociation involves C–H, O–H or N–H dissociation is to use the deuterated isotope, since this often greatly suppresses the dissociation probability during TPD (via the primary kinetic isotope effect), so that molecular desorption can now dominate⁹³.

If adsorption is dissociative but the two adsorbed products are attracted to each other and prefer to populate neighboring sites, their associative desorption kinetics can be treated as a pseudo-first-order process using the same first-order analyses as described above to get E_d . This still requires that the adsorption \rightleftharpoons desorption process be reversible and the activation energy for adsorption be negligible (i.e., sticking probability near unity). We will analyze some cases like this below.

2.3: Intact Molecular Adsorption and Noble Gas Adsorption on MgO(100)

Table 2.1 summarizes reported measurements of the adsorption enthalpies and entropies determined on MgO(100) by EAI for several noble gases and molecules which remain intact upon adsorption. The standard entropies of the gas phase species at the average temperature of the measurement, S_{gas}^0 , are included for comparison. Part A shows results for MgO(100) smoke where the surface coverage was measured by volumetric techniques and Part B is for planar MgO(100) single crystals where the surface coverage was measured using ultrahigh vacuum (UHV) techniques. Note that for several of these studies, the structure of the adlayer as determined by neutron diffraction or other diffraction-based techniques was also reported.

Table 2.1. Enthalpies and entropies of molecular adsorption on MgO(100) determined by equilibrium adsorption isotherms in a temperature range with the specified average temperature. When a range of enthalpy or entropy values are given, the arrow indicates that this is the direction of increasing coverage.

adsorbate	$-\Delta H_{ad}^0$ /(kJ/mol)	$-\Delta S_{ad}^0(T)$ /(J/mol/K)	$S_{ad}^0(T)$ /(J/mol/K)	$S_{gas}^0(T)$ /(J/mol/K)	temperature / K	citation
PART A: MgO(100) smoke						
Ar	8.4				60	7
Kr	11.7				85	7
Xe	15.5				115	7
N ₂	14.7					94
NH ₃	71 → 25	36 → 161	126 → 1	162	170	95
methane	12	91	49.5	141	77	96
ethane	18	100	93.9	193	120	96
propane	23	96	138	234	140	96
butane	27	100	169	269	163	96
pentane	31	140	161	301	185	96
neopentane	30.4	146	112	258	200	97
hexane	34	142	198	340	207	96
methanol	72	124	112	235	264	98
CH ₃ Cl	25±4				168	99
PART B: Flat MgO(100) crystals						
H ₂ O ^a	50 → 85±2				203	100
C ₂ H ₂ (2×2) ^b	29±2				91	101

a HAS = He atom scattering

b LEED = low energy electron diffraction

2.3.1: Entropies of Adsorption on MgO(100) and Other Surfaces: Correlation with Gas-Phase Entropies

Figure 2.4 shows the standard entropies of these adsorbates ($S_{\text{ad}}^0 = S_{\text{gas}}^0 + \Delta S_{\text{ad}}^0$) on MgO(100) surface, determined by EAI from Table 2.1, plotted versus the standard entropy of the gas phase species at the temperature of the measurement. We add to this plot the standard entropies of these same and other adsorbates determined from desorption prefactors measured in TPD (at different temperatures), using transition state theory as described next. The values of these prefactors, desorption temperatures, heats of adsorption and corresponding adsorbate entropies based on TPD data are listed in Table 2.2, to be described in more detail below.

When the adsorption \rightleftharpoons desorption process is reversible and the activation energy for adsorption is negligible, as it is for the cases in Table 2.2, the transition state for desorption is the molecule with its center of mass constricted to lie on a plane parallel to the surface at some distance far enough away from the surface that its interaction with the surface is negligible for any angle of rotation. In this case, the transition state is very well defined. Its entropy ($S_{\text{TS, des}}^0$) is identical to that for the gas (S_{gas}^0) at the same temperature, except that it is missing one translational degree of freedom (the one perpendicular to the surface):

$$S_{\text{TS, des}}^0 = S_{\text{gas}}^0 - S_{\text{gas, 1D-trans}}^0. \quad (2.7)$$

The value of $S_{\text{gas, 1D-trans}}^0$ for any gas can easily be calculated using statistical mechanics (the Sackur-Tetrode equation)²⁶, assuming that each translational degree of freedom contributes 1/3 of the total 3D translational entropy. This gives that:

$$S_{\text{gas, 1D-trans}}^0 = (1/3)\{ S_{\text{Ar, 298K}}^0 + R \ln[(m/m_{\text{Ar}})^{3/2}(T/298\text{K})^{5/2}]\}, \quad (2.8)$$

where m is the molar mass of the gas, m_{Ar} is that for argon, and $S_{\text{Ar, 298K}}^0$ is the entropy of Ar gas at 1 bar and 298 K ($= 18.6R$).

Table 2.2. Adsorption enthalpies and entropies for molecularly adsorbed species on MgO(100) determined by TPD, showing also the peak temperature and heating rate. Prefactor and enthalpy values in bold were determined in the original paper by careful analysis of the TPD data, so the resulting adsorbate’s entropy at T_p determined from this prefactor using Eq. (11) are also in bold. The remaining prefactor, enthalpy and entropy values not in bold were estimated using Eqs. (16), (6) and (11), resp. The entries in bold under “Adsorption site” are as reported in the original paper. Those not in bold are based on our tentative assignments as justified in Section 4. When a range of T_p and enthalpy values are given, the arrow indicates that this is the direction of increasing coverage.

adsorbate	adsorption site	T_p / K	$\beta / (\text{K/s})$	$\log(\nu / \text{s}^{-1})$	$-\Delta H_{\text{ad}}^0 / (\text{kJ/mol})$	$S_{\text{ad}}^0(T_p) / R$	$S_{\text{gas}}^0(T_p) / R$	citation
H ₂ O	Mg	235	3	14.5	67.9	11.9	21.7	102
CO		59 → 57	0.2	13.8	16.9 → 16.3	9.38 → 9.30	18.1 → 18.0	103
		63 → 59	0.6	13.9 → 13.8	17.6 → 16.5	9.53 → 9.40	18.3 → 18.1	49
	c(4×2) phase	45	0.6	13.7	12.3	8.72	17.2	49
NO		84 → 75	0.5	14.0	24.1 → 21.3	10.4 → 10.1	19.6 → 19.2	104
methane		47	0.6	13.1	12.3	8.20	15.0	24
ethane		75	0.6	14.9	22.5	9.76	20.9	24
propane		93	0.6	15.6	29.4	11.9	24.9	24
butane		111	0.6	15.7±1.6	35.4±3.9	15.8	27.8	8
hexane		144	0.6	16.0	47.0	22.3	36.4	24
octane		175	0.6	17.9	63.6	27.4	46.1	24
decane		204	0.6	19.1	77.9	34.9	56.3	24
benzene	parallel to surface	175	5	15.0	51.1	16.5	28.3	105
	tilted	148	5	14.9	42.6	15.9	27.3	105
methanol	Mg	296 → 275	3	15.3	90.5 → 83.7	16.9 → 16.6	28.8 → 28.4	106
	oxygen	240	3	15.2	72.3	16.2	27.8	106

Within transition state theory¹⁰⁷, the desorption prefactor is given by:

$$\nu = k_B T/h \exp(\Delta S_{\text{TS, des}}^0/R) = k_B T/h \exp[(S_{\text{TS, des}}^0 - S_{\text{ad}}^0)/R], \quad (2.9)$$

where k_B is Boltzmann's constant and h is Planck's constant. Substitution using Eq. (2.7) gives:

$$\nu = k_B T/h \exp[(S_{\text{gas}}^0 - S_{\text{gas,1D-trans}}^0 - S_{\text{ad}}^0)/R]. \quad (2.10)$$

This can be rearranged to give an expression for calculating S_{ad}^0 from an experimentally determined value of ν :

$$S_{\text{ad}}^0 = (S_{\text{gas}}^0 - S_{\text{gas,1D-trans}}^0) - R \ln [\nu h/(k_B T)], \quad (2.11)$$

where all entropies are for the same temperature T as the measurement of ν . This expression was used to calculate the adsorbate entropies listed in Table 2.2 and Table 2.3 and plotted in Fig. 2.4 for the points from TPD. The values of S_{gas}^0 for these molecules are found in standard thermodynamic tables and, when necessary, extrapolated to different temperatures using tabulated heat capacities. The validity of Eq. (2.11) is verified by the excellent agreement seen in Fig. 2.4 between the adsorbate entropies on MgO(100) obtained using Eq. (2.11) and those directly measured by EAI. Below we summarize its applications to understanding the thermodynamics of adsorption, some of which have already been described⁹, and which prove quite powerful.

By combining the adsorbate entropies on MgO(100) measured by both EAI and TPD in Fig. 2.4, one can see that there is a nearly perfect linear correlation between S_{ad}^0 and S_{gas}^0 , with a slope of 0.70, a y -intercept of $-4.7R$ and a correlation coefficient (R^2) of 0.96 (standard deviation = $1.6R$). Note that this is for temperatures where desorption is fast enough to perform these EAI and TPD measurements ($\sim 10^{-3}$ to 100 ML/s), which are the most relevant temperatures for many types of experiments. We showed that this correlation becomes a direct proportionality if we first subtract from S_{gas}^0 the entropy associated with one degree of translational freedom,

$S_{\text{gas,1D-trans}}^0$, to correct for the fact that an adsorbate has very restricted motion (i.e., sits in a very steep potential well) in the direction perpendicular to the surface, z ⁹. The proportionality:

$$S_{\text{ad}}^0 = 0.68 (S_{\text{gas}}^0 - S_{\text{gas,1D-trans}}^0) \quad (2.12)$$

was found to fit the data very well, with $R^2 = 0.96$ and a standard deviation of $1.7R$. This proves that the adsorbate maintains $\sim 2/3$ of the entropy of the gas-phase species (after subtracting the entropy of its z translation motion).

As shown in Fig. 2.5, the linear relationship between S_{ad}^0 and S_{gas}^0 for MgO(100) in Fig. 2.4 was found to hold with the same slope and almost as high R^2 (0.94) when we include entropies for all the other molecules whose prefactors for desorption had been determined experimentally from fitting TPD data in a reliable way on any other oxide single crystal surface (as listed in Table 2.3, to be discussed below) and our own experimental determinations of prefactors for linear alkanes on graphite(0001) and Pt(111) from TPD data¹⁰. Again, Eq. (2.11) was used to convert measured prefactors into adsorbate entropies. The equation for this line in Fig. 2.5:

$$S_{\text{ad}}^0(T) = 0.70 S_{\text{gas}}^0(T) - 3.3R \quad (2.13)$$

agrees very well with the measured entropies, with a standard deviation of only $2.2R$. Including this much larger data set shifted the y -intercept only very slightly (up by $1.4R$) from the line for MgO(100), and the slope stayed the same. This indicates that this linear relationship is independent of both the surface material and the adsorbed molecule. As we show below, Eq. (2.13) provides a very useful and simple method for estimating adsorption entropies for molecularly adsorbed gases on oxide surfaces. We also show below that this can be applied to estimate pre-exponential factors in rate constants for reactions involving adsorbates, like desorption.

The explanation we offered for the slope of $\sim 2/3$ in Figs. 2.4 and 2.5 and Eqs. (2.12) and (2.13) is that there is a very weak corrugation of the molecule / surface interaction potential for translational and rotational motions parallel to the surface, with saddle points that are lower than RT at temperatures where desorption is fast enough for EAI and TPD, but a steep energy well for motion perpendicular to the surface. Thus, all x and y components of translational and rotational motion of the gas molecule are maintained upon adsorption, but any z components are lost. If the entropies of these motions are equally distributed between x , y and z directions in the gas, then $2/3$ of the entropy will be maintained after adsorption (when vibrational entropy is negligible)⁹.

We found that the behavior is somewhat different for molecules with gas entropies above $\sim 60R$, where the slope increased to almost unity up to $100R$ (i.e., for n -alkanes with >10 atoms)⁹. The reason for this change is the slower increase of the rotational entropy in the gas phase molecules due to the bends in these longer-chain alkanes and the increased importance of vibrational entropy in these larger molecules (which desorb at higher temperatures)⁹. This is the same reason that the prefactors for n -alkane desorption stop increasing with chain length above 10 carbons^{25, 108}, as explained on the basis of molecular dynamics simulations¹⁰⁹⁻¹¹¹.

The only case where ΔS_{ad}^0 was measured versus coverage by EAI is for NH_3 on $\text{MgO}(100)$ smoke, which shows a large decrease with coverage from -47 J/mol/K (after defects are populated) to -172 J/mol/K⁹⁵. A large decrease in ΔS_{ad}^0 is predicted for an ideal 2D lattice gas model where adsorbate-adsorbate interactions are negligible, due to the large decrease in configurational entropy of the adsorbate as the fractional occupation of sites (θ) increases⁶⁶:

$$S_{\text{config}} = R \ln [(1-\theta)/\theta]. \quad (2.14)$$

The accompanying decrease in the heat of adsorption with coverage, from 71 to 25 kJ/mol here ⁹⁵, indicates that there are repulsive lateral interactions between adsorbed ammonia molecules. However, at low coverage where the average adsorbate-adsorbate separation is large, these can be neglected and the adlayer still should have very large configurational entropy. The point for NH₃ was omitted from Fig. 2.5 since it drops from 5*R* above the line to 10*R* below the line (i.e., ~zero) with increasing coverage. No variation with coverage was reported for the other adsorbates studied by EAI, attributed to the fact that they had attractive interactions and thus condensed into islands. Thus, Fig. 2.5 and Eq. (2.13) are only valid for cases with such attractive interactions. A huge decrease in S_{ad} with coverage is probably characteristic of adsorbates with strong repulsive interactions.

There is no significant configurational entropy for the adsorbates that gave rise to the linear relationships of Figs. 2.4 and 2.5 and Eqs. (2.12) and (2.13). Those were for high coverages and mainly for cases where there are attractive adsorbate-adsorbate interactions, so they cluster into 2D islands. The usual statistical mechanics model adapted for that case is the 2D *crystal lattice* model, and *not* the 2D *ideal lattice gas* model, which is only appropriate when there are negligible or weakly repulsive adsorbate-adsorbate interactions. There is no configurational entropy in a 2D *crystal lattice*, only vibrational entropy (including frustrated rotational and translational entropy). It is surprising that ~2/3 of the entropy associated with motion in the gas phase remains after adsorption, suggesting that these 2D islands may be liquid-like at these temperatures where desorption is fast enough for TPD and EAI measurements. Rotations and translations parallel to the surface somehow remain unhindered in such adsorbate islands. The data points in Fig. 2.5 are also reasonably fit by the trend predicted for 3D liquids based on Trouton's Rule ⁹, which again illustrates how large these adsorbate entropies are.

Table 2.2 summarizes TPD measurements of the activation energies (E_d) and pre-exponential factors (ν) for desorption determined on MgO(100) for molecules which remain intact upon adsorption and desorption. We first list the peak temperatures for desorption (T_p) and heating rates (β). We also list the values reported for E_d and ν when the analysis method used to determine these was rigorous, and the enthalpy of adsorption determined from E_d using Eq. (2.3). We do not include here reported values for E_d and ν in those cases where the value for ν was simply assumed. Instead, we list here what we believe to be a more reliable estimate for ν (determined based on the entropy correlation of Fig. 2.5 and Eq. (2.13) and transition state theory, as described next), and its corresponding value for E_d (determined from T_p , ν and β , using simple first-order Redhead analysis, Eq. (2.6)).

2.3.2: Predicting Desorption Prefactors using this Adsorption Entropy Correlation

Combining Eq. (2.7) with the approximation for S_{ad}^0 given by Fig. 2.5 and Eq. (2.13) (i.e., $S_{ad}^0 = 0.70 S_{gas}^0 - 3.3R$), we get that the standard entropy of activation, $\Delta S_{TS, des}^0$, is:

$$\begin{aligned}\Delta S_{TS, des}^0 &= S_{TS, des}^0 - S_{ad}^0 = (S_{gas}^0 - S_{gas, 1D-trans}^0) - (0.70 S_{gas}^0(T) - 3.3R) \\ &= 0.30 S_{gas}^0 + 3.3R - S_{gas, 1D-trans}^0,\end{aligned}\quad (2.15)$$

where $S_{gas, 1D-trans}^0$ can be calculated from Eq. (2.8). Simply plugging this value for $\Delta S_{TS, des}^0$ into Eq. (2.9) gives the prefactor ν :

$$\begin{aligned}\nu &= (k_B T/h) \exp(\Delta S_{TS, des}^0/R) = k_B T/h \exp[(0.30 S_{gas}^0 + 3.3R - S_{gas, 1D-trans}^0)/R] \\ &= (k_B T/h) \exp\{0.30 S_{gas}^0/R + 3.3 - (1/3)\{18.6 + \ln[(m/m_{Ar})^{3/2}(T/298K)^{5/2}]\}\}.\end{aligned}\quad (2.16)$$

Figure 2.6 shows a plot of the predictions of this equation plotted versus experimentally measured desorption prefactors for all molecules on single crystal oxides listed in Table 2.3, plus our own values for alkanes on Pt(111) and graphite(0001)¹⁰. The predictions agree very well

with these experimental prefactors with a standard deviation in $\log(\nu/s^{-1})$ of only 0.86, confirming the validity of Eq. (2.16) for estimating prefactors. Several discussions of the values for desorption prefactors have been published, but none of these have presented any relationships with prediction integrity anywhere near as good as Eq. (2.16)¹¹²⁻¹¹⁸.

For the other molecules/surfaces listed in Tables 2.2 and 2.3 where the desorption prefactor was not measured by fitting TPD data, we used Eq. (2.16) to estimate ν , and then used this ν in Eq. (2.6) to estimate E_d , and from that the heat of adsorption. These are the values listed in Tables 2.2 and 2.3 for those systems (except for the species at defect sites). Using twice the standard deviation on $\log(\nu/s^{-1})$ of 0.86 in Fig. 2.6 gives a factor of 50 maximum error in ν at the 95% confidence limits, corresponding to a maximum error in the heat of adsorption of $4.0RT_p$, or 8 kJ/mol when $T_p = 250$ K.

Note that Eq. (2.16) is for the majority sites on single crystal surfaces, and therefore appropriate for species on terraces only. We do not think it is appropriate for the entries in these tables that are assigned to defect sites. These are most frequently at step edges, and we have shown previously that metal adatoms have a desorption prefactor that is 10^5 -fold large at step edges than at terraces on Mo(100), due to the loss of all translational motion except in the one direction along the step edge¹¹⁸. For this reason, the prefactors in Table 2.3 for all species at defect sites have been taken as the predicted value from Eq. (2.16) but increased by this same factor of 10^5 . We do not know the accuracy of these prefactors for defect sites.

2.3.3: Trends in Adsorption Enthalpies on MgO(100)

Table 2.1 shows that, within a given class of adsorbates (like noble gases or alkanes), the heat of adsorption onto MgO(100) measured by EAI increases with the mass of the adsorbate. This is attributed to the increase in polarizability with the mass of the atoms and the number of atoms in the molecules. As an example, Fig. 2.7 shows that the adsorption enthalpies for noble gases increase almost linearly with atomic number.

Table 2.1 also shows that molecules containing accessible lone pairs of electrons (water, ammonia, methanol, ethyne) have higher heats of adsorption compared to the other molecules, which we attribute to a strong attraction associated with the donation of this lone pair into the unoccupied orbitals of the Mg^{2+} ion. The coverage dependence of ΔH_{ad}^0 in the 1st ML was determined by EAI only for the cases of NH_3 and H_2O . Surprisingly, it changes in the opposite direction, increasing from ~50 to 85 kJ/mol with coverage for H_2O , but decreasing from 71 to 25 kJ/mol for NH_3 . We attribute this to the fact that the only lone pair in each NH_3 binds to a Mg^{2+} ion, so that the only NH_3 - NH_3 interactions will be their dipole-dipole repulsion (see below), whereas for H_2O , one lone pair of the O can bind to Mg^{2+} while the other lone pair binds to a H atom in a neighboring H_2O molecule, to form an attractive hydrogen bond.

These NH_3 - NH_3 repulsive lateral interactions have also been observed in desorption kinetics¹¹⁹. The most stable binding configuration has the NH_3 axis perpendicular to the surface with the N lone pair donating to the Mg^{2+} ion^{119, 120}. Such oriented dipoles always give rise to repulsive adsorbate-adsorbate interactions. Part of the decrease in heat of adsorption is probably also associated with the reported change to a less stable adsorbate structure at higher coverage, wherein one H atom of NH_3 makes a hydrogen bond to an O^{2-} ion of the MgO¹²⁰. Surprisingly, the heat of adsorption of NH_3 on MgO(100) (71 to 25 kJ/mol) is much higher than that

reported from calorimetric measurements on normal powdered MgO with heterogeneous surfaces (14 to 6 kJ/mol¹²¹).

Combining the adsorption energy values from Tables 2.1 and 2.2 allows us to make a number of conclusions about how adsorption enthalpies on MgO(100) depend on the adsorbate. Figure 2.8 shows that the adsorption enthalpies for alkanes at $\frac{1}{2}$ ML coverage (by TPD) increases nearly proportional to chain length, with a slope of 7.1 kJ/mol per C atom. We add here results for graphite (0001) and Pt(111) to show that this trend seems to be independent of substrate, with a proportionality constant that increases with the electrical conductivity (and therefore polarizability) of the substrate: MgO < C < Pt. This suggests that the bonding interaction is dominated by induced dipole / induced dipole interactions, which increase proportional to polarizability. It is surprising that the permanent dipole of MgO does not dominate over the induced dipoles in graphite and Pt, suggesting that the bonding mechanism(s) may be somewhat more complex. In any case, the adsorption energy scales nearly proportionally with the number of CH_x groups for these alkanes, with a slight offset indicating that CH₃ and CH₄ have slight more attraction than CH₂ groups.

The adsorption energies for alkanes on MgO(100) smoke determined by EAI at full, saturated ML coverage are also shown in Fig. 2.8. At short chain length, these agree with the TPD results at $\frac{1}{2}$ ML, but as chain length increases, these full ML energies drop further and further below the $\frac{1}{2}$ ML results. We attribute this to repulsive interactions which come into play at the highest coverage which are not present at $\frac{1}{2}$ ML total coverage, in spite of the fact that this condition probably corresponds to islands held together by attractive interactions at high-local-coverages (but not as high as at the true saturation coverage before second ML growth probed by EAI measurements). The other oxides in Fig. 2.8 will be discussed below.

2.4: Intact Molecular Adsorption on Oxide Single Crystal Surfaces: Adsorption Enthalpies from TPD Studies of Desorption Energies

Table 2.3 summarizes TPD measurements of the activation energies (E_d) and pre-exponential factors (ν) for desorption determined on single crystal oxide surfaces for molecules which remain intact upon adsorption and desorption. The format is the same as Table 2.2, listing first T_p and β , followed by reported values for E_d , ν and ΔH_{ad}^0 when the analysis method used to determine ν was rigorous fitting to TPD data. For all the other cases, the values for E_d , ν and ΔH_{ad}^0 listed here were those determined using the value for ν estimated using Eq. (2.16), based on the entropy correlation of Fig. 2.5 and transition state theory. The table is organized by the molecules, and under each molecule the oxides are listed according to the position of the cation in the periodic table, moving from its top left to its bottom right. As noted below, the heats of adsorption for some molecules correlate with the position of the oxide's cation in the periodic table, with the maximum heats being observed near the center of the transition metals where the d orbitals are approximately half filled.

While the nature and structure of the oxide surface sites for many of the adsorbate / substrate systems listed in Tables 2.1 through 2.3 have been characterized in depth using experimental measurements (spectroscopy, diffraction, etc.) and /or ab initio modeling methods, we do not describe those results in any detail here.

Table 2.3: Adsorption enthalpies and entropies for molecularly adsorbed species on oxide surfaces determined by TPD, showing also the peak temperature and heating rate. Prefactor and enthalpy values in bold were determined in the original paper by careful analysis of the TPD data, so the resulting adsorbate’s entropy at T_p determined from this prefactor using Eq. (2.11) are also in bold. The remaining prefactor, enthalpy and entropy values not in bold were estimated using Eqs. (2.16), (2.6) and (2.11), resp. The entries in bold under “Adsorption site” are as reported in the original paper. Those not in bold are based on our tentative assignments as justified in the text. When a range of T_p and enthalpy values are given, the arrow indicates that this is the direction of increasing coverage.

Adsorbate	oxide surface	adsorption site	T_p / K	β / (K/s)	$\log(\nu / \text{s}^{-1})$	$-\Delta H_{\text{ad}}^0$ / (kJ/mol)	$S_{\text{ad}}^0(T_p)$ / R	$S_{\text{gas}}^0(T_p)$ / R	citation
N ₂	TiO ₂ (110)	metal	105 → 90	1	14.1 → 14.0	29.7 → 25.3	10.3 → 9.91	19.4 → 18.8	122
		oxygen	70 → 45	1	13.8 → 13.6	19.3 → 12.0	9.29 → 8.21	18.0 → 16.4	122
O ₂	TiO ₂ (110)	metal	71 → 60	1	13.9 → 13.8	19.6 → 16.4	9.69 → 9.27	18.5 → 17.9	122
		oxygen	44 → 41	1	13.6	11.8 → 10.9	8.53 → 8.37	16.9 → 16.7	122
	TiO ₂ (110) 8% reduced	oxygen vacancies	410	2	19.8*	162	14.0	24.7	123
	Cr ₂ O ₃ (0001)		320 → 310	4	14.7 → 14.6	93.5 → 87.3	13.4 → 13.2	23.8 → 23.6	124
	PdO(101)	metal	250 → 233	1	14.5	74.7 → 69.2	12.8 → 12.6	23.0 → 22.7	125
		oxygen	117	1	14.1	33.4	10.9	20.3	125
CO	MgO(100)		59 → 57	0.2	13.8	16.9 → 16.3	9.38 → 9.30	18.1 → 18.0	103
			63 → 59	0.6	13.9 → 13.8	17.6 → 16.5	9.53 → 9.40	18.3 → 18.1	49
		c(4×2) phase	45	0.6	13.7	12.3	8.72	17.2	49

Table 2.3 (continued)

Adsorbate	oxide surface	adsorption site	T_p / K	β / (K/s)	$\log(\nu / \text{s}^{-1})$	$-\Delta H_{\text{ad}}^0$ / (kJ/mol)	$S_{\text{ad}}^0(T_p)$ / R	$S_{\text{gas}}^0(T_p)$ / R	citation
CO	TiO ₂ (110)		153 → 137	1	14.3	44.5 → 39.6	11.7 → 11.4	21.4 → 21.0	122
			170 → 135	0.5	14	42.1 → 32.8	13.1 → 11.9	21.8 → 21.0	126
	Cr ₂ O ₃ (0001)	metal	180 → 175	1	14.4	52.9 → 51.4	12.1 → 12.0	22.0 → 21.9	127
			105	1	14.1	29.9	10.8	20.1	127
	Fe ₃ O ₄ (111)	Fe³⁺ step edges	230	3	19.6*	88.1	12.7	22.9	128
		Fe²⁺ terraces	200 → 180	3	14.5 → 14.4	57.4 → 51.3	12.4 → 12.1	22.4 → 22.0	128
			110	3	14.2	30.4	10.9	20.3	128
	NiO(100)		137 → 115	3	14.3 → 14.2	38.4 → 31.9	11.4 → 11.0	21.1 → 20.4	103, 104
	ZnO(10-10)		360	2.5	14.8	108	13.8	24.4	129
	NO	MgO(100)		84 → 75	0.5	14.0	24.1 → 21.3	10.4 → 10.1	19.6 → 19.2
TiO ₂ (110)			129 → 126	0.5	13.5	35.7 → 34.8	13.3 → 13.2	21.1 → 21.0	130
RuO ₂ (110)			495 → 430	3	15.0 → 14.9	150 → 129	14.8 → 14.4	25.8 → 25.3	131
			250	3	14.6	72.8	13.1	23.4	131
NiO(100)			220 → 216	3	14.6 → 14.5	63.6 → 62.4	12.8 → 12.7	22.9	103, 104

Table 2.3 (continued)

Adsorbate	oxide surface	adsorption site	T_p / K	β / (K/s)	$\log(\nu / \text{s}^{-1})$	$-\Delta H_{\text{ad}}^0$ / (kJ/mol)	$S_{\text{ad}}^0(T_p)$ / R	$S_{\text{gas}}^0(T_p)$ / R	citation
H ₂ O	MgO(100)	metal	235	3	14.5	67.9	11.9	21.7	102
	CeO ₂ (111)	metal	271	2	14.6	79.9	12.3	22.3	132
			320 → 265	1	14.7 → 14.6	97.1 → 79.5	12.8 → 12.3	23.0 → 22.2	133
		oxygen	185 → 170	2	14.4 → 14.3	53.2 → 48.6	11.3 → 11.0	20.8 → 20.4	132
			207 → 195	1	14.4	61.1 → 57.3	11.6 → 11.4	21.2 → 21.0	133
	CeO _{1.93} (111)	metal	265 → 240	1	14.6 → 14.5	79.5 → 71.5	12.3 → 12.0	22.2 → 21.8	133
		oxygen	190	1	14.4	55.8	11.4	20.9	133
	CeO ₂ (001)	oxygen	200	2	14.4	57.8	11.5	21.1	134
	TiO ₂ (110)	metal	306 → 278	1	14.7 → 14.6	92.6 → 83.7	12.7 → 12.4	22.5	122
			300 → 272	5	14.7 → 14.6	86.8 → 78.2	12.6 → 12.4	22.7 → 22.3	135
		oxygen	189 → 183	1	14.4	55.5 → 53.6	11.3 → 11.2	20.9 → 20.7	122
			170	7.5	14.3	46.8	11.0	20.4	135
	TiO ₂ (101)	metal	257 → 246	1	14.6 → 14.5	76.9 → 73.4	12.2 → 12.1	22.1 → 21.9	136
		oxygen	190	1	14.4	55.8	11.3	20.9	136
	TiO ₂ (100)	metal	280 → 250	1.8	14.6 → 14.5	83.0 → 73.5	12.4 → 12.1	22.4 → 22.0	137
		oxygen	171	1.8	14.3	49.0	11.1	20.5	137

Table 2.3 (continued)

Adsorbate	oxide surface	adsorption site	T_p / K	β / (K/s)	$\log(v / s^{-1})$	$-\Delta H_{ad}^0$ / (kJ/mol)	$S_{ad}^0(T_p)$ / R	$S_{gas}^0(T_p)$ / R	citation
H ₂ O	α -Cr ₂ O ₃ (001)	metal	310	2	14.7	92.2	12.7	22.6	138
		oxygen	210	2	14.4	60.9	11.6	21.3	138
		oxygen	185	2	14.4	53.2	11.3	20.8	138
	α -Cr ₂ O ₃ (001) 2% strained	metal	295	2	14.6	87.4	12.6	22.8	138
		oxygen	210	2	14.4	60.9	11.6	21.3	138
		oxygen	185	2	14.4	53.2	11.3	20.8	138
	Fe ₃ O ₄ (111)	oxygen	210 → 190	1	14.6 → 14.5	76.9 → 73.4	12.2 → 12.1	21.3 → 20.9	139
	Fe ₃ O ₄ (001)	oxygen ¹³⁹	225	2	14.5	65.5	11.8	21.6	140
	RuO ₂ (110)	metal	400	4	14.8	119	13.4	23.9	141
	PdO(101)	oxygen	197	1	14.4	58.0	11.4	21.0	142
	Cu ₂ O(100)	oxygen	210 → 183	2	14.4	60.9 → 52.6	11.6 → 11.2	21.3 → 20.7	143
	ZnO(0001)	metal	320	7.5	14.7	91.9	12.8	23.0	144
	ZnO(000-1)	oxygen	207	5	14.4	58.4	11.6	21.2	145
			190	7.5	14.4	52.7	11.3	20.9	144
	ZnO(10-10)	metal	370	1	14.8	113	13.2	23.6	146
			340	7.5	14.7	98.1	13.0	23.2	144
		oxygen	190	7.5	14.4	52.7	11.3	20.9	144

Table 2.3 (continued)

Adsorbate	oxide surface	adsorption site	T_p / K	β / (K/s)	$\log(v / s^{-1})$	$-\Delta H_{ad}^0$ / (kJ/mol)	$S_{ad}^0(T_p)$ / R	$S_{gas}^0(T_p)$ / R	citation
CO ₂	TiO ₂ (110)	oxygen vacancies	206 → 200	2	19.6*	79.7 → 77.2	13.5 → 13.4	24.1 → 24.0	147
		metal	177 → 158	2	13.6	49.2 → 39.2	15.3 → 14.9	23.5 → 23.1	147
	ZnO(0001)	metal	135 → 125	1.3	14.4 → 14.3	39.0 → 35.9	12.5 → 12.3	22.6 → 22.3	148
SO ₂	CeO ₂ (111)	oxygen	380	3	15.4	118	18.0	30.5	149
Methane	MgO(100)		47	0.6	13.1	12.3	8.20	15.0	24
	PdO(101)		143 → 140	1	14.7	40.6 → 44.6	9.15 → 8.95	19.4 → 19.2	150
Ethane	MgO(100)		75	0.6	14.9	22.5	9.76	20.9	24
	PdO(101)	unsaturated	182 → 165	1	14.7	54.6 → 49.2	13.8 → 13.6	24.5 → 24.1	150
		saturated	100	1	14.4	28.8	12.2	22.1	150
Propane	MgO(100)		93	0.6	15.6	29.4	11.9	24.9	24
	PdO(101)		205 → 184	1	15.1	63.1 → 56.3	16.4 → 16.1	28.1 → 27.6	151
			151 → 135	1	14.9	45.6 → 40.5	15.5 → 15.2	26.9 → 26.4	151
<i>n</i> -butane	MgO(100)		111	0.6	15.7±1.6	35.4±3.9	15.8	27.8	8
	PdO(101)		222 → 218	1	15.9	71.6 → 70.2	20.6 → 20.5	34.2 → 34.0	152
			175	1	15.6	55.1	19.1	32.0	152
			160 → 152	1	15.5 → 15.4	50.0 → 47.2	18.5 → 18.2	31.1 → 30.7	152
			137	1	15.3	42.1	17.5	29.7	152

Table 2.3 (continued)

Adsorbate	oxide surface	adsorption site	T_p / K	β / (K/s)	$\log(\nu / \text{s}^{-1})$	$-\Delta H_{\text{ad}}^0$ / (kJ/mol)	$S_{\text{ad}}^0(T_p)$ / R	$S_{\text{gas}}^0(T_p)$ / R	citation
<i>n</i> -butane	ZnO(0001)	metal	190 → 165	1.3	15.7 → 15.5	60.0 → 51.3	19.6 → 18.7	32.7 → 31.4	148
Isobutene	ZnO(0001)	metal	140 → 130	1.6	13.4	39 → 33	20.7 → 20.0	28.6 → 27.9	153
<i>n</i> -hexane	MgO(100)		144	0.6	16.0	47.0	47.0	36.4	24
<i>n</i> -octane	MgO(100)		175	0.6	17.9	63.6	61.5	46.1	24
<i>n</i> -decane	MgO(100)		204	0.6	19.1	77.9	34.9	56.3	24
Cyclohexane	ZnO(000-1)	oxygen	210	5	15.6	63.6	19.4	32.4	154
Ethylene	Cr ₂ O ₃ (0001)		220 → 210	4	14.8	64.2 → 61.1	14.2 → 14.1	25.0 → 24.8	155
			120 → 130	4	14.5	33.6 → 36.6	12.5 → 12.7	22.5 → 22.8	155
	RuO ₂ (110)		320	3	15.1	96.7	15.5	26.8	156
		repulsive interactions	120 to 250	3	14.5 to 14.9	33.9 to 74.2	12.5 to 14.6	25.5 to 22.5	156
Propene	TiO ₂ (110)		180	5	15.2	53.3	16.9	28.8	157
Isobutene	TiO ₂ (110)		210 → 190	2	15.6 → 15.5	65.5 → 58.7	19.3 → 18.7	32.3 → 31.5	158
Benzene	MgO(100)	parallel to surface	175	5	15.1	51.3	16.6	28.5	105
		tilted	148	5	15.0	42.8	16.0	27.6	105
	Al ₂ O ₃ (111)	parallel to surface	163	5	15.0	47.5	16.3	28.1	105
		tilted	156	5	15.0	45.3	16.4	27.9	105
	ZnO(000-1)		250	5	15.4	75.6	18.3	31.0	159
	ZnO(10-10)		260 → 235	5	15.5 → 15.4	78.9 → 70.6	18.5 → 18.0	31.1 → 30.4	160

Table 2.3 (continued)

Adsorbate	oxide surface	adsorption site	T_p / K	β / (K/s)	$\log(\nu / \text{s}^{-1})$	$-\Delta H_{ad}^0$ / (kJ/mol)	$S_{ad}^0(T_p)$ / R	$S_{gas}^0(T_p)$ / R	citation
methanol	MgO(100)	metal	296 → 275	3	15.3	90.5 → 83.7	16.9 → 16.6	28.8 → 28.4	106
		oxygen	240	3	15.2	72.3	16.2	27.8	106
	TiO ₂ (101)	metal	295 → 260	1	15.3 → 15.2	92.8 → 81.1	16.9 → 16.4	28.8 → 28.1	136
		oxygen	170	1	14.9	51.5	15.1	26.2	136
	TiO ₂ (110)	metal	370 → 323	1.5	15.5 → 15.4	117 → 101	17.8 → 17.3	30.2 → 29.3	161
			350 → 295	2	15.5 → 15.3	110 → 91.1	17.6 → 16.9	29.8 → 28.8	162
		oxygen	183	1.5	15.0	55.1	15.3	26.5	161
			165	2	14.9	49.0	15.0	26.1	162
	ZnO(1010)		440	1.5	15.7	141	18.7	31.3	163
	Al ₂ O ₃ (0001)		325 → 217	5	15.4 → 15.1	98.7 → 64.0	17.3 → 15.8	29.4 → 27.3	164
Ethanol	TiO ₂ (110)	metal	395 → 337	1.5	16.3 → 16.1	131 → 110	22.3 → 21.2	36.6 → 35.0	161
			310	4.5	16.0	97.5	20.7	34.2	165
		oxygen	188	1.5	15.5	58.4	18.3	30.8	161
			225 → 185	4.5	15.6 → 15.5	68.8 → 55.7	19.0 → 18.2	31.9 → 30.7	165
1-propanol	TiO ₂ (110)	metal	413 → 352	1.5	17.1 → 16.8	143 → 120	26.9 → 25.3	43.1 → 40.9	161
		oxygen	204	1.5	16.0	65.6	21.5	35.4	161
Isopropanol	TiO ₂ (110)	metal	400 → 340	1.5	16.5 → 16.8	137 → 114	25.5 → 23.9	41.2 → 38.9	161
		oxygen	213	1.5	15.8	67.8	20.6	34.0	161

Table 2.3 (continued)

Adsorbate	oxide surface	adsorption site	T_p / K	β /(K/s)	$\log(\nu / \text{s}^{-1})$	$-\Delta H_{\text{ad}}^0$ /(kJ/mol)	$S_{\text{ad}}^0(T_p)$ / R	$S_{\text{gas}}^0(T_p)$ / R	citation
1-butanol	TiO ₂ (110)	metal	438 → 366	1.5	17.9 → 17.5	159 → 130	31.8 → 29.5	50.2 → 46.8	161
		oxygen	206	1.5	16.5	68.1	24.3	39.4	161
2-butanol	TiO ₂ (110)	metal	425 → 347	1.5	17.8 → 17.3	154 → 122	31.3 → 28.7	49.4 → 45.7	161
		oxygen	213	1.5	16.5	70.3	24.2	39.2	161
<i>t</i> -butanol	TiO ₂ (110)	metal	430 → 351	1.5	17.4 → 16.9	152 → 120	28.8 → 26.1	45.8 → 42.0	161
		oxygen	225	1.5	16.0	72.6	21.9	35.9	161
Acetone	CeO ₂ (111)	metal	300	2	16.1	97.2	21.5	35.6	166
		metal	210	2	15.7	65.9	19.5	32.7	166
	TiO ₂ (110)	oxygen	375	2	16.5	125	23.2	38.0	167
		metal	320 → 285	2	16.2 → 16.1	104 → 91.9	22.0 → 21.2	36.2 → 35.1	167
formic acid	NiO(111)		375	5	15.6	116	18.6	31.4	168
	ZnO(000-1)		167	5	15.0	48.7	15.8	27.3	169

*Prefactors at defects were calculated using the value from Eq. (16) multiplied by 10⁵ (see text).

2.4.1: CO

The heats of adsorption of CO on the oxides in Table 2.3 seem to maximize for the oxides of metals near the middle of the transition metals in the periodic table (e.g., Fe and Ru), which probably have the maximum number of valence d electrons available for bonding to CO. Transition metals farther to the left may have used up all their d electrons in bonding to lattice O, and transition metals further to the right have fewer d electrons anyway and are well known for their lack of reactivity. The weakest bonds to CO in this table are for MgO(100), which has no valence d electrons for bonding.

2.4.2: Alkanes

Adsorption enthalpies of alkanes on MgO(100) were discussed in detail above. As shown in Fig. 2.8, the heats of adsorption of linear alkanes are ~ 30 kJ/mol higher on the PdO(101) surface than on MgO(100). Indeed, this Pd oxide surface binds alkanes even more strongly than the Pd metal itself, a very unusual and unexpected result, and it even dissociates alkanes during TPD. The reasons for this have been discussed in light of DFT calculations^{150, 170}. Note that for the larger alkanes on PdO(101), dissociation competes with desorption, but much less so when using the perdeuterated alkane, yet the TPD peak temperature hardly shifts upon perdeuteration¹⁷¹. Therefore, Redhead analysis of the TPD data for PdO(101) to get heats of adsorption should not be changed by more than 5% due to this competition. Both the Zn- and O- polar faces of ZnO(0001) bind alkanes with the same number of carbon atoms slightly more strongly than MgO(100) (Table 2.3).

2.4.3: Water

Molecularly adsorbed water generally shows two TPD peaks from oxides, one near 300 K due to binding through its O atom to metal cation sites (with perhaps H-bonding to O anions) and one near 200 K due to water bound to oxygen anion sites. We will refer to these states below as corresponding to metal and oxygen sites, respectively. In general, the metal sites are populated first, and saturate at one water per metal site. As shown in Table 2.3, the heat of adsorption at the metal sites generally falls in the range 70-100 kJ/mol. This is considerably stronger than water binds to late transition metal surfaces (e.g., 51 kJ/mol for Pt(111)⁸⁵). The heats of adsorption for the O sites are in the range 50 to 60 kJ/mol, similar to that for water on Pt(111) and only slightly larger than the sublimation enthalpy of bulk water (47 kJ/mol⁻¹). Note that in the cases indicated in Table 2.3, we used the TPD peak temperatures to assign the site of that water binding, based on the general trend outlined above, indicating there if this differs from the assignment in the original paper (but not if there was no such assignment).

In some cases, the TPD peak due to molecularly adsorbed water on metal sites does not appear, due to the fact that these species dissociate to make an -OH at the metal site and an -H bound to the neighboring O site, or two different types of surface hydroxyls. We will discuss the water TPD peaks due to the recombinative desorption of these adsorbed dissociation products (OH+H) below when we discuss TPD studies of associative desorption energetics. There, we will also discuss the same species when produced instead at surface defects. In many cases, this TPD peak is at much higher temperature than the ~300 K characteristic of molecularly adsorbed water at metal sites, but in some cases, the peak is near or just above 300 K. In those cases, it has generally been difficult to determine what fraction of the desorption intensity is due to molecularly adsorbed water and what fraction is associative desorption, and the assignments to

one or the other in some cases are debatable. Indeed, it seems that there may be an equilibrium between molecularly adsorbed water (dominant) and dissociated water (minority species) in this state, which complicates assignments. For these species, we analyzed this peak to get the heats of adsorption listed in Table 2.3 as if it were purely molecularly adsorbed.

2.4.4: Alcohols

Molecularly adsorbed methanol on oxides, like water, generally shows two TPD peaks at high coverage, one near 300 K generally attributed to methanol binding to metal cation sites through its own O atom (with perhaps H-bonding to the oxygen atoms of another methanol or to O anions) and one nearer to 200 K attributed to methanol bound to oxygen anion sites. Although these site assignments are not yet definitive, we will refer to these states below as corresponding to metal and oxygen sites, respectively. In general, the metal sites are populated first, and saturate at one methanol per metal site. As shown in Table 2.3, the heats of adsorption at the metal sites generally fall in the range 80 to 100 kJ/mol. This is considerably stronger than methanol bonds to late transition metal surfaces (e.g. 57 kJ/mol for Pt(111)⁵³). The heat of adsorption at the O sites is in the range 49 to 72 kJ/mol, similar to that for methanol on Pt(111) and only slightly larger than the sublimation enthalpy of methanol (45 kJ/mol¹). Note that in the cases indicated in Table 2.3, we used the TPD peak temperatures to assign the site of that methanol binding, based on the general trend outlined above.

It has generally been difficult to determine whether the TPD peak at ~300 K from oxides surfaces is due to molecularly adsorbed methanol or associative desorption or some combination of both, and the assignments to one or the other is often based on limited evidence. Where available, direct STM images show mainly a single bump for this species on the terrace metal

sites ¹⁷²⁻¹⁷⁴, implying that molecular adsorption is more favorable there. This is also the case for larger alcohols ¹⁷⁵⁻¹⁷⁸. As with water above, it seems that there may be an equilibrium between molecularly adsorbed methanol (dominant) and dissociated water (minority species) in this peak, with the two states quite similar in energy for many oxides (see, for example, the combined experimental and DFT study on TiO₂(110) ¹⁷⁴), which complicates TPD peak assignments. For these species, we analyze this peak to get the heats of adsorption listed in Table 2.3 as if it were purely molecularly adsorbed, since this seems to be the dominant structure. Further evidence to support this is presented below, where we show that when analyzed in this way the heats of adsorption of linear alcohols on TiO₂(110) increases with the number of C atoms with the same average slope (7 kJ/mol per C) as that for alkanes on MgO(100).

For some oxide surfaces, a TPD peak near 300 K for molecularly adsorbed methanol on metal sites does not appear, due to the fact that methanol on metal sites instead dissociates to make methoxy at the metal site and an -H bound to the neighboring O site. In these cases, a methanol TPD peak appears at considerably higher temperature and has been attributed to the recombinative desorption of these adsorbed dissociation products (OCH₃+H). We will discuss these cases below when we discuss TPD studies of associative desorption energetics, where we also discuss associative desorption of these same species when they are instead produced at defect sites on oxide surfaces.

Ethanol at high coverage has a TPD peak near 340 K, slightly above that for methanol. Again, it now seems that this state is mainly due to molecularly adsorbed ethanol on metal sites, which are probably in equilibrium with some dissociated ethanol (ethoxy plus -H) ^{177, 178}. We initially assigned this TPD peak on TiO₂(110) to dissociated ethanol, based on the fact that it was also seen at the same temperature when ethoxy was added to the surface by a different route

(the dissociation of adsorbed tetraethoxy silane), albeit in the presence of surface or subsurface H¹⁶⁵. However, since ethanol was the observed gas phase product, it could have resulted mainly from the desorption of molecularly adsorbed methanol, produced at lower temperature by the association of surface ethoxy plus -H. We now think that this was the case, based on STM showing that ethanol on terrace Ti sites is mainly molecularly adsorbed^{177, 178}.

Figure 2.9 shows a plot of the heat of adsorption of linear alcohols up to butanol on the Ti and O sites of rutile TiO₂(110) versus the number of carbon atoms. (Again, the assignments to metal and O sites are still tentative.) As with the *n*-alkanes on MgO(100) (Fig. 2.8), there is a linear increase with the number of C atoms, with a slope of 4.6 and 9.4 kJ/mol per C atom for O and Ti sites, respectively. The slope versus carbon number, averaged over both O and Ti sites (7.0 kJ/mol per C atom), is the same as that for the *n*-alkanes on MgO(100) at ½ ML (7.1 kJ/mol per C atom), and both are more than twice the slopes of the heats of vaporization of both bulk alkanes and bulk alcohols (~3 kJ/mol per C atom). The larger slopes here imply that the van der Waals interactions of the CH_x groups are stronger with both TiO₂ and MgO than with other alkane chains. The large, constant slope in Fig. 2.9 can only be understood if these alcohols are lying flat along the surface, which would allow near optimal van der Waals interaction with the oxide for every CH_x group. This strongly supports the interpretation that these TPD peaks are due to simple desorption of molecularly adsorbed alcohols, rather than associative desorption of its fragments, which would instead have an activation barrier associated with H addition to the O atom of the alkoxy and thus should be much less dependent on chain length. The *y*-intercept here (50 and 91 kJ/mol for O and Ti sites, respectively) is much larger than for alkanes (7 kJ/mol). This is clearly due to the strong interaction of both the O and metal sites with the -OH group, and possibly hydrogen bonds between neighboring -OH groups, that are not present for

the alkanes. The intercept is larger for the Ti sites due to the stronger interaction of -OH with the metal sites than the O sites.

2.4.5: Comparison to Adsorption Calorimetry on Powdered Oxides

Cardona-Martinez and Dumesic¹²¹ have reviewed calorimetry measurements of adsorption energies of a variety of molecules on powdered oxide samples which had much more heterogeneous surface structures than the samples discussed above. These included studies of molecular adsorption on powdered oxides of Mg, Al, Si, Zn, Fe and Ti. As might be expected, for a given metal oxide and molecule, those heats on powdered samples generally covered a much broader range than the heats reported above for single crystalline oxide surfaces, which we attribute to the heterogeneity of sites on those powdered samples. Due to this complexity, we found it too challenging to identify other trends which we should mention here in comparison to the more well-defined single crystal oxide surfaces, which are the focus of this present review. However, since powdered samples are used in most industrial applications of oxides as catalysts or sorbents, understanding their heterogeneous site distributions is also highly important. Also, for specific adsorbate / oxide combinations, we have found it very helpful for interpreting results on single crystal samples to use information from published data on powdered samples, and vice versa. For example, our early study of water on TiO₂(110) relied heavily on insights from TPD and FTIR data from powdered samples¹³⁵. However, that type of integration of data requires a level of detailed analysis of the literature for specific systems that is beyond the scope of this review.

2.5: Reversible Dissociative Adsorption on Oxides: Adsorption Enthalpies by TPD

As noted above, when adsorption is dissociative but the two adsorbed products have attractive interactions and thus prefer to occupy neighboring sites, or if they are immobile and simply remain at neighboring sites, their associative desorption kinetics can be treated as a pseudo-first-order process. Therefore, one can use Eq. (2.4) through (2.6) to get E_d and, with Eq. (2.3), the enthalpy of adsorption. This is only valid when the adsorption \rightleftharpoons desorption process is reversible and the activation energy for adsorption is negligible (i.e., when the sticking probability is near unity). In Table 2.4, we have analyzed some cases in this way, mainly for cases where the two adsorbed fragments are expected to have attractive interactions (i.e., -OH and -H in the case of dissociatively adsorbed water and -OCH₃ and -H in the case of dissociatively adsorbed methanol). Based on the gas exposures reported for all these species (less than ~30 L), the initial sticking probabilities were estimated to be large enough (>0.05), given the surface temperature during exposure, that the activation energies for adsorption were negligible (and certainly below 7 kJ/mol).

In most cases, calculating the adsorption enthalpy for these dissociatively adsorbed species requires the use of an assumed prefactor for recombinative desorption. For this, we assumed a value of 10^{17} s^{-1} , based on the value we think is the most reliable prefactor actually determined experimentally for the associative desorption of similar species on single crystal oxides, as reported for water on $\alpha\text{-Fe}_2\text{O}_3(012) (1\times 1)$ ¹⁷⁹. This prefactor is higher than that for desorption of molecularly adsorbed water. This is expected within transition state theory, since the adsorbed fragments (-OH and -H in the case of dissociatively adsorbed water) are expected to have a tighter binding to the surface, wherein free motions like rotations of the undissociated molecule have been converted into vibrational motion of the fragments with respect to the

surface. Since vibrations contribute less to the partition function, this gives a lower partition function to the initial state for the reaction and thus a higher prefactor.

The energetics of the dissociative adsorption of H₂ on ZnO were measured by Griffin and Yates¹⁸⁰. Although these results were obtained on ZnO powders, the three states observed were so beautifully characterized by infrared spectroscopy that one can hope to relate them to more recent observations on ZnO single crystal surfaces. They observed three dissociatively adsorbed states for H₂ with distinct peaks in the TPD spectra for associative recombination. State I_a, which has a Zn–H stretching frequency, $\nu(\text{Zn–H})$, of 1710 cm⁻¹, $\nu(\text{O–H})$ of 3455 cm⁻¹ and $T_p = 170$ K, has a heat of adsorption of 31 kJ/mol and an activation energy for adsorption of 21 kJ/mol. State I_b and I_c both have $\nu(\text{Zn–H}) = 1710$ cm⁻¹ and $\nu(\text{O–H})$ of 3498 cm⁻¹, but I_b has $T_p = 232$ K with a heat of adsorption of 52 kJ/mol and an activation energy for adsorption of 17 kJ/mol, and I_c has $T_p = 300$ K with a heat of adsorption of 57 kJ/mol and an activation energy for adsorption of 33 kJ/mol. The latter frequencies are not greatly different than the values of 1613 and 3670 cm⁻¹ observed after dosing atomic H gas to the most stable face of ZnO, the (10-10) surface, which also starts to desorb as H₂ at a similar temperature of 250 K upon heating in UHV¹⁸¹. In contrast, dosing H gas to the ZnO(0001)-Zn surface leads to much higher temperature peaks in the removal rate of adsorbed H upon heating in UHV, at 383 and 536 K^{182,183}.

Table 2.4. Adsorption enthalpies for dissociatively adsorbed molecules on oxide surfaces, based on TPD analysis of peaks for their associative desorption. Prefactor and enthalpy values in bold were determined in the original paper by careful analysis of the TPD data. The remaining prefactors not in bold were assumed to be 10^{17} s^{-1} as justified in the text, and the corresponding enthalpies were estimated using Eqs. (2.6) and (2.3). For all these species, the sticking probabilities are large enough to analyze TPD assuming negligible activation energy for dissociative adsorption.

dissociatively adsorbed molecule	oxide surface	adsorption site	T_p / K	β / (K/s)	$\log(\nu/\text{s}^{-1})$	$-\Delta H_{\text{ad}}^0$ / (kJ/mol)	citation
O ₂	PdO(101)	defects	760	1	17	269	125
H ₂ O	CeO ₂ (001)	defects exposing metal sites	275	2	17	93.5	134
	TiO ₂ (110)	defects	507	1.5	17	176	161
	TiO ₂ (100)	metal	340 → 320	1.8	17	116 → 109	137
	α-Cr ₂ O ₃ (001)	metal	355	2	17	121	138
	α-Cr ₂ O ₃ (001) 2% strained	metal	345	2	17	118	138
	Fe ₃ O ₄ (111)	metal	282 → 268	5	17	93.8 → 89.0	139
	Fe ₃ O ₄ (001)	defects	520	2	17	179	140
	Fe ₃ O ₄ (001)	metal	325 → 260	2	17	111 → 88.2	140
	α-Fe ₂ O ₃ (012) (1X1)	metal	350	2	17	118	179
	α-Fe ₂ O ₃ (012) (2X1)	metal	405 → 380	2	17	139 → 130	179
	PdO(101)	defects	354	1	17	123	142
	Cu ₂ O(100)	metal	465	2	17	160	143
	ZnO(000-1)	defects exposing metal sites	315	7.5	17	104	144
	ZnO(10-10)	metal	450	1	17	157	146
	α-Al ₂ O ₃ (0001)	metal	395	1	17	138	184
MeOH	TiO ₂ (101)	defects	410	1	17	143	136
	TiO ₂ (110)	defects	480	2	17	165	162
	ZnO(10-10)	ordered bi-layer	370	1.5	17	127	163

2.6: Metal Atom Adsorption on Oxide Surfaces and Metal / Oxide Interfacial Adhesion

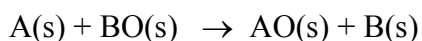
Metal / oxide interfaces play key roles in many technologically important applications, including metal / oxide contacts in microelectronics and photovoltaic devices, metal / oxide seals in device and medical implant construction, coatings for corrosion passivation, and novel structural materials based on metal / ceramic composites. One would therefore like to understand the atomic-level structure of metal / oxide interfaces, the electronic character of the metal atoms at these interfaces, their interfacial chemical bond strengths to the oxide, and the thermodynamic stability of these interfaces. These must control their technologically-relevant functional properties such as the efficiency of photovoltaic devices, the speed and size of microelectronics, the corrosion resistance of passivation layers, the peel strength of metal / oxide contacts, and the hardness of composite materials. Oxide surfaces that are decorated with sub-monolayer amounts of metals as either adsorbed cations or small metal nanoparticles are also extremely important in energy and environmental technologies as catalysts, electrocatalysts, photocatalysts and gas-sensors. Again, one would like to know the atomic-level structure of the surface, the electronic character of the metal atoms at these oxide surfaces, and their chemical bond strengths to the oxide, since these properties should correlate with the catalytic activity and selectivity of oxide-supported metal nanoparticles or cations, their resistance to sintering, and the sensitivity and lifetime of sensors. Our understanding of these key scientific questions about metals on oxide surfaces has improved considerably over the past two decades^{2, 33, 185-205}.

Here we review progress which has been made in understanding the adsorption energy of isolated metal atoms to oxide surfaces and how that adsorption energy of metal atoms depends on coverage due to metal-metal bonding as metal particles grow for mid to late transition metals, or alternatively due to metal-metal repulsions for alkali metals. First, we start with a discussion

of how chemical bonding enthalpies can be used to predict which chemical structure forms when a metal is deposited onto an oxide surface, and the observed relationships between interfacial chemical bonding strength as measured by metal atom adsorption energies and the adhesion energies at the thick metal film / oxide interface.

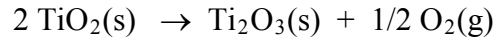
2.6.1: Predicting when the Adsorbing Metal Will Reduce the Underlying Oxide

It is easy to predict what bulk phase(s) should form at equilibrium (i.e., in the absence of any kinetic constraints) when a large amount of metal is dosed onto an oxide, since this simply depends on the relative thermodynamic stabilities of the various bulk oxides and intermetallic compounds that might form³³. If metal A is deposited onto oxide BO, then A should reduce the surface of BO to metallic B and itself become oxidized to AO if the reaction



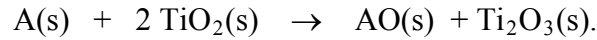
is thermodynamically downhill (i.e., if it has a negative standard free energy change). (Here, s will refer to solids, and g to gas.) Neglecting differences in formation entropies of the oxides, this occurs when the standard heat of formation, ΔH_f^0 , of the bulk oxide of A is more negative than that of the bulk oxide of B. It is reasonable to neglect entropy differences, since the entropies of formation of metal oxides (per mole of oxygen) is nearly independent of the metal²⁰⁶. To take more complex stoichiometries like A_3O_4 into account, one should make this comparison using heats of formation *per mole of oxygen*, using the most negative value amongst all oxides of A (i.e., the value for the most stable oxide of A). Many of these heats of formation have been tabulated¹. The late transition metals have the least stable oxides (least negative ΔH_f^0), and therefore the lowest affinity for oxygen. The affinity of transition metals for oxygen generally decreases from left to right across the periodic table.

If the substrate oxide can be easily reduced to a lower oxide, as in the case of TiO₂:



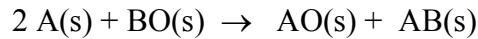
$$(\Delta H^0 = \Delta H_{\text{f},\text{Ti}_2\text{O}_3}^0 - 2\Delta H_{\text{f},\text{TiO}_2}^0 = 368 \text{ kJ/mol at 298 K}),$$

then one must also consider the possibility for reactions like:



This type of reaction should occur when ΔH_{f}^0 of the oxide of A is more negative than $-\Delta H_{\text{reaction}}^0$ for the reduction of the substrate to its lower oxide, when compared *per mole of oxygen*. Evidence for this is seen for several metals on rutile TiO₂, for example²⁰⁷⁻²¹².

If the two metals form stable intermetallic compounds, then one must also consider whether reactions like:



are thermodynamically downhill. This often occurs when depositing metals with very stable oxides onto alumina^{213,214}, or when depositing Al onto oxides²¹⁵, since metal aluminides tend to be very stable. Finally, one must consider any mixed oxides that are known to form. For example, NiAl₂O₄(s) is known to form at the Ni/Al₂O₃ interface, but only when the deposition is done in the presence of oxygen gas²¹⁴. Heats of formation of many single metal oxides are conveniently tabulated¹. Those of mixed oxides and intermetallic compounds are harder to find (see, for example²¹⁶).

Experimental measurements of thick metal films on oxides at room temperature often fail to give these thermodynamically expected bulk phases, due to kinetic limitations (e.g., slow diffusion). However, *the first monolayer usually shows evidence for the onset of the thermodynamically expected bulk reaction, and thin interfacial layers of the thermodynamically expected phases can often still be seen at thicker layers*^{33,211-214}. *This agreement implies that the*

energetics of metal adsorption in such cases where the adsorbing metal steals oxygen from the substrate oxide are similar to the bulk $\Delta H_{\text{reaction}}^0$ discussed for the above types of reactions.

Since this quantitative explanation of the observed reactivity trends is based on bulk heats of formation, and since heats of formation for both the metal and the oxide can depend on particle size (see below), finite size effects may be important. Thus, these predictions based on bulk thermodynamics will not always apply.

Note that for late transition metals on semiconducting oxides like $\text{TiO}_2(110)$ and $\text{ZnO}(0001)\text{-O}$, bulk thermodynamics predict neutral metal adsorption, and that is observed. However, even in these cases it is common for the first few percent of a monolayer to donate electron density into the oxide and induce downward band bending on the order of a few tenths of an eV³³.

2.6.2: Metal / Oxide Adhesion Energies and Wetting of Oxide Surfaces by Metal Films

Whether or not wetting occurs when metal is evaporated onto an oxide can be predicted based on a comparison of the metal / oxide interfacial free energy, $\gamma_{\text{m/ox}}$, with the difference between the surface free energy of the clean oxide in vacuum, $\gamma_{\text{v/ox}}$, and that of the clean metal, $\gamma_{\text{v/m}}$ ³³. If the metal wets the oxide, then $\gamma_{\text{m/ox}}$ equals $\gamma_{\text{v/ox}} - \gamma_{\text{v/m}}$ at equilibrium. In this case, a continuous metal film is formed whose thickness is simply related to the volume of metal deposited. If

$$\gamma_{\text{m/ox}} > \gamma_{\text{v/ox}} - \gamma_{\text{v/m}} \quad (2.17)$$

then the metal does not wet the oxide / vacuum interface^{217, 218}. In this case, the metal should make thicker, three dimensional (3D) particles and leave regions of clean oxide surface between particles.

The interfacial free energy, $\gamma_{m/ox}$, reflects the strength of metal - oxide bonding. All real interfacial energies γ are positive, and strong bonding between the phases at the metal / oxide interface would lead to small positive values of $\gamma_{m/ox}$. Since the surface free energy of metals is usually larger than or comparable to that of oxides²¹⁹, Eq. (2.17) means that the metal / oxide interfacial free energy must be very small; or there must be very, very strong bonding at the metal / oxide interface; for wetting to occur.

The adhesion energy or the work of adhesion, E_{adh} , is the work needed to separate the metal / oxide interface in vacuum. It is given by^{217, 218, 220}:

$$E_{adh} = \gamma_{v/m} + \gamma_{v/ox} - \gamma_{m/ox}. \quad (2.18)$$

Therefore another way of specifying the thermodynamic criterion for wetting is simply that, if wetting occurs at equilibrium:

$$E_{adh} = 2 \gamma_{v/m}. \quad (2.19)$$

If $E_{adh} < 2 \gamma_{v/m}$, then wetting does not occur and 3D metal particles are instead expected to form on the oxide surface.

Adhesion energies have been measured using the contact angle method for liquid metals on alumina, silica, MgO and ZrO₂, often under controlled inert gas or H₂ atmospheres (although not under conditions of proven surface cleanliness), and have been tabulated²¹⁹). A contact angle of less than 100° was never reproducibly observed for mid to late transition metals on any of these oxides²¹⁹⁻²²⁶. The values of E_{adh} were usually only 20-70% of $\gamma_{v/m}$ for these metals, and thus a factor of at least three too low for wetting. Contact angles have also been measured for liquid metals on more reducible oxides (ZnO, chromia, etc.)^{221, 227}, and even here the late transition metals usually have a contact angle near or above 90°. Assuming that the solid metal has a similar interfacial energy on the oxide as the liquid metal, and realizing that $\gamma_{v/m}$ is even

larger for the solid than for the liquid metal (typically by $\sim 18\%$ ²²⁸), this indicates that these metals as solids also should not wet such oxides. Indeed, *the mid-to-late transition metals as solids do not wet such oxides*, in the thermodynamic sense, under clean UHV conditions, but instead form 3D solid particles on these surfaces ³³. Adsorbed gases also influence the wetting thermodynamics: the adsorption of gases like CO which can bind much more strongly to metals than to these oxides can add a large enthalpic driving force for wetting ³³.

2.6.3: Relating Metal Atom Adsorption Energies with Metal / Oxide Adhesion Energies and Sublimation Energies of the Bulk Metal

Metal atom adsorption enthalpies have been connected to adhesion energies by a thermodynamic cycle ³³. That cycle proved that the integral heat of adsorption per mole, $q_{\text{ad, int}}$, at some multilayer coverage where the differential heat of adsorption has just reached the bulk heat of sublimation of the metal per mole, ΔH_{sub} , is given by:

$$q_{\text{ad, int}} = \Delta H_{\text{sub}} - (2\gamma_{\text{v/m}} - E_{\text{adh}})/(n/A), \quad (2.20)$$

where n/A is the coverage in moles of metal atoms per unit area. We used here the convention adopted above that both $q_{\text{ad, int}}$ and ΔH_{sub} are positive, and neglected entropy. For metals which don't wet, $q_{\text{ad, int}} < \Delta H_{\text{sub}}$. Roughness factors must be incorporated into the above derivation to account for any surface roughness of the multilayer metal film, which is done by simply replacing $2\gamma_{\text{v/m}}$ with $(1 + f_r) \cdot \gamma_{\text{v/m}}$, where f_r is the roughness factor ³³. This can even be applied to cases where the metal film is not continuous but instead is in the form of large particles, as shown below.

If we imagine the hypothetical case where the metal had grown in a layer-by-layer fashion, and assume that the adsorption energy of a metal onto an oxide is equal to its

sublimation energy in all layers beyond the first monolayer, the (hypothetical) integral heat of adsorption in the first monolayer is given from the above equation as:

$$q_{\text{ad,int,ML}} = \Delta H_{\text{sub}} - (2\gamma_{\text{v/m}} - E_{\text{adh}})/(n_1/A), \quad (2.21)$$

where n_1/A is the coverage for one ML. Combining this with the result that E_{adh} is usually 20 to 100% of $\gamma_{\text{v/m}}$ for late transition metals on alumina, silica and zirconia³³, we have shown that³³:

$$q_{\text{ad,int,ML}} = \Delta H_{\text{sub}} - (1.4 \pm 0.4) \cdot \gamma_{\text{v/m}} / (n_1/A). \quad (2.22)$$

Overbury et al.²¹⁹ have shown from experimental data for many solid metals that:

$$\gamma_{\text{v/m}} = (0.16 \pm 0.02) \cdot (n_1/A) \Delta H_{\text{sub}}. \quad (2.23)$$

Substituting this into Eq. (2.22) gives a simple way to estimate heats of adsorption for late transition metals on those oxides³³:

$$q_{\text{ad,int,ML}} = (0.77 \pm 0.09) \Delta H_{\text{sub}}. \quad (2.24)$$

This estimate is based upon surface free energies and adhesion energies measured without the aid of tests that prove surface cleanliness. Experimental measurements of the heats of adsorption for late transition metals on MgO(100), CeO₂(111), Fe₃O₄(111), alumina and silica (summarized below) are at least qualitatively consistent with this prediction that $q_{\text{ad,int,ML}}$ is some fraction of ΔH_{sub} , but we cannot yet verify that this fraction is generally in the range 0.77 ± 0.09 . Using that E_{adh} is usually 20 to 100% of $\gamma_{\text{v/m}}$ for such systems, together with Eq. (2.23), we showed that³³:

$$E_{\text{adh}} = (0.10 \pm 0.07) \cdot (n_1/A) \Delta H_{\text{sub}}. \quad (2.25)$$

This gives a very imprecise way of estimating the range of adhesion energies for such systems.

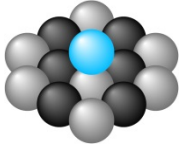
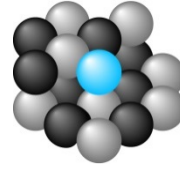
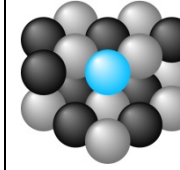
2.6.4: SCAC Studies of Metal Adsorption Enthalpies on Single Crystal Oxide Surfaces

Our group has calorimetrically measured the heats of adsorption of a variety of different metal atoms onto a number of different single crystal oxide surfaces, including MgO(100), CeO₂(111), and Fe₃O₄(111)^{2, 11-17, 29, 81, 229-233}. Example heats of adsorption versus coverage data are shown in Fig. 2.10, expressed here as the standard enthalpies of adsorption, ΔH_{ad}^0 , at the stated temperature (where standard simply implies one bar gas pressure). These calorimetric measurements have allowed us for the first time to *directly* assess the energetic stability of metal atoms on a well-defined oxide surfaces and that of metal atoms within metal nanoparticles supported on these oxide surfaces. Here we review those studies, showing how the heat of metal atom adsorption, its coverage dependence, and the metal adhesion energy are determined by the position of the metal in the periodic table; the nature of the oxide material; and the presence of hydroxyls, steps and oxygen vacancies on the oxide surface. Finally, we show how the stability of oxide-supported metal clusters depends on cluster size and the nature of the oxide surface.

2.6.4.1: Adsorption Enthalpies of Different Metal Atoms on Defective MgO(100)

Our studies of metal adsorption enthalpies on MgO(100) used ordered, 4 nm thick MgO(100) thin films grown epitaxially on Mo(100)^{11-13, 29, 81, 229-233}. These MgO(100) surfaces contain ~5% defect sites, mainly step and kink sites^{233, 234}. Example measurements are shown in Fig. 2.10. Heats of adsorption for Ca, Li, Cu, Ag and Pb measured at 300 K are summarized in Table 2.5, where they also are compared to DFT calculations for terrace, step and kink sites when available.

Table 2.5: Comparison of the initial heats of adsorption (ΔH_{ad}^0) measured calorimetrically for selected metals on MgO(100) at 300 K with values for the adsorption energy of isolated metal atoms on the most stable sites where they can adsorb on terraces, steps and kinks calculated with DFT slab models at 0 K. Included are also the measured initial sticking probability (S_0) and the heat of sublimation of the bulk metal (ΔH_{sub} , from ¹). Light grey spheres represent oxygen atoms, black magnesium, and light blue adsorbed metal atoms. Reprinted with permission from Reference ². Copyright 2009 Elsevier.

system	(experimental)		(bulk)	$-E_{ad}$ from DFT /(kJ/mol)		
	$-\Delta H_{ad}^0$ /(kJ/mol)	S_0	ΔH_{sub} /(kJ/mol)	 terrace	 step	 kink
Ca / MgO(100)	410 ¹³	1.00 ¹³	178	82 ¹³	205 ¹³	376 ¹³
Li / MgO(100)	260 ²³²	0.97 ²³²	159	78 ^{232, 233} 58, 85 ²³⁵	161 ^{232, 233}	343 ^{232, 233}
Cu / MgO(100)	240 ²⁹	1.00 ²⁹	337	60 ²³⁶ , 90 ²³⁷ , 91 ²³⁸	144 ²³⁸	228 ²³⁸
Ag / MgO(100)	176 ¹²	0.94 ¹²	285	52 ²³⁹ , 38 ²³⁶ , 47 ²⁴⁰	-	-
Pb / MgO(100)	103 ¹¹	0.70 ¹¹	195	-	-	-

The calorimetry results in Table 2.5 are probably best understood for the cases of Ca and Li on MgO(100), since these calorimetry studies also included complementary DFT calculations and kinetic simulations by our collaborators (Graeme Henkelman and Lijun Xu) ^{13, 233, 241, 242}. The calorimetry and film morphology measurements for the slightly defective MgO(100) surface and this surface after intentionally adding increasing numbers of defect sites (mainly steps, with some kinks) were well fitted by a kinetic model which included the following heats of adsorption: defect sites (mainly steps) = 420 kJ/mol for Ca and 400 kJ/mol for Li, and terrace sites at the edges of 2D clusters = 174 kJ/mol for Ca and 159 kJ/mol for Li. According to DFT, the binding energies at steps and kinks are 205 and 376 kJ/mol for Ca and 161 and 343 kJ/mol

for Li, respectively. It thus appears that DFT must be underestimating the strength of Ca- and Li-MgO binding at steps by ~50%. According to DFT, the binding energies at the edge of 2D islands on terraces are 100 and 116 kJ/mol for Ca and Li, respectively, which is again too low, now by 30 to 40%.

According to DFT^{233, 241, 242}, small 2D clusters of Li atoms nucleated at step edges are more stable than Ca atom clusters, which tend to dissociate at room temperature. That is, for the case of Li, when a third metal adatom diffuses to a terrace site nearest to two neighboring metal adatoms both bound on a step edge, it makes a stable trimer, whereas for the case of Ca it would continue migrating until it found a third defect site or a 3D Ca particle. The kinetic simulations mentioned above included this effect, and proved that it can explain the observed tendency for Li to maintain 2D growth to higher coverages than Ca²³³.

These DFT calculations showed charge transfer from adsorbed Ca and Li monomers to the MgO(100) terrace of -0.24 e and -0.35 e, respectively, and much more at steps^{241, 242}. In agreement, the work function was observed to decrease between 0 and 0.5 ML by 1.1 and 1.8 eV for Ca and Li, respectively^{13, 232}. It is surprising that in spite of their large charges and the expected charge-charge and dipole-dipole repulsions, both Ca and Li adatoms show attractive interactions and 2D clustering on MgO(100) in both experiments and DFT^{13, 232, 233, 241, 242}.

The heats of formation of CaO (-152 kJ/mol O) and Li₂O (-141 kcal/mol O) are very similar to that for MgO (-144 kJ/mol), such that some transfer of oxygen from the lattice to the admetal might be expected based on thermodynamics. This was not observed, but the low temperature (300 K) may have prevented overcoming an activation barrier.

In contrast to the case of Ca and Li on the left side of the periodic table, the metals Cu, Ag, and Pb from the right side of the periodic table do not bind very strongly to the steps and

kinks on MgO(100). One can conclude this easily by looking at their heat of adsorption versus coverage curves (Fig. 2.10), which start low and increase toward the heat of sublimation with coverage^{11, 12, 29, 81, 229-231}, exactly the opposite as seen for Ca and Li^{13, 232}. This very weak bonding of late transition metals to step sites on MgO(100) is supported by DFT calculations, which found that a palladium atom has an adsorption energy of only ~185 kJ/mol at steps, which is only about half of its heat of sublimation of 377 kJ/mol but is still ~47 kJ/mol stronger than adsorption at terrace sites²⁴³. The same trend is seen in the DFT results in Table 2.5 for Cu at steps and kinks on MgO(100) by Henkelman²³⁸.

Metals from the right side of the periodic table (Cu, Ag and Pb) show correlations between their measured heats of adsorption on MgO(100) and their bulk heats of sublimation, sticking probabilities, and film growth morphologies²³¹. These metals were all found to grow as 3D clusters on MgO(100). Late transition metals are typically observed to nucleate at step edges when microscopy data are available^{33, 190, 193, 195, 198, 244}. At the lowest coverage studied (~2% of a monolayer), these metals are probably adsorbed at step and/or kink sites, possibly in tiny, two-dimensional (2D) clusters. The measured initial heats of adsorption in Table 2.5 thus include not only the bond energies of these metal atoms to the step edges on the MgO(100) surface, but possibly some contribution from metal-metal bonding. As seen in Table 2.5, the initial heats of adsorption for these three metals increase with their bulk sublimation enthalpies, and their initial sticking probabilities at 300 K increase with their initial heats of adsorption²³¹. The resulting saturation number densities of metal particles also were found to increase with the magnitude of their initial heats of adsorption²³¹. (The number of clusters per unit area grows initially with coverage, but quickly reaches a saturation value at very low coverage^{33, 245, 246}.) This supports a transient mobile precursor model for adsorption²³¹, which is consistent with DFT-calculated

energetics for adatoms at terrace sites (see Table 2.5) and with estimated diffusion barriers. It is also consistent with classic mechanistic / kinetic models developed by Venables to explain electron microscopy observations of cluster nucleation and growth for such systems²⁴⁵⁻²⁴⁸.

The effect of surface hydroxyl groups on the adsorption energies of Cu and Pb on MgO(100) was also investigated²³⁰. It was found that surface hydroxyls increase the initial heat of adsorption for both metals (by ~10 and 20 kJ/mol, respectively). The saturation number density of metal nanoparticles also increased, consistent with the trends and nucleation / growth model mentioned above.

As noted previously, the adhesion energy between a multilayer metal film and the underlying oxide surface can also be determined from the integral heat of metal adsorption on the oxide^{31, 33, 79}. This was done for several systems^{11, 12, 29, 81, 229}. On MgO(100), the reported adhesion energies are: Pb = 77 ± 20 $\mu\text{J}/\text{cm}^2$, Ag = 30 ± 30 $\mu\text{J}/\text{cm}^2$, and Cu = $\sim 192 \pm 50$ $\mu\text{J}/\text{cm}^2$. Thus, the adhesion energy does not clearly increase with the initial heat of adsorption and the bulk sublimation enthalpy (see Table 2.5), as one might expect. That the value for Pb is higher than Ag may be related to the fact that Pb–O bonding is much stronger than Ag–O bonding, as evidenced by the much larger heat of formation (per mole metal) for the most stable bulk oxide of Pb than for that of Ag¹. These adhesion energies have been discussed together with adhesion energy data from contact angle measurements for Pd on MgO(100)²³¹, where it was found that these adhesion energies correlate with the sum of the magnitudes of the metal's bulk sublimation enthalpy plus the heat of formation of the bulk oxide of the metal per mole of metal atoms. This suggests that local chemical bonds, both metal–oxygen and covalent metal–Mg, dominate the interfacial bonding. Similarly, STM observations of whether metals grow as flat 2D films or as 3D particles when deposited onto TiO₂(110) were shown to correlate with a combination of the

metal's bulk sublimation enthalpy and the heat of formation of the bulk oxide of the metal per mole of metal atoms ²⁴⁹.

For metals that grow as 3D particles, heat of adsorption versus coverage data of the type shown in Fig. 2.10 can be replotted as heat of adsorption versus average particle size, if the mapping between coverage and average particle size can be determined. We did this first for the case of Pb on MgO(100) ¹⁵, as shown in Fig. 2.11. Careful measurements of Pb and MgO peak intensities versus coverage in Auger electron spectroscopy (AES) were well fitted by a quantitative intensity model (with accurate, *in situ* measurements of relative sensitivities and mean-free paths) assuming that the Pb grows as three-dimensional (3D) Pb particles with a fixed number density (N) of 8×10^{11} particles/cm², independent of Pb coverage ¹¹. As noted above and shown in many experiments and by Venables' kinetic models ^{245, 246}, it is common for such systems that as metal is first deposited the number of nuclei at first increases, but after only a few percent of a monolayer the number density of clusters reaches a saturation value, N_{sat} , and stays constant thereafter (until the particles start growing so large that they touch neighboring particles, after which N decreases). Thus, the assumption of a constant number density for the coverage range applied is justified. It was further assumed that the particles have the shape of a hemispherical cap. The data is not sensitive to the exact shape of the 3D particles, and is equally well fitted by any shape with an aspect ratio (thickness \div length parallel to the oxide surface) of $\sim 1:3$. Dividing the Pb coverage (atoms/cm²) by N_{sat} (particles/cm²) gives the average number of Pb atoms per particle at any given Pb coverage, which can be combined with the bulk density of Pb (atoms/cm³) to give the average particle volume (V) at each coverage. This hemispherical volume then gives the average Pb particle diameter at that coverage: $d = (6V/\pi)^{1/3}$.

We were thus able to plot the heat of adsorption versus Pb coverage data from Fig. 2.10 instead as heat versus Pb particle radius¹⁵, as shown in Fig. 2.11. As can be seen, the heat of adsorption decreases dramatically with particle radii below 3 nm (diameters below 6 nm). This is due to the fact that when a Pb atom adsorbs to a very small Pb cluster, it makes fewer Pb–Pb bonds than it does to a very large Pb particle, where it makes six Pb–Pb bonds, on average. For example, when a fourth Pb atom adds to a Pb trimer, it makes only three Pb–Pb bonds. Also, the bonds of Pb atoms to the underlying MgO are weaker than Pb–Pb bonds.

A widely used approach for estimating the dependence of particle energy on size has been to use the Gibbs-Thompson (GT) relation, which states that the chemical potential (partial molar free energy) of a metal atom in a particle of radius R , $\mu(R)$, differs from that in the bulk, $\mu(\infty)$, by:

$$\mu(R) - \mu(\infty) = 2\gamma\Omega/R \quad (2.26)$$

where γ is the surface free energy of the metal and Ω is the volume per atom in the bulk solid²⁵⁰. Neglecting entropy differences, this gives that:

$$\Delta H_{\text{ad}}(R) + \Delta H_{\text{sub}} = \mu(R) - \mu(\infty) = 2\gamma\Omega/R, \quad (2.27)$$

remembering that we define ΔH_{ad} as a negative number in this review. As seen in Fig. 2.11, this GT model severely overestimates the stability of Pb in small Pb particles, by ~60 kJ/mol at 1 nm radius. This is because the surface energy increases substantially as the radius decreases below ~3 nm, since the average coordination number of the surface atoms decreases. This is the same reason more open or stepped crystal facets of metals (i.e., where the metal atoms have lower coordination numbers) have higher surface energies^{33, 251}.

The simple, modified pairwise bond-additivity (MBA) model shown in Fig. 2.11 reproduces the dramatic dependence of adsorption enthalpy on cluster size surprisingly well. In

this MBA model, described in detail elsewhere^{15, 252}, the energies of discrete, compact clusters were calculated assuming that all metal-metal bond energies equal their bulk value (32.5 kJ/mol for Pb, which is 1/6 of the sublimation energy of the bulk solid¹). Very stable cluster shapes were chosen by adding successive hexagonal close-packed layers. The effective radius, R , of each such cluster was calculated from its volume (V) assuming hemispherical shape using the equation $V = (\text{number of atoms per cluster}) \cdot \Omega = 2\pi R^3/3$. The energies for other cluster sizes were assumed to vary linearly with radius between these compact clusters, thus modifying true bond-additivity. There are two compensating errors in this MBA model. First, metal-metal bond energies actually increase as the coordination number of the metal atoms involved decreases^{253, 254}. Second, MBA interpolates linearly between points calculated only for the most compact clusters, whereas atoms in most small clusters are actually less stable due to their lower average coordination number. Because these errors roughly compensate, there is reasonable agreement with the data.

We also used molecule beam / surface scattering of a beam of Pb atoms from an MgO(100) surface (prepared in the same way as prepared for the SCAC measurements above) to mass-spectrometrically determine the surface residence times of Pb adatoms on this surface at 300 K. We measured the average lifetimes of the Pb adatoms which transiently adsorbed but did not permanently stick on the MgO(100) surface at 300 K (while the other 70% stick permanently to Pb clusters on the MgO), and extracted from these the heats of adsorption of these transiently adsorbed Pb adatoms, resulting in heats of 69 to 78 kJ/mol and 92 to 101 kJ/mol for the two weakest adsorption sites¹¹⁸. These may be attributed to monomers (or clusters smaller than the critical nucleus size) at terrace and step sites, respectively. (“Critical nucleus size” here is defined, based on its use in kinetic models for nucleation and growth of metal clusters during

metal vapor deposition onto oxide surfaces^{33, 245}, as the size wherein the metal atoms have the highest chemical potential. Smaller clusters spontaneously decompose but large clusters are thermodynamically stable and continue to grow.) The initial heat of adsorption measured calorimetrically at 300 K (103 kJ/mol, from Table 2.5) is slightly larger than the heat of adsorption at steps, consistent with cluster formation on the surface during the first gas pulse during calorimetry. This initial calorimetric heat of adsorption was almost identical at 190 K and 300 K^{11, 81}. Given the strong increase in heat with cluster size noted above, this implies that the same average cluster size was formed in the first pulse of metal gas at 190 and 300 K, even though the saturation number density of clusters was much larger at 190 than at 300 K and took more pulses to reach⁸¹. Using the saturation number density of clusters measured at higher coverage and 300 K (8.1×10^{11} clusters/cm²) and the average coverage during the first pulse (1.2×10^{13} atoms/cm²)¹¹ gives that these clusters contain 15 Pb atoms on average during the first pulse's heat measurement¹¹. For Ag on MgO(100), this number is 12 atoms at 300 K¹².

Oxide-supported metal nanoparticles are among some of the most important heterogeneous catalysts in use today. These metal particles supported on oxides often sinter or ripen with time during standard industrial operation, starting from a collection of many small, highly dispersed particles and eventually converting to their thermodynamically-preferred state: fewer, larger particles^{33, 250, 255-270}. Thus, understanding the kinetics of sintering is quite important. Before the results of Fig. 2.11 were published, the use of the GT relation was implicit in all atomistic models for catalyst sintering²⁶⁵⁻²⁶⁷, starting with the pioneering models of Wynblatt and Gjostein^{250, 255}. We have shown that when incorporated into kinetic models for catalyst particle sintering, the MBA model helps provide a much more accurate kinetic model for sintering, with physically more reasonable parameters, and it helps explain previous anomalies in

sintering kinetics^{15, 252}. It also helps explain the size-focusing observed in colloidal nanoparticle growth from liquid solutions²⁷¹.

2.6.4.2: Silver Atom Adsorption Enthalpies on Different Oxide Surfaces

To assess how different oxides affect the stability of nanoparticles of the same metal, SCAC was used to measure the adsorption enthalpies of Ag atoms onto several different oxides: the MgO(100) surface, two slightly-reduced CeO₂(111) surfaces, and the Fe₃O₄(111) surface. The Ag film morphology was measured versus Ag coverage at 300 K by measuring the AES and He⁺ ISS peak intensities for the Ag and for the oxide elements (O and/or the oxidized metal) versus Ag coverage. For all these oxide surfaces, these AES and ISS data was well fitted by assuming the Ag particles have the shape of hemispherical caps, with a fixed number density that is independent of Ag coverage after the first 2% of a ML^{12, 17}, where the fits were shown to give saturation Ag particle densities (N) of 2.5×10^{12} , 4×10^{12} , and 4×10^{12} particles/cm² for MgO(100), CeO₂(111), and Fe₃O₄(111), respectively. This value of N was the same for CeO₂(111) independent of whether the surface had a reduced stoichiometry of CeO_{1.9}(111) or CeO_{1.8}(111) within the probe depth of XPS. For the less reduced CeO_{1.9}(111) surface, most of the oxygen vacancies are thought to reside at the step edges¹⁷. (Calculations by DFT generally indicate that oxygen vacancies are much more stable at step edges than on terraces of oxide surfaces.) Dividing the Ag coverage (atoms/cm²) by N (particles/cm²) gives the average number of Ag atoms per particle at any given Ag coverage, which is converted to the average Ag particle diameter at that coverage just as described above for Pb on MgO(100).

Figure 2.12 shows the measured heat of adsorption of Ag gas atoms on these four oxide surfaces plotted versus the average Ag particle diameter to which it adds, using the above

approach to convert from Ag coverage to Ag particle diameter. As can be seen, the heat of adsorption increases rapidly with Ag particle size (coverage) on all these oxides, but reaches a saturation value for large silver particles which is indistinguishable from the bulk heat of Ag sublimation (285 kJ/mol^{-1} , shown by the horizontal line).

Figure 2.12 also shows that there are large differences between the different surfaces in the stability of metal atoms adding to particles of the same size. Most notably, Ag atoms bind much more strongly to sub-4-nm Ag particles on the $\text{Fe}_3\text{O}_4(111)$ and reduced $\text{CeO}_2(111)$ surfaces than to the same size particles on $\text{MgO}(100)$. When a pulse of metal atoms adds to the particles, some add on the tops and sides of the particles but some add to the perimeters, where they bind to the oxide as well. The difference in average adsorption energy may come from this nearest-neighbor bonding difference, with perhaps a lesser contribution from next-nearest-neighbor sites. Also, the growing Ag lattice may adopt its lattice parameter to that of the oxide surface, and vice versa, thus providing sites for the next Ag atom where the Ag–Ag bond energies are different due to lattice strain effects. For example, a slightly stretched oxide lattice might provide thermodynamically more stable sites for Ag adsorption. This type effect cannot continue forever, since lattice strain builds up as the Ag island gets larger.

In all four oxide surfaces, the metal particles are probably nucleated mainly at step edges^{17, 18, 33, 190, 193, 195, 198, 244}, but the particles are big enough in the 1.5 to 4 nm range that most of the metal atoms at the metal / oxide interface are *not* directly bonding to oxide step atoms, but instead bind to terrace atoms. This can be seen, for example, in the STM image of Ag particles grown on this same type of $\text{CeO}_2(111)$ film (here only 2.6 nm thick) by Luches et al.¹⁸ (Fig. 2.13). Thus, these heat data indicate that the bonding of Ag particles to the oxide is stronger also at the terrace sites of $\text{Fe}_3\text{O}_4(111)$ and reduced $\text{CeO}_2(111)$ than $\text{MgO}(100)$.

The data in Fig. 2.12 are all for oxide thin films that are 4 nm thick, grown on a metal single crystal support. For $\text{CeO}_2(111)$, we also measured heats of Ag adsorption using oxide films that were only 1, 2 and 3 nm thick (all grown on $\text{Pt}(111)$). While the 2, 3 and 4 nm films all gave the same results as shown here, the 1 nm thick oxide gave considerably higher heats of adsorption for the same particle size, by 20-50 kJ/mol for Ag particles below 1.5 nm diameter¹⁷. This indicates that 1 nm oxide films are not thick enough to represent the bulk, whereas 2 nm and above are. In this case, the Ag feels additional attraction to the surface when the CeO_2 film is only 1 nm thick, probably due to long-range electronic interactions with the underlying $\text{Pt}(111)$ substrate. Other related effects have been observed experimentally and theoretically in this ≤ 1 nm thickness range, with the extent of charging of the adsorbed metal even being affected by oxide thickness^{202, 232, 239, 272}.

Another way to view the data in Fig. 2.12 is to plot the enthalpy of a metal atom after it adds to a particle relative to its enthalpy in bulk Ag (or the partial molar enthalpy) versus particle size, as shown in Fig. 2.14. In this figure, we express particle size as the number of metal atoms per particle, rather than as diameter. The increase in stability with particle size in all these curves is dominated by the effect of particle size on the number of metal-metal bonds per atom, as it was in Fig. 2.11. The Pb data for $\text{MgO}(100)$ from Fig. 2.11 fall almost on top of the Ag / $\text{MgO}(100)$ data (as shown in¹⁷, where they are presented in the same plot). These $\text{MgO}(100)$ data are distinctly different from the Ag data for the $\text{CeO}_{2-x}(111)$ and $\text{Fe}_3\text{O}_4(111)$ surfaces. As seen, Ag atoms are 30 to 70 kJ/mol more stable in Ag nanoparticles for any given size smaller than ~1000 atoms when those particles are attached to $\text{CeO}_{2-x}(111)$ and $\text{Fe}_3\text{O}_4(111)$ surfaces than to $\text{MgO}(100)$ surfaces. This difference gets smaller for larger particles, and essentially

disappears by ~ 5000 atoms/particle, where the energy of the added metal atom reaches the stability of the bulk solid even on MgO(100).

The curves in Fig. 2.14 directly reflect the thermodynamic driving force for nanoparticle sintering. If a metal atom is on a relatively small particle within a collection of particles on an oxide, it is less stable and prefers to migrate to a larger particle where it is more stable (i.e., move down and to the right on each of these curves until it reaches the minimum, or zero). Such migration of individual monomers from smaller to larger particles (typically by diffusion across the surface of the oxide) is referred to as Ostwald ripening, and is the same effect that gives rise to raindrops in clouds, where water monomers migrate through the gas. Similarly, it is downhill in enthalpy for two small particles to diffuse together and form one larger particle. This mechanism for sintering is called particle diffusion / coalescence. Both mechanisms have been observed experimentally (see ^{250, 252, 255, 256} and references therein).

The enthalpic driving force for sintering shown in Fig. 2.14 drops below 10 kJ/mol already for ~ 400 -atom (3 nm) particles on the CeO_{2-x}(111) and Fe₃O₄(111) surfaces, but similar energies are not reached until ~ 3000 -atom (6 nm) particles on MgO(100). Clearly, sintering will stop at much smaller particles on CeO₂ and Fe₃O₄(111) surfaces! Since Au nanoparticles are very active for several catalytic reactions when 3 nm in diameter but almost completely inactive above 6 nm ^{42, 273-277}, this range of particular sizes is critical. Our derivation of kinetic rate equations for sintering by both mechanisms showed that this enthalpy in Fig. 2.14 is exponentially reflected in the sintering rate, as a negative contribution to the apparent activation energy ^{15, 252, 271}. Thus, the sintering rates for small particles should be much, much slower on CeO₂ and Fe₃O₄(111) surfaces than on MgO(100). This is consistent with observations that ceria offers a more sinter-resistant support for late transition metals than other oxides ^{278, 279}.

In Fig. 2.14 we also see that small Ag nanoparticles (<1.5 nm or 30 atoms) on CeO_{2-x}(111) are ~15 kJ/mol more stable on the more reduced CeO_{1.8}(111) surface than on CeO_{1.9}(111). This increase in stability with vacancy concentration is consistent with DFT calculations that Ag adatoms bind >100 kJ/mol more strongly to vacancy sites on CeO_{2-x}(111) than to stoichiometric sites²⁸⁰.

We have integrated the measured heat versus coverage curves (up to the coverage where the heat reaches the bulk sublimation energy), for each of these oxide surfaces, and extracted from that integral the adhesion energies for Ag nanoparticles to these oxide surfaces using Eq. (2.20) and the roughness factor of hemispherical caps ($f_r = 2$). This is exactly the same procedure as outlined in Ref.¹², which gave an adhesion energy of 0.3 J/m² for Ag on MgO(100). In all cases, we assumed a hemispherical shape for the Ag nanoparticles. The results are summarized in Table 2.6.

Table 2.6. The calorimetrically-measured adhesion energies of Ag nanoparticles to MgO(100), two reduced CeO_{2-x}(111) surfaces and Fe₃O₄(111), and the initial heats of Ag adsorption ($\Delta H_{ad,init}^0$) for the first pulse (~0.03 monolayer) of Ag gas at 300 K. Also listed are the Ag particle size and Ag coverage used to get the adhesion energy. The adhesion energy for Ag on Ag (i.e., twice the surface energy of bulk solid Ag) is given for comparison.

substrate surface	E_{adh} / (J/m ²)	Ag coverage / (atoms/cm ²)	Ag particle size / nm	$-\Delta H_{ad,init}^0$ / (kJ/mol)
MgO(100)	0.3±0.3 ¹²	9.6x10 ¹⁵	6.6	176
CeO _{1.9} (111)	2.3±0.3	2.8x10 ¹⁵	3.6	200
CeO _{1.8} (111)	2.5±0.3	2.8x10 ¹⁵	3.6	220
Fe ₃ O ₄ (111)	2.5±0.3	2.8x10 ¹⁵	3.6	220
Ag(solid)	2.44 ¹²	∞ ^a	∞ ^a	285 ^b

a. Bulk Ag(solid), so the high coverage / large particle limit.

b. Heat of sublimation of bulk Ag(solid).

These results show that the adhesion energies of Ag nanoparticles to CeO₂(111) and Fe₃O₄(111) are much larger than for the same particles to MgO(100), and that this adhesion energy increases with the extent of reduction of the CeO₂. These adhesion energies correlate with the initial adsorption energy of the first Ag gas pulse (Table 2.6). Both values reflect the strength of Ag–oxide bonding.

The adhesion energies of Ag nanoparticles to these CeO_{2-x}(111) and Fe₃O₄(111) surfaces (~2.3 to 2.5 J/m²) approach and even exceed the adhesion energy of Ag to itself (2.44 J/m² ¹²). For an adhesion energy equal to or larger than the Ag–Ag adhesion energy, one would generally not expect the Ag to cluster into 3D islands, but instead to wet the surface. However, these Ag particles bind *locally* to some part of the oxide surface where there is greater defect (step, kink, or vacancy) concentration than elsewhere, and thus the local adhesion energy is likely less on the stoichiometric oxide terraces. Furthermore, the lattice mismatch between Ag(111) and the underlying oxide will cause the Ag lattice to expand or contract to match the underlying oxide lattice, and also cause the oxide lattice under the Ag island to contract or expand to gain interfacial bonding stability. This strain in the oxide under a Ag island will also force the oxide lattice immediately adjacent to the island to strain in the opposite direction, thus destabilizing Ag bonding there more and more as the island size grows (and also causing particle-particle repulsions) ¹⁷.

The strain arising from such lattice mismatch has been directly observed by electron microscopy for Pd particles on MgO(100), where measurements of the 3D particle shape showed that the adhesion energy increases with decreasing Pd particle size from 0.91 J/m² for 10 to 15 nm particles up to >1.64 J/m² below 5 nm ²⁸¹. Such tiny Pd particles were seen to increase their lattice parameter to match that of the MgO, whereas regularly-spaced Pd dislocations appeared at

the interface for particles larger than 10 nm. STM measurements of the 3D particle shape for Cu particles on the ZnO(0001)-Zn surface gave an adhesion energy of 3.4 J/m^2 ²⁸².

The types of calorimetric results summarized above may eventually reveal correlations between the strength of metal–oxide bonding and the structural, electronic, chemisorption, and catalytic properties of oxide-supported metal nanoparticles, their dispersion, and their resistance to long-term sintering. This would substantially improve our fundamental understanding of structure / function relationships in heterogeneous catalysis.

2.6.5: TPD studies of Metal Atom Adsorption Enthalpies on Oxides

The probability that a metal gas atom striking an oxide surfaces become at least transiently adsorbed has always been observed to be >0.1 at 300 K or colder for the papers reviewed here and in the Section 2.6.4 on SCAC studies of metal adsorption energies on ordered oxide surfaces. Therefore, it is safe to assume that the activation energy for adsorption is <10 kJ/mol. As described above, the activation energy for desorption determined from TPD studies can be used to estimate the heat of adsorption when the activation energy for adsorption is small by simply adding $\frac{1}{2} RT_p$. Adsorption enthalpies determined from TPD measurements of sub-monolayer coverages of metals adsorbed on oxides are summarized in Table 2.7.

Table 2.7: Adsorption enthalpies for metal atoms adsorbed on oxide surfaces, listing the parameters in Eq. (2.28) used to fit the coverage dependence. Desorption energies at each initial coverage were determined by Redhead analysis of the TPD data in the citations listed, using T_p and the prefactor estimated using Eq. (2.16) (also listed for the range of T_p values analyzed). Also listed are the bulk metal's sublimation enthalpy and surface energy from the literature, and the metal /oxide adhesion energy and contact angle determined from these using Eqs. (2.30-2.32).

adsorbate	oxide surface	$T_p /$ K	$\log(\nu / \text{s}^{-1})$	$-\Delta H_{\text{ad,init}}$ /(kJ/mol)	ΔH_{sub} /(kJ/mol)	θ_c / ML	$\gamma_{\text{v/m}}$ /(J/m ²)	E_{adh} /(J/m ²)	θ_{contact}	citation
Pd	disordered SiO ₂ /Mo(110)	1140 → 1290	14.5	304	373	1.2	2.00	2.8	66°	283
Cu	α -Al ₂ O ₃ (0001) or γ -Al ₂ O ₃ (111) /Mo(110)	980 → 1130	14.4 → 14.5	279	337	1.2	1.76	2.6	62°	20
	disordered SiO ₂ /Mo(110)	980 → 1140	14.4 → 14.5	271		1.3		2.3	71°	284
Ag	α -Al ₂ O ₃ (0001) or γ -Al ₂ O ₃ (111) /Re(0001)	740 → 900	14.3 → 14.4	224	285	1.0	1.22	1.6	71°	21, 22
Au	TiO ₂ (001) /Mo(100)	1080 → 1180	14.4 → 14.5	318	377	2.3	1.54	1.8	79°	285
	disordered SiO ₂ /Mo(110)	1070 → 1250	14.4 → 14.5	314		1.3		2.0	73°	19

2.6.5.1: TPD studies of the Adsorption of Late Transition Metals and Noble Metals

Figure 2.15 shows TPD spectra as a function of coverage for Au particles on a 5 nm thick SiO₂ thin film on Mo(110)¹⁹. As shown in this typical example, the TPD peak temperatures increase strongly with coverage for sub-monolayer coverages of late transition metals on such oxides. This has been attributed to the influence of metal particle size on the adsorption energy, associated with the decrease in the number of metal-metal bonds that form as the metal particles become smaller^{19, 20, 286}, which is consistent with our SCAC results above. The inset shows heat of adsorption calculated from the desorption energies determined from these TPD spectra by leading-edge analysis, as reported in the original paper¹⁹. Next, we show why desorption energies determined in this way are highly inaccurate for low coverages of late transition metals which grow as 3D particles, and explain the alternate method we have adopted for estimating desorption energies for such cases to get the values listed in Table 2.7. Heats of adsorption determined with this preferred method are also shown in the inset of Fig. 2.15.

While leading-edge analysis and so-called complete analysis of TPD spectra are usually excellent methods for extracting accurate desorption energies, we feel that it has serious problems when applied to systems like late transition metals on oxides, where the adsorbates clusters into 3D particles and the adsorption energy varies so strongly with particle size, as we have shown above. This is because of a breakdown of the basic assumption used in applying Eq. (2.4) above to extract E_d . Equation (2.4) assumes that the surface species are always in equilibrium so that the desorption rate is a single-valued function of coverage and temperature: $r(\theta, T)$. This is far from true here, since sintering is fast for tiny particles but the sintering rate decreases so dramatically with particle size (see Section 2.6.4.2). As shown above, the same total coverage of large metal particles (>6 nm in diameter) will have a much larger E_d (larger

heat of adsorption) than particles with size ~ 1 nm. The large particles will also have a much smaller total surface area. The net effect is a desorption rate that is many orders of magnitude slower at the same temperature for an oxide surface with large metal particles than for one with small particles, when both samples have the same total coverage. We are convinced that this is the reason that Arrhenius plots of constant-coverage cuts from TPD spectra for Ag on alumina²¹ do not show straight lines, but instead the slope decreases dramatically with temperature. This is because the average particle size gets larger with temperature during a TPD experiment, due both to the selective removal of smaller particles because of their faster desorption rates, and to sintering driven by the increasing temperature. For the same reason, leading-edge analysis will give an Arrhenius plot that has a slope that is biased toward smaller magnitude (resulting in lower E_d than reality) since the fastest desorption rates are for the smallest particles in the distribution of initial particle sizes present, but these particles disappear almost immediately and further desorption is biased toward slower and slower rates.

For these reasons, we propose that a simple 1st-order Redhead analysis using the desorption peak temperature for each coverage with a prefactor estimated as suggested above is a much better method for estimating desorption energies from TPD for such systems. To support this, Figure 2.16 compares heats of adsorption versus coverage for Cu and Ag on single-crystalline Al_2O_3 surfaces determined from TPD data reported by Goodman's group^{20, 22} and by Van Campen et al.²¹ using this preferred method (i.e., using the first-order Redhead equation with a prefactor of $\sim 10^{15} \text{ s}^{-1}$ from Eq. (2.16)) with those determined from the same data by the original authors using leading-edge analysis. (We also added $\frac{1}{2} RT$ to the desorption energies originally reported to convert to heats of adsorption.) At low coverages, the values reported in the original papers fall far below the values from our preferred Redhead analysis. At the lowest-

coverages here, this leading-edge analysis gives a prefactor of only $\sim 10^5 \text{ s}^{-1}$ for Ag, which are many orders of magnitude too low according to transition state theory estimates with any reasonable assumptions. Leading-edge analysis of the low-coverage Cu data gave a prefactor of only $\sim 10^{10} \text{ s}^{-1}$, also lower than expected.

Table 2.7 summarizes the analyses we performed in this way for late transition metals on oxides. The prefactor was estimated in each case using Eq. (2.16) based on the entropy correlation we summarized above in Section 2.3.2.

As shown in Fig. 2.16, for both Cu and Ag on these ordered Al_2O_3 surfaces, the heat of adsorption increases by 60 to 70 kJ/mol with coverage, eventually leveling off at the heat of sublimation. As shown, these heats of adsorption are all well fitted by an equation of the form:

$$q_{\text{ad}}(\theta) = q_{\text{ad},0} + (\Delta H_{\text{sub}} - q_{\text{ad},0})(1 - e^{-\theta/\theta_c}), \quad (2.28)$$

where $q_{\text{ad},0}$ is the heat of adsorption in the limit of zero coverage, θ is the initial coverage for each TPD spectrum used in this Redhead analysis, and θ_c is a constant proportional to how quickly the heat increases with coverage between $q_{\text{ad},0}$ and ΔH_{sub} . The value for ΔH_{sub} was not treated as a fitting parameter but instead taken from the literature¹. The data in Fig. 2.15 were also well fitted by this equation.

Similar analyses to those in Fig. 2.16 were performed on many previously published TPD spectra for late transition metals on oxides. The results are summarized in Table 2.7. We list there the parameters $q_{\text{ad},0}$, ΔH_{sub} and θ_c which characterize the heat versus coverage curves thus obtained and fitted to Eq. (2.28). That these data were all well fitted by Eq. (2.28) proves that this Redhead analysis and the choice of prefactors using Eq. (2.16) gives accurate values of $q_{\text{ad}}(\theta)$. Otherwise, the data points would not so nicely approach ΔH_{sub} asymptotically at high coverage in each case.

If Eq. (2.28) is integrated versus coverage to high coverage, and is combined with Eq. (2.20) (assuming the metal makes a flat film), it can be rearranged to give the adhesion energy in terms of these parameters:

$$E_{\text{adh}} = 2\gamma_{\text{v/m}} - (\Delta H_{\text{sub}} - q_{\text{ad},0})(n/A)\theta_c. \quad (2.29)$$

Correcting for surface roughness gives:

$$E_{\text{adh}} = (1 + f_r)\gamma_{\text{v/m}} - (\Delta H_{\text{sub}} - q_{\text{ad},0})(n/A)\theta_c, \quad (2.30)$$

where f_r is the roughness factor of the metal film. If the metal film consists of spherical caps each with a contact angle to the oxide surface of θ_{contact} , it is a simple geometric derivation to prove that:

$$f_r = 2 \cdot [1 - \cos(\theta_{\text{contact}})] / [\sin^2(\theta_{\text{contact}})]. \quad (2.31)$$

The adhesion energy is also related to the contact angle by the equation of Young and Dupre³³:

$$E_{\text{adh}} = \gamma_{\text{v/m}} [1 + \cos(\theta_{\text{contact}})]. \quad (2.32)$$

After substituting Eq. (2.31) into Eq. (2.30) to remove f_r , Eqs. (2.30) and (2.32) provide two equations in two unknowns, E_{adh} and θ_{contact} . For systems where the parameters for Eq. (2.28) have already been measured, such as for the systems in Table 2.7, these can be solved to provide E_{adh} and θ_{contact} . Note that the initial coverages in the TPD curves that most strongly influence the values of $q_{\text{ad},0}$ and θ_c are low enough that the surface is only partly covered by individual particles during desorption, whereas the overall analysis of Eq. (2.30) involves integration of Eq. (2.28) to much higher coverages. This is valid because $q_{\text{ad}}(\theta)$ already closely approaches ΔH_{sub} at the higher coverages where the particles merge into a continuous film and the surface roughness factor from Eq. (2.31) is no longer reasonable.

The metal / oxide adhesion energies and contact angles estimated in this way for the systems in Table 2.7 are also listed there. The surface free energies for the metals were taken

from ^{12, 29, 228, 287}, and n/A was taken as the packing density of the (111) face of the metal. In Table 2.7, we have listed θ_c using the definition of one monolayer (ML) as given in the original TPD paper cited, which was defined as one adatom per surface atom of the *underlying* metal substrate (i.e., *under the oxide thin film*). (The definition was not always clearly stated, but it is the way that group generally defined ML in these types of studies.) To use θ_c in Eq. (2.29), it must first be converted from those units to the fraction n/A .

2.6.5.2: TPD Studies of the Adsorption of Alkali Metals

Since alkali metals have repulsive lateral interactions as adatoms on oxides (see below), the problem with analyzing TPD data to extract desorption energies mentioned above for late transition metals is not a problem here.

The TPD spectra of Cs from TiO₂(110) is shown in Fig. 2.17 as a function of coverage ²³. The sharp peak at ~300 K in the highest coverage spectrum in the lower panel and ~285 K in the upper panel is due to multilayer Cs. Using Eq. (2.16) to estimate a desorption prefactor for this 285 K multilayer peak gives a prefactor of 10^{14} s^{-1} . Analyzing this peak temperature with the 1st-order Redhead equation gives a heat of adsorption of 78 kJ/mol for this multilayer, in nearly perfect agreement with the standard enthalpy of sublimation of bulk Cs(solid) of 78.2 kJ/mol ¹. Starting from the lowest coverage shown, there is a continuous population of desorption intensity to increasingly lower temperature with Cs coverage. Coverages below 0.4 ML do not start to desorb until above the highest temperature studied (800 K). This reflects a nearly continuous decrease in heat of adsorption with coverage from above 200 kJ/mol down to the sublimation enthalpy of bulk Cs, 78 kJ/mol. A very similar large, smooth decrease in adsorption energy with coverage is also typically observed for alkali metals on metal surfaces, where it is attributed to

increasing dipole-dipole repulsions as these positively charged adsorbates pack closer and closer together⁹¹. These repulsions lead to mutual depolarization of the alkali adsorption complexes with increasing coverage within the first monolayer on metals⁹¹. This also occurs for alkali metals on oxide surfaces, as judged by the decrease in local dipole moment with coverage³³. Work function measurements for Cs on TiO₂(110) indicate that the adsorbate-substrate complex has a local dipole moment of ~6 Debye at 0.1 ML coverage, but that the dipole moment decreases at higher coverage²³.

Adsorbed Cs on alumina also shows TPD spectra similar to Fig. 2.17 in that Cs desorption extends in a broad peak from 1100 to 300 K, reflecting a continuous decrease in the Cs adsorption energy from 263 to 75 kJ/mol with increasing Cs coverage²⁸⁸. Photoemission also showed that this Cs is cationic at low coverages. Similarly for K on TiO₂(110)²⁸⁹, TPD spectra showed evidence for strongly repulsive K–K interactions in the first layer, with a peak extending from ~780 K down to 380 K. Note that the timescale of the experiment is important for the Cs and K on TiO₂ systems, where reduction of the oxide by the metal is thermodynamically allowed but only marginally, so that it does occur but only after long waiting times³³.

TPD for both K and Cs on NiO(100)²⁹⁰⁻²⁹², where thermodynamics strongly favor reduction, showed results consistent with strong reduction of the NiO by the alkali metal³³.

2.7: Figures

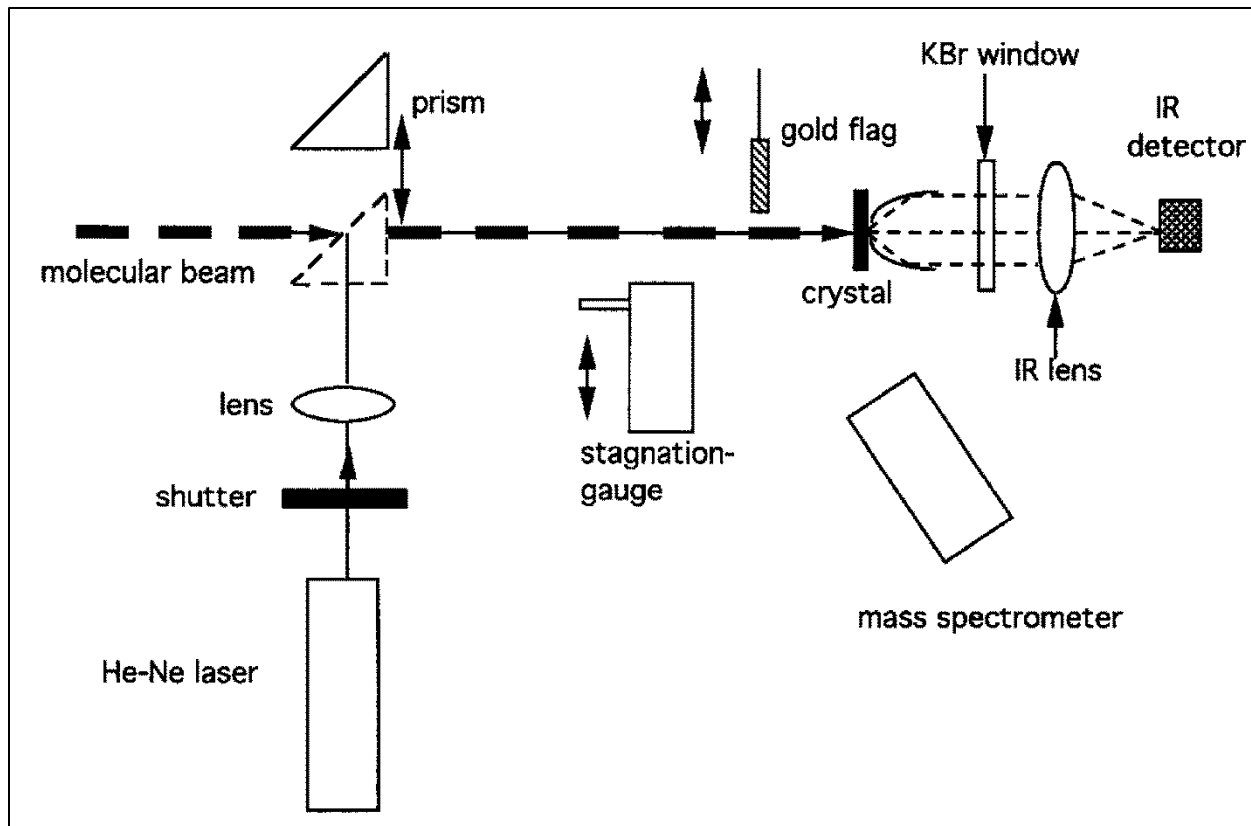


Figure 2.1. Schematic of the single crystal adsorption calorimeter developed by the group of Sir David King. Pulses of a molecular beam impinge on the clean surface of a very thin single crystal, held in ultrahigh vacuum. The transient temperature rise is measured by infrared optical pyrometry of the back of the crystal. The heat signal associated with this temperature rise was calibrated using pulses of light of known power from a He-Ne laser, which are directed down the molecular beam path. Reprinted with permission from Reference ⁶. Copyright 1996 Elsevier.

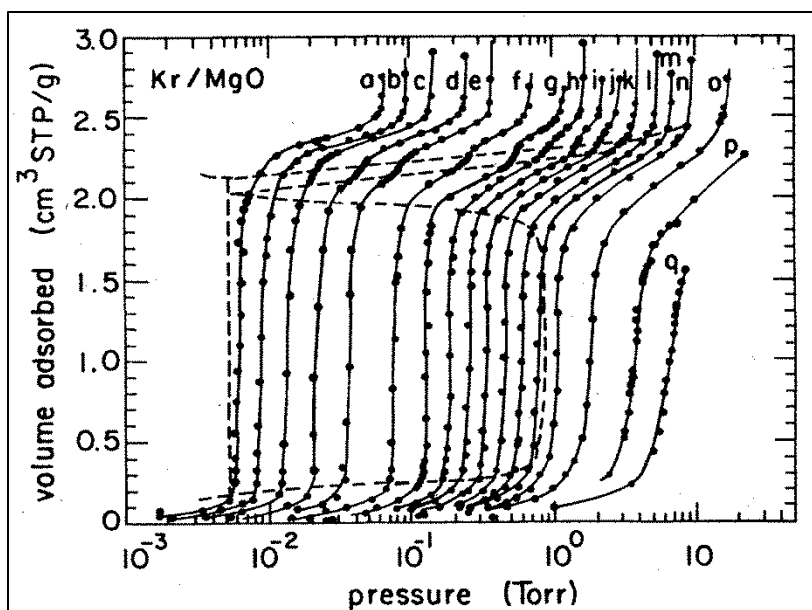


Figure 2.2. Typical equilibrium adsorption isotherm (EAI) data, in this case volumetric measurements of Kr adsorption on MgO(100) smoke. Isotherm temperatures (in K): (a) 66.76, (b) 67.82, (c) 69.10, (d) 70.97, (e) 72.56, (f) 75.21, (g) 77.47, (h) 78.97, (i) 80.28, (j) 81.59, (k) 83.16, (l) 84.52, (m) 85.87, (n) 87.56, (o) 90.88, (p) 95.21, and (q) 98.66 K. The Kr pressure ($P_{\theta,eq}$) at the adsorbed volume in the middle of the first large vertical riser (i.e., at $\theta_{eq} = \frac{1}{2}$ ML coverage) was used to determine the enthalpy and entropy of the first monolayer from a plot of $\ln(P_{\theta,eq}/P^0)$ versus $1/T$, as described in the text. Dashed lines indicate estimated phase boundaries. Reprinted with permission from Reference ⁷. Copyright 1984 American Physical Society.

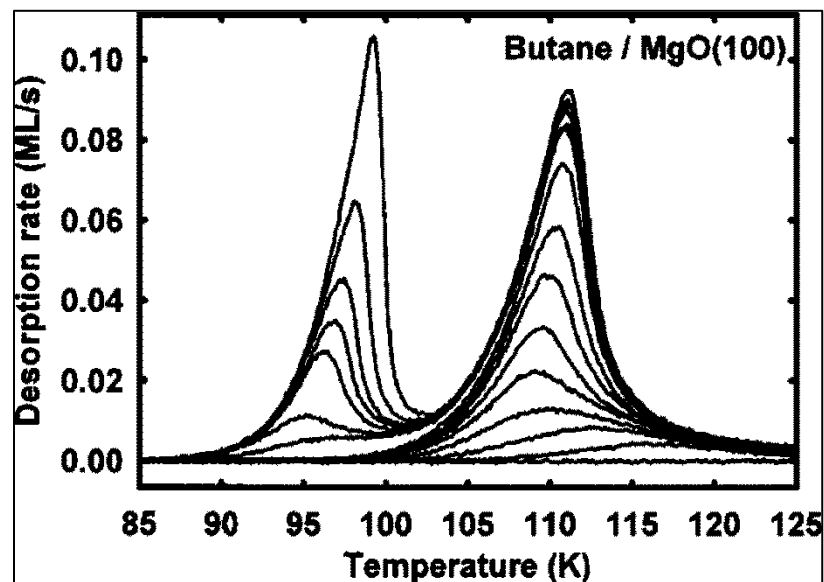


Figure 2.3. Typical TPD data for butane on MgO(100) at a heating rate of 0.6 K/s for 16 initial coverages in the range of 0–1.76 ML: 0.00, 0.10, 0.19, 0.28, 0.42, 0.51, 0.66, 0.76, 0.88, 1.05, 1.13, 1.21, 1.31, 1.38, 1.52, and 1.76 ML. Two desorption peaks are resolved, multilayer (99 K) and first-layer (110 K) desorption, as well as a high-temperature tail on the first-layer peak due to desorption from defect sites on the surface (mainly step edges). Reprinted with permission from Reference ⁸. Copyright 2005 American Institute of Physics.

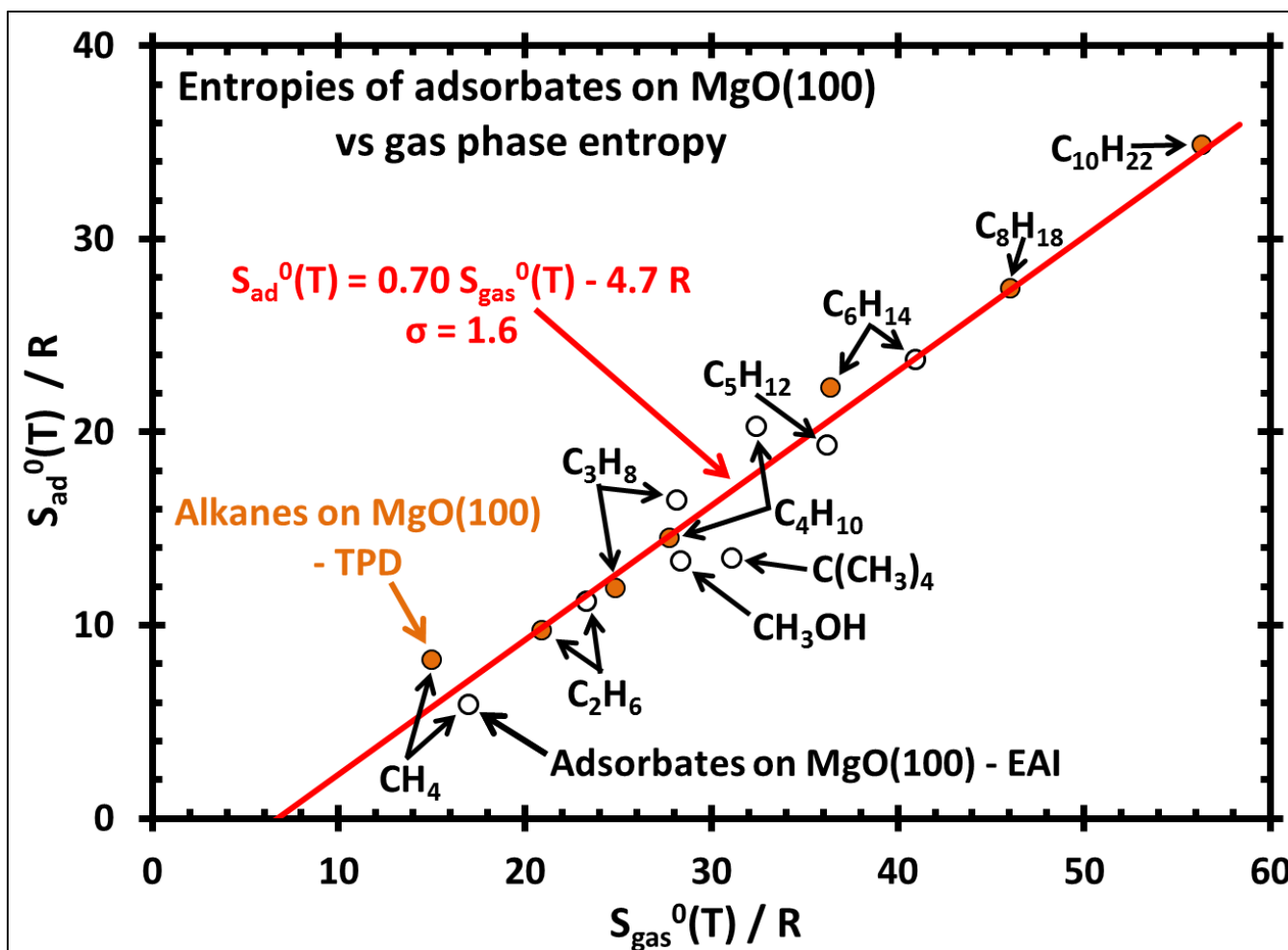


Figure 2.4. Plot of the standard entropies of adsorbates ($S_{ad}^0 = S_{gas}^0 + \Delta S_{ad}^0$) on MgO(100) smoke determined by equilibrium adsorption isotherms (EAI) plotted versus the standard entropy of the gas phase species at the same temperature from Table 2.1. The standard entropies of these same and other adsorbates determined using desorption prefactors and peak temperatures from TPD data together with Eq. (2.11) are also included from Table 2.2. The agreement with EAI results proves the accuracy of this method. The best linear fit to these data is also shown, along with the standard deviation (σ) of the adsorbate entropies from this line. Reprinted with permission from Reference⁹. Copyright 2012 American Chemical Society.

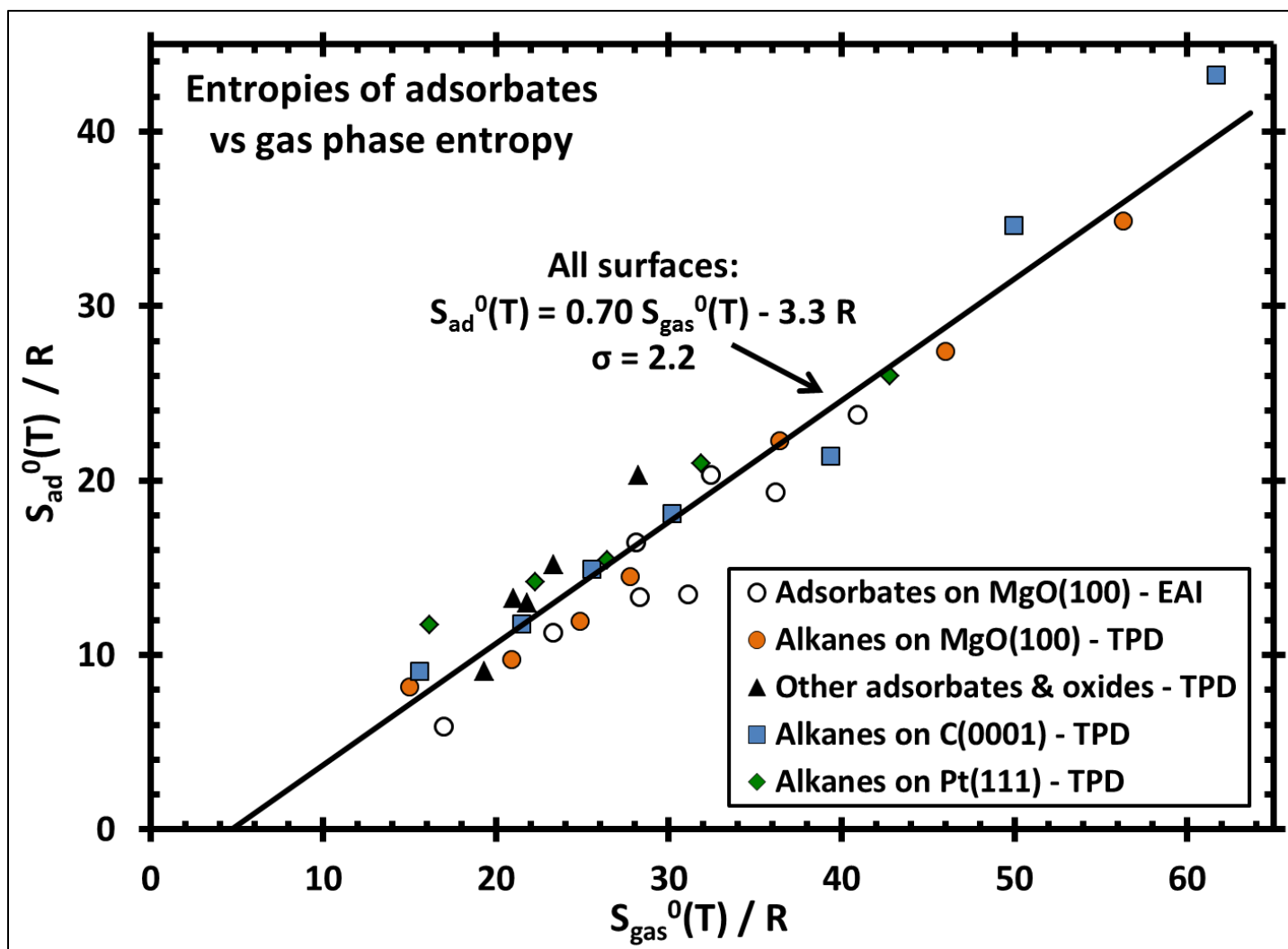


Figure 2.5. Plot of the standard entropies of adsorbates (S_{ad}^0) on several surfaces plotted versus the standard entropy of the gas phase species at the same temperature. Data for MgO(100) and other oxides are from Tables 2.1 through 2.3. Entropies for linear alkanes on Pt(111) and graphite(0001) were calculated using Eq. (2.11) with experimental prefactors and peak temperatures reported in ⁶⁷. The best-fit line is also shown. Adapted with permission from Reference ⁹. Copyright 2012 American Chemical Society.

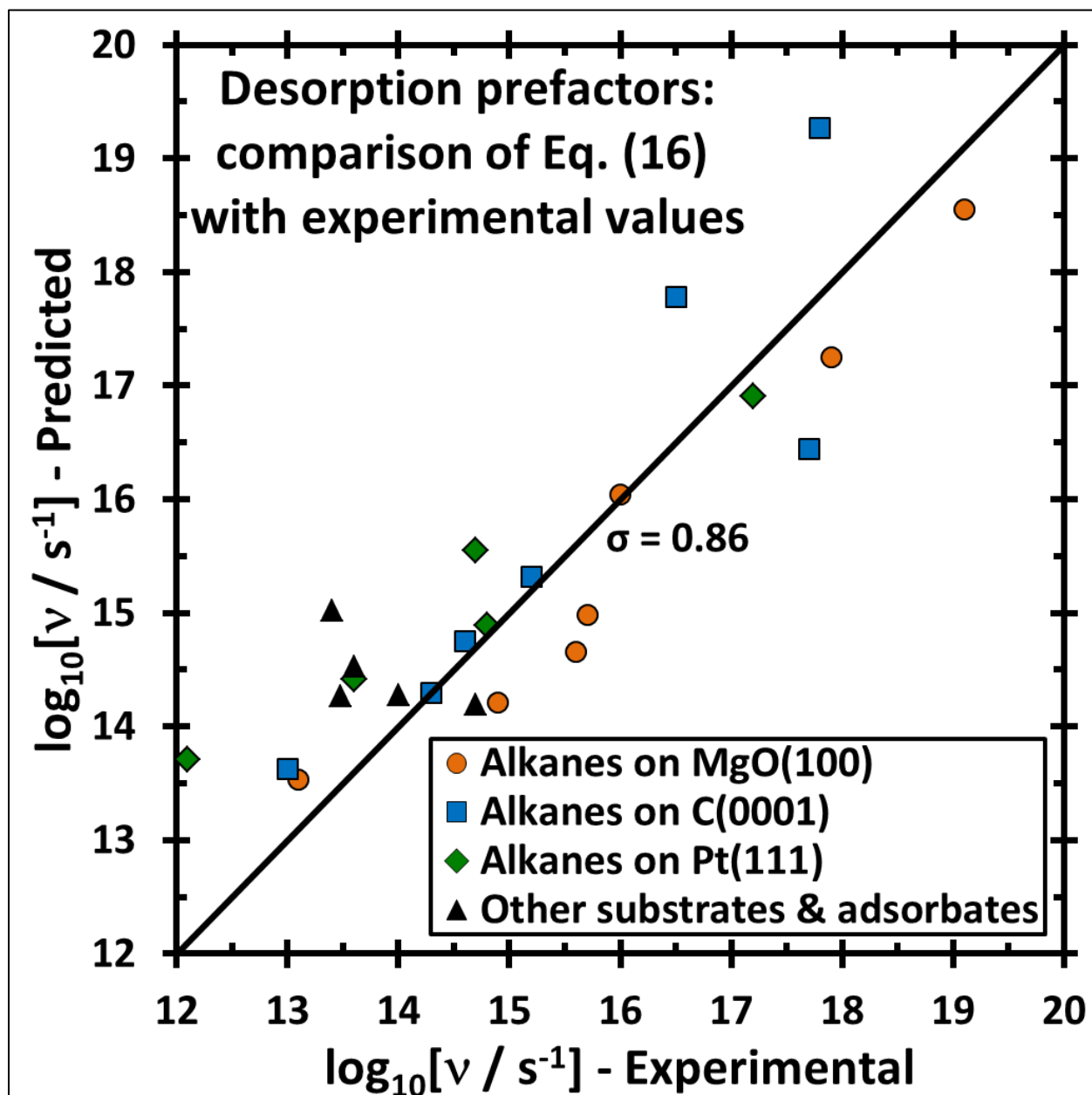


Figure 2.6. Prefactors for the desorption of molecularly adsorbed species as predicted from the gas-phase entropies using Eq. (2.16) (which was derived from the linear relationship in Fig. 2.5 using transition state theory) plotted versus the experimentally measured prefactors. Data are mostly for molecules on oxide single crystals from Table 2.3, but also shown are data for *n*-alkanes on graphite(0001) and Pt(111), from ¹⁰. The line shows the expectation based on Eq. (2.16), which the data fit with a standard deviation in $\log(\nu / \text{s}^{-1})$ of 0.86. Reprinted with permission from Reference ⁹. Copyright 2012 American Chemical Society.

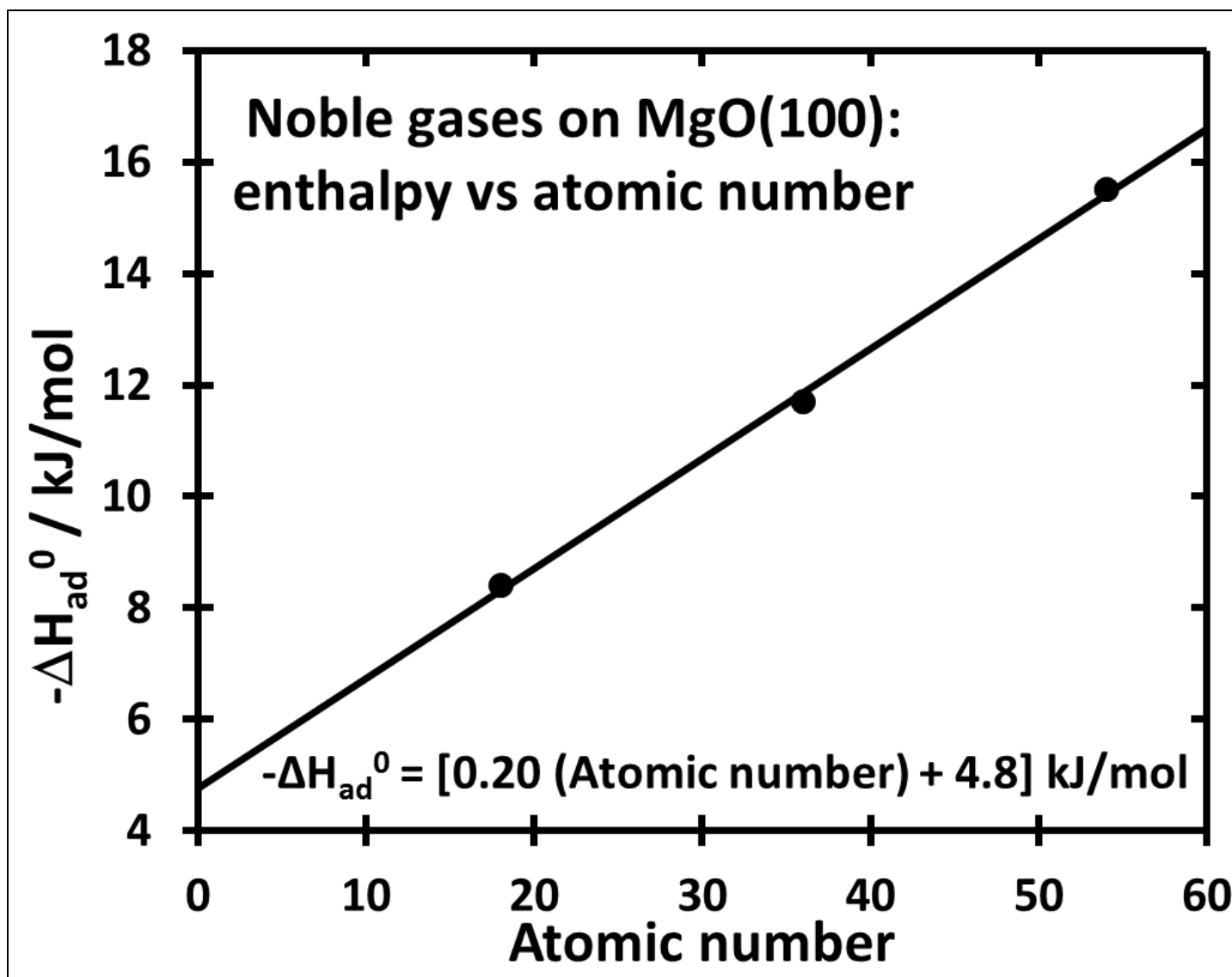


Figure 2.7. Heats of adsorption for noble gases on MgO(100) determined by EAI versus atomic number. Data from Reference ⁷, and also listed in Table 2.1. Reprinted with permission from Reference ³. Copyright 2013 American Chemical Society.

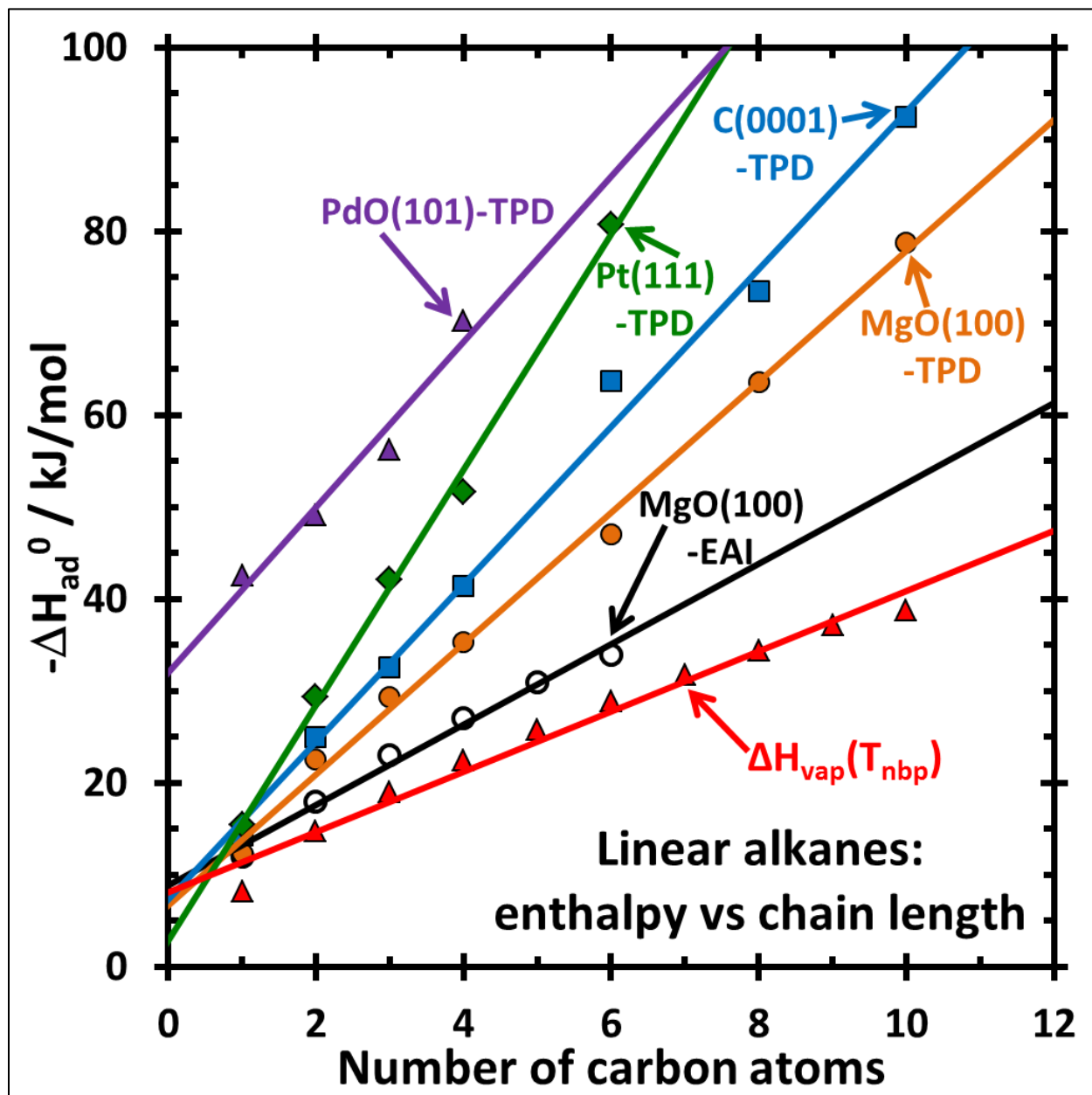


Figure 2.8. Heats of adsorption determined by TPD for linear alkanes on MgO(100), graphite(0001) and Pt(111), all at $\frac{1}{2}$ ML coverage plotted versus alkane chain length, from Reference ¹⁰. Also plotted are adsorption enthalpies for alkanes on PdO(101) from TPD (Table 2.3) and on MgO(100) smoke determined by EAI at full, saturated ML coverage (Table 2.1). For comparison, the bulk vaporization enthalpies of pure liquid alkanes at their normal boiling point are also shown, from Reference ¹. Reprinted with permission from Reference ³. Copyright 2013 American Chemical Society.

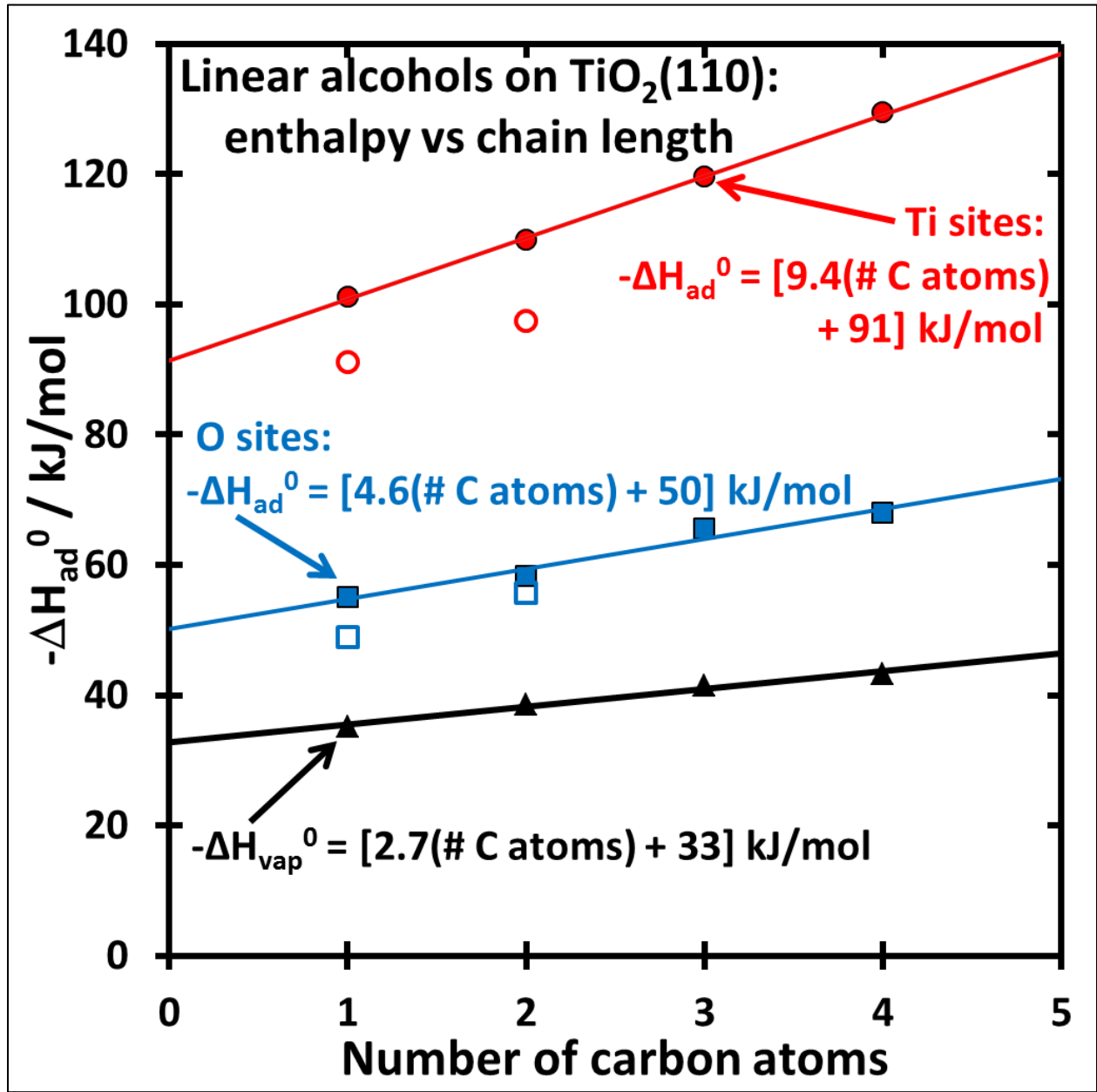


Figure 2.9. Heats of adsorption for linear alcohols on rutile TiO₂(110) near saturation coverage (determined by TPD, see Table 2.3) plotted versus the number of carbon atoms in the alcohol molecule. Data for both the Ti sites and O sites are shown. For comparison, the bulk vaporization enthalpies of the pure liquid alcohols are also shown, from Reference ¹. Reprinted with permission from Reference ³. Copyright 2013 American Chemical Society.

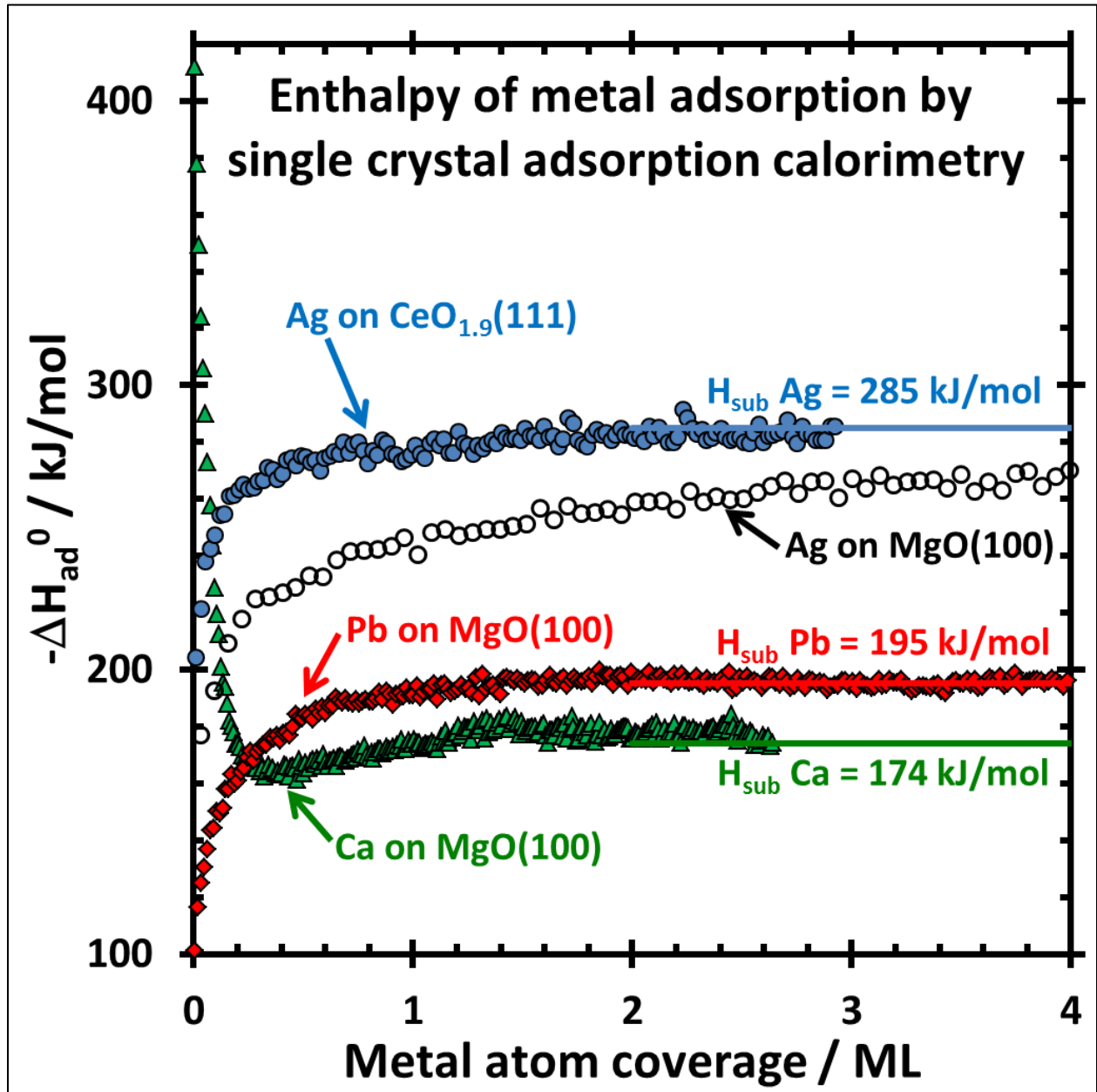


Figure 2.10. Example heats of adsorption versus coverage data for metals on single crystal oxides as measured by SCAC at 300 K. Data are shown for: Pb, Ag and Ca on MgO(100) as well as Ag on CeO₂(111) (with 5% oxygen vacancies in XPS probe depth). Data from References ¹¹⁻¹⁴; where these original papers show data to higher coverages. One monolayer here is defined as the number of oxygen ions per unit area in the topmost atomic plane ($1.12 \times 10^{15} \text{ cm}^{-2}$ for MgO(100) and $7.9 \times 10^{14} \text{ cm}^{-2}$ for CeO₂(111)). Solid horizontal lines mark the bulk heats of sublimation from the literature. Reprinted with permission from Reference ³. Copyright 2013 American Chemical Society.

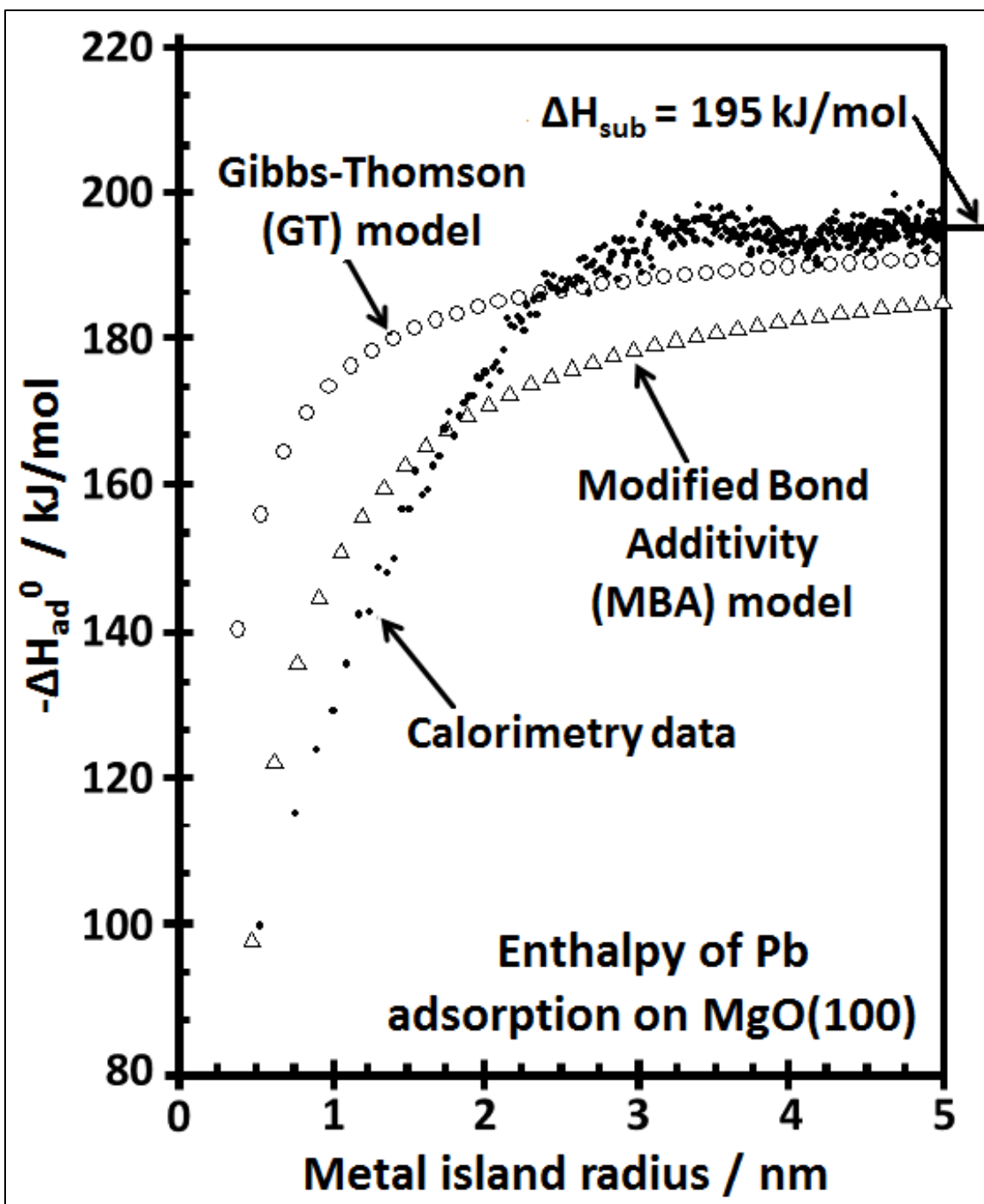


Figure 2.11. Heat of adsorption of Pb onto Pb nanoparticles on MgO(100) versus average Pb particle radius. Also shown is the Gibbs-Thomson model of Eq. (2.26), which assumes that the surface energy is the bulk value, independent of particle size. This is seen to fit the experimental data very poorly at small radii. In contrast, the modified bond additivity (MBA) model, which is also shown (see details in text), is a much better estimate for the experimental data. Adapted with permission from Reference ¹⁵. Copyright 2002 American Association for the Advancement of Science.

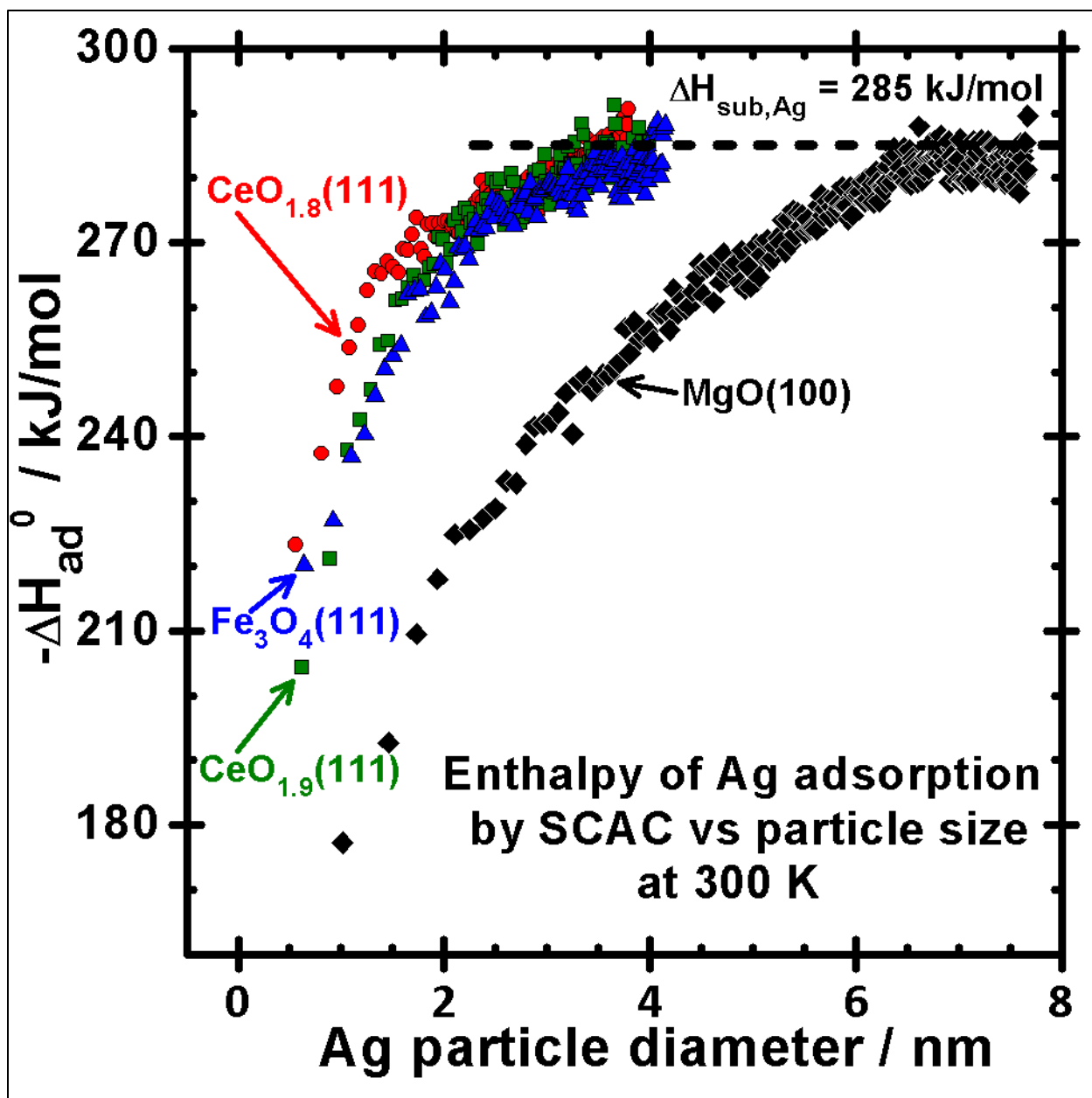


Figure 2.12. The heat of Ag atom adsorption during experiments where Ag is vapor deposited onto oxide surfaces at 300 K where Ag atoms transiently adsorb on clean parts of the oxide surface but quickly diffuses across the surface and add to growing Ag particles on the surface. Plotted here is the measured heat of Ag atom adsorption versus the Ag particle diameter to which it adds (i.e., the average Ag particle size at the Ag coverage corresponding to that heat value). Data are shown for four different surfaces: $\text{Fe}_3\text{O}_4(111)$ thin film and two $\text{CeO}_2(111)$ thin films with different extents of surface reduction ($x \sim 0.1$ and 0.2 in CeO_{2-x}), all grown on $\text{Pt}(111)$ to 4 or 5 nm thickness, and a 4 nm thick $\text{MgO}(100)$ film grown on $\text{Mo}(100)$. The data for $\text{Fe}_3\text{O}_4(111)$ are from Reference ¹⁶ and those for $\text{CeO}_2(111)$ and $\text{MgO}(100)$ are from Reference ¹⁷. Adapted with permission from Reference ¹⁶. Copyright 2011 Royal Society of Chemistry.

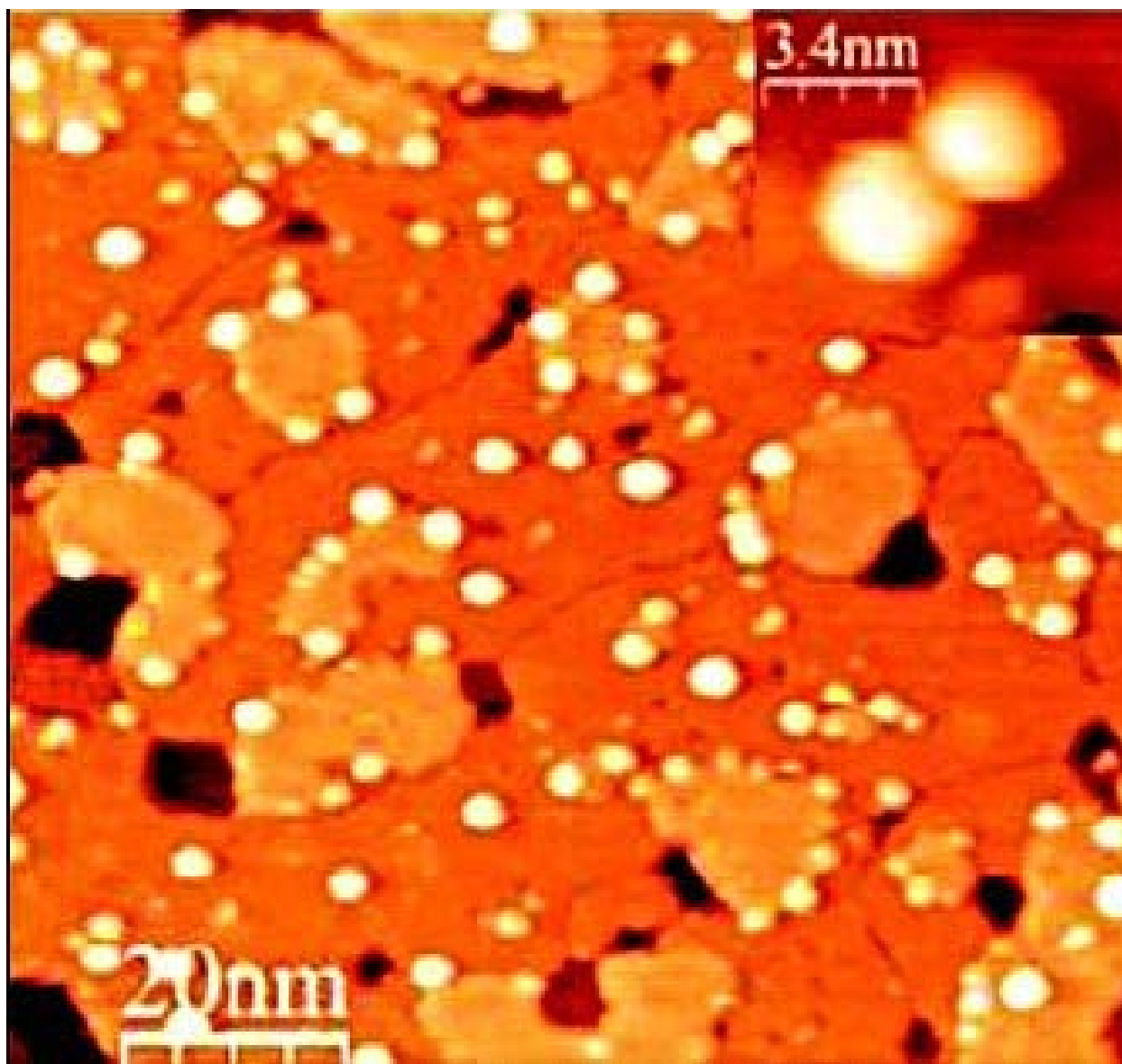


Figure 2.13. An STM image of Ag nanoparticles grown on the same type of $\text{CeO}_2(111)$ film on Pt(111) as in Fig. 2.12 (here only 2.6 nm thick). Reprinted with permission from Reference ¹⁸. Copyright 2012 American Chemical Society.

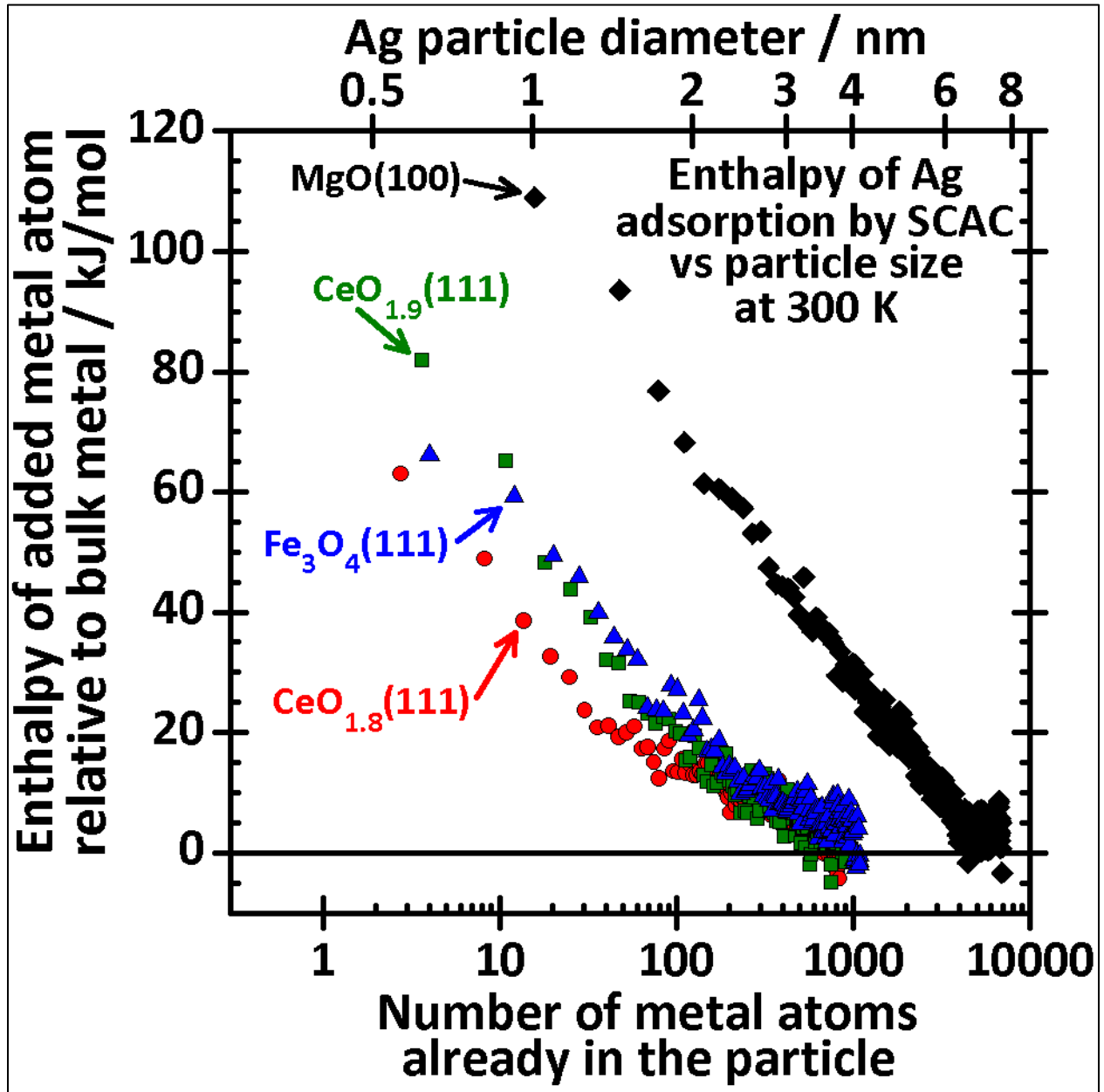


Figure 2.14. Partial molar enthalpy of Ag atoms in Ag nanoparticles (i.e., the enthalpy of the last Ag atom to be added to the particle (relative to bulk solid Ag) versus the average Ag particle size for Ag adsorption on different oxide surfaces. These enthalpies were taken from the data in Fig. 2.12. Copyright 2013 American Chemical Society.

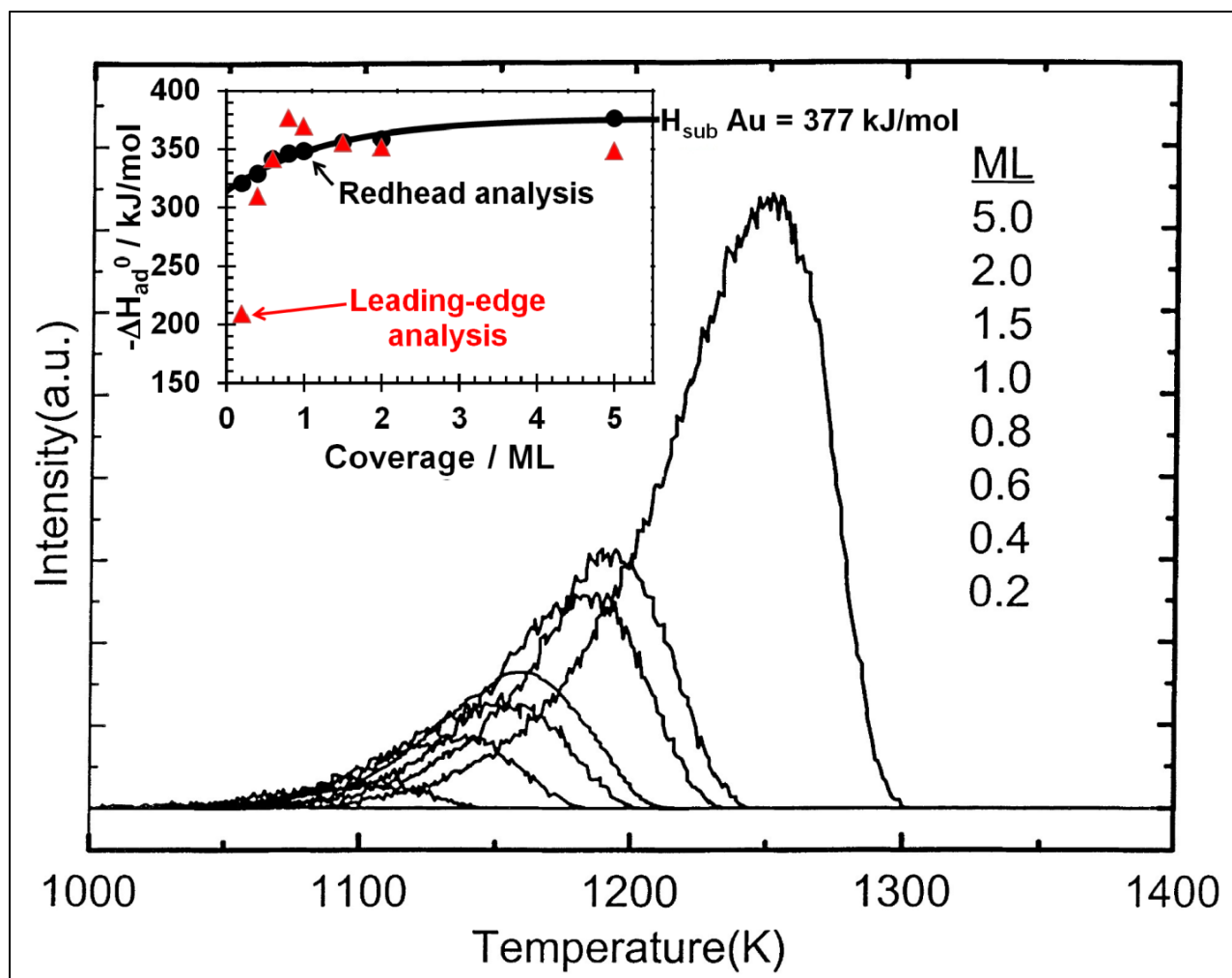


Figure 2.15. TPD spectra from different Au coverages adsorbed on a 2.5 nm thick SiO₂ film on Mo(110). Reprinted with permission from Reference ¹⁹. Copyright 2001 Elsevier. The insert shows the heat of adsorption as a function of initial Au coverage determined from the peak temperatures as described in the text, and, for comparison, as determined by the original authors by fitting the leading edge of each TPD spectrum to the Arrhenius law. We present several reasons in the text why such an analysis leads to very large errors at low coverage. Reprinted with permission from Reference ³. Copyright 2013 American Chemical Society.

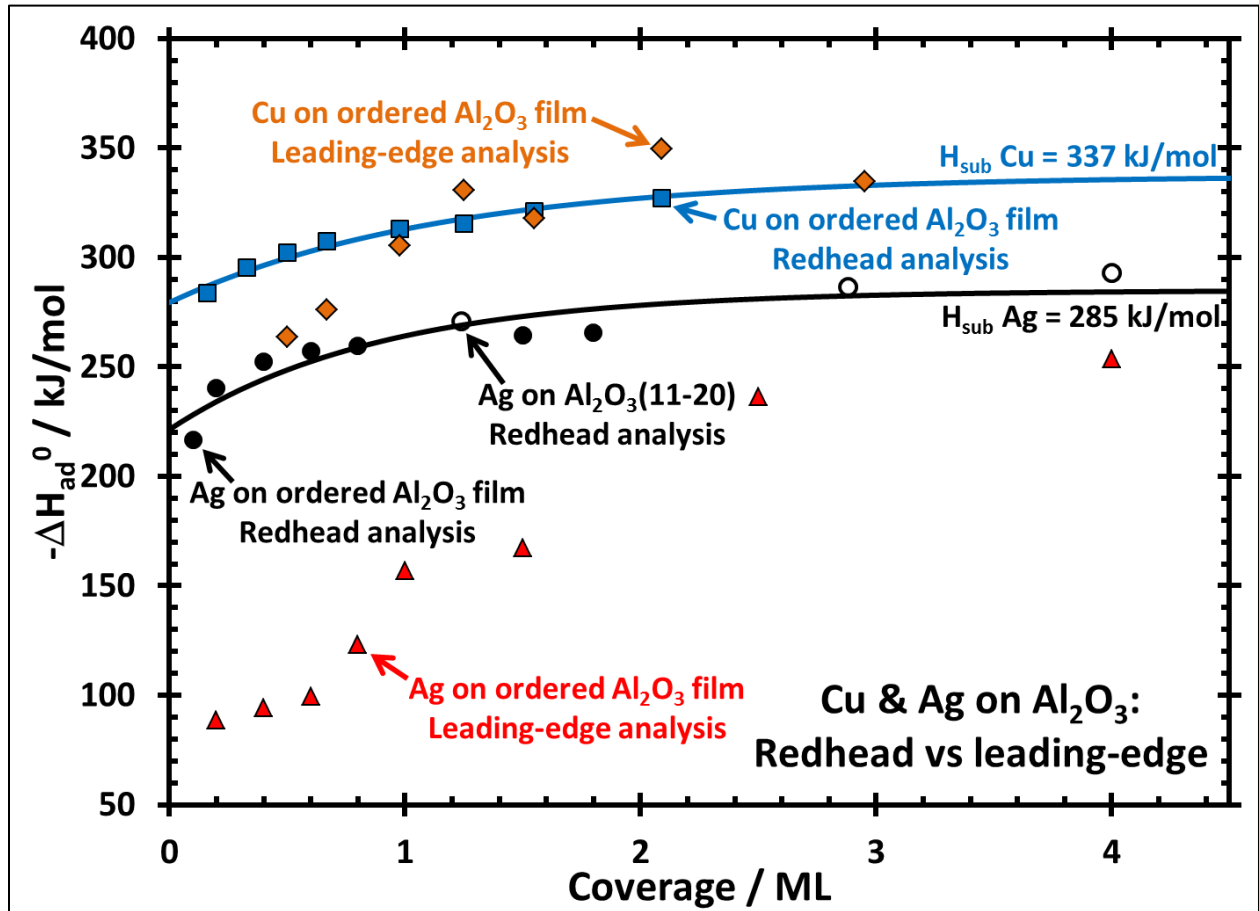


Figure 2.16. Comparison of heats of adsorption for Cu (upper curves) and Ag (lower curves) on alumina determined from TPD data by simple first-order Redhead analysis assuming a prefactor for desorption based on Eq. (2.16) using the entropy correlation of Eq. (13), which gives a prefactor of $\sim 10^{15} \text{ s}^{-1}$. Also shown for comparison are the results by leading-edge analysis as reported by the original authors. The Cu data are for an ordered Al_2O_3 film grown on Mo(110) whose hexagonal LEED pattern was attributed to either $\alpha\text{-Al}_2\text{O}_3(0001)$ or $\gamma\text{-Al}_2\text{O}_3(111)$ ²⁰. The Ag data are from a bulk sapphire $\alpha\text{-Al}_2\text{O}_3(11\text{-}20)$ surface and a thin Al_2O_3 film grown on Re(0001) (also to either $\alpha\text{-Al}_2\text{O}_3(0001)$ or $\gamma\text{-Al}_2\text{O}_3(111)$), from References²¹ and ²², respectively. The lowest-coverage heat of adsorption for Ag by the leading-edge analysis gave a prefactor of only $\sim 10^5 \text{ s}^{-1}$, which is clearly many orders of magnitude too low. The text argues that the results from our Redhead analysis are much more accurate. Also shown are best fits of Eq. (28) to these data analyzed by this preferred method. Reprinted with permission from Reference³. Copyright 2013 American Chemical Society.

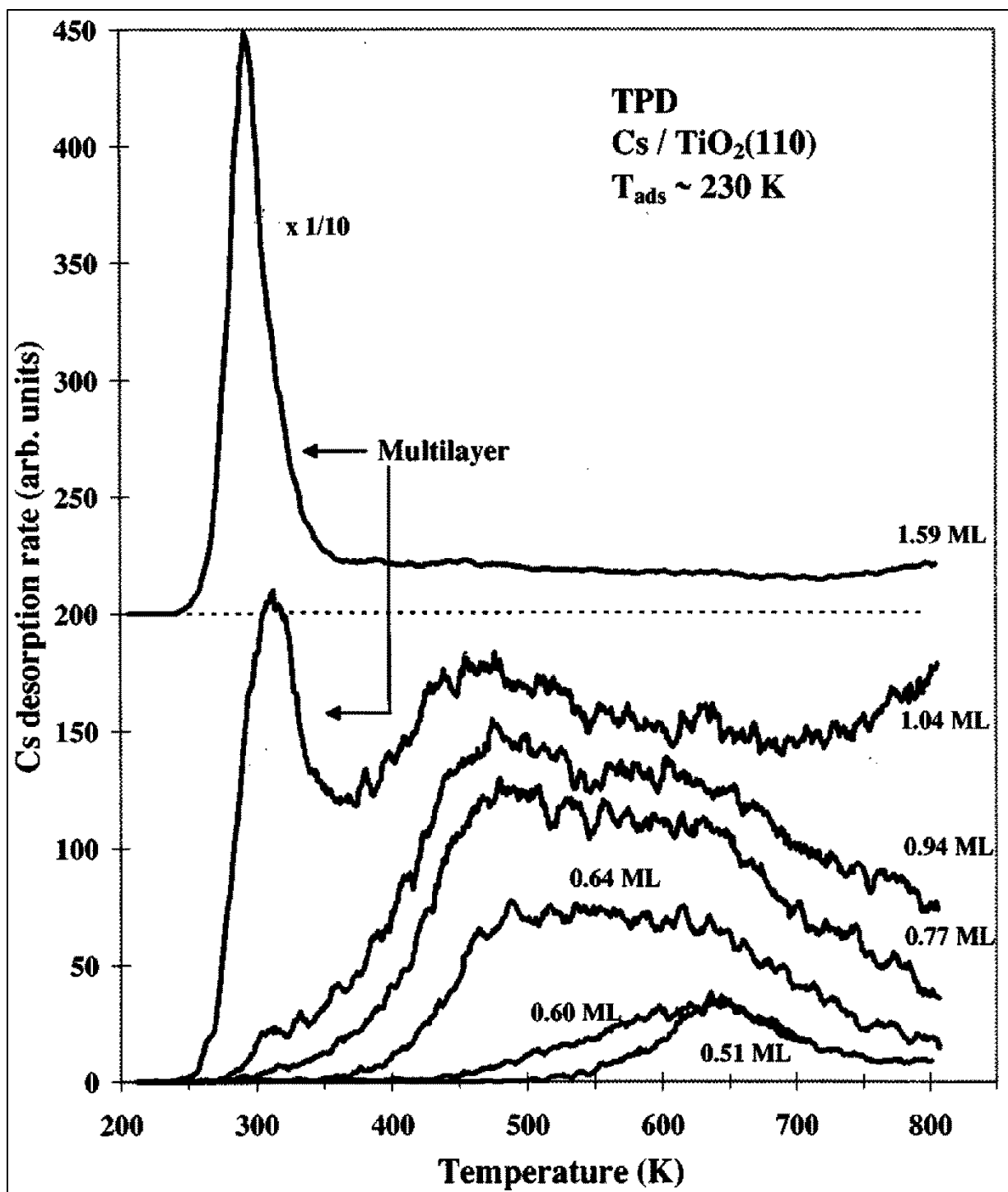


Figure 2.17. TPD curves for Cs desorption from TiO₂(110) after adsorption at ~230 K to increasing initial coverages of Cs. The completion of a monolayer is easily identified by the appearance of the sharp multilayer peak at ~300 K. Coverages below 0.4 ML are so strongly bound that they do not desorb by the highest TPD temperature. The heating rate was ~5 K/s. Reprinted with permission from Reference ²³. Copyright 1997 American Physical Society.

Chapter 3

The Entropies of Adsorbed Molecules

Adsorbed molecules are involved in many reactions on solid surface that are of great technological importance. As such, there has been tremendous effort worldwide to learn how to predict reaction rates and equilibrium constants for reactions involving adsorbed molecules. Theoretical calculation of both the rate constant and equilibrium constant for such reactions require knowing the entropy and enthalpy of the adsorbed molecule. While much effort has been devoted to measuring and calculating the enthalpies of well-defined adsorbates, few measurements of the entropies of adsorbates have been reported. We present here a new way to determine the standard entropies of adsorbed molecules (S_{ad}^0) on single crystal surfaces from temperature programmed desorption data, prove its accuracy by comparison to entropies measured by equilibrium methods, and apply it to published data to extract new entropies. Most importantly, when combined with reported entropies, we find that at high coverage they linearly track the entropy of the gas-phase molecule at the same temperature (T), such that $S_{\text{ad}}^0(T) = 0.70 S_{\text{gas}}^0(T) - 3.3R$ (R = the gas constant), with a standard deviation of only $2R$ over a range of $50R$. These entropies, which are $\sim 2/3$ of the gas, are huge compared to most theoretical predictions. This result can be extended to reliably predict prefactors in the Arrhenius rate constant for surface reactions involving such species, as proven here for desorption.

3.1: Introduction

Surface chemical reactions play a central role in many technologies that will be crucial for our energy and environmental future, including solar cells, microelectronics, computer chips, chemical and biochemical sensors, prosthetic medical devices, reflective and protective coatings,

optical, electro-optic and opto-electric devices, adhesives, sorbents, solid reactants, catalysts for clean fuels and chemicals production and pollution cleanup, photocatalysts, fuel cells and batteries. It is well established that one must know the enthalpies and entropies of the reactants if one is to develop systematic theories that can predict equilibrium constants and rate constants for chemical reactions of any type. While the enthalpies of adsorbates involved in surface reactions are starting to be understood, our knowledge of the entropies of adsorbates is very poor. Indeed, we know of no previous systematic studies of how the entropies of adsorbed species depend on their physical properties.

Surface chemists usually think about adsorbate entropies in terms of the two limiting cases that have been discussed in statistical thermodynamics texts: the 2D lattice gas model and the 2D ideal gas model⁶⁶. In calculating rate constants for surface reactions based on quantum mechanical calculations (mainly density functional theory, DFT) of reactant and transition state energies, surface chemists almost exclusively rely on harmonic transition state theory approaches, which assume that each adsorbate is a localized oscillator with only vibrational modes. Vibrations generally have very low entropy compared to translations and rotations of their gas-phase analogues. We show here that these common approximations greatly underestimate the entropies of adsorbed molecules even when they are held together in islands by attractive interactions. Instead, their entropies are almost 2/3 of the entropy of their gas-phase analogue (at temperatures high enough to measure desorption rates or adsorption \rightleftharpoons desorption equilibria), suggesting that all components of motions in two out of the three dimensions are nearly as labile as in the gas phase. We further show that the correlation we have discovered here between the entropies of adsorbed and gas-phase molecules can be quite useful in predicting rate constants for adsorbed molecules.

3.2: Experimental and Theoretical Methods

While writing a review of the energetics of adsorption on single crystalline oxide surfaces recently, we also collected data for the standard entropies of adsorption (ΔS_{ad}^0 where the superscript 0 refers to the standard pressure of 1 bar) that had been experimentally measured³, which were rather few. All of these had been measured at high coverages by the volumetric equilibrium adsorption isotherm (EAI) method on MgO(100) smoke (a powder consisting of tiny cubes terminated in (100) faces). We calculated the standard entropies of these adsorbates at the measurement temperature, T , by simply adding the entropy of the gas at T : $S_{\text{ad}}^0 = S_{\text{gas}}^0 + \Delta S_{\text{ad}}^0$. The values of S_{gas}^0 for these molecules were found in standard thermodynamic tables and, when necessary, extrapolated to different temperatures using tabulated heat capacities. These values of ΔS_{ad}^0 , S_{gas}^0 , S_{ad}^0 and T are tabulated in³, and reproduced in Table 3.1. Figure 2.4 presented in the previous chapter is a plot of S_{ad}^0 versus S_{gas}^0 for those data.

Table 3.1. Adsorbate and gas-phase entropies determined by EAI and by using the prefactors determined from TPD data analysis as described in the text, taken from Reference³.

adsorbate	surface	T / K	β /(K/s)	$\log(\nu/\text{s}^{-1})$	$-\Delta S_{\text{ad}}^0$ / R	$S_{\text{gas}}^0(T)$ / R	$S_{\text{ad}}^0(T)$ / R	citation
equilibrium adsorption isotherms								
methane	MgO(100)	77			11.0	16.9	5.95	96
ethane		120			12.0	23.3	11.3	
propane		140			11.6	28.1	16.5	
n-butane		163			12.1	32.4	20.3	
n-pentane		185			16.8	36.2	19.4	
neopentane		200			17.1	40.9	23.8	97
n-hexane		207			17.6	31.1	13.5	96
CH ₃ OH		264			15.0	28.3	13.3	98

Table 3.1 (Continued)

adsorbate	surface	T / K	β /(K/s)	$\log(\nu/s^{-1})$	$-\Delta S_{ad}^0$ / R	$S_{gas}^0(T)$ / R	$S_{ad}^0(T)$ / R	citation
temperature programmed desorption								
CO	TiO ₂ (110)	170	0.5	14	8.81	21.8	13.0	126
NO	TiO ₂ (110)	128.5	0.5	13.5	7.77	21.0	13.2	130
CO ₂	TiO ₂ (110)	177	2	13.6	8.16	23.3	15.2	147
methane	MgO(100)	47	0.6	13.1	6.77	15.0	8.20	24
	PdO(101)	143	1	14.7	10.2	19.3	9.06	150
	Pt(111)	63	0.6	12.1	4.41	16.1	11.7	10
methane	C(0001)	55	0.6	13.0	6.51	15.6	9.09	10
ethane	MgO(100)	75		14.9	11.1	20.9	9.76	24
	Pt(111)	106		13.6	8.10	22.3	14.2	10
	C(0001)	87		14.3	9.74	21.5	11.8	
propane	MgO(100)	93		15.6	12.9	24.9	11.9	24
	Pt(111)	139		14.8	11.0	26.5	15.5	10
	C(0001)	110		14.6	10.6	25.5	14.9	
n-butane	MgO(100)	111		15.7	13.3	27.8	14.5	8, 24
	Pt(111)	171		14.7	10.9	31.9	21.0	10
	C(0001)	135		15.2	12.1	30.2	18.1	
isobutane	ZnO(0001)	130	1.6	13.4	7.96	28.2	20.3	153
n-hexane	MgO(100)	144	0.6	16.0	14.1	36.4	22.3	24
	Pt(111)	229		17.2	16.8	42.8	26.0	10
	C(0001)	179		17.7	18.0	39.4	21.4	
n-octane	MgO(100)	175		17.9	18.6	46.0	27.4	24
	C(0001)	218		16.5	15.3	50.0	34.6	10
n-decane	MgO(100)	204		19.1	21.4	56.3	34.9	24
	C(0001)	254		17.8	18.4	61.7	43.3	10

Inverse gas chromatography has also been used to determine adsorbate entropies on high-area powders, but to our knowledge it has not been applied to single crystalline surfaces (e.g., MgO(100) smoke) where the adsorbates are more well defined, which is the focus here.

Temperature programmed desorption (TPD) has been widely used to measure activation energies for desorption (E_d) on single crystals. To extract E_d from TPD data, the surface species are always assumed to be in equilibrium, in which case the measured desorption rate is a single-valued function of coverage (θ) and temperature: $r(\theta, T)$. For the case of importance here, molecular adsorption / desorption, it is generally assumed that desorption is a first-order process, in which case the Polanyi-Wigner equation gives: $r(\theta, T) = -d\theta/dt = \nu \exp(-E_d(\theta)/RT) \theta$, where ν is the pre-exponential factor and R is the gas constant. One typically assumes that ν does not vary with coverage or temperature but that E_d does (as $E_d(\theta)$). One then finds the prefactor and $E_d(\theta)$ that best match the measured rates over a large range of coverages and temperatures. This method has been widely used. We next show how the prefactor found in this way can be used to get the adsorbate entropy, S_{ad}^0 , at the desorption peak temperature, T_p .

When the adsorption \rightleftharpoons desorption process is reversible and the activation energy for adsorption is negligible, as it is for many cases of molecular adsorption of interest here, the transition state (TS) for desorption is the molecule with its center of mass constricted to lie on a plane parallel to the surface at some distance far enough away from the surface that its interaction with the surface is negligible for any angle of rotation^{24, 293}. In this case, the transition state is very well defined. Its entropy ($S_{TS, des}^0$) is identical to that for the gas (S_{gas}^0) at the same temperature, except that it is missing one translational degree of freedom (the one perpendicular to the surface):

$$S_{TS, des}^0 = S_{gas}^0 - S_{gas, 1D-trans}^0. \quad (3.1)$$

The value of $S_{\text{gas,1D-trans}}^0$ for any gas can easily be calculated using statistical mechanics (the Sackur-Tetrode equation)²⁶, assuming that each translational degree of freedom contributes 1/3 of the total 3D translational entropy. A useful formula for doing this is:

$$S_{\text{gas,1D-trans}}^0 = (1/3)\{S_{\text{Ar,298K}}^0 + R \ln[(m/m_{\text{Ar}})^{3/2}(T/298\text{K})^{5/2}]\}, \quad (3.2)$$

where m is the molar mass of the gas, m_{Ar} is that for argon, and $S_{\text{Ar,298K}}^0$ is the entropy of Ar gas at 1 bar and 298 K (= 18.6R). Within transition state theory¹⁰⁷, the desorption prefactor is given by:

$$\nu = k_{\text{B}}T/h \exp(\Delta S_{\text{TS, des}}^0/R) = k_{\text{B}}T/h \exp[(S_{\text{TS, des}}^0 - S_{\text{ad}}^0)/R], \quad (3.3)$$

where k_{B} is Boltzmann's constant. Substitution using Eq. (3.1) gives:

$$\nu = k_{\text{B}}T/h \exp[(S_{\text{gas}}^0 - S_{\text{gas,1D-trans}}^0 - S_{\text{ad}}^0)/R]. \quad (3.4)$$

This can be rearranged to give an expression for calculating S_{ad}^0 from a measured value of ν :

$$S_{\text{ad}}^0 = (S_{\text{gas}}^0 - S_{\text{gas,1D-trans}}^0) - R \ln(\nu h/(k_{\text{B}}T)), \quad (3.5)$$

where all entropies are for the same average temperature as the measurement of ν (or $\sim T_{\text{p}}$).

We also applied Eq. (3.5) to get the entropies of a variety of reversibly adsorbed molecules on MgO(100) from their measured desorption prefactors as reported in the literature. The values are also found along with ν , T_{p} and $S_{\text{gas}}^0(T_{\text{p}})$ in Table 2.3, and reproduced here in Table 3.1.

3.3: Results

In Fig. 2.4, the standard adsorbate entropy, S_{ad}^0 , for molecularly adsorbed species on the MgO(100) surface, as measured by the equilibrium adsorption isotherm (EAI) method on MgO(100) smoke (from Table 3.1), is plotted versus the gas-phase entropy at the same temperature, S_{gas}^0 . There is a strong, linear correlation between S_{ad}^0 and S_{gas}^0 .

The entropies of a variety of reversibly adsorbed molecules on MgO(100), determined from their reported, experimentally-measured desorption prefactors by using Eq. (3.5) (and tabulated in ³), were also added to Fig. 2.4. The excellent agreement between the adsorbate entropies on MgO(100) obtained in this way and those directly measured by EAI verifies the accuracy of Eq. (3.5). To our knowledge, this is the first experimental verification that one can indirectly measure adsorbate entropies from TPD data for such systems. Below are its first applications, which prove quite powerful.

By combining the adsorbate entropies on MgO(100) measured by both methods in Fig. 2.4, one can see that there is a nearly perfect linear correlation between $S_{\text{ad}}^0(T)$ and $S_{\text{gas}}^0(T)$:

$$S_{\text{ad}}^0(T) = 0.70 S_{\text{gas}}^0(T) - 4.7R, \quad (3.6)$$

with a correlation coefficient (R^2) of 0.96 (standard deviation = $1.6R$). Note that each point here is for a different molecule (or method) at a temperature where its desorption was fast enough to perform the EAI and TPD measurements ($\sim 10^{-3}$ to 100 monolayers/s), which is the most relevant temperature for applications.

As shown in Fig. 3.1, this linear correlation becomes a direct proportionality if we first subtract from S_{gas}^0 the entropy associated with one degree of translational freedom, $S_{\text{gas,1D-trans}}^0$. This plot is for the data on MgO(100) only, obtained by both EAI and TPD. That this plot now goes through (0,0) shows that the x -intercept in Fig. 2.4 was approximately $S_{\text{gas,1D-trans}}^0$. This much of the gas phase entropy is totally lost in the adsorbates due to the fact that they generally sit in a potential energy well that is very steep in the direction perpendicular to the surface (the z direction). Thus they have very restricted center-of-mass motion in z , appearing now only as a nearly negligible vibrational entropy. The proportionality constant between S_{ad}^0 and $S_{\text{gas}}^0 - S_{\text{gas,1D-trans}}^0$ is 0.68 in Fig. 3.1, so that:

$$S_{\text{ad}}^0 = 0.68 (S_{\text{gas}}^0 - S_{\text{gas,1D-trans}}^0). \quad (3.7)$$

This proportionality, which has $R^2 = 0.96$ and a standard deviation of $1.7R$ over a range of $40R$, shows that the adsorbate maintains $\sim 2/3$ of the entropy of the gas-phase species (after subtracting the entropy of its z translation motion).

Encouraged by the excellent agreement between the entropies extracted from TPD prefactors using Eq. (3.5) and those directly measured by EAI in Figs. 2.4 and 3.1, we calculated the entropies of a variety of other adsorbed molecules on single crystal from their experimentally determined desorption prefactors. This includes all the prefactors we could find for adsorbates on other oxide single crystal surfaces³, for linear alkanes on Pt(111)¹⁰ and graphite(0001)^{10, 25, 108}. As shown in Fig. 3.2, a very similar linear relationship between S_{ad}^0 and S_{gas}^0 as found in Fig. 2.4 for MgO(100) alone was found to hold when we include also the entropies for all these other molecularly adsorbed species and other types of surfaces. For the same range of data as in Fig. 2.4 (i.e., up to $S_{\text{gas}}^0 = \sim 60R$), these measured entropies were very well fitted by the line:

$$S_{\text{ad}}^0(T) = 0.70 S_{\text{gas}}^0(T) - 3.3R, \quad (3.8)$$

with a standard deviation of only $2.2R$ over a range of $\sim 50R$. Including this much larger data set shifted the y -intercept only very slightly (up by $1.4R$) from the line for MgO(100) alone, and the slope stayed the same. This indicates that this linear relationship is nearly independent of the molecule and the solid material. Thus, Eq. (3.8) provides a very useful and simple method for estimating adsorption entropies for molecularly adsorbed gases on oxide surfaces when S_{gas}^0 is below $\sim 60R$. We also show below that this can be applied to estimate pre-exponential factors in rate constants for reaction involving adsorbates, like desorption.

Table 3.2 shows that Eq. (3.8) is independent of the material. Here we list the slope and y -intercept values of the best-fit straight lines (below $S_{\text{gas}}^0 = \sim 60R$) to subsets of the data in

Fig. 3.2 corresponding to the different surfaces. As seen, the slope varies from 0.56 to 0.76 between the different surfaces, but these slopes are all within two standard deviations of each other. More importantly, the standard deviation of the data for each subset about the line given by Eq. (3.8) is always less than $2.8R$, versus $2.18R$ for the full data set in Fig. 3.2. We also show here the best-fit parameters to the EAI data alone for MgO(100).

In Figs. 2.4 and 3.1, we have labeled the identities of the molecules. While most of the points are for linear alkanes, the plot includes neopentane (which is nearly spherical) and methanol (which binds specifically through its O atom to Mg sites). Figure 3.2 includes all these type molecules and also points for CO, NO, CO₂ and isobutane. There are no points for large molecules on corrugated surfaces, so it is not clear if this can be generalized to highly corrugated surfaces.

The behavior is somewhat different for molecules with gas entropies above $\sim 60R$, as seen in Fig. 3.2, where the slope increased to 1.0 at high entropy (i.e., for molecules with >35 atoms). We will discuss these separately below.

Table 3.2. Parameters for best linear fits to subsets of the data in Fig. 3.2 corresponding to different materials' surfaces.

data set	slope	std. dev. of slope	y-intercept / R	std. dev. in $S_{ad}^0(T) / R$	std. dev. in $S_{ad}^0(T) / R$ from Eq. (3.8)
all points in Fig. 3.2	0.70	0.03	-3.25	2.18	2.18
MgO(100) data only	0.70	0.04	-4.69	1.60	2.18
Pt(111) data only	0.56	0.05	-2.00	3.61	2.36
C(0001) data only	0.76	0.05	-4.42	5.01	2.34
MgO(100) EAI data only	0.72	0.10	-5.92	4.96	2.75

3.4: Discussion

One possible explanation for the slope of $\sim 2/3$ in Figs. 2.4, 3.1 and 3.2 is to remember that the motions of the gas molecule which give rise to most of its entropy are its translations and rotations, and these can be decomposed into their x , y and z components. If we assume their associated entropy is equally divided between x , y and z components, with all components of motion in the x and y directions (e.g., x and y translation and helicopter rotations) not changed from the gas, but with all components of motion in the z direction (e.g., z translation and cartwheel rotations) frozen out by the steep interaction potential well in the z direction, we arrive at a proportional relationship with slope $2/3$ in Figs. 2.4 and 3.2. This is certainly too simplified, but captures the dominant physical effect at play here. It is consistent with a very weak corrugation of the molecule – surface interaction potential for translational and rotational motions parallel to the surface, with saddle points that are lower than RT at temperatures where desorption is fast enough to perform EAI and TPD, but a steep well for any type of molecular motion perpendicular to the surface. This is similar to the model offered to explain trends in prefactors for alkane desorption^{10, 24}.

The weak corrugation parallel to the surface for polyatomic molecules is probably due to “lattice mismatch” between the surface’s lattice constant and the bond lengths within the adsorbate: The farther the molecule extends along the surface, the bigger the fraction of its atoms not fitting in their most stable binding sites¹⁰⁹. This is the same reason that the activation barrier for diffusion of a small 2D metal islands decreases with island size when the lattice mismatch with the underlying substrate is large²⁹⁴. Furthermore, within a given class of adsorbates (like alkanes), the larger the adsorbate, the larger is its adsorption energy and the hotter is T_p , so that

the barrier to motions parallel to the surface could even increase in energy with size while remaining the same relative to RT_p (i.e., remain smaller than these barriers).

The entropy $S_{\text{gas}}^0 - S_{\text{gas,1D-trans}}^0$ plotted in Fig. 3.1 is approximately $R \ln q$, where q is the partition function corresponding roughly to the number of quantum states of the gas molecule that are thermally accessible in rotational, vibrational and 2D translational motion. The average value of $\sim 25R$ in Fig. 3.1 corresponds to $\sim 10^{11}$ accessible states. The slope of 2/3 here implies that the number of accessible states drops to $\sim (10^{11})^{2/3} = \sim 10^7$ after adsorption. That is a large number of states, but still down by a factor of $\sim 10^4$ from the gas phase.

The only case where ΔS_{ad}^0 was measured versus coverage by EAI is for NH_3 on $\text{MgO}(100)$ smoke, which shows a large decrease with coverage from -47 J/mol/K (after defects are populated) to -172 J/mol/K⁹⁵. A large decrease in ΔS_{ad}^0 is predicted for an ideal 2D lattice gas model where adsorbate-adsorbate interactions are negligible, due to the large decrease in configurational entropy of the adsorbate as the fractional occupation of sites (θ) increases⁶⁶:

$$S_{\text{config}} = R \ln [(1-\theta)/\theta]. \quad (3.9)$$

The accompanying decrease in the heat of adsorption with coverage, from 71 to 25 kJ/mol⁹⁵, indicates that there are repulsive lateral interactions between adsorbed ammonia molecules. However, at low coverage where the average adsorbate – adsorbate separation is large, these can be neglected and the adlayer still should have very large configurational entropy, as observed. We have left the point for NH_3 off of Fig. 2.4 since it drops from $5R$ above the line to $10R$ below the line (i.e., \sim zero) with increasing coverage. No variation with coverage was reported for the other adsorbates studied by EAI. That is, the shapes of their EAI curves were well fit by assuming that the entropy does not vary with coverage. We think this lack of coverage variation is due to the fact that they had attractive interactions and thus condensed into islands. Attractive

adsorbate-adsorbate interactions are expected for these alkanes and alcohol, due to van der Waals attractions and hydrogen bonding, respectively. Since ammonia has a large dipole moment oriented perpendicular to the surface, it instead is expected to have repulsive adsorbate-adsorbate interactions, as observed. Thus, Fig. 2.4 and Eq. (3.6) are only valid for cases with attractive interactions. A huge decrease in S_{ad} with coverage is probably characteristic of adsorbates with strong repulsive interactions.

Equation (3.9) brings up the question: What is the configurational entropy for those other systems that gave rise to the linear relationships of Fig. 2.4 and 3.1 and Eqs. (3.6) and (3.7)? Those were generally for cases where it appears that there are attractive adsorbate – adsorbate interactions at coverages of $\frac{1}{2}$ ML and above, so they are clustered into 2D islands. The most common statistical mechanics model for that case is the 2D *crystal lattice* model, and *not* the 2D *ideal lattice gas* model, which is only appropriate when there are negligible or weakly repulsive adsorbate – adsorbate interactions. There is no configurational entropy in a 2D *crystal lattice*, only vibrational entropy (including frustrated rotational and translational entropy). Recognizing this, it was surprising to these authors that 2/3 of the entropy associated with rotational and 2D translational motion in the gas phase still remains after adsorption. It must be that rotations and translations parallel to the surface somehow remain unhindered in such adsorbate islands. Thus, it may be more appropriate to think of these adsorbate islands at these temperatures as 2D liquids rather than as 2D crystals.

Indeed, Eq. (3.8) is similar to Trouton's Rule, which says that the standard entropy of the liquid at the normal boiling point varies approximately linearly with S_{gas}^0 with a slope of unity and a y-intercept of $-10.3R$ ¹⁰⁷. For comparison, we show liquid entropies at the normal boiling point (as estimated by Trouton's Rule) in Fig. 3.2. Adsorbate entropies drop below 3D liquid

entropies only when S_{gas}^0 exceeds $\sim 30R$, but then above $\sim 60R$, they start tracking the liquid entropies with the same slope (within 1%), but remaining lower by a constant amount of $10.4R$. Interestingly, this offset is almost exactly the same amount that liquid entropies fall below standard-state gas entropies according to Trouton's Rule ($10.3R$).

Although in some cases these adsorbate islands are probably in equilibrium with a low-density 2D gas phase adsorbed in the empty areas between islands (and on top of the islands), and desorption may be happening from these low-density phases^{10, 111}, the standard entropies we report here are for adsorbates within the dense islands themselves, and not for any low-density phases that may be in equilibrium with them. This is because the measurements upon which these entropies are based tracked the dominant-species coverage in the islands and not the low density phase(s). Note too that in the derivation of transition state theory, one only assumes that equilibrium is established between the reactant and the transition state, and so it does not change when there are intermediate states between them.

The reason for the change in slope to 1.0 above $\sim 60R$ in Fig. 3.2 is the same reason that the prefactors for *n*-alkane desorption stop increasing with chain length above 10 carbons, which has been examined thoroughly^{25, 108} and beautifully reproduced in molecular dynamics simulations¹⁰⁹⁻¹¹¹. Below C_{10} , there is a large increase in gas-phase entropy with chain length mainly due to the increasing translational entropy with mass and then the increasing moment of inertia and thus rotational entropy of these rigid-rod like molecules as they get longer. Due to the increasing probability for bends as the chains grow longer than C_{10} , the rotational entropy stops increasing above C_{10} , and the increasing entropy with chain length is now mainly due to increases in vibrational entropy. These vibrations are not effected by adsorption, so the slope goes to unity. That is, this change in slope is associated with a change in the reason that gas-

phase entropies increase with molecular size: Below $\sim 60R$, the entropy increase is mainly due to increases in translational and rotational entropy (of which $\sim 1/3$ is lost upon adsorption), whereas above $\sim 60R$, the gas-phase entropy increases with molecular size mainly due to increasing vibrational entropy (which is nearly unchanged upon adsorption). Since all the points above $60R$ in Fig. 3.2 are for linear alkanes, it is not clear if this change in slope will be generally true. It may not appear for other classes of molecules that do not have this change from linear to non-linear structure at a size corresponding to $\sim 60R$.

The adsorbate entropies plotted here are huge compared to most prior models for adsorbates. In particular, the harmonic approximation, which is very widely applied to DFT calculations of adsorbate energies to estimate their rate constants, is only valid at low temperatures, but it dramatically underestimates their entropies at the temperatures of Figs. 2.4, 3.1, and 3.2, where desorption rates and equilibria are measured. This is not because the 2nd derivatives of energy versus distance at the energy minima are incorrect (as that would lead to much smaller errors), but instead due to the low energies of the next maxima in the potential energy surface (relative to RT). This is the same reason that the hindered rotation of one methyl group about the C–C axis in gas-phase ethane contributes only low vibrational entropy at low temperature but, when RT exceeds the barrier for that methyl rotation, that mode becomes a free rotor; and, when RT is only 15% of the barrier, there is already a very large increase in entropy²⁶. The large error of the harmonic approximation in estimating prefactors was recently pointed out for propane desorption from PdO(101)¹⁷⁰.

Note that the conclusion of Eq. (3.8), that the adsorbate entropy is a large fraction of the gas-phase entropy, is qualitatively consistent with the findings of Santiago et al.²⁹⁵. They approximated the entropy of an adsorbed species as a fraction F_{loc} of the gas-phase entropy

minus that for its three translational components, $S_{\text{ad}}^0 = F_{\text{loc}} (S_{\text{gas}}^0 - S_{\text{gas,3D-trans}}^0)$, where F_{loc} is the fraction of the non-translational entropy that is preserved upon adsorption. By fitting a microkinetic model to kinetic data for the selective reduction of acetic acid, methyl acetate, and ethyl acetate over silica-supported copper catalysts, they found F_{loc} to be very large, between 0.91 and 1.00. Three later studies also found large values near 0.95 for other adsorbates on metal catalysts using similar fitting methods, as reviewed by Goldsmith²⁹⁶. We next show that one can use the entropy correlation of Fig. 2.4 (Eq. (3.8)) to make reliable estimates of prefactors in rate constants for adsorbate reactions using transition state theory. We demonstrate this for the simplest case: desorption after non-activated molecular adsorption with attractive adsorbate – adsorbate interactions. Substituting Eq. (3.8) into Eq. (3.4) gives the prefactor:

$$\begin{aligned} \nu &= (k_{\text{B}}T/h) \exp[(0.30 S_{\text{gas}}^0 + 3.3R - S_{\text{gas,1D-trans}}^0)/R] \\ &= (k_{\text{B}}T/h) \exp\{0.30 S_{\text{gas}}^0/R + 3.3 - (1/3)\{18.6 + \ln[(m/m_{\text{Ar}})^{3/2}(T/298\text{K})^{5/2}]\}\}. \end{aligned} \quad (3.10)$$

where $S_{\text{gas,1D-trans}}^0$ can be calculated from Eq. (3.2). A plot of the predictions of Eq. (3.10) plotted versus experimentally measured desorption prefactors for all the molecules on single crystals surfaces in Fig. 3.2 except alkanes longer than C_{10} was shown previously in Fig. 2.6. The predictions agree very well with these experimental prefactors with a standard deviation in $\log(\nu/\text{s}^{-1})$ of only 0.86, confirming the validity of Eq. (3.10) for estimating prefactors. For alkanes longer than C_{10} , the prefactor stays constant at $\sim 10^{19} \text{ s}^{-1}$ ^{25, 108}. Several discussions of the values for desorption prefactors have been published, but none of these have presented any relationships with prediction integrity anywhere near as good as Eq. (3.10)^{10, 24, 25, 108-118, 297}. Using twice the standard deviation on $\log(\nu/\text{s}^{-1})$ of 0.86 in Fig. 2.6 gives a factor of 50 maximum error in ν at the 95% confidence limits. This analysis corresponds to terrace sites. We are not confident in the accuracy of its application to defect sites, since we have shown

previously that metal adatoms have a desorption prefactor that is 10^5 -fold larger at step edges than at terrace sites on Mo(100), due to the loss of all translational motion except in the one direction along the step edge¹¹⁸.

While this potential error in rate constant seems terrible, it marks a huge improvement over the current state. There are two dominant applications of estimated prefactors. The most important is in using adsorbate and transition state energies calculated with DFT together with prefactors (estimated using the second derivative of energy with coordinates and the harmonic approximation) to estimate rates of elementary steps in catalysis, and from this to propagate rates from microkinetic models of catalytic reactions²⁹⁸⁻³⁰². As noted above, the harmonic approximation is much worse. The second use of prefactors is in extracting desorption energies from TPD data. Here, the maximum error in ν of 50 corresponding to a maximum error in the desorption energy of only $4.0RT_p$ (<10 kJ/mol when $T_p = 300$ K).

Note that Eq. (3.10) is based on Fig. 3.2's experimental correlation between adsorbate and gas-phase entropies (i.e., Eq. (3.8)). Since most of the entropies plotted in Fig. 3.w come from the same prefactors as plotted in Fig. 2.6, it is thus not surprising that Eq. (3.10) fits the prefactors in Fig. 2.6 rather well. However, many of the points in Fig. 3.2 are from entropies that were instead directly determined by EAI and not from prefactors. More importantly, Fig. 3.2 shows that EAI entropies (when plotted alone) are well fitted by Eq. (3.8), and Table 3.2 shows that a fit to the EAI data alone gives a very similar slope and y-intercept. Thus, a line with a very similar slope and y-intercept to Eq. (3.10) in Fig. 2.6 would also result if we had not used any of the entropies determined from prefactors to get Eqs. (3.8) and (3.10), and instead used only EAI entropies.

3.5: Figures

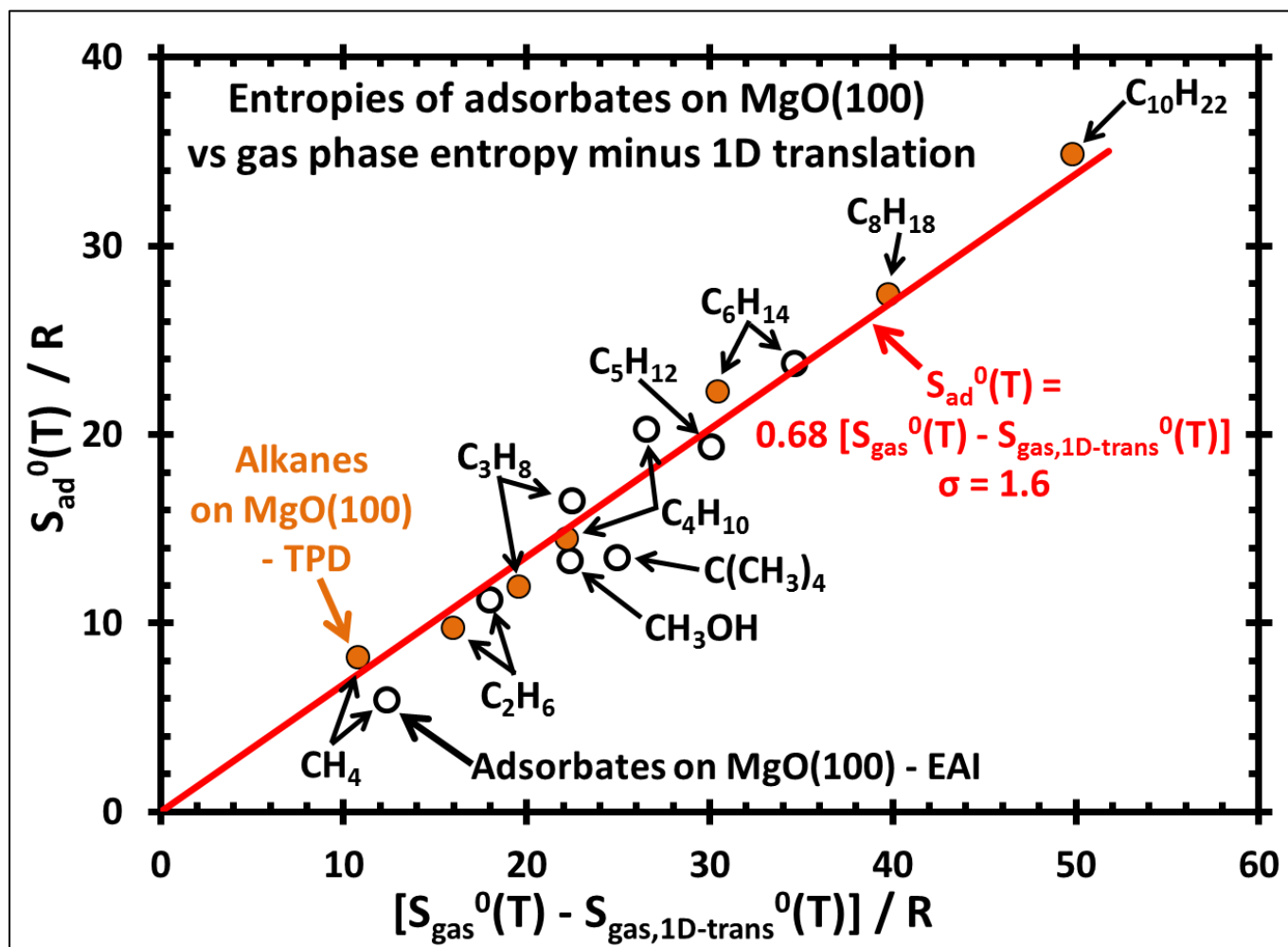


Figure 3.1. Plot of the standard entropies of molecular adsorbates ($S_{ad}^0 = S_{gas}^0 + \Delta S_{ad}^0$) on MgO(100) determined by EAI and TPD, from ³, plotted versus the standard entropy of the gas-phase molecule at the same temperature minus the entropy for one degree of translational freedom. Reprinted with permission from Reference ⁹. Copyright 2012 American Chemical Society.

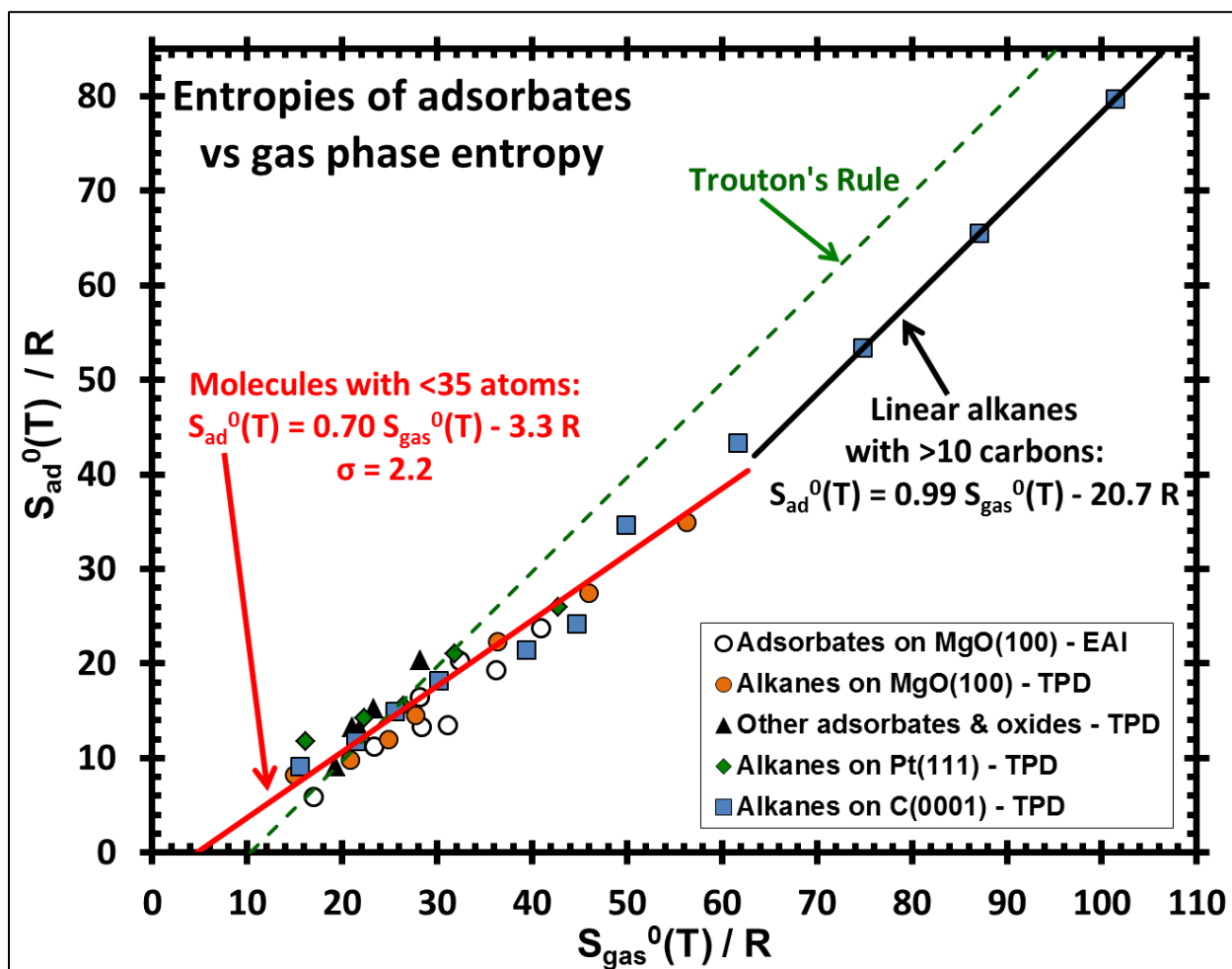


Figure 3.2. Plot of the standard entropies of molecular adsorbates (S_{ad}^0) on several surfaces plotted versus the standard entropy of the gas-phase molecule at the same temperature. Data for MgO(100) and other oxides are from ³. Entropies for linear alkanes on Pt(111) and graphite(0001) calculated using Eq. (3.5) with experimental prefactors reported in ^{10, 24, 25}. (Since the prefactor was shown to be constant between C₁₂ and C₂₄ ²⁵, we used the C₁₂ prefactor value for C₁₄ and C₁₆.) The best linear fits to the data for molecules smaller and larger than 35 atoms are also shown. For comparison, the standard entropies of bulk 3D liquids at the normal boiling point (as estimated by Trouton's Rule) are also shown. Reprinted with permission from Reference ⁹. Copyright 2012 American Chemical Society.

Chapter 4

Kinetic Prefactors of Reactions on Solid Surfaces

Adsorbed molecules are involved in many reactions on solid surface that are of great technological importance. As such, there has been tremendous effort worldwide to learn how to theoretically predict rates for reactions involving adsorbed molecules. Theoretical calculations of rate constants require knowing both their activation energy and prefactor. Recent advances in *ab initio* computational methods (e.g., density functional theory with periodic boundary conditions and van der Waals corrections) promise to soon provide activation energies for surface reactions with sufficient accuracy to have real predictive ability. However, to predict reaction rates, we also need accurate predictions of prefactors. We recently discovered that the standard entropies of adsorbed molecules (S_{ad}^0) linearly track the entropy of the gas-phase molecule at the same temperature (T), such that $S_{\text{ad}}^0(T) = 0.70 S_{\text{gas}}^0(T) - 3.3R$ (R = the gas constant), with a standard deviation of only $2R$ over a range of $50R$. This correlation, which applies only to conditions where their surface residence times are shorter than ~ 1000 s, provides a powerful new method for estimating the partition functions for adsorbates and the kinetic prefactors for their reactions. For desorption, we show that the prefactors obtained with DFT using transition state theory (TST) and the harmonic oscillator approximation to get the partition function predicts prefactors for desorption that are of order 10^3 times larger than experimental values while our approach gives much better estimates. We also explore the applications of this approach to estimate prefactors within TST for the main classes of adsorbate reactions: desorption, diffusion, dissociation and association, and discuss its limitations. We discuss general issues associated with applying TST to rate laws and multi-step mechanisms in surface

chemistry, and argue that rates of adsorbate reactions which are often taken to be proportional to coverage (θ), might better be taken as proportional to $\theta/(1 - \theta)$ (unless the adsorbate forms islands), to account for the configurational entropy or excluded volume effects on the adsorbate's chemical potential.

4.1: Introduction

Chemical reactions on solid surfaces play a central role in many technologies that will be crucial for our energy and environmental future, including the production and use of solar cells, catalysts for clean fuels and chemicals production and pollution cleanup, photocatalysts, fuel cells, batteries, sorbents and solid reactants. They are also critical to a number of other technologies including microelectronics, computer chips, chemical and biochemical sensors, prosthetic medical devices, reflective and protective coatings, optical, electro-optic and optoelectric devices and adhesives. Thus, there is great motivation to learn how to accurately predict rate constants for the elementary steps that occur in chemical reactions on solid surfaces. To this end, there have been decades of outstanding research from both experimental and theoretical perspectives to measure and calculate rate constants for elementary steps on solid surfaces. The calculations have been largely guided by various adaptations of transition state theory (TST) as introduced for simple gas reactions by Eyring and Polanyi³⁰³. By far the most common current approach for *ab initio* calculations of rate constants for surface reactions involves the use of Density Functional Theory (DFT) with periodic boundary conditions to calculate potential energy surfaces in the most important regions around the minima (reactants and products) and saddle points (transition states). These generally use efficient saddle-point-finding algorithms such as the Nudged Elastic Band (NEB³⁰⁴) and Dimer methods³⁰⁵ to locate the transition state.

The harmonic oscillator approximation is generally invoked around these minima and maxima to calculate the partition functions (q) of the adsorbed reactants and transition states (except for the transition state for desorption, which is more often a 2D gas) in calculating the rate constant. This is referred to as harmonic transition state theory (HTST) and assumes that all modes of any adsorbed reactant or transition state are vibrations³⁰⁶.

Our recent discovery of the very high entropies of adsorbed molecules at the temperatures where their desorption equilibria and rates are measured implies that the harmonic approximation grossly underestimates adsorbate partition functions at such temperatures⁹. Here, we explore the implications of this discovery with respect to predicting rate constants for surface reactions, and particularly their pre-exponential factors, ν , and suggest new approximations for estimating these prefactors which go beyond HTST. We discuss in detail when this new approach will be necessary. We expect that HTST remains valid at temperatures where all the reactants involved in the elementary step have rates of desorption below 10^{-3} monolayers/s, which includes a very wide range of important processes.

4.2: Entropies of Adsorbed Molecules

We recently presented the first extensive tabulation of the experimentally-measured entropies of adsorbed molecules on well-defined surfaces⁹. From this, we found that their standard entropies at the measurement temperature, $S_{\text{ad}}^0(T)$, linearly track the standard entropy of the gas-phase molecule at the same temperature, $S_{\text{gas}}^0(T)$, such that

$$S_{\text{ad}}^0(T) = 0.70 S_{\text{gas}}^0(T) - 3.3R, \quad (4.1)$$

where R is the ideal gas constant. As shown previously in Figs. 2.5 and 3.2, this correlation is essentially independent of the surface material, with a standard deviation of only $2R$ over a range

of $50R$. These entropies, which are $\sim 2/3$ of the gas, are huge compared to most theoretical predictions. Note that these entropies were measured at temperatures T such that desorption could be observed (i.e., at T such that the desorption rate was at least $\sim 10^{-3}$ monolayers (ML) per s), or more appropriately, where the surface residence time τ is less than ~ 1000 s.

4.3: Prefactors for Desorption

The total instantaneous desorption rate of an adsorbed molecule is typically assumed to be a single-valued function of its coverage (θ) and temperature (T), $r(\theta, T)$, given by:

$$r(\theta, T) = -d\theta/dt = k_{\text{des}} \theta = \nu_{\text{des}} \exp(-E_{\text{des}}(\theta)/RT) \theta, \quad (4.2)$$

where k_{des} is the first-order rate constant and ν_{des} is the pre-exponential factor, which is typically assumed not to vary with coverage or temperature, and $E_{\text{des}}(\theta)$ is the coverage-dependent desorption activation energy. This approximation will certainly fail in some cases since it neglects the excluded-volume of adsorbates, which is the first correction to a 2D ideal gas model for the adsorbate³⁰⁷, and since the first-order factor of θ at the end here should be replaced by $\theta/(1-\theta)$ in the ideal lattice gas approximation (see below), which is closely related to the excluded-volume effect. Much more sophisticated models have been put forth³⁰⁷⁻³⁰⁹.

When the activation energy for adsorption is negligible and the sticking probability is near unity, as is usually the case for molecular adsorption, the transition state for desorption is the molecule with its center of mass constricted to lie in a plane parallel to the surface at some distance far enough away from the surface that its interaction with the surface is negligible for any angle of rotation^{112, 310}. In this case, the transition state is very well defined. Its entropy ($S_{\text{TS,des}}^0$) is identical to that for the gas (S_{gas}^0) at the same temperature, except that it is missing one translational degree of freedom (the one perpendicular to the surface):

$$S_{\text{TS, des}}^0 = S_{\text{gas}}^0 - S_{\text{gas,1D-trans}}^0. \quad (4.3)$$

The value of $S_{\text{gas,1D-trans}}^0$ for any gas can easily be calculated using statistical mechanics (the Sackur-Tetrode equation)²⁶, assuming that each translational degree of freedom contributes 1/3 of the total 3D translational entropy. This gives:

$$S_{\text{gas,1D-trans}}^0 = (1/3)\{S_{\text{Ar,298K}}^0 + R \ln[(m/m_{\text{Ar}})^{3/2}(T/298\text{K})^{5/2}]\}, \quad (4.4)$$

where m is the molar mass of the gas, m_{Ar} is that for argon, and $S_{\text{Ar,298K}}^0$ is the entropy of Ar gas at 1 bar and 298 K (= 18.6R). The value of S_{gas}^0 can generally be found from standard thermodynamic tables, using the heat capacity to extrapolate to unlisted temperatures.

Within transition state theory, the rate constant for first-order desorption is given by^{112, 307, 310}:

$$k_{\text{des}} = (k_{\text{B}}T/h) (q_{\text{TS}}^0/q_{\text{i}}^0) \exp(-\Delta E_{\text{TS}}^0/k_{\text{B}}T), \quad (4.5)$$

where q_{TS}^0 is the partition function for the transition state (omitting motion in the coordinate perpendicular to the surface) and q_{i}^0 is the partition function for the adsorbate. The superscript "0" in both cases means that these are both evaluated about their zero-point energies (i.e., taking all energies relative to the ground state for that species), and ΔE_{TS}^0 is the difference between these two zero-point energies. The desorption prefactor (approximately equal to $(k_{\text{B}}T/h) (q_{\text{TS}}^0/q_{\text{i}}^0)$) is given by¹⁰⁷:

$$v_{\text{des}} = k_{\text{B}}T/h \exp(\Delta S_{\text{TS, des}}^0/R) = k_{\text{B}}T/h \exp[(S_{\text{TS, des}}^0 - S_{\text{ad}}^0)/R], \quad (4.6)$$

where k_{B} is Boltzmann's constant and h is Planck's constant, and E_{des} is the standard enthalpy of activation. (If one takes the strict definition of activation energy as $-R$ times the slope of $\ln(\text{rate constant})$ versus $1/T$, one gets that $E_{\text{des}} = -\Delta H_{\text{ad}}^0(T) - \frac{1}{2}RT$ ⁸⁷), where $\Delta H_{\text{ad}}^0(T)$ is the standard enthalpy of adsorption. One also gets an additional factor of \exp in the expression for

ν_{des} in Eq. (4.6), which arises from the contribution of $k_B T/h$ to this slope³¹¹, and which we neglect below.) Substitution using Eq. (4.3) gives:

$$\nu_{\text{des}} = k_B T/h \exp[(S_{\text{gas}}^0 - S_{\text{gas,1D-trans}}^0 - S_{\text{ad}}^0)/R], \quad (4.7)$$

where all entropies are for the same temperature T as the measurement of ν_{des} . We show below that if one uses the harmonic oscillator approximation to get S_{ad}^0 (i.e., HTST) for this equation, it results in prefactors that are many orders of magnitude too large. We further show that using the empirical correlation of Figs. 2.5 and 3.2 to get S_{ad}^0 gives much, much better results.

Equation (4.7) can be rearranged to give an expression for calculating S_{ad}^0 from an experimental value of ν_{des} :

$$S_{\text{ad}}^0 = (S_{\text{gas}}^0 - S_{\text{gas,1D-trans}}^0) - R \ln [\nu_{\text{des}} h / (k_B T)]. \quad (4.8)$$

We used this approach to obtain the entropies for many of the points in Figs. 2.5 and 3.2, but many also were obtained from more direct measurements using equilibrium adsorption isotherms. Note that if we included the neglected factor of \exp in Eq. (4.6) mentioned above, all these S_{ad}^0 values determined from TPD in Figs. 2.5 and 3.2 would increase by R , increasing the y -intercept in Eq. (4.1) for S_{ad}^0 from $-3.3R$ to $-2.5R$ with no change in slope. However, all of this difference (except $0.2R$) cancels when we then turn around and use these entropies to estimate prefactors using Eq. (4.6), which is our main focus below. Similarly, the y -intercept for the line in Fig. 3.2 for alkanes longer than C_{10} would increase from $-20.7R$ to $-19.7R$.

The entropy correlation of Figs. 2.5 and 3.2 (Eq. (4.1)) can be used to estimate S_{ad}^0 , and this allows for more reliable estimates of prefactors in rate constants for adsorbate reactions using transition state theory than HTST. We have already demonstrated this for the simplest case, desorption after non-activated molecular adsorption with attractive adsorbate – adsorbate interactions, as follows⁹. Substituting Eq. (4.1) for S_{ad}^0 into Eq. (4.7) gives the prefactor:

$$\begin{aligned} \nu &= (k_B T/h) \exp[(0.30 S_{\text{gas}}^0 + 3.3R - S_{\text{gas,1D-trans}}^0)/R] \\ &= (k_B T/h) \exp\{0.30 S_{\text{gas}}^0/R + 3.3 - (1/3)\{18.6 + \ln[(m/m_{\text{Ar}})^{3/2}(T/298\text{K})^{5/2}]\}\}. \end{aligned} \quad (4.9)$$

where $S_{\text{gas,1D-trans}}^0$ can be calculated from Eq. (4.4). In Fig. 2.6 a plot of the predictions of Eq. (4.9) plotted versus experimentally measured desorption prefactors for all the molecules on single crystals surfaces in Fig. 2.5 was shown. The predictions agree very well with these experimental prefactors with a standard deviation in $\log(\nu_{\text{des}}/\text{s}^{-1})$ of only 0.86, confirming the validity of Eq. (4.9) for estimating prefactors. For alkanes longer than C_{10} , the prefactor stays constant at $\sim 10^{19} \text{ s}^{-1}$ ^{25, 108}. Several discussions of the values for desorption prefactors have been published^{10, 24, 25, 108-118, 297}. This analysis corresponds to terrace sites. We showed previously that metal adatoms have a desorption prefactor that is 10^5 -fold larger at step edges than at terrace sites on $\text{Mo}(100)$, due to the loss of all translational motion except in the one direction along the step edge¹¹⁸.

There is a huge difference between the prefactor for desorption one gets using Eq. (4.1) to get S_{ad}^0 (which gives Eq. (4.9)) compared to that obtained using instead the harmonic oscillator approximation to get S_{ad}^0 (i.e., HTST), in both cases starting from Eq. (4.7). For example, consider the case of methanol on $\text{Pt}(111)$. We recently measured the prefactor for its desorption at 210 K to be $4 \times 10^{15 \pm 0.5} \text{ s}^{-1}$, with a heat of adsorption of $61.2 \pm 2.0 \text{ kJ/mol}$ ⁵³. Using Eq. (4.9) gives $\nu_{\text{des}} = 1.3 \times 10^{15} \text{ s}^{-1}$, which agrees within a factor of 3. In contrast, DFT calculations combined with HTST gives a value that is 1000-fold too large. We performed DFT calculations for methanol on $\text{Pt}(111)$ using VASP³¹²⁻³¹⁴ with the projector augmented wavefunction (PAW) method^{315, 316} together with the GGA-PBE and GGA-PW91³¹⁷⁻³¹⁹ functionals. The $\text{Pt}(111)$ surface consisted of 45 atoms (3×3 unit cell, five layers deep) with one methanol per unit cell. During optimization, the top two Pt layers were allowed to relax, and the

methanol was found to adsorb with the oxygen atom on the atop site and two carbonic hydrogens pointing towards the surface, in good agreement with earlier DFT results³²⁰. Then, the frequencies for all the normal vibrational modes of the methanol atoms were calculated for the adsorbed molecule, keeping all the Pt atoms frozen. The calculated frequencies of these vibrations are in excellent agreement with those same previously reported calculations³²⁰ which, however, did not report the six lowest-frequency modes that contribute essentially all of the entropy. In the harmonic approximation, our DFT frequencies give a vibrational partition function at 210 K (evaluated about its zero-point energy) of only $q_{\text{vib}}^0 = 65$ to 187, depending on the functional (PBE and PW91, respectively), and an entropy for the adsorbate at 210 K, $S_{\text{ad,HO}}^0$ (equal to the sum over all vibrational modes of $R\{(h\nu_{\text{vib}}/kT)/[\exp(h\nu_{\text{vib}}/k_B T) - 1] - \ln[1 - \exp(-h\nu_{\text{vib}}/k_B T)]\}$, where ν_{vib} is the frequency of that mode²⁶) of only 77 J/mol/K (for the PW91 functional, even less for PBE). Using Eq. (4.3) and (4.4) together with gas-phase entropies (obtained by extrapolating from tabulated values at the nearest temperature using tabulated heat capacities, from standard tables³²¹) gives an entropy for the transition state for its desorption ($S_{\text{TS,des}}^0$) of 177 J/mol/K. Using these two entropies in Eq. (4.6) gives $\nu_{\text{des}} = 7 \times 10^{17} \text{ s}^{-1}$ or more, which is larger than the experimental value by a factor of 200 or more. *This huge discrepancy arises because the entropy for the adsorbate estimated in this harmonic approximation is at least 53 J/mol/K lower than the value of 130 J/mol/K estimated using Fig. 2.5 and Eq. (4.1).* One gets even worse agreement if one estimates the entropy for the adsorbate in the harmonic approximation as $R \ln(q_{\text{vib}}^0)$, which is essentially what is done in HTST when the prefactor is estimated as $\nu_{\text{des}} = (k_B T/h)(q_{\text{TS}}/q_i^0)$. This gives an entropy of only 44 J/mol/K for the PW91 functional (even less for PBE) and a prefactor of $4 \times 10^{19} \text{ s}^{-1}$, 10^4 -fold larger than the experimental value (or $\sim 10^5$ larger for PBE).

4.4: Why Do Adsorbates Have Such Large Entropies?

Before we can extend the above approach for estimating prefactors to other classes of surface reactions besides desorption, and before we can even understand how generally valid Eq. (4.9) is for estimating ν_{des} , we must first examine the origin of the very high entropies of adsorbed molecules and the slope of $\sim 2/3$ seen in Figs. 2.5 and 3.2. Our qualitative explanation of this has been published⁹. Briefly, the motions of the gas molecule which give rise to most of its entropy are its translations and rotations, and these can be decomposed into their x , y , and z components. If we assume their entropy is equally divided between x , y , and z components, with all components of motion in the x and y directions (e.g., x and y translation and helicopter rotations) not changed from the gas, but with all components of motion in the z direction (e.g., z translation and cartwheel rotations) frozen out by the steep interaction potential well in the z direction, we arrive at a proportional relationship with slope $2/3$ in Figs. 2.5 and 3.2. It implies a very weak corrugation of the molecule / surface interaction potential for translational and rotational motions parallel to the surface, with saddle points that are lower than $k_{\text{B}}T$ at the measurement temperature, but a steep well for any type of molecular motion perpendicular to the surface. This same model was offered to explain trends in prefactors for alkane desorption^{10,24}.

The weak corrugation parallel to the surface for polyatomic molecules is probably due to “lattice mismatch” between the surface’s lattice constant and the bond lengths within the adsorbate: In Fig. 4.1(a), it can be seen that the farther a 2D island, or analogously a polyatomic molecule, extends along the surface, the bigger the fraction of its atoms not fitting in their most stable binding sites¹⁰⁹, thereby increasing the energy of the adsorbates. This is the same reason that the activation barrier for diffusion of small 2D metal islands decrease with island size when the lattice mismatch with the underlying substrate is large²⁹⁴. Notice that when the 11-atom

island in Fig. 4.1 is translated to move from a situation in which the central atom is in its (a) most favorable binding site to one in which it is at its (b) least favorable binding site the per atom diffusion barrier is reduced to only ~28% of the single atom diffusion barrier due to the 4% lattice mismatch. This diffusion barrier could decrease even more if such large adsorbates were to form islands.

Eq. (4.1) is similar to Trouton's Rule (the entropy of a liquid at the normal boiling point $= S_{\text{gas}}^0 - 10.3R$ ¹⁰⁷), also plotted in Fig. 3.2. As seen, adsorbate entropies are nearly as high as liquid entropies. *This is far above what would be expected based on the statistical thermodynamics models most widely applied to adsorbates, the lattice gas and 2D lattice crystal models, which only include vibrational entropy through the harmonic (or harmonic oscillator, HO) approximation. While this is clearly valid at very low temperatures, it dramatically underestimates their entropies at the temperatures of Figs. 2.5 and 3.2, where the surface residence time is less than 1000 s.* This is not mainly because the 2nd derivatives of energy versus distance at the energy minima are incorrect (as that would lead to much smaller errors), but instead due to the low energies of the next maxima in the potential energy surface (relative to $k_B T$). This is the same reason that the hindered rotation of one methyl group about the C–C axis in gas-phase ethane contributes only low vibrational entropy at low temperature but, when $k_B T$ exceeds the barrier for that methyl rotation, that mode becomes a free rotor; but even when $k_B T$ is only 15% of the barrier, there is already a very large increase in entropy ²⁶. The large error of the HO approximation in estimating prefactors was recently pointed out for propane desorption from PdO(101) ³²².

The most well studied example of a hindered rotor involves the rotation of one methyl group about the C–C axis in gas-phase ethane. Its potential energy (V) versus rotational angle

(ϕ), shown in Fig. 4.2, is a repeating cosine wave that has a maximum potential barrier of W repeating every 120° . For the generalized hindered rotor, the potential can be written:

$$V = (W/2)(1 - \cos n\phi), \quad (4.10)$$

where W is the height of the potential barrier and n is the number of equivalent minima in a full rotation (3 for Fig. 4.2). This potential gives a Schrödinger's equation for motion that has been solved numerically, with the eigenvalues tabulated; and these have been used to compute the partition function and entropy versus temperature^{26, 323}. Note that this potential looks like a HO near the energy minima and consequently has energy levels similar to those of a HO, with separations approximately given by $\varepsilon = (nh/2\pi)(W/2I)^{1/2}$, where I is the reduced moment of inertia of the rotor. When the ratio $r = W/\varepsilon$ is huge, these equal the HO energies, but at lower W/ε these have lower energy separations than ε .

Goddard's group³²³ has calculated approximate analytical solutions for the eigenvalues and the partition function (q) for this hindered rotor problem versus W/ε and $k_B T/\varepsilon$, and has constructed a simple-to-calculate interpolation function, called the Hindered Rotor Density-of-States (HRDS) interpolation function, having these asymptotic forms. This HRDS function allows one to easily calculate q and S at any temperature for a potential energy function like Fig. 4.2 or the more general Eq. (4.10). One could easily calculate the partition function and entropy associated with the hindered rotations of adsorbates parallel to the surface using this HRDS approach, and would get a far more accurate result than the harmonic approximation. Periodic DFT could be used to calculate estimates for the only three parameters in this model (W , n , and I) as described below. (Note that ε is a simple function of these parameters.) Other efficient computational approaches have been used to estimate entropies of hindered internal rotations³²⁴, and these could also be adapted to these helicopter-type rotations of adsorbates on

surfaces. Note too that hindered internal rotations of adsorbates should also be treated properly when $k_B T$ is not small compared to the barriers for these hindered internal rotations.

It might even be possible to apply the same HRDS approach to calculate the partition function and entropy associated with the translations of adsorbates parallel to the surface. Note that the potential energy of Fig. 4.2 and Eq. (4.10) for rotations parallel to the surface maps directly into that for adsorbate diffusion if we simply replace $n\phi$ with $2\pi x/a$, where x is distance and a is the site-to-site separation along the surface. Here W is the diffusion barrier. If we replace ϕ with x and I with mass (m), Schrödinger's equation has the same form (albeit with different boundary conditions), so one might be able to modify this HRDS approach³²³ to estimate the partition function and entropy associated with such hindered translational motions of adsorbates as well. In this case, the high-temperature-limit entropy should resemble that of an ideal 2D gas instead of a free rotor. A closely related approach has already been proposed by Hill⁶⁶, which may be nearly as accurate. Again, DFT could be used to calculate the parameters in this modified-HRDS model or in Hill's model (i.e., a and W , with ε being a simple function of a and W .) As an example, our reported DFT calculations for water on Pt(111) give a diffusion barrier $W = 19$ kJ/mol and site-to-site separation $a = 0.28$ nm.³²⁵ When fitted to cosine wave like Eq. (4.10), these give a second derivative at the minimum corresponding to a vibrational frequency of ~ 67 cm⁻¹, or ~ 0.8 kJ/mol excitation energy.

Note that many or even most of the adsorbates systems in Figs. 2.5 and 3.2 have attractive lateral interactions and exist mainly as 2D islands⁹. In the simplest model, this should lead to more restricted motions parallel to the surface. However, if one considers concerted motions of groups of adsorbates, this can lead to much smaller values of W , especially when the preferred adsorbate-adsorbate separation does not match the site-to-site separation on the lattice.

Now that we understand the origin of the empirical relationship in Fig. 3.2 and Eq. (4.1) between (high) adsorbate entropies and gas-phase entropies, we can predict that it will also hold for more strongly-bound adsorbates for the following reason. For a given surface, the barrier height W for different adsorbates should increase roughly proportional to the desorption energy, E_{des} . The temperature (T) on Figs. 2.5 and 3.2 and Eq. (4.1) is limited to the range where desorption has the proper rate to perform equilibrium adsorption isotherm (EAI) and temperature-programmed desorption (TPD) measurements (i.e., $\sim 10^{-3}$ to 100 monolayers/s). Thus, T is also roughly proportional to E_{des} . So for the temperature range where Figs. 2.5 and 3.2 and Eq. (4.1) are expected to hold, T/W is expected to be nearly independent of E_{des} , and it is this ratio that determines to what extent the system has approached the high-temperature limit. For a similar reason, Trouton's Rule is independent of the heat of vaporization, since it only applies at the normal boiling point, and this T increases proportional to the heat of vaporization.

To test this expectation, Fig. 4.3 reproduces Fig. 2.6 but now also includes several experimental prefactors reported for more strongly bound adsorbates (CO, NO and Pb). The details of these new data points, which are for low coverages, are listed in Table 4.1. Except for the case of Pb at step edges on Mo(100), these data are also reasonably well predicted by Eq. (4.9), but on average it underestimates these by a factor of ~ 3 . Table 4.1 is not nearly an exhaustive list of experimental prefactors for these species, but is representative and probably biased toward higher values than average. As noted previously¹¹⁸, the energy barrier for Pb to detach from the step edges of Mo(100) is so high that it loses another degree of freedom (i.e., surface diffusion away from the step edge) compared to Pb at terraces, so its entropy is much lower and its desorption prefactor is correspondingly 20,000-times larger. Similarly, the ratio

Table 4.1. Experimentally measured prefactors for desorption of strongly adsorbed small adsorbates and comparison to the predictions of Eq. (4.9).

adsorbate	surface	T / K	$\log(\nu_{\text{des}}/\text{s}^{-1})$ experiment	$\log(\nu_{\text{des}}/\text{s}^{-1})$ from Eq. (4.9)	$S_{\text{gas}}(T)$ / R	$S_{\text{ad}}(T)$ / R	citation
CO	Ru(001)	477	16.0	15.0	25.4	12.1	310
	Ni(110)	435	15.7	14.9	25.1	12.4	326, 327
	Pt(111)	410	15.5	14.9	24.9	12.7	328
	Pt(111)	600	15.1	15.1	26.2	15.0	329
NO	Pt(111)	575	14.5	15.1	26.2	16.4	330
MeOH	Pt(111)	210	15.6	15.1	27.1	14.5	53
Pb	Mo(100) terraces	1210	15.7	14.5	24.6	11.1	118
	Mo(100) steps	1210	20.0	14.5	24.6	1.3	118

W/E_{des} should depend on the surface's atomic-scale corrugation with, for example, a larger W/E_{des} ratio expected for the (110) than (111) faces of FCC metals, so there may be some crystal face dependence. A weak trend in this respect seems apparent in the data for CO on Ni surfaces⁷⁴.

At least from looking at the example of CO/Pt(111) from Table 4.1, it seems that HTST also greatly overestimates the desorption prefactor for these more strongly bound adsorbates. To estimate this, we used the vibrational frequencies for this system calculated by DFT reported by Greeley et al. for atop sites⁵⁷ except for the two lowest frequency modes, which were not reported. For these, we used the same group's reported DFT values for Cu(111) instead (193 and 194 cm^{-1} ³³¹), which should be even smaller than on Pt since CO bonds more weakly to Cu. These give a prefactor in HTST at 600 K of $\sim 10^{19} \text{ s}^{-1}$, which is larger than the experimental values by a factor of $\sim 10^4$.

We repeat that Figs. 2.5 and 3.2 and Eq. (4.9) only hold at temperatures high enough for desorption rates to exceed $\sim 10^{-3}$ ML/s (i.e., where τ is less than ~ 1000 s). At some point, the adsorbate entropy will decrease and the prefactor will increase as temperature is lowered such that $k_B T$ is much less than W .

4.5: Estimating Prefactors for Other Elementary Surface Reactions

We now estimate prefactors for other elementary surface reactions using the qualitative picture of the potential energy surface for individual adsorbates in Fig. 4.3 together with the limiting case entropy represented by Eq. (4.1) and Figs. 2.5 and 3.2, which applies when the temperature is high enough for desorption to be observed in EAI or TPD measurements. Again, this is for terrace sites only since species at step edges have much lower entropies.

4.5.1: Adsorbate Diffusion

Within TST, the rate constant for adsorbate diffusion is given by:

$$k_{\text{diff}} = (k_B T/h) (q_{\text{TS}}^0/q_i^0) \exp(-\Delta E_{\text{TS}}^0/k_B T), \quad (4.11)$$

where q_{TS}^0 is the partition function for the transition state (omitting one mode of motion along the reaction coordinate) and q_i^0 is the partition function for the adsorbate. The superscript "0" in both cases means that these are both evaluated about their zero-point energies (i.e., taking all energies relative to the ground state for that species), and ΔE_{TS}^0 is the difference between these two zero-point energies. To be most rigorous, one would plot $\ln(k_{\text{diff}})$ versus $1/T$ to get the activation energy (E_{act} = the slope at the temperature of interest times $-R$) and the prefactor ν_{diff} (where $\ln(\nu_{\text{diff}})$ = the y -intercept). Both will vary slowly with T . Alternatively, one can get the prefactor from $\nu_{\text{diff}} = k_B T/h \exp[(S_{\text{TS, diff}}^0 - S_{\text{ad}}^0)/R]$, where both entropies are evaluated at the

temperature of interest. As noted above, within HTST, the entropy of both species is calculated from the sum over all vibrational modes of $R\{(h\nu_{\text{vib}}/kT)/[\exp(h\nu_{\text{vib}}/kT) - 1] - \ln[1 - \exp(-h\nu_{\text{vib}}/kT)]\}$. For simplicity, ν_{diff} is often approximated as $(k_{\text{B}}T/h)(q_{\text{TS}}^0/q_{\text{i}}^0)$, with E_{act} approximated as ΔE_{TS}^0 . This is not as accurate as these other two methods for calculating either separate value (ν_{diff} or E_{act}), but their combination obtained in this way at any temperature gives the correct rate constant.

Diffusion rates are usually measured at temperatures where $k_{\text{B}}T$ is very small compared to the barriers in Fig. 4.2 for motion parallel to the surface. In this case, HTST should be accurate, wherein both q_{TS}^0 and q_{i}^0 are pure vibrational partition functions. Note that this is for temperatures far below those where Figs. 2.5 and 3.2 and Eq. (4.1) are valid, since those are valid only when desorption rates are fast enough to measure (which requires much higher temperature than diffusion for the same adsorbate). Thus HTST has been used, for example, together with embedded atom potentials to calculate the barrier, fundamental vibrational frequencies and prefactor for diffusion of Cu on Cu(100), and this gave good agreement with experimental results³³². We used it together with energetics and vibrational frequencies calculated using DFT with periodic boundary conditions to calculate the prefactors for the diffusion of small Pd_n clusters ($n = 1$ to 4) on MgO(100)³³³. The values at 250 K were in the range $\sim 10^{11}$ to 10^{14} s⁻¹, with the tetramer having a prefactor 100- to 1000-fold larger than the monomer and dimer, due to a "floppy" transition state.

It is possible that some adsorbates might have relatively free rotations parallel to the surface while $k_{\text{B}}T$ is still very small compared to the barrier for diffusion. In these cases, it is unlikely that the partition function for these rotations will be much different between the

adsorbed state and its transition state for diffusion, so the rotational contributions will nearly cancel. Hence, HTST should still offer a reasonable approximation for ν_{diff} .

If one is trying to predict diffusion rates at much higher temperatures (i.e., where desorption rates are fast enough to measure), then HTST is no longer valid. Instead, the entropies for the initial state and the transition state should both be much larger than the vibrational entropies and similar to the entropy given by Eq. (4.1). Keeping this in mind, the ratio q_{TS}^0/q_i^0 in Eq. (4.1) can be estimated by recognizing that q_{TS}^0 and q_i^0 will be very similar except that q_{TS}^0 is missing one translational mode (the reaction coordinate for diffusion). The entropy for this translational mode, $S_{\text{gas,1D-trans}}^0$, can be calculated using Eq. (4.4), and the prefactor is given by:

$$\nu_{\text{diff}} = k_{\text{B}}T/h \exp(-S_{\text{gas,1D-trans}}^0/R). \quad (4.12)$$

This is much smaller than the value that would be predicted by Eq. (4.11) using HTST, which reflects the increasing contribution to the partition function of the initial adsorbate state of the motion in the direction of the reaction coordinate (i.e., motion in the direction of diffusion) with increasing temperature. Note that this contribution is not included in the partition function of the transition state.

4.5.2: Adsorbate Dissociation

Consider an adsorbate's dissociation reaction of the type:



where $\text{AB}_{\text{ad,TS}}$ is the transition state. We have previously tabulated a list of 25 values of the prefactor for the dissociation of different adsorbates on different single crystal surfaces ¹¹⁶.

Those values showed a clear trend in that the prefactor for dissociation (ν_{diss}) was only 1/10 to

$1/10^5$ of the prefactor for desorption (ν_{des}) of the same molecule at the same temperature, with an average ratio ($\nu_{\text{diss}}/\nu_{\text{des}}$) of $\sim 1/1000$. (This was for low coverages where both reactions were assumed to be first-order in coverage.) In that work, the main emphasis was on this ratio of prefactors rather than the absolute value for ν_{diss} , since the latter was usually only determined by multiplying the experimentally measured ratio by some assumed value of ν_{des} , typically 10^{13} s^{-1} which we showed above can be many orders of magnitude too low (Fig. 2.6). A recent experimental study of the kinetic competition between dissociation and desorption of propane on PdO(101) also shows a ratio $\nu_{\text{diss}}/\nu_{\text{des}}$ of $\sim 1/1000$, that was also reproduced by DFT calculations when the extra entropy of the adsorbates mentioned above was approximately included³²².

The low value for the ratio $\nu_{\text{diss}}/\nu_{\text{des}}$ can be understood as follows. If a relatively freely moving part of the adsorbate starts forming a new bond to the surface in the transition state, the partition function of this three-center transition state will naturally be smaller than that of the reactant. An example is shown in Fig. 4.4, where adsorbed methoxy on a metal surface (metal-OCH₃) loses a methyl H to form adsorbed -OCH₂ plus -H. In the reactant, the methyl could be nearly a free rotor both around its own central axis of symmetry and around the metal-O bond axis, but those motions are lost as the methyl starts to form its own bond to the metal in the transition state. This effect is analogous to the situation in gas-phase or solution-phase reactions where the partition function is generally lowered when forming three-center transition states³³⁴. For a similar reason, the cyclization of a more linear molecule generally leads to decrease in entropy.

The simplest approach to estimating ν_{diss} for dissociation of adsorbates is to multiply the value of ν_{des} for the same molecule, estimated from Eq. (4.9), by this average ratio of 10^{-3} mentioned above:

$$\nu_{\text{diss}} = \sim 10^{-3} \nu_{\text{des}}. \quad (4.14)$$

Since dissociation rates for molecular adsorbates are usually measured in the same temperature range as desorption rates, using Eq. (4.9) for ν_{des} is treating its behavior in the proper temperature regime. However, this is often not true for non-molecular adsorbates (i.e., molecular fragments) like the methoxy species shown in Fig. 4.4, which would have a much higher desorption temperature (to make a methoxy radical) than the temperatures where it is typically seen to dissociate (i.e., one often wants to evaluate ν_{diss} at temperatures where the surface residence time exceeds ~ 1000 s). For the dissociation of such adsorbed molecular fragments, it may be better to estimate ν_{des} (or ν_{diss} directly) using HTST. One must do something like what is recommended in Section 4 above to get partition functions or entropies that would be more generally accurate.

4.5.3: Association of Two Adsorbates

Consider the association reaction of two adsorbates of the type:



where $AB_{\text{ad,TS}}$ is again the transition state. The standard entropy change for this net reaction, ΔS_{ass}^0 , must equal the sum of ΔS_{step}^0 for the two elementary steps in Reaction (4.15) above:

$$\Delta S_{\text{ass}}^0 = \Delta S_{\text{step1}}^0 + \Delta S_{\text{step2}}^0 = \Delta S_{\text{TS, ass}}^0 - \Delta S_{\text{TS, diss}}^0, \quad (4.16)$$

where $\Delta S_{\text{TS, diss}}^0$ is the standard entropy of activation for dissociation Reaction (4.13), which is the reverse of this association Reaction (4.15). Here we have used the fact that $\Delta S_{\text{step2}}^0 = -\Delta S_{\text{TS, diss}}^0$. Dividing both sides by R and then taking the exponent of both sides gives:

$$\exp(\Delta S_{\text{ass}}^0/R) = \exp(\Delta S_{\text{TS, ass}}^0/R - \Delta S_{\text{TS, diss}}^0/R) = \exp(\Delta S_{\text{TS, ass}}^0/R) / \exp(\Delta S_{\text{TS, diss}}^0/R). \quad (4.17)$$

Since $\nu_{\text{step}} = k_B T/h \exp(\Delta S_{\text{TS,step}}^0/R)$ for each step, the ratio on the right side of this expression is just $\nu_{\text{ass}}/\nu_{\text{diss}}$, so that:

$$\nu_{\text{ass}} = \nu_{\text{diss}} \exp(\Delta S_{\text{ass}}^0/R) = \nu_{\text{diss}} \exp[(S_{\text{AB,ad}}^0 - S_{\text{A,ad}}^0 - S_{\text{B,ad}}^0)/R]. \quad (4.18)$$

One can estimate ν_{ass} using Eq. (4.18) by getting ν_{diss} by the method described in the previous section and getting $S_{i,\text{ad}}^0$ for each adsorbed species i (A, B and AB) from Figs. 2.5 and 3.2 or Eq. (4.1). Obtaining any adsorbate's entropy using Figs. 2.5 and 3.2 or Eq. (4.1) requires knowing its standard gas-phase entropy at the same temperature, which is easy to estimate^{26, 107} by extrapolating from tabulated entropies at similar conditions using tabulated heat capacities (such as the NIST tables of thermodynamic data).

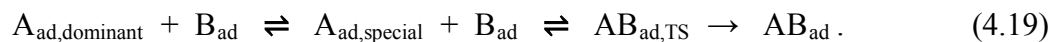
One cannot use Figs. 2.5 and 3.2 to estimate the entropy for adsorbed A or B in this application if one is studying the rate of their association reaction at a temperature far below its desorption temperature, since Figs. 2.5 and 3.2 is only known to be valid for temperatures where the desorption rate is at least 10^{-3} ML/s ($\tau < \sim 1000$ s). For example, a prefactor of 10^{17} s⁻¹ was determined experimentally for the associative desorption of water from adsorbed -OH plus -H on $\alpha\text{-Fe}_2\text{O}_3(012)$ (1x1)¹⁷⁹. This prefactor is higher than that for desorption of molecularly adsorbed water, and higher than would be expected based on the above analysis. This was attributed to the expectation that at the low temperature of that study, most of the translational and rotational motion of these adsorbed fragments (-OH and -H) have probably been frozen out into vibrational modes, thus lowering their entropy below that predicted by Figs. 2.5 and 3.2³. At such temperatures, standard HTST should be valid.

4.6: Dealing with Mechanistic Complexity: When an Adsorbate Must Assume Some Special Minority Structure Before Producing the Transition State

In surface reactions, it is very common for the adsorbate in its dominant form on the surface to first convert to some minority species before producing the transition state for the types of reactions discussed above. For example, for most of the desorption reactions in Fig. 2.6, the dominant form of the adsorbate is in 2D islands, yet at coverages below 50% of saturation, it probably desorbs by first detaching from the islands to make adsorbed monomers (as a dilute 2D lattice gas or ideal 2D gas), and then desorbing from this dilute state. Similarly, association reactions often occur by a mechanism where one species is in islands and the other diffuses up to populate a special site at the edge of those islands (where it may be much less stable in energy than as an isolated monomer at a site well separated from island). Also, dissociation reactions for adsorbates often happen mainly at defect sites.

How does one relate the rates for such processes that involve minority structures for an adsorbate to the coverage of the dominant state of that adsorbate, which is usually the only type of coverage that one can actually measure? One of the beauties of TST is that its derivation requires thermal equilibrium between the reactants and transition state. Thus, it does not matter how many intermediate states there are between the measureable reactants and the transition state, if they are also in equilibrium with the reactants one arrives at the same rate expression. Thus, one only needs to be able to fully describe the measureable reactants and the transition state to use its results. For example, consider the association reaction of two adsorbates of the type originally considered in Reaction (4.15) above, but let us now add the mechanistic complexity that the dominant form of reactant A is now in islands ($A_{ad,dominant}$), but that it must

be in some special minority form ($A_{ad, special}$), like an isolated monomer or at some defect site, before it can react with B_{ad} :



As long as $A_{ad, dominant}$ is in equilibrium with $A_{ad, special}$, one can ignore this intermediate state in deriving the TST rate expression, and one still arrives at the same result. Since surface migration processes are often so fast compared to the rate-controlling step(s) in the overall surface reaction mechanism, it is often safe to assume that the equilibrium $A_{ad, dominant} \rightleftharpoons A_{ad, special}$ is fast enough to apply this. For example, in catalytic reactions, the rate-controlling steps usually have much larger activation energies than surface migration steps. Also, this assumption is particularly likely to be true under steady-state reaction conditions where the surface coverages of all species are constant. Of course, if the transition state is at some special site like a defect, one must take this into consideration in describing the nature (energy and partition function) for the transition state, but one need not know how to describe $A_{ad, special}$ in any detail, or even know that it exists.

4.7: Statistical Models for Adsorbates: 2D Ideal Gas, 2D Lattice Gas, and 2D Crystals

Surface chemists usually think about the statistical mechanics of adsorbates in terms of the two limiting cases that have been discussed in statistical thermodynamics texts: the 2D ideal gas model and the 2D lattice gas model, with or without lateral adsorbate-adsorbate interactions⁶⁶ (for more sophisticated models and applications, see also³⁰⁷⁻³⁰⁹). If adsorbates have attractive interactions and form large 2D islands, one can also treat them as perfect 2D crystals. Depending on which model is used to represent each adsorbate, one gets different expressions for the rate constant and the coverage dependence of the rate using transition state theory. These differences arise entirely through the different expressions one gets when

calculating the concentration of the transition state assuming it is in equilibrium with the reactants, as shown below.

Consider again Reaction (4.15), the association of two adsorbates: $A_{\text{ad}} + B_{\text{ad}} \rightleftharpoons AB_{\text{ad,TS}} \rightarrow AB_{\text{ad}}$. If adsorbed A, B and the transition state are all ideal 2D gases, the TST rate for Reaction (4.15), r_{ass} , is:

$$r_{\text{ass}} = k_{\text{ass}} C_A C_B \quad (4.20)$$

where C_i is the concentration of adsorbed i (in moles per unit area) and k_{ass} is the rate constant in units of $(\text{moles per area} \times \text{time})^{-1}$, so that r_{ass} has units of (moles AB produced per area per time). By equating the chemical potential of $AB_{\text{ad,TS}}$ with the sum of the chemical potentials for $A_{\text{ad}} + B_{\text{ad}}$ (i.e., the equilibrium criterion), the rate constant in TST can be shown to equal:

$$k_{\text{ass}} = N_A(k_B T/h) \{ (q_{\text{TS}}^0/A) / [(q_A^0/A)(q_B^0/A)] \} \exp(-\Delta E_{\text{TS}}^0/k_B T), \quad (4.21)$$

where q_i^0/A is the molecular partition function per unit area for each species i evaluated about its own zero-point energy (i.e., taking its zero-point energy as energy = 0), and ΔE_{TS}^0 is the difference in zero-point energy between the reactants and transition state. Note that q_{TS}^0 has a special definition in that one must remove from it one degree of freedom (the reaction coordinate's contribution, which is related to the A–B stretching vibration of the product AB). (As usual in the derivation of the TST rate, this contribution cancels with a factor in the rate at which the transition state itself converts to products.) Such removal also applies to all its uses below. Since all three partition functions in Eq. (4.17) include two degrees of translational motion, their values are proportional to area A , and so A cancels out in k_{ass} . Its prefactor-like product $N_A(k_B T/h) \{ (q_{\text{TS}}^0/A) / [(q_A^0/A)(q_B^0/A)] \}$ will usually be much, much less than $N_A(k_B T/h) = \sim N_A(10^{13} \text{ s}^{-1})$ since this ratio of q values includes two more degrees of translational motion in its denominator.

If A, B and TS are all treated instead as ideal (i.e., non-interacting) 2D lattice gases, the TST rate for Reaction (4.15) is:

$$r_{\text{ass,LG}} = k_{\text{ass,LG}} [\theta_A/(1 - \theta_A)][\theta_B/(1 - \theta_B)], \quad (4.22)$$

where θ_i is the fractional occupation of sites by adsorbed i (unitless) and $k_{\text{ass,LG}}$ is the rate constant in units of time^{-1} , so that r_{ass} has units of time^{-1} (which really means monolayers converted per unit time). (This equation assumes that A and B use different, independent sites. If A and B compete for the same sites, which is more likely, the denominators here should both be changed to $(1 - \theta_{\text{total}})$, where θ_{total} is the total coverage of all adsorbates.) The rate constant in TST is:

$$k_{\text{ass,LG}} = (k_B T/h) [q_{\text{TS}}^0/(q_A^0 q_B^0)] \exp(-\Delta E_{\text{TS}}^0/k_B T), \quad (4.23)$$

where q_i^0 is the molecular partition function for each species i evaluated about its own zero-point energy, and ΔE_{TS}^0 is the difference in zero-point energy between the reactants and transition state. Again, these equations can be derived by equating the chemical potential of $\text{AB}_{\text{ad,TS}}$ with the sum of the chemical potentials for $\text{A}_{\text{ad}} + \text{B}_{\text{ad}}$ (i.e., assuming equilibrium), with an identical derivation to that above except for the difference in the expressions for the chemical potentials of ideal 2D lattice gases versus ideal 2D gases. Note that q_i^0 has only vibrational contributions at low temperature, but the adsorbate might be a hindered rotor or even free rotor in its lattice site at higher temperatures, but still not so hot that the lattice site model breaks down.

The unusual $1/(1 - \theta_i)$ factors in this rate expression arise because the chemical potential of i includes the term $k_B T \ln[\theta_i/(1 - \theta_i)]$ in the ideal 2D lattice gas model, which increases with θ_i below $1/2$ monolayer but decreases above that, due to the configurational entropy of the adsorbate⁶⁶.

If one derives the rate expression for desorption of molecularly adsorbed species for cases where the sticking probability is near unity (i.e., non-activated adsorption, like the situations treated in Chapter 4.3 above), TST gives that the rate of desorption is also proportional to $\theta/(1 - \theta)$ for the ideal lattice gas model. This arises from equating the chemical potential of the adsorbed 2D lattice gas (which includes $k_B T \ln[\theta/(1 - \theta)]$) with that for the transition state (an ideal 2D gas). The sharp decrease in activation energy for desorption (E_d) with increasing coverage near saturation so commonly seen as θ approaches 1 when rates are analyzed as proportional to θ_i as in Eq. (4.2) instead of $\theta/(1 - \theta)$ is at least partly an artifact of omitting this $\theta/(1 - \theta)$ in the denominator. Similarly, the exponential increase in apparent prefactor for desorption with coverage reported for some cases³⁰⁷ can be attributed at least partially to neglecting this. Note that we cancelled the $1/(1 - \theta_{TS})$ factor in the derivation of this rate expression for association above, since it is safe to assume that the coverage of the transition state is so low that this factor equals unity. Note too that this $\theta/(1 - \theta)$ factor leads properly to the first-order Langmuir adsorption isotherm relating θ to gas pressure when derived using equilibrium thermodynamics⁶⁶, and it is also easily derived from kinetics by setting this desorption rate equal to the adsorption rate for this case where the sticking probability (S) is 1 at all coverages. This derivation gives the same result as the more common kinetic derivation which assumes the desorption rate is proportional instead to θ and S is proportional to $(1 - \theta)$, but conceptually it is quite different. When measured carefully, sticking probabilities are often observed to be very close to unity right up to saturation, with the apparent decrease in long-term sticking probability above 90% of saturation coverage actually due to desorption of transiently adsorbed species^{53, 84, 335}. This $(1 - \theta)$ factor in the desorption rate expression fully explains

their short lifetimes on the surface at such high coverages: new sites or strongly repulsive lateral interactions are not needed to qualitatively explain such observations.

Returning to the case of associative desorption, Reaction (4.15), if we assume that A and B are both 2D crystal islands (i.e., are lattice gases but have attractive interactions so they reside in larger, perfect 2D islands of pure A and pure B), but that TS is still a lattice gas, then the coverage dependence drops completely out of the rate expression in Eq. (4.18). In this case, the rate simply equals the rate constant ($r_{\text{ass,crystal}} = k_{\text{ass,crystal}}$), where the rate constant $k_{\text{ass,crystal}}$ equals $k_{\text{ass,LG}}$, the same expression as Eq. (4.20).

If one must use different models for the two adsorbates (e.g., ideal 2D gas for A and ideal 2D lattice gas for B), derivation of the TST rate expression starting with the equilibrium assumption again shows that one can still calculate the rate constant using Eq. (4.23) but one must replace q_i^0 with $q_i^0/(N_A A)$ for every species that is treated as an ideal 2D gas. In the rate expression, Eq. (4.22), one must also replace $\theta_i/(1 - \theta_i)$ with C_i for every reactant species that is treated as an ideal 2D gas. One must take the units on N_A to be mole^{-1} so that the units work, with the rate having units of moles produced per area per s, or s^{-1} (i.e., monolayer per s), depending on whether the transition state is treated as an ideal 2D lattice gas or ideal 2D gas.

4.8: Figures

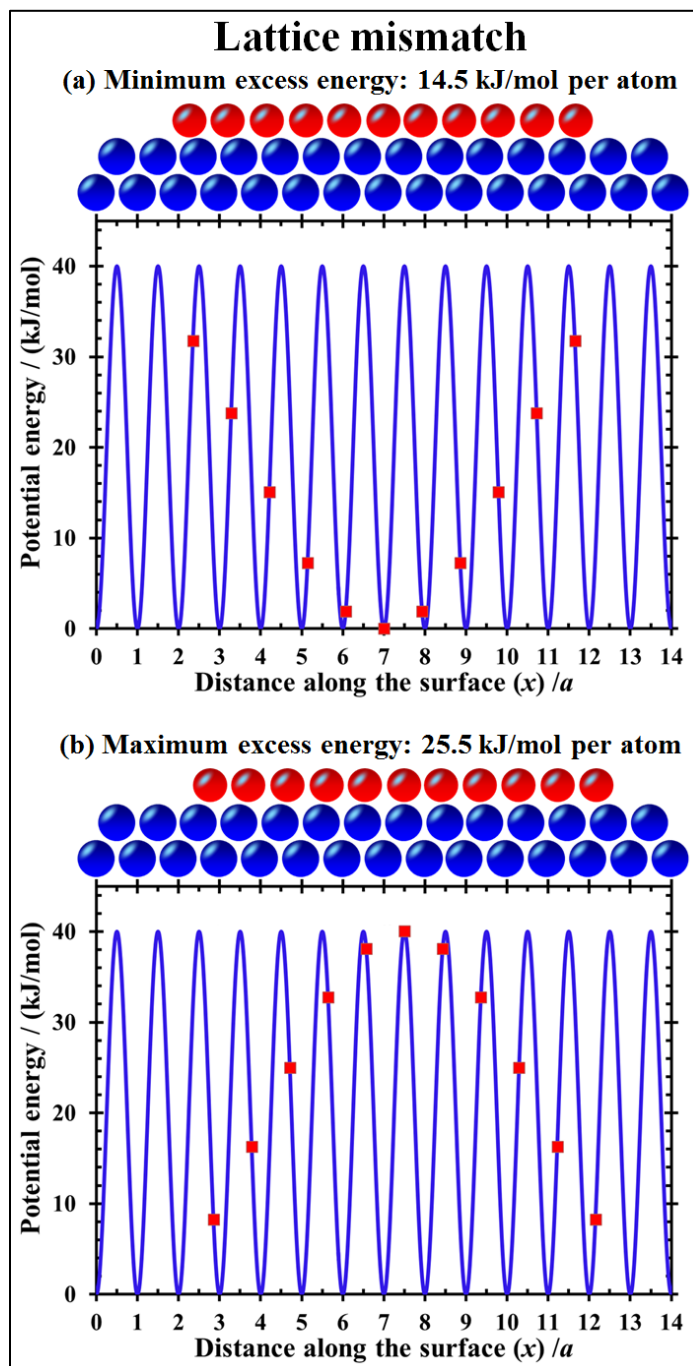


Figure 4.1. An illustration of the effects of a lattice mismatch of 4% between an adsorbate and an underlying support for a 40 kJ/mol hypothetical diffusion barrier across the surface. (a) This leads to an increase in the energy of 14.5 kJ/mol per atom with the central atom at the most ideal binding site. (b) When the central atom is translated to its least ideal binding site, this energy increases by only 11 kJ/mol per atom, so that the barrier for diffusion is just 28% of the single atom diffusion barrier. This logic could also be applied to explain why large polyatomic adsorbates whose atom-to-atom spacing does not match the substrate have low diffusion barriers.

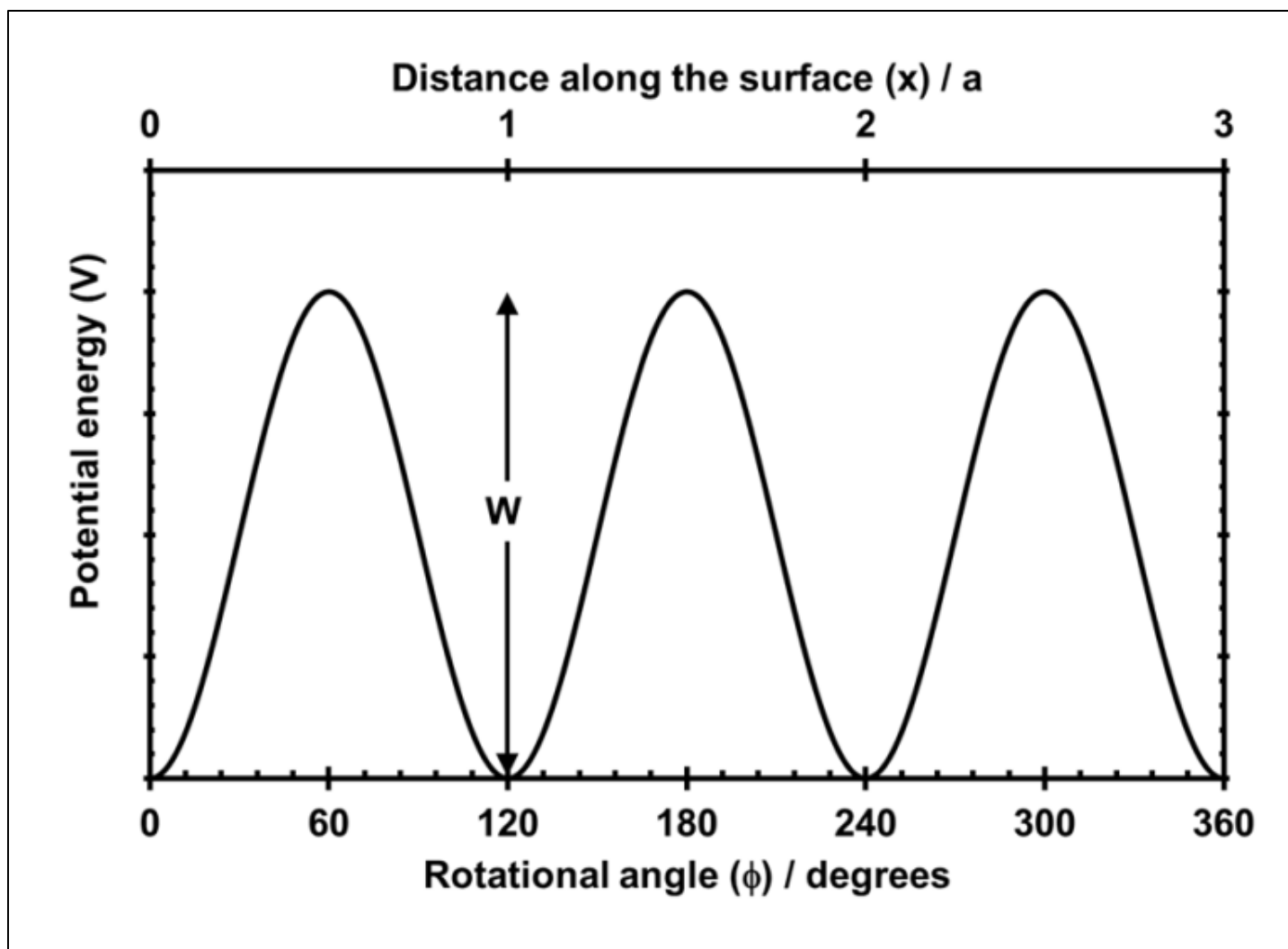


Figure 4.2. Bottom axis: The classic hindered rotor: Potential energy versus rotational angle for the rotation of one methyl group about the C–C axis in gas-phase ethane. From McQuarrie²⁶. The same form of potential applies to helicopter-type rotations of an adsorbate. Top axis: Potential energy versus distance along the surface (x) for the diffusion of an adsorbate, where a = site-to-site separation. Reprinted with permission from Reference²⁷. Copyright 2013 de Gruyter.

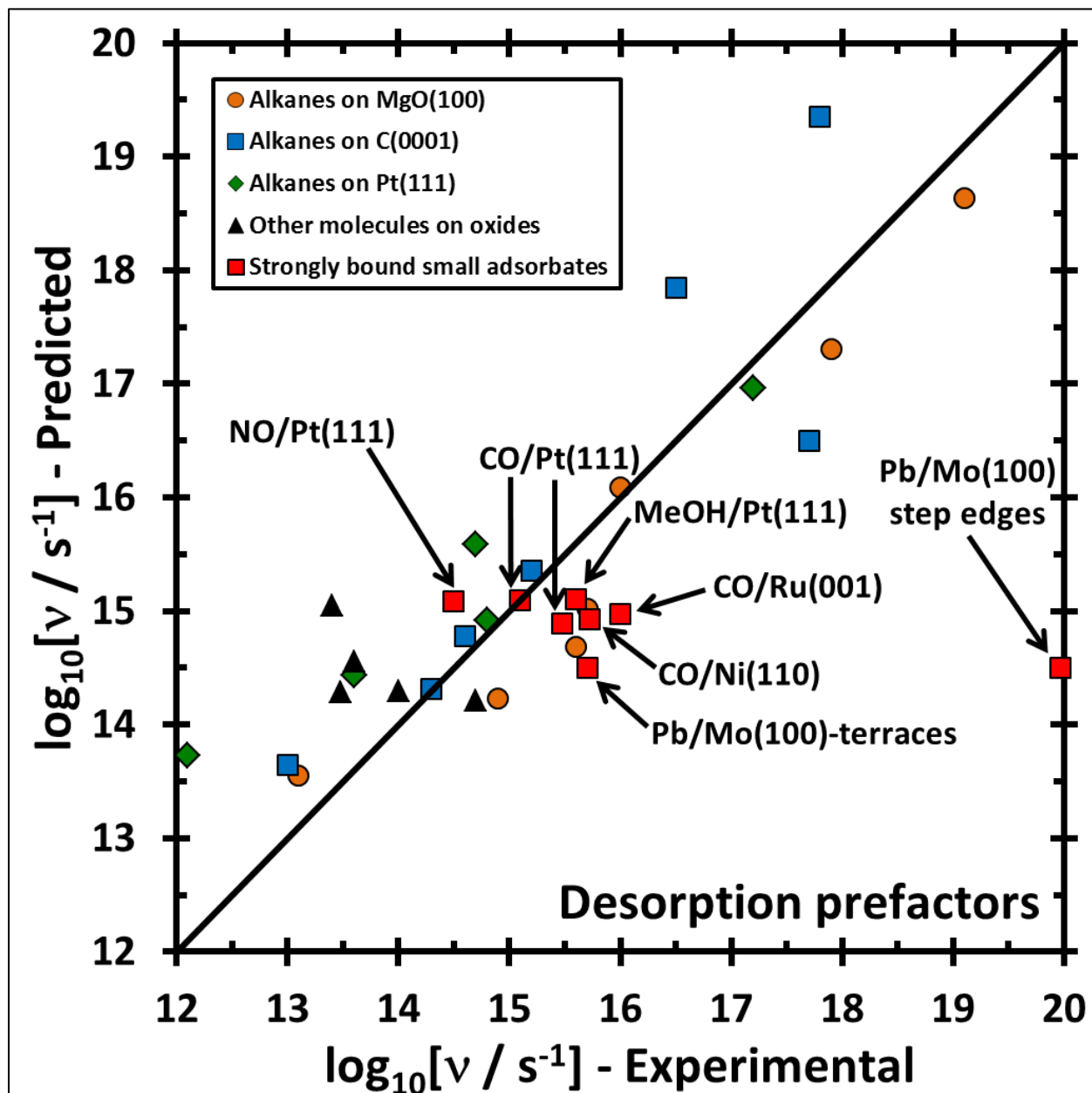


Figure 4.3. Prefactors for the desorption of adsorbed species as predicted using Eq. (4.9) plotted versus the experimentally measured prefactors. The line shows the expectation based on Eq. (4.9). Most of the data points were already shown in Fig. 2.6, but the new points (red squares) are for more strongly bound adsorbates (see Table 4.1 for details). Reprinted with permission from Reference ²⁷. Copyright 2013 de Gruyter.

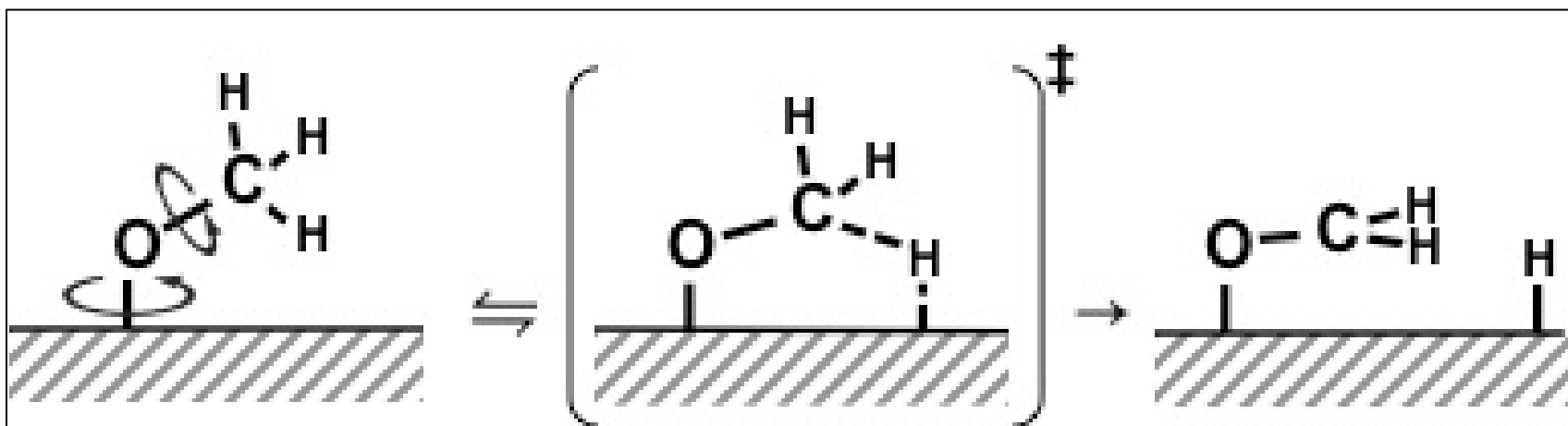


Figure 4.4. Schematic representation showing how entropy is lost in the transition state for the dissociation of an adsorbate, in this example for an adsorbed methoxy on a metal surface losing a methyl H to form adsorbed -OCH₂ plus -H. The reactant has two relatively free rotations, but those motions are lost as the methyl starts to form its own bond to the metal in the transition state. Reprinted with permission from Reference ²⁷. Copyright 2013 de Gruyter.

Chapter 5

Anchored Metal Nanoparticles: Effects of Support and Size on Their Energy, Sintering Resistance and Reactivity

Many catalysts consist of metal nanoparticles anchored to the surfaces of oxide supports. These are key elements in technologies for the clean production and use of fuels and chemicals. We show here that the chemical reactivity of the surface metal atoms on these nanoparticles is closely related to their chemical potential: the higher their chemical potential, the more strongly they bond small adsorbates. Controlling their chemical potential by tuning the structural details of the material can thus be used to tune their reactivity. As their chemical potential increases, this also makes the metal surface less noble, effectively pushing its behavior upwards and to the left in the periodic table. Also, when the metal atoms are in a nanoparticle with higher chemical potential, they experience a larger thermodynamic driving force to sinter. Calorimetric measurements of metal vapor adsorption energies onto clean oxide surfaces in ultrahigh vacuum show that the chemical potential increases with decreasing particle size below 6 nm, and, for a given size, decreases with the adhesion energy between the metal and its support, E_{adh} . The structural factors that control the metal / oxide adhesion energy are thus also keys for tuning catalytic performance. For a given oxide, E_{adh} increases with $(\Delta H_{\text{sub,M}} - \Delta H_{\text{f,MOx}})/\Omega_{\text{M}}^{2/3}$ for the metal, where $\Delta H_{\text{sub,M}}$ is its heat of sublimation, $\Delta H_{\text{f,MOx}}$ is the standard heat of formation of that metal's most stable oxide (per mole of metal), and Ω_{M} is the atomic volume of the bulk solid metal. The value $\Delta H_{\text{sub,M}} - \Delta H_{\text{f,MOx}}$ equals the heat of formation of that metal's oxide from a gaseous metal atom plus $\text{O}_2(\text{g})$, so it reflects the strength of the chemical bonds which that metal atom can make to oxygen, and $\Omega_{\text{M}}^{2/3}$ simply normalizes this energy to the area per metal atom, since E_{adh} is the adhesion energy per unit area. For a given metal, E_{adh} to different clean oxide

surfaces increases as: $\text{MgO}(100) \approx \text{TiO}_2(110) \leq \alpha\text{-Al}_2\text{O}_3(0001) < \text{CeO}_{2-x}(111) \leq \text{Fe}_3\text{O}_4(111)$.

Oxygen vacancies also increase E_{adh} , but surface hydroxyl groups appear to decrease E_{adh} , even though they increase the initial heat of metal adsorption.

5.1: Introduction

Metal nanoparticles dispersed across the surfaces of oxide and carbon supports form the basis for many catalysts and electrocatalysts of importance to future energy technologies, pollution prevention and environmental protection, all necessary for any sustainable technological infrastructure that maintains a high quality of life. The catalytic activity per surface metal atom and selectivity can vary with particle size when the metal particles are below about 7 nm in diameter^{42, 44, 187, 277, 336-349}, in some cases dramatically^{42, 274, 275, 277, 350-357}. Measurements have even shown that the activity depends on the nanoparticle shape for particles of the same size³⁵⁸. The activity can also depend strongly on the choice of support, even for particles of the same size^{42, 44, 277, 336, 340, 342, 344, 354, 357, 359-371}, the extent of reduction if an oxide support^{41, 357, 372-375}, and the extent of oxidation if a carbon support^{368, 369, 376}.

In general, these effects are poorly understood, largely due to the difficulty in structurally characterizing high-area catalysts with sufficient detail, resulting in an inability to analyze thoroughly any structure / reactivity relationships that control the effects. Furthermore, the metal nanoparticles often sinter rapidly under catalytic reaction conditions, resulting in particle growth and loss of metal area during activity measurements, and thus challenging the ability to even measure area-specific activity let alone correlate it to size and support. The relationships of sintering kinetics to catalyst structure are also poorly understood.

In order to better understand structure / reactivity relationships in such catalysts and their sintering kinetics, a number of researchers including our own group have adopted a model-catalysts approach whereby structurally well-defined samples of metal nanoparticles on oxides are prepared by vapor deposition of the metal onto single-crystalline oxide surfaces^{33, 34, 185-193, 204, 350-354, 356, 357, 372, 373, 377-410}. The deposited metal atoms generally nucleate small particles, whose size and number density can be controlled by the amount of deposited metal and the temperature. The aim of this approach is to correlate the metal's chemisorption, catalytic, sintering and/or electronic properties with the lateral diameter, thickness and composition of the nanoparticles and with the structure and extent of reduction of the oxide support upon which they sit.

In this chapter, we review studies of well-defined model metal nanoparticulate catalysts supported on clean, single-crystalline oxide surfaces, structurally characterized using a variety of ultrahigh vacuum surface science techniques. The main goal here is to relate the reactivity of late transition metal nanoparticles and the rates at which they sinter with the energies of metal atoms in these supported nanoparticles measured using unique adsorption calorimetry tools. To better understand how the choice of oxide support material affects the energies of metal atoms in nanoparticles, we also analyze temperature programmed desorption (TPD) measurements of metal desorption energies from metal nanoparticles anchored to clean oxide surfaces as well as measurements of metal / oxide adhesion energies obtained from microscopic measurements of metal particle and molten metal droplet shapes.

We find that the concept of metal atom chemical potential is very powerful for predicting how chemisorption bond strengths and sintering rates depend on metal particle size for a given support, and on the support material for a given particle size of late transition metal. We further

show how this chemical potential depends on the structural properties of the catalyst including the metal particle size and the composition and extent of reduction of the oxide support surface.

5.2: The Chemical Potential of Metal Atoms in Anchored Nanoparticles

We will show below that in order to understand how anchored metal nanoparticles function with respect to surface reactivity, catalytic activity and sinter resistance, we must first understand how the chemical potential of the metal atoms in a nanoparticle depends on the structural details of the material. These structural details include: the nature of the metal, the composition and structure of the support surface upon which they sit, the size of the metal nanoparticle, and the shape of the metal nanoparticle. A metal atom's chemical potential is so important because it directly reflects how aggressive that atom will be in its chemical bonding to adsorbates, but at the same time it is also a direct measure of how unstable it is with respect to sintering into very large particles. We will limit this discussion of structural effects on metal chemical potential (μ , or partial molar Gibb's free energy) to a description of only the internal energy differences that arise due to these structural differences, since entropic differences are small and nearly constant in these respects, and since the difference between enthalpy (H) and internal energy (U) is also nearly constant from system to system. We will often refer to these simply as "energy."

The internal energy of a free metal (M) particle in vacuum relative to the bulk solid metal is:

$$U_M = \bar{U}_{M,\text{bulk}} n_M + \gamma_M A_M = \gamma_M A_M, \quad (5.1)$$

where $\bar{U}_{M,\text{bulk}}$ is the molar internal energy of the pure, bulk metal (which we set to the zero reference energy), n_M is the number of moles of metal atoms in the particle, γ_M is the surface

energy of the metal / vacuum interface (which we will show depends on particle diameter below 6 nm), and A_M is the particle's surface area. When this same particle adheres to a support without any change in its shape, the system's total energy decreases by the adhesion energy (E_{adh}) times the total area of metal / support contact (A):

$$\Delta U = -E_{\text{adh}} A, \quad (5.2a)$$

so that the system's total energy is given by:

$$U = U_M + U_{\text{Sup}} - E_{\text{adh}} A = \gamma_M A_M + U_{\text{Sup}} - E_{\text{adh}} A, \quad (5.2b)$$

where U_{Sup} is the internal energy of the particle-free support before adhesion. The metal's chemical potential (μ_M , relative to the bulk metal reference state) is the partial derivative of this with respect to n_M (neglecting entropy differences, which are relatively small). Both A_M and A depend on n_M (typically varying as $n_M^{2/3}$), so μ_M will have a term that increases with γ_M and a second term that decreases with E_{adh} . As the adhesion energy increases, the metal's chemical potential decreases. So, to understand how the chemical potential of metal nanoparticles depends on a nanomaterial's structural properties, we must first understand how the adhesion energy depends on these properties. Note that both γ_M and E_{adh} can depend on particle size for particles below ~ 6 nm in effective diameter^{15, 17}. We address in the next section how E_{adh} depends on the nature of the metal and of the support surface in the large-particle limit.

5.3: How Metal / Oxide Adhesion Energies Depend on the Metal and the Oxide

Metal / oxide adhesion energies have mainly been measured for molten metal drops on flat oxide surfaces, using sessile drop / contact angle techniques, often under controlled inert gas or H₂ atmospheres (although not under conditions of proven surface cleanliness). Two extensive compilations of such values have appeared^{4, 33}, with much of these data coming from Chatain

et al.^{220, 222, 223, 225}. There are similar measurements for faceted solid particles which instead of the contact angle use a ratio of distances that is similar to an aspect ratio (height / width) but which is specific to the Wulff construction of the particle shape (the ratio of the distance from the particle's center of symmetry or Wulff's point to the oxide surface divided by the distance from the Wulff's point to one exposed face of the particle)⁴¹¹. Some older values for solid particles that were collected on single crystal oxide surfaces but not under conditions of proven surface cleanliness have been summarized by Li⁴. The E_{adh} reported from such studies of molten drops and solid particles is directly proportional to the value for the bulk surface energy of the pure metal used in the data analysis, and many of the surface energy values originally used are now outdated. These E_{adh} values have been recalculated using the latest surface energies of the metals, as reported in⁵, and are presented in Table 5.1 along with the new surface energies used. More recently, such measurements have been extended to the clean conditions of ultrahigh vacuum (UHV) on single crystal oxide surfaces that were proven to be clean using surface spectroscopies. Table 5.2 lists many of those results.

Table 5.1: Adhesion energies of metals on oxide surfaces measured by sessile drop / contact angle techniques for the liquid metal drops (top section) and by the shape of the particle for solid metals (bottom section). All data are from Ref. ⁴, but the values marked with an asterisk have been recalculated based on newer values for the surface energies of the pure metals reported in Ref. ⁵. Metals are ordered by their bulk heat of sublimation ($\Delta H_{\text{sub,M}}$) divided by the area per metal atom ($\Omega_{\text{M}}^{2/3}$). Also listed is the heat of formation of the bulk oxide support (per mole of oxygen atoms), $\Delta H_{\text{f,OxSup}}$.

Liquid metal drops									
metal	oxide	apparent θ_{contact}	γ_{M} / (J/m ²)	E_{adh} / (J/m ²)	$E_{\text{adh}} / 2\gamma_{\text{M}}$	$\Delta H_{\text{sub,M}}$ / (kJ/mol)	$\Omega_{\text{M}}^{2/3}$ / (Å ²)	$-\Delta H_{\text{f,OxSup}}$ / (kJ/mol O)	atmosphere
Pb	$\alpha\text{-Al}_2\text{O}_3(0001)$	125±7°	0.44 ⁴¹²	0.19±0.05*	0.22	195.2	6.01	558.6	Ar + H ₂
In	$\alpha\text{-Al}_2\text{O}_3(0001)$	124°	0.700	0.309*	0.22	243	8.79	558.6	vacuum
Sn	$\alpha\text{-Al}_2\text{O}_3(0001)$	125°	0.709	0.302*	0.21	301.2	9.03	558.6	vacuum
Ga	$\alpha\text{-Al}_2\text{O}_3(0001)$	118°	0.881	0.467*	0.27	271.96	7.27	558.6	vacuum
Ag	$\alpha\text{-Al}_2\text{O}_3(0001)$	130°	1.22	0.436*	0.18	284.9	6.63	558.6	Ar + H ₂
Ge	$\alpha\text{-Al}_2\text{O}_3(0001)$	104°	0.555	0.421	0.38	372	8.01	558.6	vacuum
Al	$\alpha\text{-Al}_2\text{O}_3(0001)$	103±8°	1.14	0.89 ±0.16*	0.39	330.9	6.51	558.6	vacuum
Mn	$\alpha\text{-Al}_2\text{O}_3(0001)$	103°	1.54	1.19*	0.39	283.3	5.39	558.6	Ar
Au	$\alpha\text{-Al}_2\text{O}_3(0001)$	120°	1.51	0.77*	0.25	368.2	6.60	558.6	vacuum
Si	$\alpha\text{-Al}_2\text{O}_3(0001)$	80°	0.745	0.875	0.59	450.0	7.37	558.6	He
Pd	$\alpha\text{-Al}_2\text{O}_3(0001)$	120°	2.00	1.00*	0.25	376.6	6.01	558.6	He
		104°*		1.52*	0.38				vacuum
Cu	$\alpha\text{-Al}_2\text{O}_3(0001)$	128°	1.76	0.676*	0.19	337.4	5.18	558.6	vacuum, Ar + H ₂

Table 5.1 (Continued)

Liquid metal drops									
Metal	oxide	apparent θ_{contact}	γ_M /(J/m²)	E_{adh} /(J/m²)	E_{adh} / 2γ_M	$\Delta H_{\text{sub,M}}$ /(kJ/mol)	$\Omega_M^{2/3}$ / Å²	$-\Delta H_{\text{f,OxSup}}$ /(kJ/mol O)	atmosphere
Fe	CaO	132°	2.42	0.806*	0.17	415.5	5.18	634.9	Ar
	BeO	127°		0.970*	0.20			609.4	He
	MgO	123°		1.11*	0.23			601.6	vacuum
	UO ₂	123°		1.11*	0.23			542.5	Ar + H ₂
	ZrO ₂	115°		1.37*	0.28			550.3	Ar + H ₂
	α -Al ₂ O ₃ (0001)	111°		1.55*	0.32			558.6	Ar + H ₂
		109°		1.63*	0.34				Ar + H ₂
Cr ₂ O ₃	88°	2.52*	0.52	379.9	Ar				
Co	ZrO ₂	118°	2.35	1.26*	0.27	426.7	4.96	550.3	Ar + H ₂
	α -Al ₂ O ₃ (0001)	115°		1.36*	0.30			558.6	Ar + H ₂
		113°		1.53*	0.30				Ar + H ₂
	CoO	70°		3.18*	0.68			237.9	Ar
Ni	CaO	135°	2.38	0.697*	0.15	430.1	4.93	634.9	-
	MgO	132°		0.788*	0.17			601.6	vacuum
	BeO	127°		0.965*	0.20			609.4	He
	SiO ₂	125°		1.02*	0.21			455.4	vacuum
	ZrO ₂	121°		1.16*	0.24			550.3	Ar + H ₂

Table 5.1 (Continued)

Liquid metal drops									
Metal	oxide	apparent θ_{contact}	γ_{M} /(J/m²)	E_{adh} /(J/m²)	E_{adh} / 2γ_{M}	$\Delta H_{\text{sub,M}}$ /(kJ/mol)	$\Omega_{\text{M}}^{2/3}$ / Å²	$-\Delta H_{\text{f,OxSup}}$ /(kJ/mol O)	atmosphere
Ni	UO ₂	112°		1.49*	0.31			542.5	Ar
	α -Al ₂ O ₃ (0001)	111°		1.52*	0.32			558.6	Ar + H ₂
		109°		1.61*	0.34				vacuum, Ar, He, H ₂ , Ar + H ₂
	TiO ₂	105°		1.76*	0.37			472.0	vacuum
	NiO	60°		3.57*	0.75			244.3	-
	CoO	58°		3.64*	0.76			237.9	Ar
Pt	α -Al ₂ O ₃ (0001)	98°	1.70	2.16*	0.43	565.7	6.10	558.6	vacuum
Solid metal particles									
Metal	oxide	apparent θ_{contact}	γ_{M} /(J/m²)	E_{adh} /(J/m²)	E_{adh} / 2γ_{M}	$\Delta H_{\text{sub,M}}$ /(kJ/mol)	$\Omega_{\text{M}}^{2/3}$ / Å²	$-\Delta H_{\text{f,OxSup}}$ /(kJ/mol O)	atmosphere
Ag	α -Al ₂ O ₃ (0001)	125°	1.22	0.51±0.07	0.21	284.9	6.63	558.6	-
Au	α -Al ₂ O ₃ (0001)	125°	1.51	0.63±0.09	0.21	368.2	6.60	558.6	-
Cu	α -Al ₂ O ₃ (0001)	131°	1.79	0.61±0.11	0.17	337.4	5.18	558.6	-
Ni	α -Al ₂ O ₃ (0001)	130°	2.38	0.84±0.09	0.18	430.1	4.93	558.6	-
Fe	α -Al ₂ O ₃ (0001)	124°	2.42	1.06±0.17	0.22	415.5	5.18	558.6	-

Table 5.2: Adhesion energies of solid metals measured on clean oxide surfaces under ultrahigh vacuum conditions. Methods used are based either on the particle shape (HRTEM and GISAXS) or on the integral heat of adsorption of metal vapor at multilayer coverage (SCAC and TPD). All data are from the citations listed, but the values marked with an asterisk have been recalculated based on newer values for the surface energies of the pure metals reported in Ref. ⁵. Also listed is the heat of formation of the most stable bulk oxide of that metal (per mole of metal atoms), $\Delta H_{f,MOx}$. Metals are ordered by their bulk heat of sublimation divided by the area per metal atom. (Table 5.1 lists these values.)

Metal	oxide	particle size / nm	apparent $\theta_{contact}$	$E_{adh} / (J/m^2)$	$E_{adh} / 2\gamma_{v/m}$	$\Delta H_{f,MOx} / (kJ/mol M)$	method	citation
Pb	MgO(100)	10+ (4.75 ML)	72°	0.57±0.20*	0.65	-219	SCAC	11
Ag	MgO(100)	6.6	150±30°	0.30±0.30	0.12	-15.1	SCAC	12
	α -Al ₂ O ₃ (0001) or γ -Al ₂ O ₃ (111)	-	>70.8°	<1.6	<0.66		TPD	3
	CeO _{1.9} (111)	3.6	90°	2.3±0.3	0.94		SCAC	17
	CeO _{1.8} (111)	3.6	90°	2.5±0.3	1.0		SCAC	17
	Fe ₃ O ₄ (111)	3.6	90°	2.5±0.3	1.0		SCAC	16
Au	MgO(100)	1-5	124°	0.67*	0.22	9.65	HRTEM	413
	TiO ₂ (110)	2-8	130±5°	0.54±0.10*	0.18±0.03		GISAXS	414
	TiO ₂ (110)	>4	122±5°	0.71±0.11*	0.24±0.04		HRSEM	415
	TiO ₂ (001)	-	>79.1°	<1.8	<0.58		TPD	3
	disordered SiO ₂	-	>72.8°	<2.0	<0.65		TPD	3

Table 5.2 (Continued)

Metal	oxide	particle size / nm	apparent θ_{contact}	E_{adh} /(J/m²)	E_{adh} / $2\gamma_{\text{v/m}}$	$\Delta H_{\text{f,MOx}}$ /(kJ/mol M)	method	citation
Pd	MgO(100)	10-15	116°	1.11*	0.28	-85.4	HRTEM	416
		2-8	109°	1.34*	0.34		GISAXS	417
	disordered SiO ₂	-	>65.8°	<2.8	<0.70		TPD	3
Cu	MgO(100)	10+ (7 ML)	41°	1.92±0.60	0.55	-168.2	SCAC	29
	disordered SiO ₂	-	>71.4°	<2.3	<0.65		TPD	3
	α -Al ₂ O ₃ (0001) or γ - Al ₂ O ₃ (111)	-	>62.4°	<2.6	<0.74		TPD	3
Pt	MgO(100)	1-5	113°	1.51*	0.30	-54.3	GISAXS	418

Our group added another approach for determining adhesion energies, whereby we measure the heat of adsorption of metal atoms as they are vapor deposited onto the clean and ordered surface of a single-crystal oxide under UHV using single crystal adsorption calorimetry (SCAC). We derived the relationship between metal atom adsorption enthalpies on flat substrates and E_{adh} using a thermodynamic cycle³³. That cycle proved that the integral heat of adsorption per mole ($q_{\text{ad,int}}$) at some multilayer coverage where the differential heat of adsorption has just reached the bulk heat of sublimation of the metal per mole ($\Delta H_{\text{sub,M}}$) is given by:

$$q_{\text{ad,int}} = \Delta H_{\text{sub,M}} - [(1 + f_r) \gamma_{\text{M}} - E_{\text{adh}}]/(n_{\text{M}}/A), \quad (5.3)$$

where n_{M}/A is the coverage in moles of metal atoms per unit area of substrate covered by the metal and f_r is the roughness factor of the resulting multilayer metal film. We use here the convention that both $q_{\text{ad,int}}$ and $\Delta H_{\text{sub,M}}$ are positive, and neglected entropy. For metals which don't wet, $q_{\text{ad,int}} < \Delta H_{\text{sub,M}}$ ³³. This approach has also been applied to cases where the metal film is not continuous but instead the deposited metal assumes the form of large 3D particles^{16, 17, 229}. Table 5.2 lists all the values we have determined in this way.

Heats of adsorption of late transition metals on clean oxide single crystal surfaces have also been determined by temperature programmed desorption (TPD) in UHV, in a series of beautiful measurements made by the group of the late D. W. Goodman. We recently discovered that the leading-edge analysis used to analyze their TPD data, while is usually quite valid, fails for these particular types of systems due to the simultaneous increase in particle size with time (due to both sintering and selective removal of the smaller particles by desorption)³. We therefore reanalyzed much of their TPD data to get the heat of adsorption versus coverage for each system³. We then used those heats together with Eq. (5.3) to extract adhesion energies (and equilibrium contact angles, assuming the solid particle shape can be approximated as a

spherical cap to approximate the effect of surface roughness)³. Those results are also listed in Table 5.2. However, we list these values here not as we originally reported them, but instead as upper limits. This is because we originally treated A in Eq. (5.3) as if it were the full area of the oxide support surface. We recognize now that these multilayer metal films could have agglomerated into 3D particles that cover much less than 100% of the oxide during the heating of TPD prior to desorption. This is especially likely to happen on oxides with low adhesion energies. Decreasing A in Eq. (5.3) leads to lower values of E_{adh} , thus the values we reported³ should instead be considered as upper limits.

Combining the adhesion energy data in Tables 5.1 and 5.2 reveals several important trends. As shown in Fig. 5.1, the adhesion energies for different metals on a given oxide (in this case $\alpha\text{-Al}_2\text{O}_3(0001)$) increase nearly linearly with the surface energy of the metal, and with its sublimation energy ($\Delta H_{\text{sub,M}}$) divided by the area per metal atom (approximated here as the atomic volume of the bulk metal, Ω_{M} , to the 2/3 power). The adhesion energies for molten metal drops are larger than for solid particles by 50 to 100 %, but both follow the same trend. We can summarize the results for solids in Fig. 5.1b by the relationship:

$$E_{\text{adh}} = m[(\Delta H_{\text{sub,M}}/N_{\text{A}})/\Omega_{\text{M}}^{2/3}] + b, \quad (5.4)$$

where N_{A} is Avogadro's number. The slope and y -intercept for $\alpha\text{-Al}_2\text{O}_3(0001)$ are $m = 0.15$ and $b = -0.43\text{J/m}^2$, respectively.

The trends in Fig. 5.1 can be easily explained as follows. Both the heat of sublimation and the surface energy of a metal reflect the strength of metal-metal bonding in that pure bulk metal. The same electronic properties that determine the strength with which a metal surface bonds to its own metal atoms also determine to a large extent the strength with which it bonds to other elements, and thus also to oxide surfaces. Similarly, noble gases bond very weakly to

themselves, as reflected in very small sublimation energies and surface energies, and thus they also bond very weakly to all other elements and surfaces. Two important exceptions to such trends are the elements Au, which has relatively high sublimation energy but bonds very weakly to oxygen (as measured by the positive heat of formation of Au oxide ¹), and Pb, which has low sublimation energy but bonds relatively strongly to oxygen (as measured by the large negative heat of formation of Pb oxide ¹). Since the dominant bonding of the metal to the oxide is to the oxygen anions (rather than to the cations, see below), it is surprising how well Au and Pb fit the trends in Fig. 5.1.

Figure 5.2a shows the same type plot as Fig. 5.1, but now only using the E_{adh} values from Table 5.2 for different metals measured on clean MgO(100) under UHV conditions, where the oxide surface was proven to be clean. The fit for these clean-surface data is very poor (correlation coefficient = $R^2 = 0.49$). Note that the points for metals with high heat of oxide formation (Pb and Cu) fall left of this line, and those with low heats of oxide formation (Au and Ag) fall to its right.

Several other models have been offered to explain trends in metal / oxide adhesion energies ^{4, 220, 225, 226, 231, 249, 419}. We suggested earlier that the adhesion energy on a given oxide correlates better with the sum of the magnitudes of the metal's heat of sublimation plus the standard heat of formation of the most stable bulk oxide of that metal (per mole of metal atoms), $\Delta H_{f,MOx}$ ²³¹, which followed a similar suggestion by Chatain's group, where they used the enthalpy of formation of the alloy of the metal with the metal of the oxide support instead of the metal's heat of sublimation ^{220, 222, 223, 225}. In Fig. 5.2b, we have reanalyzed the same data from Table 5.2 for E_{adh} of different metals measured on clean MgO(100) in UHV based on our earlier correlation with $\Delta H_{sub,M} - \Delta H_{f,MOx}$ ²³¹, but now also dividing that by $\Omega_M^{2/3}$, as was done in

Fig. 5.1 and 5.2a. As can be seen, the correlation for MgO(100) improves markedly if we add $\Delta H_{f,MOx}$ per mol metal to $\Delta H_{sub,M}$ on the x -axis. These UHV data for MgO(100) are well fitted with the equation:

$$E_{adh} = m[(\Delta H_{sub,M} - \Delta H_{f,MOx})/N_A]/\Omega_M^{2/3} + b, \quad (5.5)$$

where $m = 0.14$ and $b = -0.56 \text{ J/m}^2$ (R^2 of 0.88). This quantity $\Delta H_{sub,M} - \Delta H_{f,MOx}$ equals the heat of formation of the metal's most stable oxide from a metal gas atom plus $O_2(g)$, so it more directly reflects the strength of the chemical bonds which each metal can make to oxygen. Obviously, this is a better way to estimate how strongly different metal surfaces can bond to the oxygen anions on the surface of an oxide like MgO than $\Delta H_{sub,M}$ alone. Again, the denominator on this axis ($\Omega_M^{2/3}$) simply normalizes this energy to the number of metal atoms per unit area, as before.

Unfortunately, replotting the non-UHV data of Fig. 5.1 for $\alpha\text{-Al}_2\text{O}_3(0001)$ using this new x -axis of Fig. 5.2b results in a poorer fit ($R^2 = 0.24$ for the liquid points, versus 0.81 in Fig. 5.1b). These non-UHV points are less reliable since these surfaces could easily have surface impurities covering a large fraction of the surface, which were proven to be absent on the UHV points using surface spectroscopies. So we believe that the correlation in Eq. (5.5) and Fig. 5.2b is more accurate than that in Figs. 5.1 and 5.2a.

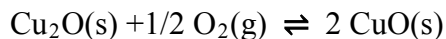
Figure 5.3 shows how the adhesion energy for a given metal varies from oxide to oxide. We have plotted these adhesion energies versus the heat of formation of the oxide support per mole of oxygen ($\Delta H_{f,OxSup}$), as suggested by earlier correlations of more limited data with this parameter^{4, 231}. The points for liquid Ni, Fe and Co are combined into a single line since, according to Fig. 5.1, these three metals should have about the same adhesion energy to any given oxide, as indeed is observed here. As seen, E_{adh} for a given metal (or similar group of

metals like Fe/Ni/Co) correlates almost linearly with $-\Delta H_{f,OxSup}$. As $-\Delta H_{f,OxSup}$ decreases (i.e., for oxides where the oxygen in the oxide lattice is less stable), the adhesion energy increases. This linear increase continues only up to a point, since E_{adh} must saturate at $2\gamma_M$. This is its maximum possible value since complete wetting occurs when E_{adh} reaches $2\gamma_M$ ³³.

To clarify the above discussion, we should point out that deciding which oxide of a given metal is more stable depends upon which perspective is being considered: the stability of the oxygen atoms or that of the metal atoms in that oxide. Consider the case of Cu oxides. The equilibrium



defines the stability and reactivity of O in these two oxides. If you have only a small amount of O, in which oxide form is it most stable? The answer is: the one with highest $-\Delta H_{f,ox}$ per mol O, which in this case is Cu_2O . (Actually, one should really compare free energies of formation, but we will neglect entropic differences here.) On the other hand, the equilibrium



defines the relative metal stability and reactivity of the metal in the oxides. If you have only a small amount of Cu in excess O_2 , in which form does Cu prefer to be? In this case the answer is: the one with highest $-\Delta H_{f,ox}$ per mol Cu, which is CuO instead. Choosing the most stable oxide depends on which perspective you are taking: that of the O stability/reactivity (as, for example, desired in Fig. 5.3 where the x -axis approximates the reactivity of the O on the surfaces of different oxides), or that of the metal stability/reactivity (like Fig. 5.2b, where the x -axis approximates instead the reactivity of different metals toward the same oxide lattice).

To explain this increase in adhesion energy with the decreasing magnitude of the heat of formation (or stability) of the oxide seen in Fig. 5.3, we will again use the principle of chemical

potential mentioned above. Note that the oxide substrates with the least negative heats of formation per mole of O (i.e., those on the far left in Fig. 5.3), have the highest chemical potential of oxygen atoms in their oxide lattice (and in their surfaces). We assume that the dominant contribution to the bonding between the metal surface and the surface of the oxide lattice is from the bonds of the metal atoms to the oxygen anions of the oxide surface, and not to the lattice anions. This is based on the fact that DFT calculations generally prove that late transition metal adatoms on stoichiometric oxide terraces prefer to bind to oxygen anions rather than cations (see, for example, ^{33, 333, 420}). We also recognize that the higher the chemical potential of the surface oxygen atoms in an oxide lattice, the more strongly these atoms can bond to the metal atoms of a metal surface to which it attaches. That is, the more weakly a surface oxygen ion is bound to its neighboring cations within the oxide lattice, the more strongly it can bond to a metal atom or metal particle that approaches its surface.

We see very different slopes for the different metals (and simultaneously different methods) in Fig. 5.3. We have no explanation for this, but the data for solids and clean surfaces are still very limited.

If we look only at the data in Table 5.2, which are from UHV studies on surfaces that were verifiably clean, and compare E_{adh} on pairs of oxides for the same metal, we get the following order of increasing adhesion energy:

$$\text{MgO}(100) \approx \text{TiO}_2(110) \leq \alpha\text{-Al}_2\text{O}_3(0001) < \text{CeO}_{2-x}(111) \leq \text{Fe}_3\text{O}_4(111). \quad (5.6)$$

According to the general trend from liquid metals that E_{adh} should decrease with $-\Delta H_{\text{f,OxSup}}$ in Fig. 5.3, this order should be: $\text{MgO} < \text{Al}_2\text{O}_3 < \text{CeO}_2 < \text{TiO}_2 \leq \text{SiO}_2 < \text{Fe}_3\text{O}_4$, which is the same as Eq. (5.6) for those five oxides except for $\text{TiO}_2(110)$, which binds more weakly than expected. Thus, this general trend in Fig. 5.3 should not be used too rigorously, especially since E_{adh}

should also depend sensitively on the crystal face of the oxide. This illustrates that there seem to be other factors besides $\Delta H_{f,OxSup}$ that determine the differences between E_{adh} for different oxide surfaces. Differences between oxides, and even between different faces of the same oxide, in the ability of surface oxygen atoms to stabilize the system by rearranging their bonding to nearby cations after the oxide surface is created, will also determine the chemical potential of the surface oxygen atoms. The x -axis in Fig. 5.3 does not take these differences into account.

Since oxygen vacancies are known to accumulate under late transition metal nanoparticles on reducible oxide surfaces³⁴⁶, oxygen vacancies appear to stabilize metal / oxide interfacial bonding. This is also supported by our calorimetric measurements which show that Ag adsorption and adhesion energies on $CeO_{2-x}(111)$ increase with the extent of surface reduction (x)^{14, 17}, and DFT calculations which show that oxygen vacancies stabilize metal adsorption on various oxides^{18, 280, 346, 421, 422}. Thus, the availability and mobility of near-surface oxygen vacancies may also play a role in determining adhesion energies. The increase in Ce^{3+} signal in XPS seen upon Ag adsorption on $CeO_{2-x}(111)$ ^{18, 64} which was not accompanied by any measureable loss of electron density from the Ag⁶⁴, could be due to the Ag-induced segregation of oxygen vacancies to the surface. The well-known availability and fast transport of oxygen ions in ceria could help explain the high adhesion energies of metals to $CeO_{2-x}(111)$.

Surface impurities surely have a large effect on adhesion energies too, so one should also be careful using the adhesion energies from Table 5.1 where the degree of cleanliness was uncertain. We should point out that “clean” oxide surfaces prepared under UHV conditions can vary in atomic-level structure and even composition depending on the details of the recipe used to prepare them. Thus, one must be careful in interpreting the phrase “clean surface” as used here. This means that impurity elements were proven to be below the detection limit of some

surface spectroscopy (generally 1-2% of a monolayer). One should refer to the literature to learn more details about the exact structures of these “clean surfaces.”

Hydroxyls are often present on the surfaces of oxide supports. We found that surface hydroxyls increase the initial heat of adsorption for Cu measured on MgO(100) by 6-17%²³⁰, showing that they stabilize metal / oxide bonding when the metal clusters are smaller than ten atoms. However, this added stability does not persist to high metal coverage, so it appears from those data that the high-coverage integral heat of adsorption goes down with -OH addition. This means that the addition of surface -OH decreases E_{adh} . Other studies have found that hydroxyls stabilize small Au clusters on MgO(100)^{403, 404}.

5.4: The chemical potential of metal atoms in nanoparticles increases quickly with decreasing particle size below 6 nm, but less quickly on “strong” supports

We have previously reported measurements by single crystal adsorption calorimetry (SCAC) of the heats of adsorption of several metal atoms (Ag, Cu, Ca, Li, and Pb) onto clean and ordered single crystal surfaces of several different oxides, including MgO(100), CeO₂(111), Fe₃O₄(111), and the p(2x1) oxide film on Mo(100)^{2, 11-17, 29, 81, 229-233}, as well as onto a clean but disordered oxide films on W(100)⁷⁹. Figure 5.4 shows the heat versus coverage data for several of these systems of most interest here. Heats are converted here to standard enthalpies of adsorption, ΔH_{ad}^0 , at the stated temperature. (“Standard” means 1 bar gas pressure, with ΔH_{ad} independent of pressure below 1 bar.)

For metals from the right side of the periodic table, the heat of adsorption starts low on these oxides and increases with coverage to eventually equal the bulk heat of sublimation, as seen for all the cases in Fig. 5.4. When such metals are vapor deposited onto single crystal

surfaces of the types of oxides used as supports for metal catalysts, they typically grow as 3D clusters rather than wetting the surface³³. The number of clusters per unit area grows initially with coverage, but usually saturates after a few percent of a monolayer (ML). With further increasing coverage, these clusters grow in size at nearly fixed number density until the particles grow together and coalesce^{33, 246}. For the systems in Fig. 5.4, this saturation cluster density is expected to have been reached already after the first pulse with the fluxes used (~0.02 ML/pulse). A variety of observations support the conclusion that isolated adatoms of metals like Ag, Cu and Pd on such oxides are highly mobile at room temperature, and diffuse rapidly from site to site across the oxide until finding a growing metal cluster⁴¹⁹. The increase in heat with coverage in Fig. 5.4 is then dominated by the increasing number of metal-metal bonds that are formed upon adsorption as the cluster size grows: The fourth atom that adds to a trimer can make 3 metal-metal bonds at most, whereas a metal atom that adds to a kink site on an extended metal surface of an FCC(111) or HCP(0001) metal makes six metal-metal bonds, giving twice the heat of adsorption in the simplest pairwise bond additivity model whereby these metal-metal bonds have the same energy independent of size, and only nearest-neighbor bonding is significant. The final heat saturates at the bulk heat of sublimation of the metal, as expected for metal atoms adsorbing on an extended metal surface (or the surface of a very large metal nanoparticle).

However, there are subtle differences in heat of metal adsorption versus coverage between different supports that arise from the differences in the bond energies (adhesion energies) between a given metal and the different oxide surfaces. Indeed, these are exactly the types of heat of adsorption versus coverage data that were integrated to obtain the adhesion energies summarized in the SCAC entries in Table 5.2 above.

To separate out the effects of metal particle size from the effect of the support oxide on the heats of adsorption such as those in Fig. 5.4, it is better to plot these heats of adsorption versus the average metal particle size at each coverage instead of directly versus coverage. We have done this for a variety of systems, by estimating the average particle size versus coverage from various spectroscopic measurements (XPS, AES and LEIS), assuming particles have the shape of hemispherical caps and a fixed number density of particles per unit area¹⁵⁻¹⁷. The data for Ag were summarized previously in Fig. 2.12, where the heat of adsorption is plotted versus the effective particle diameter (a measure of the particle volume, assuming hemispherical shape). As seen, the heat of adsorption increases rapidly with Ag particle size below 6 nm, but then saturates at the heat of sublimation (285 kJ/mol¹ for Ag). This increase with size is dominated by the effect of particle size on the number of metal-metal bonds per atom, as noted above. However, for particles smaller than 6 nm, there are also very important differences between the supports: the heat of adsorption of Ag is much larger for the same particle size on the Fe₃O₄(111) and reduced CeO₂(111) surfaces than on MgO(100). This is due to the higher adhesion energy of Ag nanoparticles to Fe₃O₄(111) and CeO_{2-x}(111) than to MgO(100), as summarized in Table 5.2 and discussed already above. Part of the heat of Ag adsorption here comes from the metal / oxide adhesion energy, since the average contact area of the particles on the oxide support also increases with coverage or size. Since these metal particles nucleate mainly at steps^{17, 18, 33}, the stronger bonding at defects also contributes. However, the steps here comprise only ~5% of the surface, so when the particles exceed ~1.5 nm diameter, most of the metal atoms at the metal/oxide interface are bonded to oxide terraces and *not* to ions at the oxide's steps.

Comparing the more reduced CeO_{1.8}(111) surface with CeO_{1.9}(111) in Fig. 2.12 also shows that Ag binds considerably more strongly to Ag clusters smaller than 2 nm when there are more oxygen vacancies present. This increase in stability at surface vacancies is consistent with DFT predictions²⁸⁰. Note too that these oxygen vacancies are expected to be mainly at the step edges on CeO_{2-x}(111)¹⁴.

Neglecting entropy differences, the chemical potential of a metal atom in a particle of diameter D is higher than that in the bulk metal (infinite diameter, which we set to zero as the reference state) by an amount:

$$\mu(D) - \mu(\infty) = \mu(D) = \Delta H_{\text{ad}}(D) + \Delta H_{\text{sub,M}}, \quad (5.7)$$

where $\Delta H_{\text{ad}}(D)$ is the differential enthalpy of adsorption at that particle diameter. Thus, the heats in Fig 2.12, when added to $\Delta H_{\text{sub,M}}$ directly, equal this chemical potential $\mu(D)$. These data have been replotted in this format in Fig. 5.5, to more directly reflect $\mu(D)$.

Anchored metal nanoparticles frequently sinter or coarsen with time during use, starting from a collection of many small, highly dispersed nanoparticles and eventually converting to their thermodynamically-preferred state: fewer, larger particles^{33, 250, 255, 259, 262, 263, 270}. The value $\mu(D)$ directly measures the thermodynamic driving force for such sintering. As seen in Fig. 5.5, it is large at small D and drops to zero as $-\Delta H_{\text{ad}}(D)$ approaches $\Delta H_{\text{sub,M}}$. This approach to $\Delta H_{\text{sub,M}}$ occurs at much smaller particle size on Fe₃O₄(111) and reduced CeO₂(111) surfaces than on MgO(100). Thus, the driving force for sintering disappears at much smaller particle size for Ag on Fe₃O₄(111) and CeO_{2-x}(111) surfaces than on MgO(100). This is entirely attributable to the much larger adhesion energies of Ag to these surfaces than to MgO(100), discussed above. Clearly, sintering should be slower for small Ag nanoparticles on CeO_{2-x} and Fe₃O₄(111) surfaces than on MgO(100) if the rate accelerates with the thermodynamic driving force as

expected. Indeed, rate equations derived based on microkinetic models of sintering mechanisms show that the quantity $\mu(D)$ enters the expression for the rate of sintering quite directly as a negative contribution to the apparent activation energy^{15, 252, 267, 271, 419}. This is true whether sintering occurs mainly via the Ostwald ripening mechanism, or instead via particle diffusion/coalescence. Thus, sintering must be much slower on CeO_{2-x} and Fe₃O₄(111) surfaces than on MgO(100). Indeed, it has been reported that ceria is a more sinter-resistant support for late transition metals than other oxides^{278, 279}. This is also consistent with our scanning tunneling microscopy (STM) and non-contact atomic force microscopy (nc-AFM) results which showed that Pd nanoparticles sinter far more rapidly on α -Al₂O₃(0001)⁴²³ than on CeO_{2-x}(111)⁴¹⁹.

In summary, the chemical potential of metal atoms in a nanoparticle of effective diameter D , $\mu(D)$, increases very quickly with decreasing particle size below ~ 6 nm. Exactly how quickly $\mu(D)$ increases with decreasing D depends on the support. This occurs much more quickly for “weak” supports like MgO(100) (i.e., ones that have a low adhesion energy to the metal particle) than for “strong” supports like CeO_{2-x}(111) or Fe₃O₄(111) (which have large adhesion energies to the particles).

The metal particle shape should also affect the metal chemical potential, since different facets have quite different surface energies⁵, and the product of these energies times the area of each facet add to the total free energy of the particle and its derivative with size. In general, one would expect that comparing two particles of the same volume and area of attachment to the same support, the shape with the larger fraction of higher-energy facets will have the higher metal chemical potential. To our knowledge, there are no experimental measurements to support this prediction.

5.5: Increasing the chemical potential of surface metal atoms by decreasing particle size or anchoring them to a “weaker” support increases the strength with which they bond adsorbed catalytic intermediates

We next show that the reactivity of a metal atom in a supported metal nanoparticle correlates with the chemical potential of that metal atom. In general, the higher the chemical potential of an atom, the more strongly it can bond to a new neighbor. A common example of this is found in organic chemistry, where the strength with which C atoms bind to other C atoms is known to depend on the energetic stability of the C atoms involved: Relative to the elements in their standard states (solid graphite and H₂ gas), the standard enthalpy of formation per mole C of -CH_x species increases in the order -CH₃ < -CH₂ < -CH^{321, 424}. Consequently, if two of each of these species is bonded together at their C atoms, the resulting C-C bond energy increases in this same order, in this case rather dramatically, from 380 to 730 to 970 kJ/mol as the number of H atoms on each of these two C atoms decreases from 3 (ethane) to 2 (ethene) to 1 (ethyne). Note that this occurs while the total bond order for each of the two C atoms remains fixed at 4. Similarly, a common trend in organometallic chemistry is that the reactivity of a metal center increases as its “degree of coordinative unsaturation” increases: the higher the degree of coordinative unsaturation of an atom, the higher its energy and the more strongly can it bond to other species. The simple bond energy - bond order (BEBO) conservation model⁴²⁵⁻⁴²⁷ quantified this qualitative trend and even proved accurate in estimating activation energies for gas-phase organic reactions⁴²⁵.

Extending this qualitative picture to metal atoms in catalytic surfaces leads to the following prediction: the more weakly a surface metal atom is bound to the surface of a catalytic material (i.e., the higher its chemical potential), the more strongly that metal atom is expected to

covalently chemisorb small molecules. This is consistent with the well-known trend that low-coordination metal atoms at steps on metal surfaces bind small molecules more strongly than do more stable metal atoms in higher-coordination environments such as in close-packed terraces. The same effect is commonly seen in bimetallic surfaces, but going in the opposite direction when the metal atoms have lower chemical potential on the bimetallic surface than on a pure metal surface of the same element. For example, when a metal atom resides in a monolayer supported on some other metal to which it binds more strongly than to itself (i.e., when its chemical potential is lower than on the surface of the pure metal), as, for example, in Pd monolayers on Ta(110), Nb(110), Re(0001) and W(110), it binds small molecules like CO more weakly, often dramatically so⁴²⁸.

Since surface metal atoms on a given support are bound more weakly to smaller metal nanoparticles than to large metal particles in the size range below 4 nm (Fig. 2.12), and have lower coordination number there, they have higher chemical potential on the smaller particles. Thus, one expects metal atoms in the smaller metal particles to bind small adsorbed catalytic reaction intermediates more strongly than larger particles, for a given support. Consistent with this are numerous cases for which CO has been reported to bind more strongly to smaller particles of late transition metals in this size range, as we summarized previously³³, including Pt on bulk α -Al₂O₃(000), Pt on a highly ordered thin alumina film on NiAl(110), Cu on ZnO(000-1)-O, Pt on ZnO(000-1)-O, Pt on ZnO(0001)-Zn, and Pd on MgO(100). Similarly, adsorbed NO shows greater dissociation probability on smaller supported nanoparticles of Pt, Pd and Rh³³. Also consistent with this model, the desorption activation energies for O adatoms on Au nanoparticles on TiO₂(110) to produce O₂ gas are ~50 kJ/mol O₂ larger from the smallest Au particles (which were only 1.3 layers thick, on average) compared to the largest particles (which

resemble step sites on bulk Au(211)). This 50 kJ per mol O₂ difference implies that O adatoms are at least 25 kJ/mol more stable on the smallest Au particles than on bulk Au^{16, 429}.

However, the calorimetrically measured heats of adsorption we reported for CO on Pd nanoparticles on Fe₃O₄(111) go in the opposite direction with particle size. The initial heat of adsorption increased by almost 30 kJ/mol as the particle size increased from 2 to 4 nm, with the particle sizes characterized by STM^{430, 431}. In marked contrast, the initial heat of adsorption (desorption activation energy) decreased by 33 kJ/mol as Pd particle size increased from 2 to 5 nm on MgO(100)⁴³². The only way to explain these apparently contradictory results, whereby the strength of bonding to CO changes by ~25% with particle size in the same size range but in opposite directions, is to attribute it to differences in the way the Pd particles interact with the two different supports used here: Fe₃O₄(111) and MgO(100). Indeed, the chemical potential concept can again explain at least the qualitative difference between these supports. As shown in Fig. 5.3, metal particles have much higher adhesion energies to Fe₃O₄(111) (which is on the far left side of this figure) than on MgO(100) (which is on the far right). Thus, the chemical potential of a Pd atom in a 2 nm Pd particle on Fe₃O₄(111) will be much lower than for that same particle on MgO(100). As shown in Fig. 5.5, the chemical potential of Ag atoms is lower by ~50 kJ/mol for 2 nm Ag particles on Fe₃O₄(111) than for that same size particle on MgO(100). Indeed, the chemical potential of Ag atoms in 2 nm Ag particles on Fe₃O₄(111) is so low it is already within 20 kJ/mol of the bulk metal, whereas on MgO(100) it is still 70 kJ/mol higher than bulk Ag(s). If this difference in chemical potential for 2 nm Ag also applies to 2 nm Pd, at least qualitatively as expected, it explains why the 2 nm Pd particle bonds CO much more strongly when on MgO(100) than on Fe₃O₄(111). This does not, however, explain why the trend with size goes in the opposite direction on Fe₃O₄(111) from what would be expected based on

the size dependence summarized above, which should apply to any support. It has been suggested that this might be connected to a weakening of the chemisorptive interaction due to the contraction of the lattice parameter of the Pd particle with decreasing size. Such lattice contractions, however, only partially reduce the effect of particle size on metal atom chemical potential (as obvious in Fig. 5.5), so that this effect is unlikely to be large enough to explain the complete *reversal* in the trend of CO adsorption energy with particle size observed. The size range where this change in CO stability was observed (2 to 4 nm) also seems to be too large for this type of effect⁴³³. Some other effect is likely at work here, which has yet to be identified. Perhaps the 2 nm Pd particles absorb a tiny amount of Fe or FeO_x, which could be too small to distinguish from the large signal for the Fe₃O₄(111) support in surface spectroscopies, but still in sufficient quantity to weaken the Pd bond strength to CO.

In any case, it seems that this concept of metal atom chemical potential will also prove to be useful for predicting how chemisorption bond strengths depend on the support material for a given particle size of late transition metal. That is, for a given particle size below 6 nm, metal atoms are much less stable on a “weak” support like MgO(100) than on “strong” supports like CeO₂(111) and Fe₃O₄(111). Thus, they are predicted to bind small adsorbates more strongly. They should also reach the large-particle limit in this respect at smaller particle sizes when on “strong” supports than when on “weak” supports.

The discussion above is related to small adsorbates like O, CO and NO on later transition metal particles, where the chemical bonds are rather strong and dominated by their covalent character. When the adsorbate is only held to the surface by van der Waals interactions, the trend with particle size mentioned above may not hold. That is because larger metal particles are more polarizable, and thus are likely to make stronger van der Waals bonds to adsorbates. Indeed,

methane has been shown to bind more strongly to larger Pd particles when supported on a highly ordered but few-atomic-layer-thick alumina film on NiAl(110), and this trend continues to rather large sizes (above 7 nm)⁴³⁴.

5.6: Figures

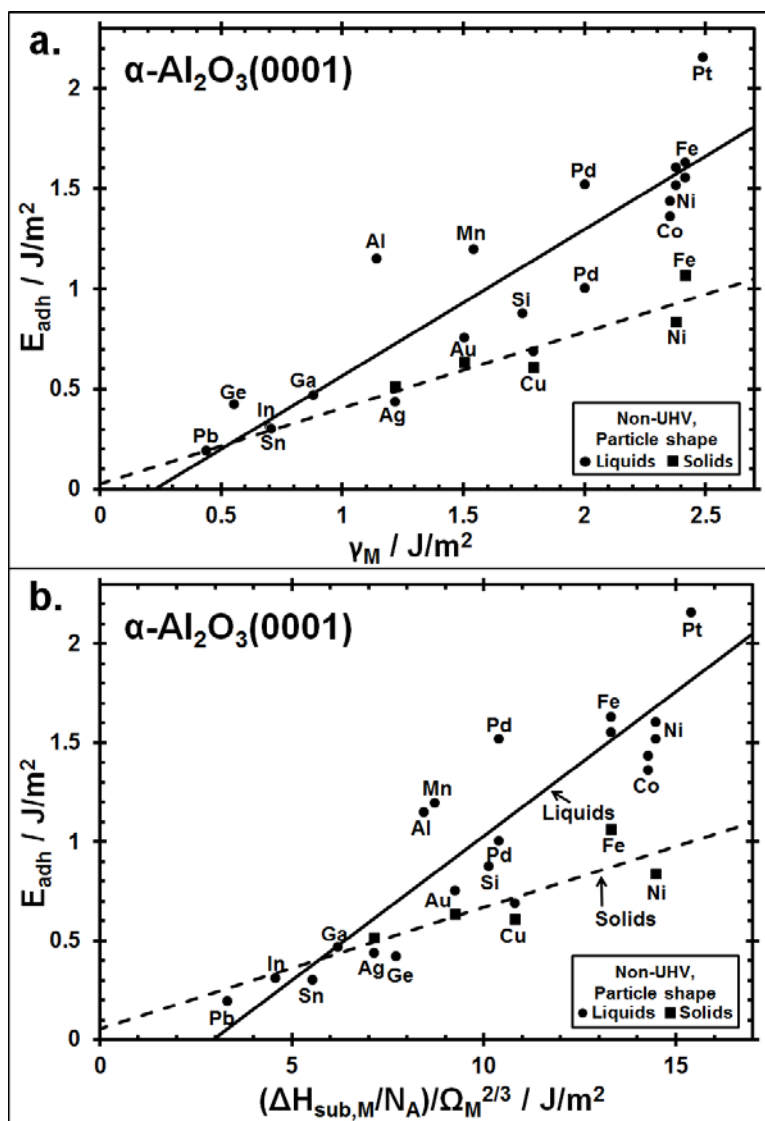


Figure 5.1. Adhesion energies of different metals on $\alpha-Al_2O_3(0001)$ plotted versus (a) the surface energy of the metal and (b) the bulk metal's sublimation enthalpy per atom ($\Delta H_{sub,M}/N_A$) divided by the area per metal atom ($\Omega_M^{2/3}$) (b). Black points are based on measurements of particle shapes for molten metal drops (round) and solid particles (squares) without verification of surface cleanliness, from Table 5.1. Lines through the subsets of data are the best linear fits. Reprinted with permission from Reference²⁸. Copyright 2013 Royal Society of Chemistry.

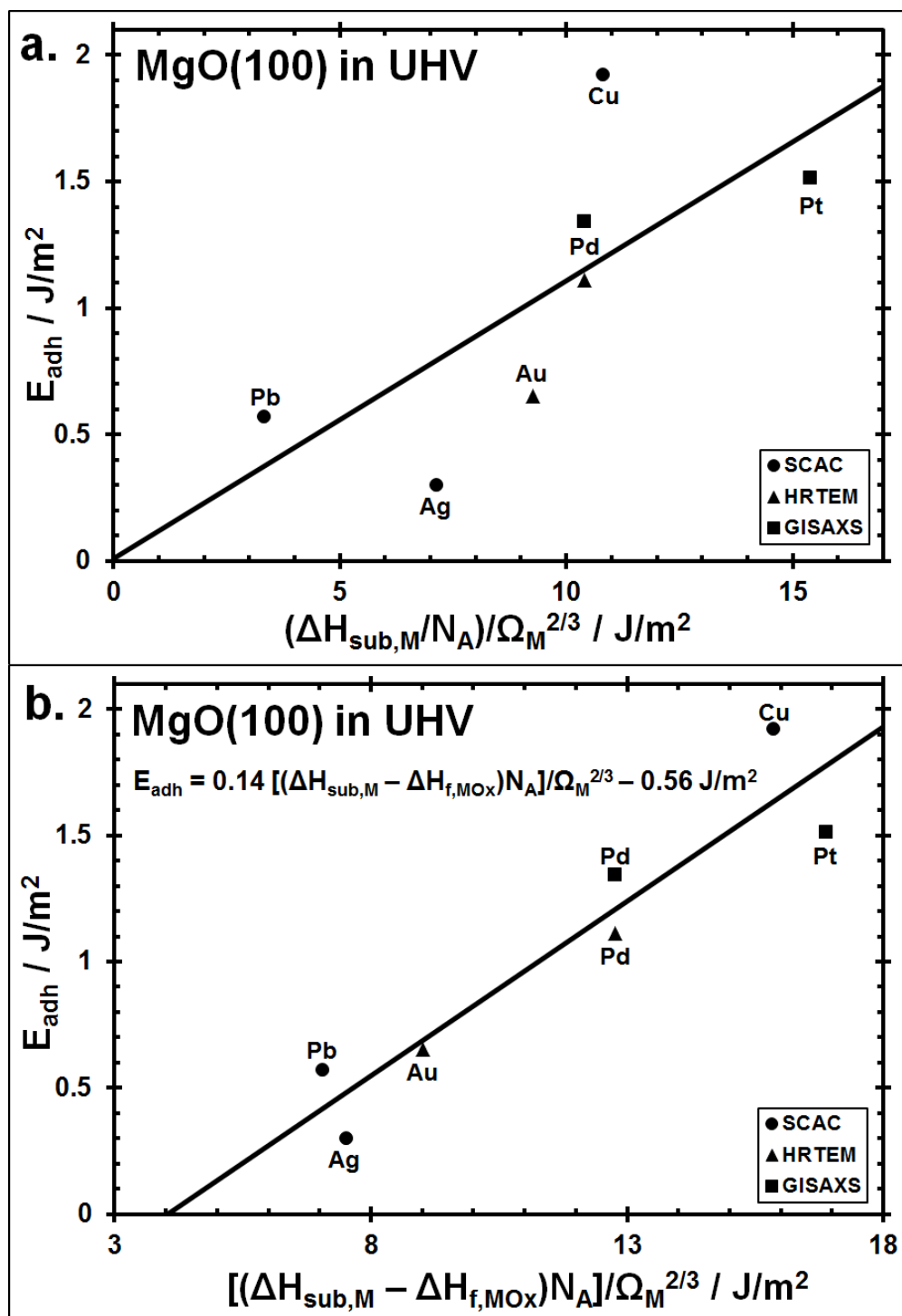


Figure 5.2. Adhesion energies of different metals on clean MgO(100) measured in ultrahigh vacuum (from Table 5.2) plotted versus the bulk metal's value of $[(\Delta H_{\text{sub,M}}/N_A)/\Omega_M^{2/3}]$ (a) and versus $[(\Delta H_{\text{sub,M}} - \Delta H_{\text{f,MOx}})/N_A]/\Omega_M^{2/3}$, where $\Delta H_{\text{f,MOx}}$ is the standard heat of formation of the most stable bulk oxide of that metal (per mole of metal atoms) (b). The best-fit lines are also shown. Different symbols correspond to different measurement methods. Reprinted with permission from Reference²⁸. Copyright 2013 Royal Society of Chemistry.

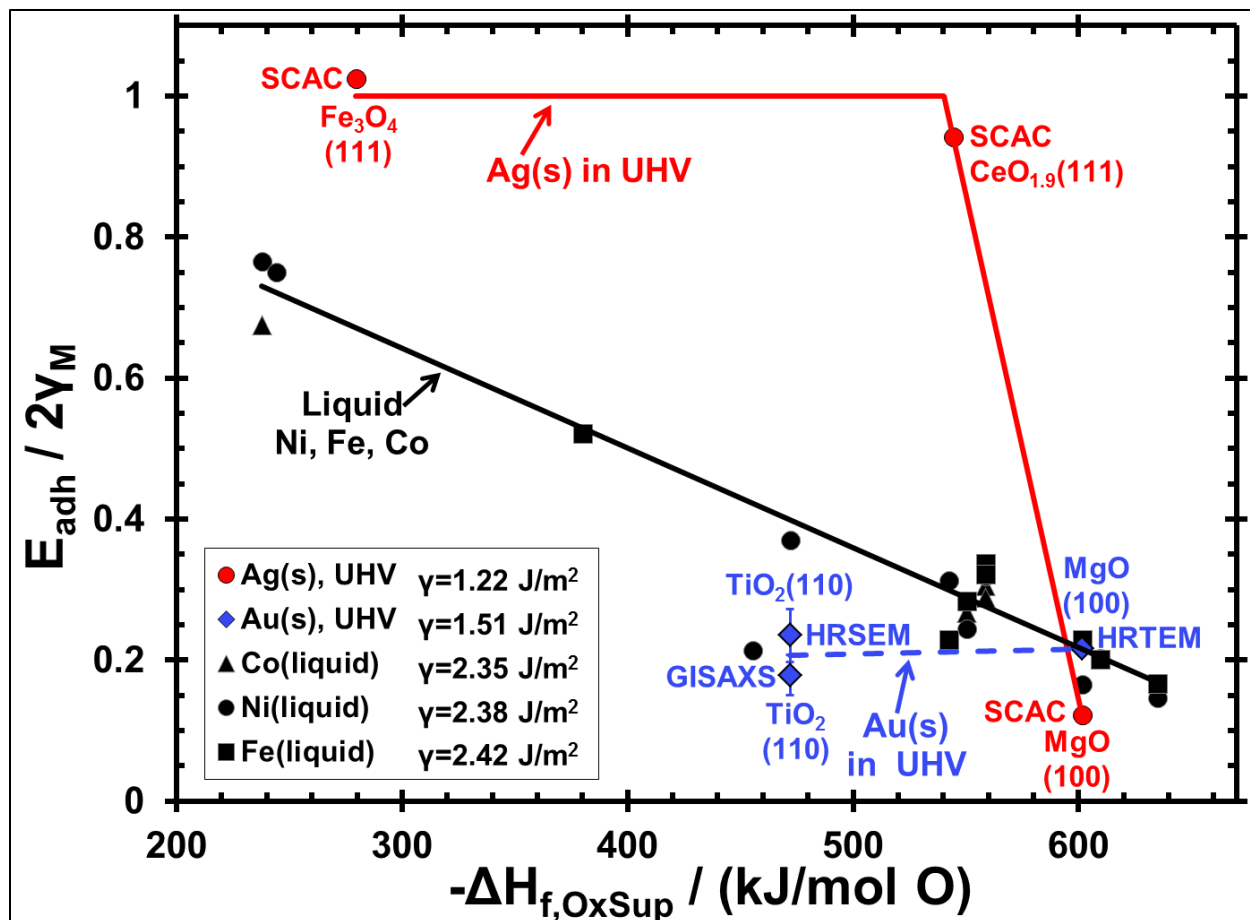


Figure 5.3. Adhesion energies of the same metal (normalized to $2\gamma_M$) on different oxide supports plotted versus the heat of formation of the oxide support per mole of oxygen ($\Delta H_{f,OxSup}$). Different colors of points and lines are for different metals. Black points are for liquid Ni, Fe and Co droplets on oxide surfaces whose cleanliness was not proven, from Table 5.1. These metals are grouped together since they have very similar sublimation energies (and thus appear at nearly the same place on the x-axis of Fig. 5.1). Colored points are for solid metals collected on clean oxide surfaces in UHV, from Table 5.2. Lines through the subsets of data are the best linear fits. Reprinted with permission from Reference ²⁸. Copyright 2013 Royal Society of Chemistry.

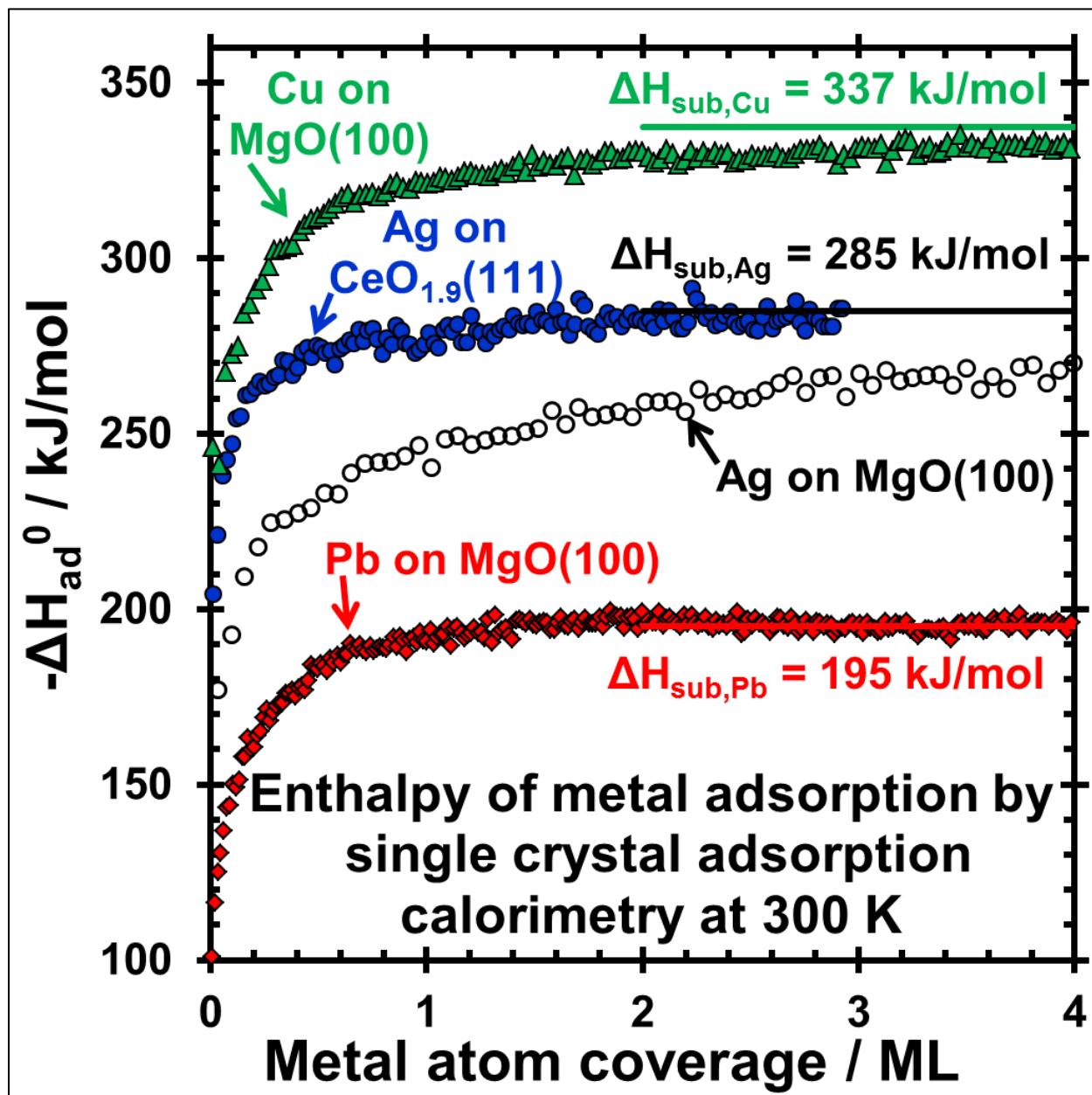


Figure 5.4. Example heats of adsorption versus coverage data for metals on single-crystal oxides as measured by calorimetry at 300 K. Data are shown for: Pb, Ag and Cu on MgO(100) and Ag on CeO₂(111) (with 5% oxygen vacancies in XPS probe depth). Data from References ^{11, 12, 14, 29}. One ML equals the number of oxygen ions per unit area in the topmost atomic plane ($1.12 \times 10^{15} \text{ cm}^{-2}$ for MgO(100) and $7.9 \times 10^{14} \text{ cm}^{-2}$ for CeO₂(111)). Horizontal lines mark the bulk heats of sublimation of the metal adsorbate. Reprinted with permission from Reference ²⁸. Copyright 2013 Royal Society of Chemistry.

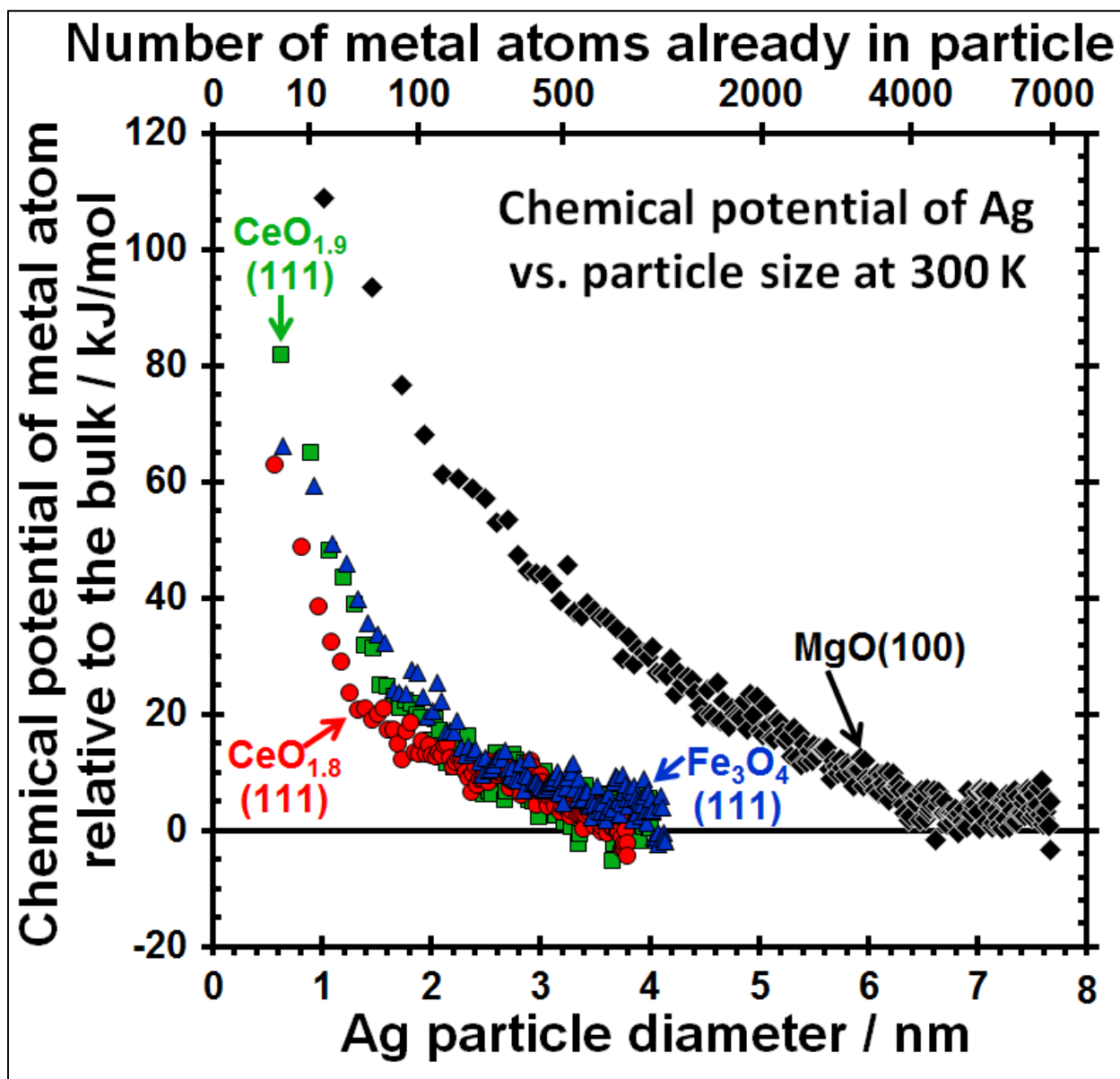


Figure 5.5. The chemical potential of Ag atoms in Ag nanoparticles on different oxide surfaces versus the average Ag particle size. The chemical potential here is estimated by the difference in magnitude between the bulk heat of sublimation of the metal and its differential heat of adsorption on particles of that size (using the data in Fig. 2.12), and neglects entropy differences. Reprinted with permission from Reference²⁸. Copyright 2013 Royal Society of Chemistry.

Chapter 6

Adsorption Calorimetry during Metal Vapor Deposition on Single Crystal Surfaces: Increased Flux, Reduced Optical Radiation, and Real-Time Flux and Reflectivity Measurements

Thin films of metals and other materials are often grown by physical vapor deposition. To understand such processes, it is desirable to measure the adsorption energy of the deposited species as the film grows, especially when grown on single crystal substrates where the structure of the adsorbed species, evolving interface, and thin film are more homogeneous and well-defined in structure. Our group previously described in this journal an adsorption calorimeter capable of such measurements on single-crystal surfaces under the clean conditions of ultrahigh vacuum (UHV)³¹. Here we describe several improvements to that original design that allow for heat measurements with ~18-fold smaller standard deviation, greater absolute accuracy in energy calibration, and, most importantly, measurements of the adsorption of lower-vapor-pressure materials which would have previously been impossible. These improvements are accomplished by: (1) using an electron beam evaporator instead of a Knudsen cell to generate the metal vapor at the source of the pulsed atomic beam, (2) changing the atomic beam design to decrease the relative amount of optical radiation that accompanies evaporation, (3) adding an off-axis quartz crystal microbalance (QCM) for real-time measurement of the flux of the atomic beam during calorimetry experiments, and (4) adding capabilities for *in-situ* relative diffuse optical reflectivity determinations (necessary for heat signal calibration). These improvements are not limited to adsorption calorimetry during metal deposition, but also could be applied to better study film growth of other elements and even molecular adsorbates.

6.1: Introduction

Thin films of metals and other materials are grown by physical vapor deposition for a wide variety of technological applications, for example in the fabrication of microelectronics and computer parts, solar cells, light-emitting diodes, reflective and protective coatings, chemical sensors, and electrodes of various types. Thin films and nanoparticles are also grown by physical vapor deposition for a wide variety of fundamental research applications aimed at studying the properties of surfaces, interfaces, nanoparticles, and nanomaterials. A great deal of basic understanding of the film growth process, the thermodynamic stability of the resulting films or nanoparticles, and the strength of chemical bonding at the resulting interface(s) is provided by measuring the adsorption energy versus coverage during such deposition processes^{15, 17, 31, 79, 435}. The strengths of chemical bonding at interfaces between materials have a remarkable impact on almost all areas of science, technology, and industrial manufacturing⁴³⁶. The adhesion energy between two solids can also be determined by measuring the adsorption energy versus coverage during vapor deposition⁷⁹, even in cases where the deposited material grows as nanoparticles rather than a continuous film¹². Adhesion energies define the relative stability of the interface, control the mechanical properties of composite materials, and define the shape of supported nanoparticles such as, for example, those used in catalytic or fuel-cell materials consisting of metal nanoparticles supported on high-area oxide or carbon supports³³. In this latter example alone, the adhesion energy also dictates how the chemical potential of the metal atoms depends on the particle size and support material, which in turn controls catalytic reactivity and its deactivation by coarsening or sintering²⁸.

Thus, there is great motivation to measure adsorption energies during physical vapor deposition of one material onto another. Such measurements are particularly enlightening when

performed on the clean surface of a single crystal of the substrate material, since this enables better structural homogeneity and structural characterization of the adsorbed precursors, nanoparticles, and thin films whose energies are being measured ^{2, 44, 437}. We previously described in this journal the first adsorption calorimeter capable of such measurements of metal adsorption energies on single-crystal surfaces in a ultrahigh vacuum (UHV) chamber where the substrate surface cleanliness and the structure of the resulting thin film or nanoparticles could also be measured with surface analysis techniques ³¹. Here we describe a new apparatus that incorporates several major improvements to the capabilities of that original design. These decrease the pulse-to-pulse standard deviation of the metal adsorption energy measurements by ~18-fold, while also improving the absolute accuracy of the energy calibration. Most importantly, these improvements allow for measurements of the adsorption energies of metals which would have been impossible to study with our earlier design, namely metals with very low vapor pressures or high heats of sublimation (e.g., Pt, Pd, Rh, Ni, Au, etc.).

The ability to determine heats of adsorption on clean surfaces of single crystals in UHV is not new. Techniques such as temperature programmed desorption (TPD) and equilibrium adsorption isotherm (EAI) analysis have often been used to measure adsorption properties of atoms and molecules on single crystalline supports. However, with these techniques, heats of adsorption are measured indirectly in a way that requires completely reversible adsorption. In cases where adsorption is not reversible, a technique for directly measuring heats of adsorption is necessary. Single crystal adsorption calorimetry (SCAC) was developed for such cases ⁷¹. This approach is particularly important for studying metal adsorption and metal thin-film growth, since metal adatoms frequently sinter into very large particles or diffuse into the substrate upon heating at temperatures well below those necessary for desorption ^{15, 48}. This was the motivation

for designing the instrument mentioned above for SCAC of metal vapors^{31, 79}. Subsequently, it has been employed to measure the adsorption energies of several metals on a variety of different single crystal surfaces as a thin metal film is grown and the metal / substrate interface is formed^{11-14, 17, 29, 79, 81, 229-233, 438}.

We describe here a new calorimeter for SCAC of metal adsorption energies which offers several important advantages over that previous design. It uses an electron beam evaporator as the metal atom source instead of the Knudsen cell metal evaporator previously used. This localizes the heat input to the surface of the metal melt and produces much less optical radiation than the Knudsen cell type metal vapor source, thereby increasing the signal/noise of the calorimetry measurements. The atomic beam design was also modified to further decrease the relative amount of optical radiation that accompanies evaporation. In addition, an off-axis quartz crystal microbalance (QCM) was added for real-time measurement of the flux of the atomic beam during calorimetry experiments, and optics were added that allow for *in-situ* relative diffuse optical reflectivity determinations (necessary for heat signal calibration).

These improvements allow more sensitive and accurate measurements of metal adsorption energies and the interfacial bonding strengths of a wider variety of metal / support systems. The methods described here are not limited to adsorption calorimetry during metal deposition, but also could be applied to study film growth of other elements and even molecular adsorbates that are relevant not only to heterogeneous catalysis, but also to technologies such as coatings, microelectronics, computers, optoelectronics and solar cells.

6.2: Experimental Details

The principles behind the design of this calorimeter have their basis in the groundbreaking designs from the group of Sir David King^{72, 75, 78}. Their original single crystal adsorption calorimeter (SCAC) design used optical pyrometry to measure the transient temperature rise that occurs upon adsorption of a pulse of gas from a molecular beam onto a ~ 0.2 μm thick single crystal. In a later experiment, the single crystal was fused directly onto a LiTaO_3 crystal, whose pyroelectric properties were used to measure the heat, allowing for improved sensitivity to heat released upon adsorption at low temperature⁷⁸, although this technique was limited since the detector could not tolerate the high temperature annealing that is necessary for creating well-ordered surfaces for many materials. This new calorimeter described here instead uses a pyroelectric ribbon as the heat detector, which we introduced and improved previously^{31, 50-52}, and which has several important advantages over the heat detectors used by King's group.

A general schematic of the new calorimeter can be seen in Fig. 6.1. A thin polyvinylidene fluoride (PVDF) ribbon serves as the heat detecting element of our calorimeters, as described in detail elsewhere^{31, 51}. Briefly, the 9 μm thick ribbon consists of amorphous PVDF in which poled β -PVDF crystals, which are both piezoelectric and pyroelectric, are embedded. When brought into gentle mechanical contact with the back of a sample, the pyroelectric properties of β -PVDF respond to a slight increase in temperature with a measurable change in the face-to-face voltage of the ribbon. This method of heat detection increases the sensitivity by a factor of ~ 100 over detection via optical pyrometry at 300 K. This improvement factor is also estimated to increase as $1/T^3$ with decreasing temperature of the single crystal

(T)⁷¹, thus allowing for routine cryogenic measurement that would have been impossible using optical pyrometry.

The samples are typically 1 μm thick single crystals³¹, although a new method for mounting the ribbons has been developed to allow the use of much thicker crystals⁵¹. When heat is transiently deposited on the face of a 1 μm crystal, as in the experiments described here, ~10% of the energy is transferred to the ribbon. The intimate thermal contact between the sample and the ribbon allows for the heat released from adsorption of a 100 ms pulse of gas to be detected almost instantaneously (i.e., with an instrument response time capable of detecting kinetic delays in heat deposition as short as 10 ms⁴³⁹). The measured calorimetric heat response in these instruments corresponds to the change in internal energy for the adsorption of the hot metal atoms in the beam onto the single crystal at its chosen temperature. The difference in temperature between the gas and the support is accounted for as described previously to give the adsorption energy for the system, with both gas and surface at the crystal's temperature, which is the negative of the internal energy change for adsorption (ΔU_{ad})³¹. Since the ideal gas law holds up to 1 bar, the standard enthalpy of adsorption (ΔH_{ad}) is just RT less than this change in internal energy: $\Delta H_{ad} = \Delta U_{ad} - RT$, where R is the gas constant and T is the temperature of the single crystal³¹. The heat of adsorption is defined here as the negative of this standard adsorption enthalpy. With this setup, we have been able to determine heats of adsorption to within 3% accuracy in most cases and with a point-to-point standard deviation of only 0.6 kJ/mol when depositing 2% of a monolayer per pulse, and a temperature range of 100 to 350 K⁵¹.

The basic design of this new calorimeter is similar to two other calorimeters that have been constructed previously by our group for measuring the heats of adsorption for various systems^{31, 50, 51}. The metal atom adsorption calorimetry, sample preparation, and surface

characterization are all performed in a single UHV system, with a four-axis translator used to manipulate the sample in vacuum.

Surface characterization spectroscopies are performed using a PHI 10-360 precision energy analyzer equipped with a PHI 72-250 position sensitive detector, which is used to measure the kinetic energy distribution of electrons or ions originating from the sample surface after irradiation by an electron beam for Auger electron spectroscopy (AES), an x-ray beam for x-ray photoelectron spectroscopy (XPS), or an ion beam for low energy ion scattering spectroscopy (LEIS). This combination of techniques provides detailed information on the surface structure, with XPS or AES analysis providing information on the elemental composition of a surface down to ~ 3 nm from the surface, and LEIS providing the elemental composition of the top-most atomic layer. The chamber is also equipped with a low-energy electron diffraction (LEED) screen, which allows for verification of the crystallinity of the sample and any thin film grown on its surface. The instrument also includes a sample preparation chamber that can be closed off with a gate valve during preparation of the single crystal's surface in order to protect the UHV conditions in the calorimeter and surface analysis region.

The most significant improvement in this calorimeter involves the method for generating the pulsed atomic beam of metal atoms. The SCAC measurements require a very high flux from a source located far from the sample in order to reduce optical radiation from the oven. Typical fluxes are 4×10^{14} atoms/cm²/s at the sample, which corresponds to $>4 \times 10^{17}$ atoms/cm²/s at the source located 353 mm away (if we approximate the source as a 15 mm diameter sphere). The original metal atom adsorption microcalorimeter design uses a Knudsen cell type thermal evaporator as the metal adatom source³¹. In the Knudsen cell, the entire metal crucible is heated to the temperature required to evaporate or sublimate the metal of interest. This system has been

used successfully to study the heats of adsorption of Li ²³², Ca ¹³, Pb ^{81, 438}, Ag ¹², and Cu ²⁹. However, heating this large element to the high temperatures (upwards of 1660 K for Cu) required for the very high fluxes necessary in our calorimetry experiments produced too much background radiation that also contributes to the measured heat signal, and it therefore proved unsuitable for studying metals with larger enthalpies of vaporization than that of Cu. The excessive heat load from the Knudsen cell also causes problems with background pressure increase for such metals, which can give rise to surface impurities.

To overcome this issue, we have instead used a Thermionics 150-0010 crucible-fed electron beam evaporator as the source for the metal atom beam. Its 4 kV electrons are focused directly onto the surface of the metal to be evaporated, thereby localizing the heating to the metal itself. The metal to be evaporated is electrically grounded so that there is no difference in potential between the metal source and the single crystal, thus preventing acceleration of any charged species from the source to the sample. We found that electron beam evaporation allows for a significant flux of evaporated metals with a significant reduction in the heat and source radiation output when compared to a traditional Knudsen cell, and therefore will allow us to use this new calorimeter with metals such as Pt, Pd, Rh, Ni, and Au. This also results in lower background pressures at higher evaporation temperatures for any metal, thus decreasing surface contamination.

The evaporated metal atoms are used to create a temporally- and spatially-resolved pulsed atomic beam by passing them through a chopper and a series of collimating apertures. The metal atom beam is typically chopped into 100 ms pulses at a rate of 0.5 Hz, although both the duration of each pulse and the time between pulses can be varied. The spatial distribution of the metal atom beam is defined by two apertures. The first 4.00 mm diameter beam-defining

aperture is located 33.4 mm from the lip of the crucible, with the metal melt estimated as being an additional 3 mm further from the aperture. A second beam-defining 4.00 mm aperture is located 295.9 mm further downstream from the first aperture, and is positioned 19.2 mm from the sample surface. This geometry results in a circular deposition area with ~89% of the metal atoms deposited within an umbra of 4.00 mm in diameter. Line of sight calculations were used to determine that the resulting spot has an outer penumbra with a diameter of 4.52 mm. Images of white light projected down the beam path accurately reproduce the ratio between the umbra and the outer penumbra. Assuming a linear gradient in the deposition thickness versus radius beyond the umbra gives an effective beam diameter of 4.26 mm and an effective deposition area of 14.3 mm² for a square beam profile of the same intensity as in the umbra and with the same area-integrated intensity as the entire real beam spot.

The flux of the metal atom beam is measured using a quartz crystal microbalance (QCM) that is positioned in front of the sample. A UTI 100C quadrupole mass spectrometer (QMS) in line-of-sight to the sample provides a signal that is proportional to the number of metal atoms reflected from the surface and can be used to determine the fraction of atoms in each pulse that stick to the surface using a modified King and Well's method⁴⁴⁰. The QMS ion source is located at the "magic angle" of $\theta = 35^\circ$ from the surface normal in order to minimize deviations in signal due to changes in the angular distribution of the atoms leaving the surface³¹. The sticking probability of each pulse is measured simultaneously with its heat. A heated Ta flag is placed in the sample position before or after these measurements to record the QMS signal associated with zero sticking probability (100% reflected), and with this information we can determine the fractional sticking probability of the gaseous atoms in each pulse. Multiplying this

sticking probability by the metal atom flux gives the incremental increase in surface coverage associated with that pulse. The details of this analysis have been presented previously⁵⁰.

The voltage response of the PVDF ribbon to the applied energy is calibrated using a stabilized HeNe laser that is first diffused with a lens and then directed along the atomic beam path using a translatable mirror. By passing the laser through the same apertures and choppers as the atomic beam, the calibration pulse reaches the sample with the same spatial and temporal distribution as that of the atomic beam pulse. The laser power at the sample position is determined by positioning a mirror in front of the sample that reflects the beam through a quartz window equipped with a power meter. This measured value is scaled using a previously determined linear relationship between the laser power at the window and the laser power at the sample position. Using this method, the voltage response of the ribbon to transient energy changes can be calibrated directly before each experiment. The heat detector's response intensity is proportional to laser pulse energy over the range of deposited energies used in our experiments³¹.

The evaporation sources used in our metal atom beams heat the metal to a temperature at which sublimation or evaporation occurs rapidly. The optical radiation from these hot sources is included with each pulse, and its contribution to the heat signal must be measured and subtracted. This is accomplished using a BaF₂ window, which can be translated into the atomic beam path. The window blocks all metal flux, but is >90% transparent to photons between 300 nm and 9.5 μm in wavelength⁴⁴¹. The heat signal from the HeNe laser passing through this window is periodically measured in order to determine its exact transparency, which decreases with use over its lifetime. Thus, the heat signal due to optical radiation from the source is measured using this BaF₂ window, corrected for transparency, and subtracted from the total heat

signal, to determine the portion of the signal that corresponds to the actual heat of metal atom adsorption, as described previously³¹.

Both the thermal reservoir of the calorimeter and the sample manipulator fork are plumbed with internal tubes for carrying gaseous or liquid nitrogen at controlled temperature, which are used to either cool or warm these parts during experiments, as described previously⁵¹. In brief, two streams of heated or cooled gases are mixed in various ratios and flowed through these lines, allowing us to perform calorimetry experiments over a wide range of temperatures. Similar setups on our other calorimeters have enabled effective measurements of heats of adsorption on surfaces at any temperature between 100 and 300 K⁵¹. In principle, hot water could also be used to heat our thermal reservoirs, allowing for stable sample temperatures between 77 and 350 K⁵¹. Since surface mobility of adsorbed metal atoms decreases with temperature, metal atoms deposited at lower temperatures will grow as smaller, more dispersed nanoparticles. Performing these calorimetry experiments over a large range of temperatures will allow us to determine the effect that particle size has on heats of adsorption. The relationship of surface dispersion and particle size to energetic stability and reactivity are extremely important for understanding heterogeneous catalytic applications of nanoparticulate metals.

6.3: Real-time Flux Determination in the Metal Atom Beam

In order to analyze the calorimetry data, the flux of the metal atoms colliding with the sample surface must be known at all times. In previous calorimeter designs for SCAC, this was accomplished by measuring the flux before and after the experiment to prove that it had been stable during the calorimetry measurements^{31, 50, 71}. However, this requires a stable beam flux, which is more difficult to accomplish with metals with high vaporization enthalpies, as desired

here. In other groups, stabilization of the metal flux of an e-beam evaporator has been accomplished by controlling the e-beam emission current with feedback loops which monitor either the ion current associated with the $\sim 1\%$ of metal atoms that are ionized in by the e-beam evaporator of the atomic beam^{442, 443} or the atomic adsorption spectrum of the metal atoms in the beam⁴⁴⁴. This new system was originally set up with a rod-fed e-beam evaporation source. Attempts were made to stabilize this source using the ion current, but it was found that, with the high fluxes required, sudden changes in the shape of the tip of the rod caused large instabilities in the flux which could not be overcome. To minimize the effects of the changing shape of the metal source on the flux, we switched to the crucible-fed evaporator described above.

An off-axis QCM was installed so that the flux of the source can be monitored at all times during the calorimetry experiments. This monitor QCM was installed 225 mm from the metal source (compared to 353 mm to the sample) at a 70° angle from the atomic beam path to the sample. This QCM head was mounted directly onto a cooled 4.5" conflat flange to reduce its temperature drift and fluctuation. Using a QCM to stabilize the flux of an e-beam evaporator is a well-established practice⁴⁴⁵, but in our system the ratio between the flux at the sample position and the flux at the monitor QCM was found to increase as the flux decreases over time when the evaporator is run at constant emission current, as can be seen in Fig. 6.2. For this reason, simple feedback regulation of the flux failed in this instrument.

Instead, we developed a scheme to determine the real-time flux at the sample position based on the flux at the monitor QCM (seen in Fig. 6.1), which can be recorded simultaneously with the calorimetry data. An example run using Cu is illustrated in Fig. 6.2(a), where the physically measured values are plotted along with the calculated fits. The ratio between the fluxes of the two QCMs is measured before and after the calorimetry experiments. As shown in

Fig. 6.2(b), this ratio was found to increase linearly with time while the source is being operated at constant emission current (provided the source has not used up almost all of its metal load). A linear fit to the ratio of the experimentally measured fluxes at the beginning and end of the calorimetry experiment (seen as a solid black line in Fig. 6.2(a)) was used to scale the flux at the monitor QCM so that it represents the actual flux at the sample position in real time over the entire duration of the calorimetry experiment. The end result is plotted in Fig. 6.2(a) as a solid red line. Monitoring flux in real time in this way not only allows for more accurate calculations of heats of adsorption vs. coverage, but also allows us to use data sets in which there is a sudden shift in the flux of the metal atom beam, which can occur due to flow effects in the metal melt in the crucible and are especially problematic at high evaporation rates⁴⁴⁶.

6.4: Optical Radiation from the Metal Atom Beam

When any metal evaporation source is used as a directed doser, as is the case in our calorimetry experiments, the atomic flux is also accompanied by optical radiation from the hot source. This contribution to the heat signal must be measured and subtracted from the signal in order to correctly determine the heat of adsorption³¹. In our instrument, the source is located 353 mm from the sample and is collimated to a 4 mm diameter beam. This distance is necessary to minimize the effect of the radiated heat from the oven, which decreases as the square of the distance. However, the flux per unit area from an effusion oven also decreases as the square of the distance. Because of this, very high temperatures in the source are required to reach the fluxes necessary for the signal/noise of our experiments ($\sim 0.5 \text{ \AA/s}$ at 353 mm). Fortunately, the flux increases with temperature as an Arrhenius equation (proportional to $e^{-\Delta H_{vap}/RT}$, where ΔH_{vap} is the enthalpy of vaporization for molten metals) while the optical radiation increases only as

$\sim T^4$. For the enthalpies of vaporization of typical metals, the increase in flux is much faster than the increase in radiation, so that higher temperatures give larger fluxes and have a smaller contribution from optical radiation in this design.

In our original metal atom source for SCAC of metal vapors, the source-to-sample distance is ~ 330 mm, with the first beam-defining aperture 108 mm from the source (which was necessary due to the dimensions of the commercial thermal evaporation oven) and only 87 mm between the first and last beam-defining apertures³¹. Geometric constraints resulted in a situation in which the sample has direct line-of-sight to not only the metal melt in the thermal evaporator, but also to a portion of the heated crucible. In this new calorimeter, we have increased the source-to-sample distance by 13% while drastically reducing the distance between the source and the first beam-defining aperture to 33.4 mm and increasing the distance between the first and last beam-defining apertures to 295.9 mm. With this new geometry, the sample can now see only a 4.90 mm diameter portion of the metal source, which is substantially less than the ~ 15 mm diameter e-beam evaporator crucible.

The overall combined effect of the changes in geometry along with the new type of metal atom source on the thermal radiation from the evaporative oven can be seen in Fig. 6.3, where the voltage responses of the pyroelectric detectors to adsorption of gaseous Cu atoms on ~ 17 ML of Cu on ~ 1 μm single crystals are shown as black lines for the different experimental setups. One monolayer (ML) here is defined as the Cu(111) surface density of 1.77×10^{15} atoms/cm². The solid blue lines are the corresponding optical radiation component in each pulse measured through the BaF₂ window, where these values have been scaled by the inverse of the measured transmission of BaF₂ ($\sim 90\%$). The difference in the two solid lines is proportional to the heat

response from only the adsorption of the gaseous metal atoms, and is plotted as a dashed red line to which the other data is normalized.

In Fig. 6.3(a), the signal for 0.014 ML Cu pulses (which correspond to a flux of $\sim 0.3 \text{ \AA/s}$ at the sample in our systems with the Cu melt at 1500 to 1510 K) adsorbing onto 17 ML of Cu on a $\sim 4 \text{ nm}$ MgO(100) film on Mo(100) from our older calorimeter using a Knudsen cell³¹ are shown. As seen, the optical radiation accounts for $\sim 65\%$ of the total heat signal. In Fig. 3(b), the signal for 0.014 ML Cu pulses adsorbing onto 17 ML of Cu on Pt(111) in this new calorimeter using an e-beam evaporator are plotted in the same manner. In this case, the optical radiation is reduced to only $\sim 14\%$ of the total signal, which greatly improves the signal/noise ratio in the final heat of adsorption determinations. Since the Cu source was almost the same distance from the sample in these two cases (it is 7% longer in this new design), and the Cu flux is the same, the effective temperature of the Cu source (which defines the evaporation rate) was almost the same, but the new e-beam source clearly generates much less optical radiation at the detector. The difference in the line shapes between the two instruments is merely due to the use of a different time constant for the high-pass filter.

It should be noted that some of this apparent improvement is probably due to the difference in reflectivity of the samples. However, based on the reflectivities of Mo ($R \approx 0.57$ ⁴⁴⁷) and Pt ($R \approx 0.76$ ³²⁵), the maximum reduction in absorbance of optical radiation for the sample used in the e-beam evaporator (compared to that in the Knudsen cell experiment) would be 44%. We instead see a reduction in the absorbed optical radiation of 92%. This proves that there is a minimum 51% reduction in optical radiation reaching the sample with our new calorimeter using an e-beam evaporator. It is likely that this improvement is even greater considering that the reflectivities of the two samples should be approaching that of bulk Cu as

the metal coverage increases. However, this may not be entirely due to the difference in the metal sources, as it is impossible to rule out a contribution from decreased internal reflections in the atomic beam path due to improvements in the design of the light baffles.

Since this new metal atom beam is capable of easily generating much larger fluxes of gaseous metal atoms without any significant rise in the background pressure, and since the atomic flux increases with temperature much faster than the optical radiation flux, the ratio between the radiative and adsorption heats can be further improved as needed. Fig 6.3(c) shows heat pulses from the same instrument onto the same sample used in Fig. 6.3(b), but the flux has been increased by a factor of ~ 4 to 0.058 ML per pulse (a flux of $\sim 1.2 \text{ \AA/s}$ at the sample). In order to achieve this larger flux, the temperature of the melt was increased to 1600 K by increasing the emission current of the e-beam evaporator. This results in a decrease in the optical radiation with respect to the total heat signal, so that the optical radiation now only accounts for 7% of the total heat signal. This high-temperature capability also proves that we will be able to use this atomic beam to perform adsorption calorimetry measurements with metals that have higher enthalpies of vaporization than Cu, such as Au and Pt.

Based on the T^4 temperature dependence of the optical radiation, we expected an increase in optical radiation of only 26% in Fig. 6.3(c) compared to Fig. 6.3(b), yet its signal nearly doubled. This could be due to an increase in the relative contribution to the optical radiation signal from indirect light coming from the hot crucible and filaments in the e-beam evaporator. Therefore, increasing the number of baffles for blocking indirect radiation could allow for an even greater reduction of the radiation reaching the sample, which would further increase the signal/noise ratio in our calorimetry measurements.

6.5: Real-time *In-situ* Relative Diffuse Optical Reflectivity Determination

When using the laser to calibrate the calorimeter's heat response, the optical reflectivity of the sample must be taken into account. This is also true when correcting for the optical radiation from the hot metal source of the beam. Reflectivities of single crystalline metal samples are taken from literature, and are also compared to integrating sphere measurements performed at atmospheric pressure. However, deposition of a thin film changes the reflectivity of a single crystal even when the overlayer thickness is much less than the wavelength of light⁴⁴⁸⁻⁴⁵⁰. This effect is generally linear with coverage, though nanoparticulate films with particles in the 20-100 nm range cause more rapid changes in the reflectivity versus coverage than equivalent films of uniform thickness⁴⁵¹.

Previous attempts at UHV *in-situ* direct relative optical reflectivity determination have measured the change in spectral reflectivity⁸³ or attempted to estimate diffuse reflectivity by measuring the total angular-integrated change in reflectivity over a larger area¹¹. For our purposes, the diffuse reflectivity is more appropriate since we need to know the total amount of light absorbed by the sample. Determination of the relative diffuse reflectivity using the absorbed portion of an incident heat source measured with a pyroelectric detector, such as the one in our calorimeter, has also been proposed and applied^{11, 452, 453}. In previous SCAC experiments, the voltage response of the PVDF ribbon to laser pulses on the sample surface was measured as a function of coverage by interrupting the metal deposition at several points during coverage build-up¹¹. This method introduces a $\pm 3-4\%$ error associated with repositioning the mirror to reflect the laser through the atomic beam path. Also, because of the time required, it has only ever been performed over large coverage steps and is usually not repeated in successive experiments.

In an attempt to more accurately account for the change in reflectivity with coverage, and to allow real-time measurements of the reflectivity during the course of an experiment, we have designed and built a setup for performing *in-situ* relative diffuse optical reflectivity determinations. A beam sampler, seen in Fig. 6.1, picks off 5% of the HeNe laser intensity used for calibrating the calorimeter's heat response and reflects it directly onto the sample at a 45° angle of incidence. It has been shown previously that changes in optical absorbance estimated using direct measurements of the relative total angular-integrated reflected light intensity at an incident angle of 45° agree well with changes in the absorbance of laser pulses normal to surface¹¹. An external chopper and aperture are used to break the 45° beam into pulses of the same time duration and spatial distribution as that of the pulses travelling down the atomic beam, for convenience. The external chopper is synchronized with the internal chopper of the beam line, with the ability to change both the pulse window and the duration between pulses so that there is no overlap in the heat signal. This staggering is accomplished by having the chopper wheels pause in a closed position for a fixed amount of time. This setup also allows deposition of multiple pulses of metal atoms between each laser pulse, saving both time and material.

The laser-on-sample measurements can now be made without the need for any mechanical manipulation, and the change in diffuse optical reflectivity can be calculated without the noise associated with repositioning the mirror. A sample run, where the heat pulses from the calorimeter are simulated by the laser reflected down the beam path, is seen in Fig. 6.4. The black portions of the curve are the signal response due to heat from the atomic beam path, while the red portions are the response from the 45° laser pulses. All pulses still have the typical 2 s interval and 100 ms window, but with an absorbance measurement occurring after every second pulse from the beam path. In this manner it is possible to monitor the relative diffuse optical

reflectivity in real time during the entire calorimetry experiment at coverage increments as low as 1% of a monolayer. As the coverage increases, the reflectivity of the sample will eventually reach the bulk reflectivity of the deposited metal. Using literature values for bulk metal reflectivities allows for determination of the absolute diffuse optical reflectivities of clean single crystalline oxide thin films.

6.6: Absolute accuracy of Heats of Adsorption for Metals on Single-Crystalline Supports from SCAC

In this section we show a simple example application of this new atomic beam source for measuring heats of adsorption on single crystals. Figure 6.5 shows typical measurements of the heat of Cu atom adsorption on Cu multilayers on Pt(111) at 300 K. The voltage response of the β -PVDF ribbon as seen in Figs. 6.3(b) and 6.3(c), along with the flux and radiation determinations described above, were used to determine the heat of adsorption per mole for each pulse of the atomic beam, as described previously³¹. The standard small corrections for the excess translational energy of the hot, gaseous metal atoms in the beam above their energy at 300 K and for the conversion from internal energy to enthalpy have also been applied, as described elsewhere³¹, so that the y -axis values plotted in Fig. 5 equal the heat of adsorption (defined as the negative of the standard enthalpy of adsorption with both the surface and gas at 300 K, $-\Delta H_{ad}$). The heat measurements shown in Fig. 6.5 were performed for Cu pulses containing 0.017 ML of Cu adsorbing onto clean Pt(111) at 300 K. Shown here is a single run of 100 Cu pulses over the multilayer coverage range from 4.5 to 6.2 ML. Copper is known to grow layer-by-layer on Pt(111) when vapor deposited in UHV at 300 K⁴⁵⁴⁻⁴⁵⁷, so the data presented in Fig. 6.5 represents the multilayer heat of adsorption, which is equal to the enthalpy of

sublimation of bulk Cu ($337.4 \text{ kJ/mol}^{-1}$) at these conditions. This is generally true for metals that grow in a continuous film, as they typically do at room temperature and above.

The pulse-to-pulse standard deviation in the heats of adsorption in Fig. 6.5 for the 100 data points shown, about their average value (equal to the bulk enthalpy of sublimation of Cu), is 0.83 kJ/mol , or 0.25%. This standard deviation is a factor of ~ 18 better than that reported using our previous Knudsen cell atom source (which gave standard deviations for multilayer Cu adsorption of 6% using 0.01 ML/pulse and almost 2% with $\sim 0.03 \text{ ML/pulse}$ ³¹, which interpolates to 4.6 % for the flux used in Fig. 5 of 0.017 ML/pulse). The pulse-to-pulse standard deviation in measuring the heat from simple laser pulses, for the 13 calibration pulses used in the same experiment as Fig. 6.5 and which deposited almost the same amount of heat per pulse as in Fig. 6.5, was also 0.25%. This implies that this standard deviation of 0.25% in Fig. 6.5 is dominated by the noise in the pyroelectric heat detection system rather than from variations in the metal atom flux or additional noise due to heat from the optical radiation. The 18-fold decrease in relative standard deviation compared to our previous measurements of the heat of Cu adsorption is mostly due to an improvement in the design of the heat detector reported previously⁵¹ and incorporated in this new system, but approximately one-third of this improvement is due to the removal of a large amount of heat signal from optical radiation, which also contributes to the noise.

We have previously shown that the absolute accuracy of heat of adsorption measurements with this type of SCAC heat detector and laser calibration method is within 3%, after averaging several runs⁵³. This was done by comparing the average multilayer heat of adsorption of four different molecules to their known bulk enthalpies of sublimation at the same temperatures. Since these same methods are used here, similar accuracy can be expected.

6.7: Example Application of New Calorimeter: Cu Adsorption on CeO_{1.95}(111) and MgO(100) Surfaces

The first heats of adsorption versus coverage measurements for metal atoms on an oxide surface performed in this newest calorimeter are for Cu adsorption on CeO_{1.95}(111)³². This data is presented for the first time in Fig. 6.6, along with data from a previous SCAC study of Cu adsorption on MgO(100)²⁹. It can be seen that the two curves are very similar in form. This is not surprising, since it has been shown that Cu interacts only weakly with oxide films, and therefore the adsorption energy is dominated by the strength of Cu–Cu bonds^{29, 132, 458}. The most important difference is in the coverage range below 0.2 ML, where the smallest Cu particles are present. The smallest Cu nanoparticles are much more strongly bound to the CeO_{1.95}(111) surface than they are to the MgO(100) surface, by upwards of 50 kJ/mol. However, the initially high adsorption energies for Cu on CeO_{1.95}(111) that is present only up to ~0.05 ML suggests that the smallest particles are bound to defect sites, most likely the oxygen atoms on step and kink sites which are present on such CeO_{2-x} thin films as the ones grown here (see Fig. 2.12). Between 0.05 and 2 ML, the heat of adsorption is slightly larger on CeO_{1.95}(111) than on MgO(100), which agrees with the assignment of CeO_{2-x} as a “stronger” support than MgO(100), as discussed in Chapter 5, although for Cu this effect is minimal. Further measurements on Cu adsorption energies on more reduced CeO_{2-x}(111) surfaces and interpretation of these data, all done in a collaboration with Trevor James and Stephanie Hemmingson, will be presented elsewhere³².

6.8: Figures

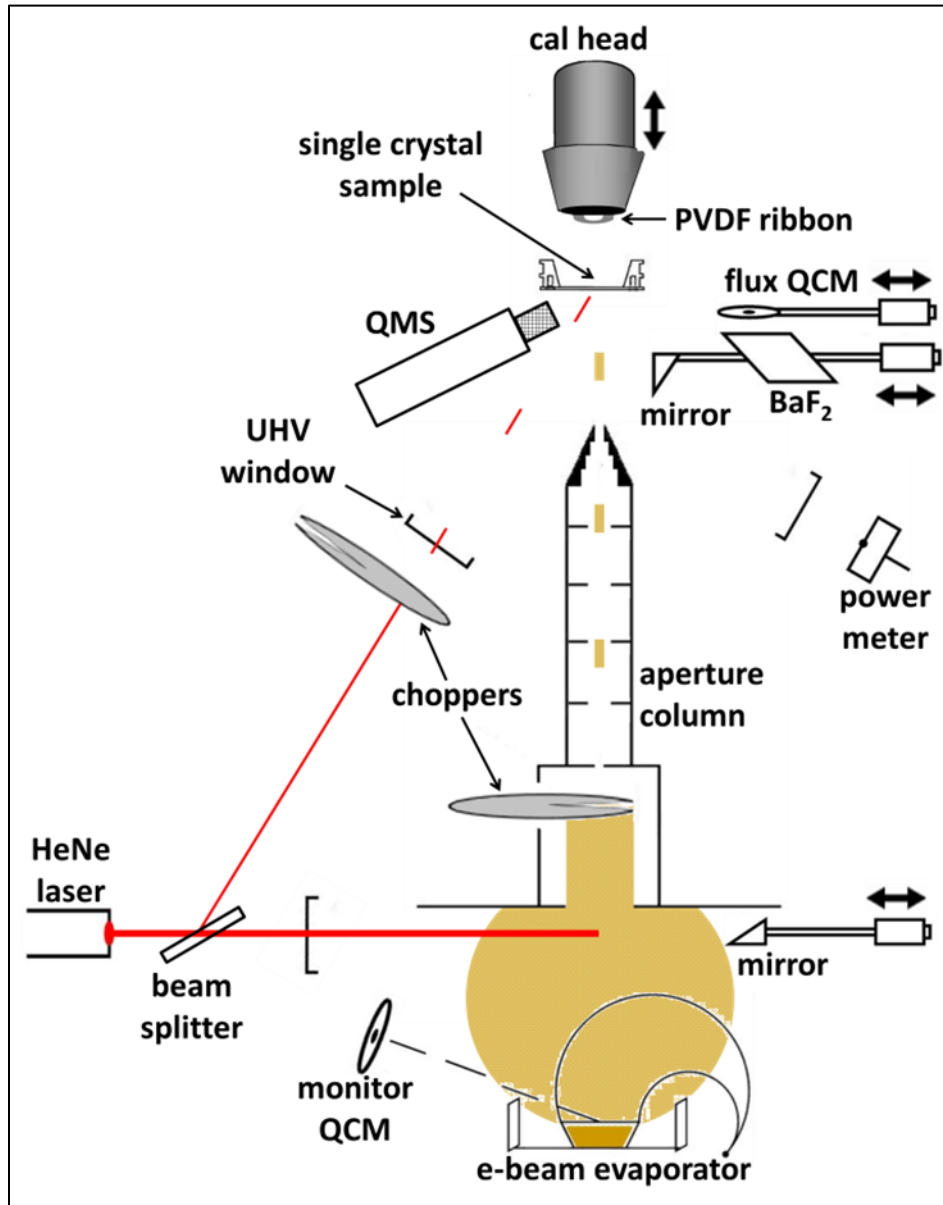


Figure 6.1. A schematic of the calorimeter, which uses an e-beam evaporator and a chopper to create a pulsed atomic beam of gaseous metal atoms (copper colored in the figure) which impinges upon the surface of a single crystalline sample. The transient heat input due to the adsorption of each gas pulse is detected by a flexible pyroelectric PVDF ribbon that is gently pressed against the back of the single crystal. As shown, this ribbon is mounted in the shape of an arch on the “cal head”, which can be translated to bring the ribbon into contact with the single crystal, or removed for crystal cleaning and surface analysis. The single crystal is mounted to a platen, which sits on a fork on a thermal reservoir during calorimetry but is moved for surface analysis. Also illustrated are the components for the real-time flux and relative reflectivity measurements. Not to scale. Reprinted with permission from Reference ³⁰. Copyright 2013 American Institute of Physics.

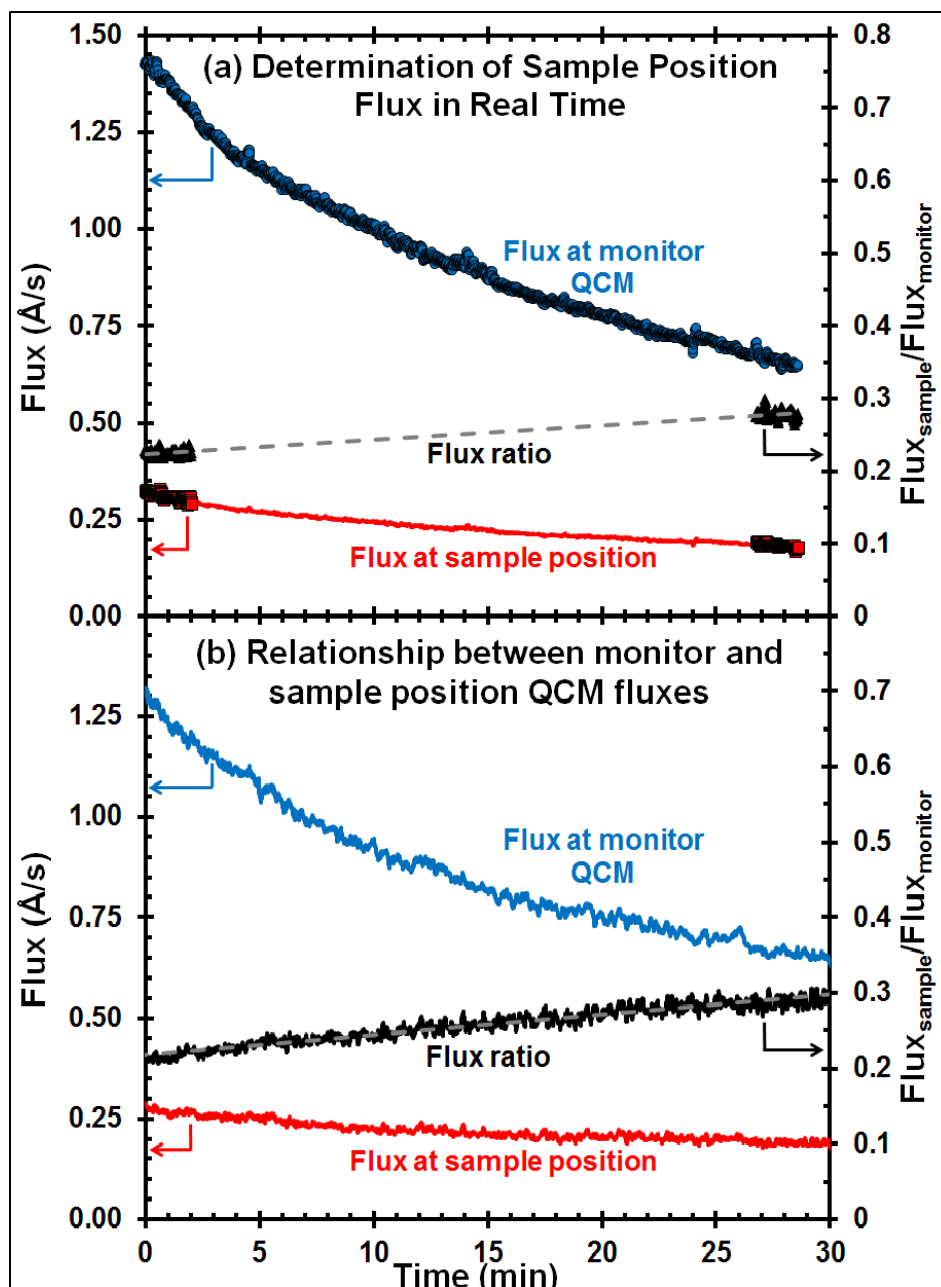


Figure 6.2. (a) Plot of the flux from the electron beam evaporator running at constant emission current vs. time at both the sample position QCM and the off-axis monitor QCM. Measured flux data are plotted as points, while the calculated flux at the sample position is plotted as a continuous red line. Also plotted is the ratio between the two fluxes, which is fit to the linear dashed line as a function of time. The flux ratio is used to calculate the flux at the sample position based on the flux at the monitor QCM. (b) Similar data for a control run where the flux was collected with a QCM located at the sample position throughout the entire experiment. This shows that the changing flux ratio is well approximated as changing linearly with time. The dashed line showing the best linear fit to the flux ratio is essentially hidden within the scatter of the data. Reprinted with permission from Reference ³⁰. Copyright 2013 American Institute of Physics.

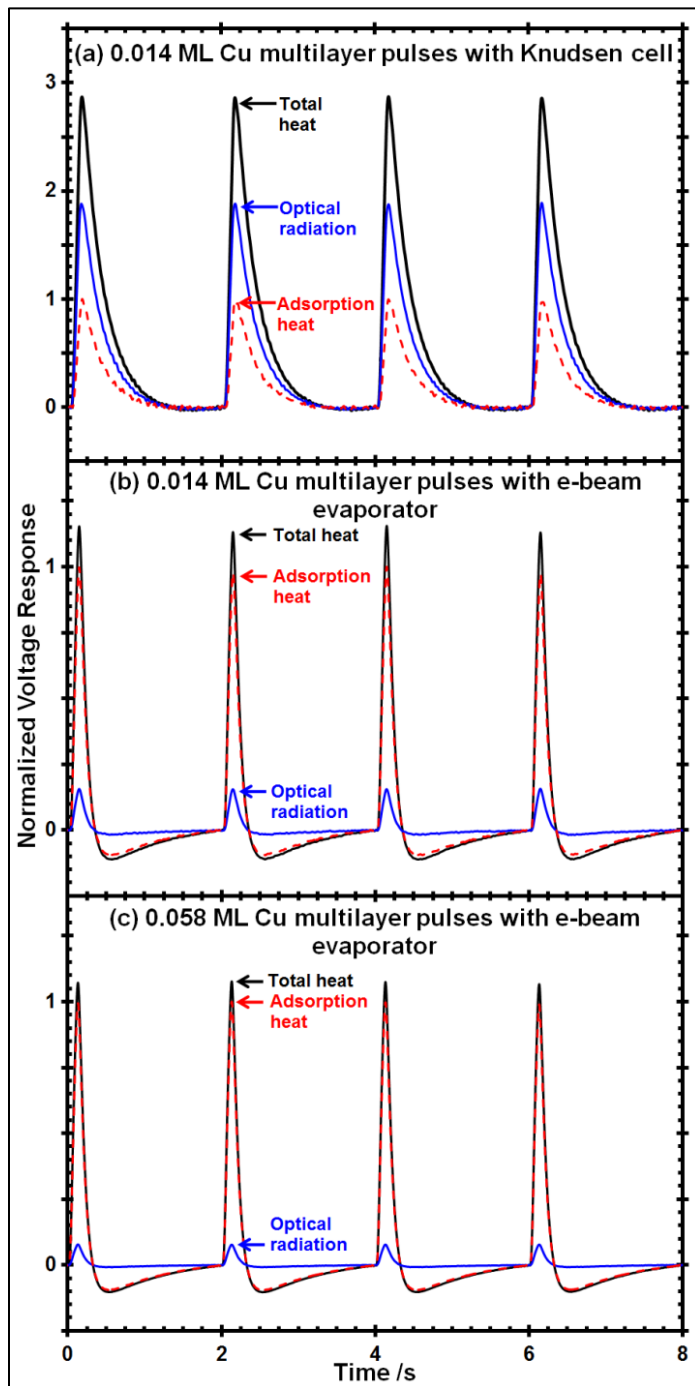


Figure 6.3. Calorimetry heat pulses as detected via SCAC from Cu adsorbing onto ~ 17 ML of Cu on $\sim 1 \mu\text{m}$ single crystals at 300 K, where the Cu vapor was generated by: (a) the Knudsen cell used in our earlier calorimeter³¹, and (b) and (c) the e-beam evaporator of this new instrument. The solid black lines are calorimetry data from Cu atom pulses, the solid blue lines are the heat due to optical radiation from the hot metal source (measured through the BaF_2 window at the end of the experiment) and the dashed red lines are the heat signal due only to Cu adsorption, as determined by the difference in the two solid curves. These signals are for (a) 0.014 ML pulses of Cu from the Knudsen cell used in our earlier calorimeter³¹ onto ~ 17 ML Cu on Mo(100) (pre-coated with 4 nm of MgO(100), which only slightly changes the reflectivity²⁹), (b) 0.014 ML pulses of Cu from the e-beam evaporator onto ~ 17 ML of Cu on Pt(111), and (c) 0.056 ML pulses of Cu from the e-beam evaporator onto ~ 17 ML of Cu on Pt(111). The differences in line shapes arise from differing time constants for the high-pass filters and differences in the quality of the thermal contact between the sample and detector. Curves were smoothed with a low-pass filter. One ML is defined as the Cu(111) surface atom density, which is 1.77×10^{15} atoms/cm². Reprinted with permission from Reference³⁰. Copyright 2013 American Institute of Physics.

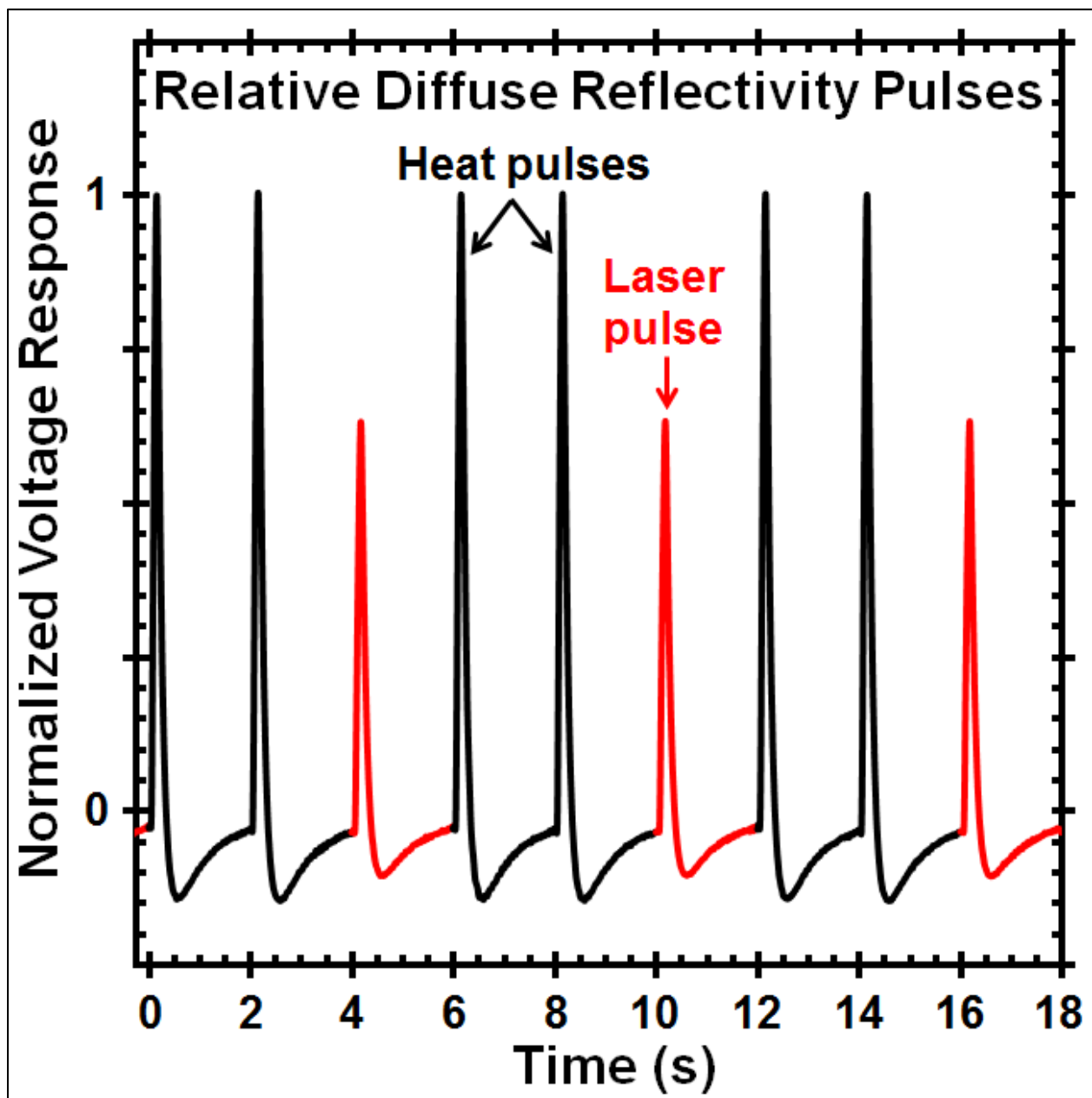


Figure 6.4. A sample run demonstrating the *in-situ* relative diffuse optical reflectivity measurement. Every third pulse from the metal atom beam line is replaced with a pulse from a HeNe laser at a 45° angle of incidence. The black portion of the curve is the response to heat deposition from the atomic beam line, while the red portions are the heat response from the laser. In this manner the absorbance of the sample at 633 nm can be monitored throughout the experiment so that the reflectivity of the sample can be accurately determined at all coverages. Heat pulses from the atomic beam were simulated with a laser directed down the atomic beam path in this example. Reprinted with permission from Reference ³⁰. Copyright 2013 American Institute of Physics.

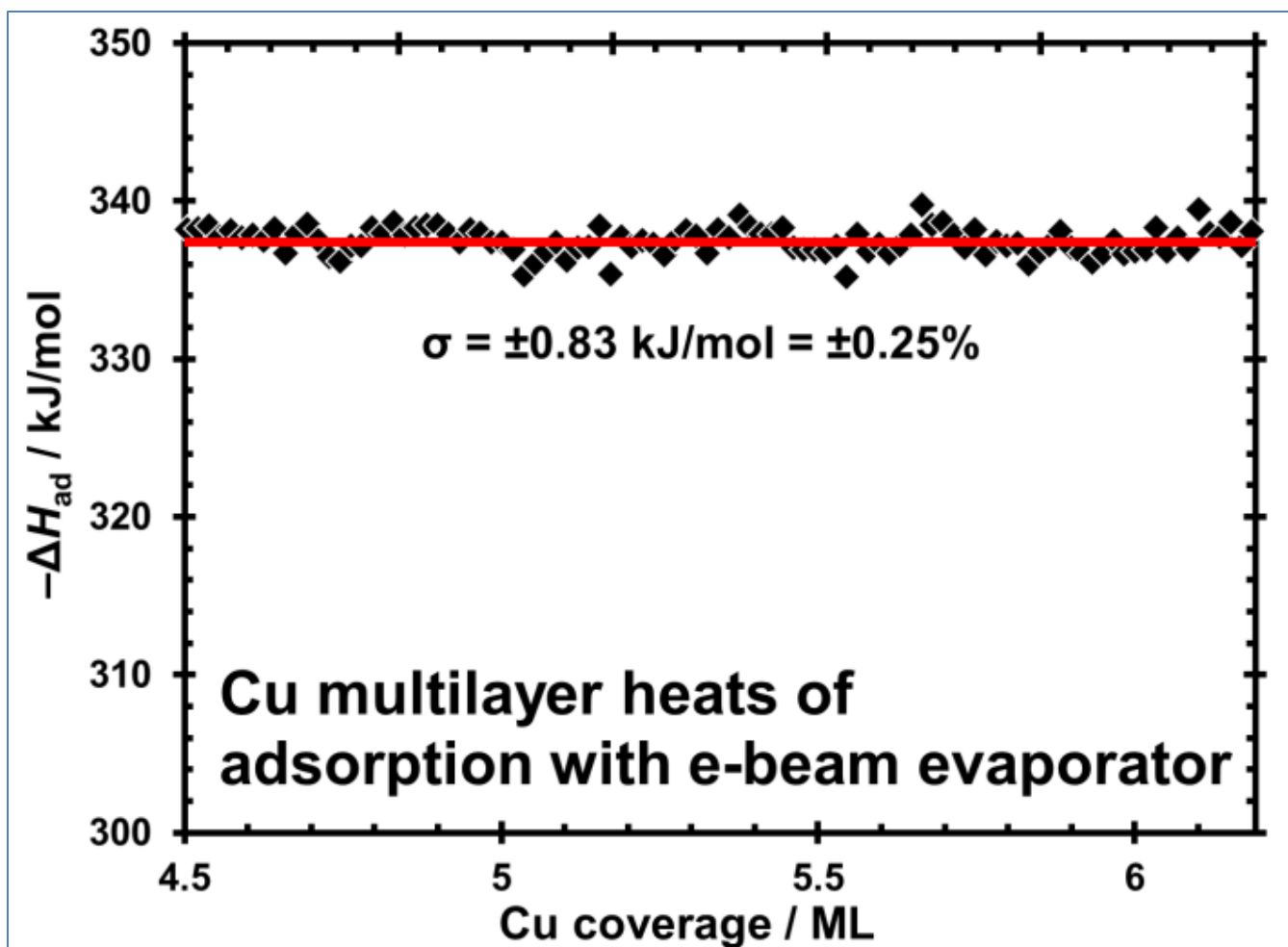


Figure 6.5. Heat of adsorption versus coverage for 100 pulses of Cu (each pulse containing 0.017 ML) onto a Cu multilayer on Pt(111) at 300 K. The data in the figure have been normalized so that their average value equals the literature value for the enthalpy of sublimation of bulk Cu solid at 300 K (337.4 kJ/mol^1 , shown as the solid red line), to remove a small error in absolute calibration. The pulse-to-pulse standard deviation is 0.83 kJ/mol. One ML is defined as the Cu(111) surface atom density, $1.77 \times 10^{15} \text{ atoms/cm}^2$. Reprinted with permission from Reference ³⁰. Copyright 2013 American Institute of Physics.

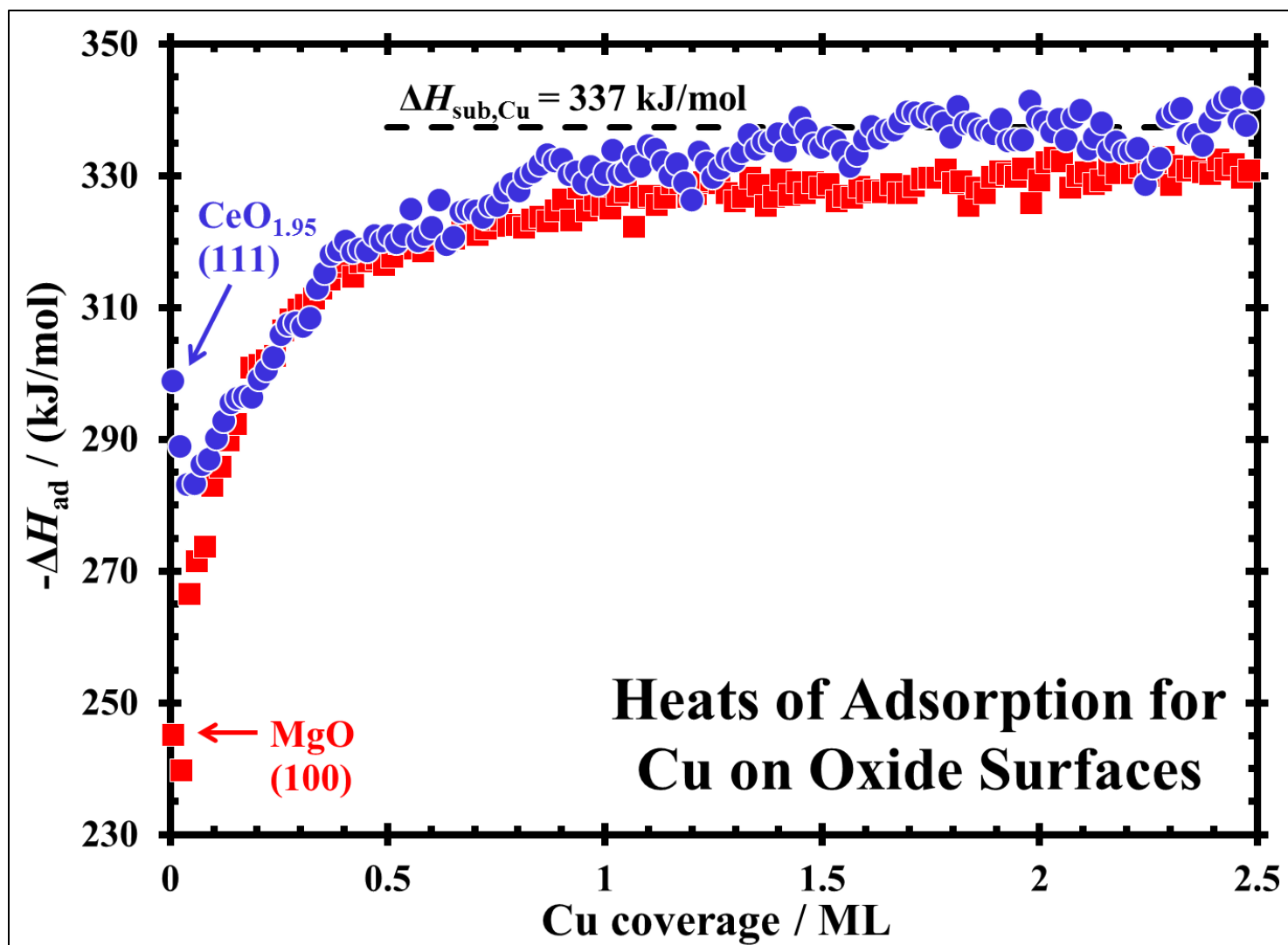


Figure 6.6. Heat of adsorption versus coverage for Cu on MgO(100)²⁹ (blue circles) and CeO_{1.95}(111)³² (red squares) at 300 K. The dashed black line is the heat of sublimation of bulk Cu solid at 300 K (337.4 kJ/mol¹). One ML is defined as the Cu(111) surface atom density, 1.77×10^{15} atoms/cm².

Chapter 7

Conclusions

In this dissertation, I have presented several advances in the understanding of and ability to measure the physical properties of adsorbates on oxide surfaces. The data presented in Chapter 2 represents the most comprehensive collection of quantitative experimental data on the enthalpies and entropies of adsorption on single crystalline oxide surfaces to date. While still rather limited, this compilation of data reveals a number of important trends. Heats of molecular adsorption track molecule size, with linear relationships and similar slopes found for both *n*-alkanes and linear alcohols versus the number of carbon atoms in the chain. The heats of adsorption of noble gases vary linearly with atomic number. The heats of adsorption of late transition metals on MgO(100) are less than, but increase with, the bulk metal's sublimation energy. The heat of adsorption of the same late transition metal atom can vary widely between different oxides. Alkali and alkaline earth metals bind more strongly to oxides, dramatically so at defects. The late transition metals cluster into 3D nanoparticles on oxides of the type used for catalyst supports. The heat of adsorption of the metal atoms to these nanoparticles varies strongly with particle size below 6 nm diameter, and this size dependence varies strongly with the nature of the oxide. There are almost no reliable heats of adsorption for dissociatively adsorbed molecules on single crystalline oxide surfaces, so data of that type are badly needed. While Chapter 2 summarizes many conclusions that could not have been realized without the tremendous work of a large, talented, and dedicated scientific community over the past few decades, it also highlights the need to expand upon our basic knowledge set when it comes to the properties of oxide supports and the thermodynamics of their interactions with adsorbed species.

In chapter 3, it was shown that the standard-state entropies of molecularly adsorbed species which have attractive adsorbate-adsorbate interactions are large and track their corresponding gas-phase entropies as $S_{\text{ad}}^0(T) = 0.70 S_{\text{gas}}^0(T) - 3.3R$ up to $S_{\text{gas}}^0(T) = 60R$. This relationship applies at temperatures where desorption rates are fast enough to perform EAI and TPD measurements ($\sim 10^{-3}$ to 100 monolayers/s). For longer adsorbed molecules where $S_{\text{gas}}^0(T)$ exceeds 60 K (e.g. linear alkanes with >11 carbons), their entropies remain a constant $20.7R$ below gas entropies, and $\sim 10.4R$ below Trouton's Rule for liquid entropies.

As discussed in Chapter 4, the entropy correlation presented in Chapter 3 can be used to estimate kinetic prefactors for surface reactions involving desorption, diffusion, dissociation, and association of adsorbates, provided the temperature is high enough that the adsorbate's surface residence time is less than ~ 1000 s. At these temperatures, harmonic transition state theory (HTST) does a very poor job of predicting such prefactors, but at temperatures where $k_B T$ is small compared to the barriers for adsorbate diffusion and helicopter-type rotation, HTST is more accurate. At intermediate temperatures where $k_B T$ approaches or exceeds the magnitude of the barriers for rotational and translational motions, a new approach must be developed, and Chapter 4 offers a suggestion for that approach that can be adopted from the methods used to treat hindered internal rotations of gas molecules. Whereas the rates of adsorbates' reactions are usually treated as being first-order in adsorbate coverage (θ), transition state theory shows that it is better to use $\theta/(1 - \theta)$ as the "concentration" factor (when not 2D islands), since it more accurately reflects the tremendous increase in the adsorbate's chemical potential as coverage approaches saturation due to the configurational entropy or excluded volume effect.

The analysis of temperature programmed desorption (TPD) data has been discussed in detail. The kinetic prefactors for desorption that the entropy correlation in Chapter 3 provides

have been applied as described above in Chapter 2 to improve the accuracy of desorption energies extracted from TPD data, and hence adsorption enthalpy measurements by TPD. It was also shown in Chapter 2 that TPD can be used to estimate adsorption and adhesion energies for later transition metals on oxides, but that the method for data analysis must be changed from that previously used in the literature, since leading-edge analysis fails dramatically for these systems.

The properties of adsorbed metal nanoparticles were discussed in Chapter 5, with particular focus on the effects of nanoparticle size and the identity of the support on the energy, resistance to sintering, and reactivity of these catalytically important systems. It was shown that trends in these properties are highly related to the chemical potential of the atoms in the nanoparticles. As the chemical potential of the surface metal atoms increase, the stronger they bond small molecules. Simultaneously, the surface mobility and therefore drive for sintering also increases with the chemical potential of the nanoparticle. The chemical potential of adsorbed nanoparticles is shown to be dependent upon both the nanoparticle size, increasing with decreasing size for particles below ~ 6 nm in diameter, and the strength of the interactions with the underlying support. These properties are all related to the adhesion energy of these nanoparticles, which can be tuned based on the size and nature of the support, allowing for control over their catalytic properties and stability. Experimental evidence was shown that allows us to rank several oxides in order of increasing adhesion energies to nanoparticulate metals, such that $\text{MgO}(100) \approx \text{TiO}_2(110) \leq \alpha\text{-Al}_2\text{O}_3(0001) < \text{CeO}_{2-x}(111) \leq \text{Fe}_3\text{O}_4(111)$. These results are the first step in developing a method for designing the most efficient nanoparticulate catalysts based on the physical properties the adsorbate and the substrate.

In Chapter 6, the detail of an improved UHV single crystal adsorption calorimeter for measuring heats of adsorption of metal atoms onto single crystal surfaces were presented. This

new instrument utilizes an e-beam evaporator as the metal atom source. Its decreased optical radiation as compared to a Knudsen cell type evaporator allows for an 18-fold improvement in signal-to-noise ratio. Its ability to operate at higher temperatures allows for the use of metals with higher enthalpies of vaporization than that of Cu (such as Pt, Pd, Rh, Ni, and Au), for which heats of adsorption have never been determined experimentally. The calorimetric technique has also been improved by monitoring the flux of the metal atom beam in real time, which corrects for momentary instabilities in the flux of atoms reaching the surface. The system also allows for *in-situ* relative optical reflectivity measurements on the single crystal, which improves the accuracy of the heat signal calibration and the correction for optical radiation from the hot source.

The first measurements of heats of adsorption of metal atoms on single-crystalline oxide surfaces performed on this instrument were for Cu on $\text{CeO}_{1.95}(111)$. As is typical for metal atom adsorption, Cu adsorbs less strongly to the oxide surface than it does to itself. When compared to data for Cu on $\text{MgO}(100)$, it becomes clear that the adsorption energetics of Cu are dominated by Cu–Cu interactions to such a degree that the heats of adsorption are nearly identical above 0.2 ML for both oxide surfaces. Below 0.2 ML, Cu adsorbs more strongly to $\text{CeO}_{1.95}(111)$ than it does to $\text{MgO}(100)$, which is expected due to the “strong” and “weak” characterizations of $\text{CeO}_{2-x}(111)$ and $\text{MgO}(100)$, respectively, described in Chapter 5. Cu also grows as 3D islands up to ~2.5 ML, at which point it reaches the bulk heat of sublimation of Cu metal.

While the work presented here signifies a large step forward in the general understanding of the properties of oxide surfaces and their interaction with adsorbates, it is clear that the picture is far from complete. While the correlations discussed agree with experimental results more closely than any proposed before, a more basic understanding of these systems is necessary.

Using the data contained in this dissertation as benchmarks can help improve theoretical methods, which may provide further insight into the fundamental properties that govern the behavior of oxide surfaces. The discussed trends can also be further improved by expanding the range of systems for which the adsorption energetics are well known. This is already being done in the Campbell group, where we have recently completed experiments measuring the heats of adsorption of Cu on $\text{CeO}_{2-x}(111)$ as a function of the reduction of the oxide surfaces. By cooling the single-crystalline oxide samples, we will also be able to observe the dependence of these adsorption and adhesion energies on nanoparticle size, and hopefully allow us to more accurately extract the single atom bond energy of Cu on $\text{CeO}_{2-x}(111)$. Soon to follow will be experiments with Au and Pd on $\text{CeO}_{2-x}(111)$ and $\text{Fe}_3\text{O}_4(111)$, which will be the first experimental measurements of the heats of adsorption for these catalytically important transition metals on any surface. These experiments will not only allow for further investigation into the periodic trends in metal / oxide adsorption energies which will expand upon the revelations in this dissertation, but the data can also be compared to measurements of adsorption energies of small molecules on oxide-supported metal nanoparticles, which will provide more direct insight into the catalytic properties of these supported nanoparticulate catalysts. Hopefully this dissertation represents only the beginning of many advances that will be made in the near future in understanding the properties of single-crystalline surfaces, which will ultimately play a vital role in helping advance many technologies.

References

1. W. M. Haynes, ed., *CRC Handbook of Chemistry and Physics (Internet Version)*, CRC Press / Taylor and Francis, Boca Raton, FL, 2012.
2. C. T. Campbell and O. Lytken, *Surface Science*, 2009, **603**, 1365-1372.
3. C. T. Campbell and J. R. V. Sellers, *Chemical Reviews*, 2013, **113**, 4106-4135.
4. J. G. Li, *Journal of the American Ceramic Society*, 1992, **75**, 3118-3126.
5. L. Vitos, A. V. Ruban, H. L. Skriver and J. Kollar, *Surface Science*, 1998, **411**, 186-202.
6. A. Stuck, C. E. Wartnaby, Y. Y. Yeo, J. T. Stuckless, N. Al-Sarraf and D. A. King, *Surface Science*, 1996, **349**, 229-240.
7. J. P. Coulomb, T. S. Sullivan and O. E. Vilches, *Physical Review B*, 1984, **30**, 4753-4760.
8. S. L. Tait, Z. Dohnalek, C. T. Campbell and B. D. Kay, *Journal of Chemical Physics*, 2005, **122**, 164707.
9. C. T. Campbell and J. R. V. Sellers, *Journal of the American Chemical Society*, 2012, **134**, 18109-18115.
10. S. L. Tait, Z. Dohnalek, C. T. Campbell and B. D. Kay, *Journal of Chemical Physics*, 2006, **125**, 234308.
11. D. E. Starr, D. J. Bald, J. E. Musgrove, J. T. Ranney and C. T. Campbell, *Journal of Chemical Physics*, 2001, **114**, 3752-3764.
12. J. H. Larsen, J. T. Ranney, D. E. Starr, J. E. Musgrove and C. T. Campbell, *Physical Review B*, 2001, **63**, 195410.
13. J. Zhu, J. A. Farmer, N. Ruzycski, L. Xu, C. T. Campbell and G. Henkelman, *Journal of the American Chemical Society*, 2008, **130**, 2314-2322.
14. J. A. Farmer, J. H. Baricuatro and C. T. Campbell, *Journal of Physical Chemistry C*, 2010, **114**, 17166-17172.
15. C. T. Campbell, S. C. Parker and D. E. Starr, *Science*, 2002, **298**, 811-814.
16. C. T. Campbell, J. C. Sharp, Y. X. Yao, E. M. Karp and T. L. Silbaugh, *Faraday Discussions*, 2011, **152**, 227-239.
17. J. A. Farmer and C. T. Campbell, *Science*, 2010, **329**, 933-936.
18. P. Luches, F. Pagliuca, S. Valeri, F. Illas, G. Preda and G. Pacchioni, *Journal of Physical Chemistry C*, 2012, **116**, 1122-1132.
19. K. Luo, D. Y. Kim and D. W. Goodman, *Journal of Molecular Catalysis A: Chemical*, 2001, **167**, 191-198.
20. M. C. Wu and D. W. Goodman, *Journal of Physical Chemistry*, 1994, **98**, 9874-9881.
21. D. G. Van Campen and J. Hrbek, *Journal of Physical Chemistry*, 1995, **99**, 16389-16394.
22. K. Luo, X. Lai, C. W. Yi, K. A. Davis, K. K. Gath and D. W. Goodman, *Journal of Physical Chemistry B*, 2005, **109**, 4064-4068.
23. A. W. Grant and C. T. Campbell, *Physical Review B*, 1997, **55**, 1844-1851.
24. S. L. Tait, Z. Dohnalek, C. T. Campbell and B. D. Kay, *Journal of Chemical Physics*, 2005, **122**, 164708.
25. K. R. Paserba and A. J. Gellman, *Journal of Chemical Physics*, 2001, **115**, 6737-6751.
26. D. A. McQuarrie, *Statistical Mechanics*, University Science Books, Sausalito, CA, 2000.
27. C. T. Campbell, L. Árnadóttir and J. R. V. Sellers, *Zeitschrift für Physikalische Chemie*, 2013, **227**, 1435-1454.
28. C. T. Campbell and J. R. V. Sellers, *Faraday Discussions*, 2013, **162**, 9-30.

29. J. T. Ranney, D. E. Starr, J. E. Musgrove, D. J. Bald and C. T. Campbell, *Faraday Discussions*, 1999, **114**, 195-208.
30. J. R. V. Sellers, T. E. James, S. L. Hemmingson, J. A. Farmer and C. T. Campbell, *Review of Scientific Instruments*, 2013, **84**, 123901.
31. J. T. Stuckless, N. A. Frei and C. T. Campbell, *Review of Scientific Instruments*, 1998, **69**, 2427-2438.
32. T. E. James, S. L. Hemmingson, J. R. V. Sellers and C. T. Campbell, in preparation.
33. C. T. Campbell, *Surface Science Reports*, 1997, **27**, 1-111.
34. D. W. Goodman, *Journal of Catalysis*, 2003, **216**, 213-222.
35. S. A. Chambers, *Surface Science Reports*, 2000, **39**, 105-180.
36. C. T. Campbell, *Journal of the Chemical Society-Faraday Transactions*, 1996, **92**, 1435-1445.
37. S. M. George, *Chemical Reviews*, 1995, **95**, 475-476.
38. G. Ertl, H. Knözinger, F. Schüth and J. Weitkamp, eds., *Handbook of Heterogeneous Catalysis*, Wiley-VCH, Weinheim, 2008.
39. A. T. Bell, *Science*, 2003, **299**, 1688-1691.
40. M. Chen and D. W. Goodman, in *Chemical Physics of Solid Surfaces*, ed. D. Woodruff, Elsevier, Amsterdam, 2007, vol. 12, ch. 5, pp. 201-269.
41. A. Sanchez, S. Abbet, U. Heiz, W. D. Schneider, H. Hakkinen, R. N. Barnett and U. Landman, *Journal of Physical Chemistry A*, 1999, **103**, 9573-9578.
42. M. Haruta, *Catalysis Today*, 1997, **36**, 153-166.
43. T. Schalow, B. Brandt, D. E. Starr, M. Laurin, S. K. Shaikhutdinov, S. Schauermann, J. Libuda and H.-J. Freund, *Angewandte Chemie International Edition*, 2006, **45**, 3693-3697.
44. D. W. Goodman, *Chemical Reviews*, 1995, **95**, 523-536.
45. J. G. Dash, R. Ecke, J. Stoltenberg, O. E. Vilches and O. J. Whittemore, *Journal of Physical Chemistry*, 1978, **82**, 1450-1452.
46. T. S. Sullivan, A. D. Migone and O. E. Vilches, *Surface Science*, 1985, **162**, 461-469.
47. P. A. Redhead, *Vacuum*, 1962, **12**, 203-211.
48. S. E. Wanke and P. C. Flynn, *Catalysis Reviews: Science and Engineering*, 1975, **12**, 93-135.
49. Z. Dohnalek, G. A. Kimmel, S. A. Joyce, P. Ayotte, R. S. Smith and B. D. Kay, *Journal of Physical Chemistry B*, 2001, **105**, 3747-3751.
50. H. M. Ajo, H. Ihm, D. E. Moilanen and C. T. Campbell, *Review of Scientific Instruments*, 2004, **75**, 4471-4480.
51. W. Lew, O. Lytken, J. A. Farmer, M. C. Crowe and C. T. Campbell, *Review of Scientific Instruments*, 2010, **81**, 024102.
52. M. C. Crowe and C. T. Campbell, *Annual Review of Analytical Chemistry*, 2011, **4**, 41-58.
53. E. M. Karp, T. L. Silbaugh, M. C. Crowe and C. T. Campbell, *Journal of the American Chemical Society*, 2012, **134**, 20388-20395.
54. B. Hammer and J. K. Norskov, *Surface Science*, 1995, **343**, 211-220.
55. B. Hammer, L. B. Hansen and J. K. Norskov, *Physical Review B*, 1999, **59**, 7413-7421.
56. J. K. Norskov, T. Bligaard, A. Logadottir, S. Bahn, L. B. Hansen, M. Bollinger, H. Bengaard, B. Hammer, Z. Sljivancanin, M. Mavrikakis, Y. Xu, S. Dahl and C. J. H. Jacobsen, *Journal of Catalysis*, 2002, **209**, 275-278.

57. J. Greeley and M. Mavrikakis, *Nature Materials*, 2004, **3**, 810-815.
58. J. K. Norskov, T. Bligaard, J. Rossmeisl and C. H. Christensen, *Nature Chemistry*, 2009, **1**, 37-46.
59. J. K. Norskov, F. Abild-Pedersen, F. Studt and T. Bligaard, *Proceedings of the National Academy of Sciences of the United States of America*, 2011, **108**, 937-943.
60. M. Mavrikakis, *Nature Materials*, 2006, **5**, 847-848.
61. C. Di Valentin, G. Pacchioni and A. Selloni, *Physical Review Letters*, 2006, **97**, 166803.
62. M. V. Ganduglia-Pirovano, A. Hofmann and J. Sauer, *Surface Science Reports*, 2007, **62**, 219-270.
63. Z. Hu and H. Metiu, *Journal of Physical Chemistry C*, 2011, **115**, 5841-5845.
64. D. D. Kong, G. D. Wang, Y. H. Pan, S. W. Hu, J. B. Hou, H. B. Pan, C. T. Campbell and J. F. Zhu, *Journal of Physical Chemistry C*, 2011, **115**, 6715-6725.
65. C. T. Campbell, A. W. Grant, D. E. Starr, S. C. Parker and V. A. Bondzie, *Topics in Catalysis*, 2001, **14**, 43-51.
66. D. L. Hill, *An Introduction to Statistical Thermodynamics*, Addison-Wesley, Reading, MA, 1960.
67. D. Brennan, D. O. Hayward and B. M. W. Trapnell, *Proceedings of the Royal Society of London Series A: Mathematical and Physical Sciences*, 1960, **256**, 81-105.
68. G. Wedler, *Discussions of the Faraday Society*, 1966, 108-109.
69. S. Cerny, *Surface Science Reports*, 1996, **26**, 3-59.
70. D. A. Kyser and R. I. Masel, *Review of Scientific Instruments*, 1987, **58**, 2141-2144.
71. C. E. Borroni-Bird and D. A. King, *Review of Scientific Instruments*, 1991, **62**, 2177-2185.
72. C. E. Borroni-Bird, N. Al-Sarraf, S. Andersson and D. A. King, *Chemical Physics Letters*, 1991, **183**, 516-520.
73. N. Al-Sarraf, J. T. Stuckless and D. A. King, *Nature*, 1992, **360**, 243-245.
74. J. T. Stuckless, N. Al-Sarraf, C. Wartnaby and D. A. King, *Journal of Chemical Physics*, 1993, **99**, 2202-2212.
75. N. Al-Sarraf, J. T. Stuckless, C. E. Wartnaby and D. A. King, *Surface Science*, 1993, **283**, 427-437.
76. N. Al-Sarraf and D. A. King, *Surface Science*, 1994, **307**, 1-7.
77. A. Stuck, C. E. Wartnaby, Y. Y. Yeo and D. A. King, *Physical Review Letters*, 1995, **74**, 578-581.
78. S. J. Dixon-Warren, M. Kovar, C. E. Wartnaby and D. A. King, *Surface Science*, 1994, **307-309**, 16-22.
79. J. T. Stuckless, D. E. Starr, D. J. Bald and C. T. Campbell, *Journal of Chemical Physics*, 1997, **107**, 5547-5553.
80. J. T. Stuckless, N. A. Frei and C. T. Campbell, *Sensors and Actuators B: Chemical*, 2000, **62**, 13-22.
81. D. E. Starr and C. T. Campbell, *Journal of Physical Chemistry B*, 2001, **105**, 3776-3782.
82. S. F. Diaz, J. F. Zhu, N. Shamir and C. T. Campbell, *Sensors and Actuators B: Chemical*, 2005, **107**, 454-460.
83. J.-H. Fischer-Wolfarth, J. Hartmann, J. A. Farmer, J. M. Flores-Camacho, C. T. Campbell, S. Schauer mann and H.-J. Freund, *Review of Scientific Instruments*, 2011, **82**, 024102.

84. O. Lytken, W. Lew, J. J. W. Harris, E. K. Vestergaard, J. M. Gottfried and C. T. Campbell, *Journal of the American Chemical Society*, 2008, **130**, 10247-10257.
85. W. Lew, M. C. Crowe, E. Karp and C. T. Campbell, *Journal of Physical Chemistry C*, 2011, **115**, 9164-9170.
86. W. Lew, M. C. Crowe, E. Karp, O. Lytken, J. A. Farmer, L. Arnadottir, C. Schoenbaum and C. T. Campbell, *Journal of Physical Chemistry C*, 2011, **115**, 11586-11594.
87. W. A. Brown, R. Kose and D. A. King, *Chemical Reviews*, 1998, **98**, 797-831.
88. Q. F. Ge, R. Kose and D. A. King, *Advances in Catalysis*, 2000, **45**, 207-259.
89. O. Lytken, W. Lew and C. T. Campbell, *Chemical Society Reviews*, 2008, **37**, 2172-2179.
90. G. Comsa and R. David, *Surface Science Reports*, 1985, **5**, 145-198.
91. S. W. Pauls and C. T. Campbell, *Surface Science*, 1990, **226**, 250-256.
92. J. B. Miller, H. R. Siddiqui, S. M. Gates, J. N. Russell, J. T. Yates, J. C. Tully and M. J. Cardillo, *Journal of Chemical Physics*, 1987, **87**, 6725-6732.
93. J. A. Rodriguez and C. T. Campbell, *Journal of Physical Chemistry*, 1989, **93**, 826-835.
94. M. Trabelsi and J. P. Coulomb, *Surface Science*, 1992, **272**, 352-357.
95. M. Sidoumou, V. Panella and J. Suzanne, *Journal of Chemical Physics*, 1994, **101**, 6338--6343.
96. T. Arnold, R. E. Cook, S. Chanaa, S. M. Clarke, M. Farinelli, P. Yaron and J. Z. Larese, *Physica B: Condensed Matter*, 2006, **385**, 205-207.
97. M. Trabelsi, S. Saidi, C. Chefi, S. Picaud, P. N. M. Hoang and J. P. Coulomb, *Surface Science*, 2004, **550**, 133-139.
98. M. Trabelsi, S. Saidi, C. Chefi, C. Martin, S. Lucas, D. Ferry and J. Suzanne, *Surface Science*, 2004, **566**, 789-793.
99. M. Sprung and J. Z. Larese, *Physical Review B*, 2000, **61**, 13155-13158.
100. D. Ferry, A. Glebov, V. Senz, J. Suzanne, J. P. Toennies and H. Weiss, *Surface Science*, 1997, **377**, 634-638.
101. D. Ferry and J. Suzanne, *Surface Science*, 1996, **345**, L19-L22.
102. M. J. Stirniman, C. Huang, R. S. Smith, S. A. Joyce and B. D. Kay, *Journal of Chemical Physics*, 1996, **105**, 1295-1298.
103. R. Wichtendahl, M. Rodriguez-Rodrigo, U. Hartel, H. Kuhlenbeck and H.-J. Freund, *Physica Status Solidi A*, 1999, **173**, 93-100.
104. R. Wichtendahl, M. Rodriguez-Rodrigo, U. Hartel, H. Kuhlenbeck and H.-J. Freund, *Surface Science*, 1999, **423**, 90-98.
105. S. C. Street, Q. Guo, C. Xu and D. W. Goodman, *Journal of Physical Chemistry*, 1996, **100**, 17599-17605.
106. J. Gunster, G. Liu, J. Stultz and D. W. Goodman, *Journal of Chemical Physics*, 1999, **110**, 2558-2565.
107. P. W. Atkins and J. de Paula, *Physical Chemistry*, W. H. Freeman and Company, New York, 2010.
108. A. J. Gellman and K. R. Paserba, *Journal of Physical Chemistry B*, 2002, **106**, 13231-13241.
109. K. E. Becker and K. A. Fichthorn, *Journal of Chemical Physics*, 2006, **125**, 184706.
110. K. A. Fichthorn, K. E. Becker and R. A. Miron, *Catalysis Today*, 2007, **123**, 71-76.
111. K. E. Becker, M. H. Mignogna and K. A. Fichthorn, *Physical Review Letters*, 2009, **102**, 046101.
112. R. J. Madix, G. Ertl and K. Christmann, *Chemical Physics Letters*, 1979, **62**, 38-41.

113. S. J. Lombardo and A. T. Bell, *Surface Science Reports*, 1991, **13**, 1-72.
114. M. L. Wise, B. G. Koehler, P. Gupta, P. A. Coon and S. M. George, *Surface Science*, 1991, **258**, 166-176.
115. V. P. Zhdanov, *Surface Science Reports*, 1991, **12**, 183-242.
116. C. T. Campbell, Y. K. Sun and W. H. Weinberg, *Chemical Physics Letters*, 1991, **179**, 53-57.
117. H. Sellers and J. Gislason, *Surface Science*, 1999, **426**, 147-153.
118. D. E. Starr and C. T. Campbell, *Journal of the American Chemical Society*, 2008, **130**, 7321-7327.
119. D. A. Arthur, D. L. Meixner, M. Boudart and S. M. George, *Journal of Chemical Physics*, 1991, **95**, 8521-8531.
120. R. Echterhoff and E. Knozinger, *Surface Science*, 1990, **230**, 237-244.
121. N. Cardona-Martinez and J. A. Dumesic, *Advances in Catalysis*, 1992, **38**, 149-244.
122. Z. Dohnalek, J. Kim, O. Bondarchuk, J. M. White and B. D. Kay, *Journal of Physical Chemistry B*, 2006, **110**, 6229-6235.
123. M. A. Henderson, W. S. Epling, C. L. Perkins, C. H. F. Peden and U. Diebold, *Journal of Physical Chemistry B*, 1999, **103**, 5328-5337.
124. B. Dillmann, F. Rohr, O. Seiferth, G. Klivenyi, M. Bender, K. Homann, I. N. Yakovkin, D. Ehrlich, M. Bäumer, H. Kuhlenbeck and H.-J. Freund, *Faraday Discussions*, 1996, **105**, 295-315.
125. J. A. Hinojosa, Jr., H. H. Kan and J. F. Weaver, *Journal of Physical Chemistry C*, 2008, **112**, 8324-8331.
126. A. Linsebigler, G. Q. Lu and J. T. Yates, Jr., *Journal of Chemical Physics*, 1995, **103**, 9438-9443.
127. M. Pykavy, V. Staemmler, O. Seiferth and H.-J. Freund, *Surface Science*, 2001, **479**, 11-25.
128. C. Lemire, R. Meyer, V. E. Henrich, S. Shaikhutdinov and H.-J. Freund, *Surface Science*, 2004, **572**, 103-114.
129. Q. F. Ge and P. J. Moller, *Applied Surface Science*, 1994, **82-3**, 305-309.
130. D. C. Sorescu, C. N. Rusu and J. T. Yates, Jr., *Journal of Physical Chemistry B*, 2000, **104**, 4408-4417.
131. U. A. Paulus, Y. Wang, K. Jacobi and G. Ertl, *Surface Science*, 2003, **547**, 349-354.
132. V. Matolin, I. Matolinova, F. Dvorak, V. Johaneck, J. Myslivecek, K. C. Prince, T. Skala, O. Stetsovych, N. Tsud, M. Vaclavu and B. Smid, *Catalysis Today*, 2012, **181**, 124-132.
133. M. A. Henderson, C. L. Perkins, M. H. Engelhard, S. Thevuthasan and C. H. F. Peden, *Surface Science*, 2003, **526**, 1-18.
134. G. S. Herman, Y. J. Kim, S. A. Chambers and C. H. F. Peden, *Langmuir*, 1999, **15**, 3993-3997.
135. M. B. Hugenschmidt, L. Gamble and C. T. Campbell, *Surface Science*, 1994, **302**, 329-340.
136. G. S. Herman, Z. Dohnalek, N. Ruzycski and U. Diebold, *Journal of Physical Chemistry B*, 2003, **107**, 2788-2795.
137. M. A. Henderson, *Surface Science*, 1994, **319**, 315-328.
138. M. A. Henderson and S. A. Chambers, *Surface Science*, 2000, **449**, 135-150.
139. Y. Joseph, C. Kuhrs, W. Ranke, M. Ritter and W. Weiss, *Chemical Physics Letters*, 1999, **314**, 195-202.

140. C. H. F. Peden, G. S. Herman, I. Z. Ismagilov, B. D. Kay, M. A. Henderson, Y. J. Kim and S. A. Chambers, *Catalysis Today*, 1999, **51**, 513-519.
141. A. Lobo and H. Conrad, *Surface Science*, 2003, **523**, 279-286.
142. H. H. Kan, R. J. Colmyer, A. Asthagiri and J. F. Weaver, *Journal of Physical Chemistry C*, 2009, **113**, 1495-1506.
143. D. F. Cox and K. H. Schulz, *Surface Science*, 1991, **256**, 67-76.
144. G. Zwicker and K. Jacobi, *Surface Science*, 1983, **131**, 179-194.
145. R. Zhang, A. Ludviksson and C. T. Campbell, *Surface Science*, 1993, **289**, 1-9.
146. Y. Wang, M. Muhler and C. Woll, *Physical Chemistry Chemical Physics*, 2006, **8**, 1521-1524.
147. T. L. Thompson, O. Diwald and J. T. Yates, Jr., *Journal of Physical Chemistry B*, 2003, **107**, 11700-11704.
148. J. Wang, B. Hokkanen and U. Burghaus, *Surface Science*, 2005, **577**, 158-166.
149. D. R. Mullins and T. S. McDonald, *Surface Science*, 2008, **602**, 1280-1287.
150. J. F. Weaver, C. Hakanoglu, J. M. Hawkins and A. Asthagiri, *Journal of Chemical Physics*, 2010, **132**, 024709.
151. J. F. Weaver, S. P. Devarajan and C. Hakanoglu, *Journal of Physical Chemistry C*, 2009, **113**, 9773-9782.
152. J. F. Weaver, J. A. Hinojosa, Jr., C. Hakanoglu, A. Antony, J. M. Hawkins and A. Asthagiri, *Catalysis Today*, 2011, **160**, 213-227.
153. J. Wang, B. Hokkanen and U. Burghaus, *Surface Science*, 2006, **600**, 4855-4859.
154. A. W. Grant, L. T. Ngo, K. Stegelman and C. T. Campbell, *Journal of Physical Chemistry B*, 2003, **107**, 1180-1188.
155. I. Hemmerich, F. Rohr, O. Seiferth, B. Dillmann and H.-J. Freund, *Zeitschrift für Physikalische Chemie*, 1997, **202**, 31-43.
156. U. A. Paulus, Y. Wang, H. P. Bonzel, K. Jacobi and G. Ertl, *Journal of Physical Chemistry B*, 2005, **109**, 2139-2148.
157. H. M. Ajo, V. A. Bondzie and C. T. Campbell, *Catalysis Letters*, 2002, **78**, 359-368.
158. M. D. Robbins and M. A. Henderson, *Journal of Catalysis*, 2006, **238**, 111-121.
159. L. T. Ngo, L. J. Xu, A. W. Grant and C. T. Campbell, *Journal of Physical Chemistry B*, 2003, **107**, 1174-1179.
160. D. Poss, W. Ranke and K. Jacobi, *Surface Science*, 1981, **105**, 77-94.
161. Z. Li, R. S. Smith, B. D. Kay and Z. Dohnalek, *Journal of Physical Chemistry C*, 2011, **115**, 22534-22539.
162. M. A. Henderson, S. Otero-Tapia and M. E. Castro, *Faraday Discussions*, 1999, **114**, 313-329.
163. J. Kiss, D. Langenberg, D. Silber, F. Traeger, L. Jin, H. Qiu, Y. Wang, B. Meyer and C. Woell, *Journal of Physical Chemistry A*, 2011, **115**, 7180-7188.
164. S. Y. Nishimura, R. F. Gibbons and N. J. Tro, *Journal of Physical Chemistry B*, 1998, **102**, 6831-6834.
165. L. Gamble, L. S. Jung and C. T. Campbell, *Surface Science*, 1996, **348**, 1-16.
166. S. D. Senanayake, W. O. Gordon, S. H. Overbury and D. R. Mullins, *Journal of Physical Chemistry C*, 2009, **113**, 6208-6214.
167. M. A. Henderson, *Journal of Physical Chemistry B*, 2004, **108**, 18932-18941.
168. C. M. Truong, M. C. Wu and D. W. Goodman, *Journal of Chemical Physics*, 1992, **97**, 9447-9453.

169. A. Ludviksson, R. Zhang, C. T. Campbell and K. Griffiths, *Surface Science*, 1994, **313**, 64-82.
170. A. Antony, C. Hakanoglu, A. Asthagiri and J. F. Weaver, *Journal of Chemical Physics*, 2012, **136**, 054702.
171. J. F. Weaver, private communication.
172. Z. R. Zhang, O. Bondarchuk, J. M. White, B. D. Kay and Z. Dohnalek, *Journal of the American Chemical Society*, 2006, **128**, 4198-4199.
173. C. Zhou, Z. Ren, S. Tan, Z. Ma, X. Mao, D. Dai, H. Fan, X. Yang, J. LaRue, R. Cooper, A. M. Wodtke, Z. Wang, Z. Li, B. Wang, J. Yang and J. Hou, *Chemical Science*, 2010, **1**, 575-580.
174. Z. Dohnalek, I. Lyubinetsky and R. Rousseau, *Progress in Surface Science*, 2010, **85**, 161-205.
175. Z. Zhang, O. Bondarchuk, B. D. Kay, J. M. White and Z. Dohnalek, *Journal of Physical Chemistry C*, 2007, **111**, 3021-3027.
176. O. Bondarchuk, Y. K. Kim, J. M. White, J. Kim, B. D. Kay and Z. Dohnalek, *Journal of Physical Chemistry C*, 2007, **111**, 11059-11067.
177. J. O. Hansen, P. Huo, U. Martinez, E. Lira, Y. Y. Wei, R. Streber, E. Laegsgaard, B. Hammer, S. Wendt and F. Besenbacher, *Physical Review Letters*, 2011, **107**, 136102.
178. P. Huo, J. O. Hansen, U. Martinez, E. Lira, R. Streber, Y. Wei, E. Laegsgaard, B. Hammer, S. Wendt and F. Besenbacher, *Journal of Physical Chemistry Letters*, 2012, **3**, 283-288.
179. M. A. Henderson, S. A. Joyce and J. R. Rustad, *Surface Science*, 1998, **417**, 66-81.
180. G. L. Griffin and J. T. Yates, *Journal of Chemical Physics*, 1982, **77**, 3751-3758.
181. Y. Wang, B. Meyer, X. Yin, M. Kunat, D. Langenberg, F. Traeger, A. Birkner and C. Woll, *Physical Review Letters*, 2005, **95**, 266104.
182. T. Becker, S. Hovel, M. Kunat, C. Boas, U. Burghaus and C. Woll, *Surface Science*, 2001, **486**, L502-L506.
183. T. Becker, S. Hovel, M. Kunat, C. Boas, U. Burghaus and C. Woll, *Surface Science*, 2002, **511**, 463-463.
184. J. W. Elam, C. E. Nelson, M. A. Cameron, M. A. Tolbert and S. M. George, *Journal of Physical Chemistry B*, 1998, **102**, 7008-7015.
185. U. Diebold, J. M. Pan and T. E. Madey, *Surface Science*, 1995, **331**, 845-854.
186. C. R. Henry, C. Chapon, S. Giorgio and C. Goyhenex, in *Chemisorption and Reactivity on Supported Clusters and Thin Films*, eds. R. M. Lambert and G. Pacchioni, Kluwer Acad. Publ., Amsterdam, 1997, pp. 117-152.
187. P. L. J. Gunter, J. W. Niemantsverdriet, F. H. Ribeiro and G. A. Somorjai, *Catalysis Reviews: Science and Engineering*, 1997, **39**, 77-168.
188. H.-J. Freund, *Angewandte Chemie International Edition*, 1997, **36**, 452-475.
189. R. Persaud and T. E. Madey, in *The Chemical Physics of Solid Surfaces and Heterogeneous Catalysis*, eds. D. A. King and D. P. Woodruff, Elsevier, Amsterdam, 1997, vol. 8.
190. C. R. Henry, *Surface Science Reports*, 1998, **31**, 235-325.
191. D. R. Rainer and D. W. Goodman, *Journal of Molecular Catalysis A: Chemical*, 1998, **131**, 259-283.
192. M. Bäumer and H.-J. Freund, *Progress in Surface Science*, 1999, **61**, 127-198.

193. H.-J. Freund, M. Bäumer and H. Kuhlenbeck, *Advances in Catalysis, Vol 45*, 2000, **45**, 333-384.
194. N. Nilius, A. Corper, G. Bozdech, N. Ernst and H.-J. Freund, *Progress in Surface Science*, 2001, **67**, 99-121.
195. H.-J. Freund, J. Libuda, M. Bäumer, T. Risse and A. Carlsson, *Chemical Record*, 2003, **3**, 181-200.
196. J. Libuda and H.-J. Freund, *Surface Science Reports*, 2005, **57**, 157-298.
197. W. T. Wallace, B. K. Min and D. W. Goodman, *Topics in Catalysis*, 2005, **34**, 17-30.
198. H.-J. Freund, *Catalysis Today*, 2005, **100**, 3-9.
199. C. R. Henry, *Progress in Surface Science*, 2005, **80**, 92-116.
200. M. Chen and D. W. Goodman, *Accounts of Chemical Research*, 2006, **39**, 739-746.
201. J. Schoiswohl, M. Sock, Q. Chen, G. Thornton, G. Kresse, M. G. Ramsey, S. Surnev and F. P. Netzer, *Topics in Catalysis*, 2007, **46**, 137-149.
202. H.-J. Freund, *Surface Science*, 2007, **601**, 1438-1442.
203. T. Risse, S. Shaikhutdinov, N. Nilius, M. Sterrer and H.-J. Freund, *Accounts of Chemical Research*, 2008, **41**, 949-956.
204. S. M. McClure and D. W. Goodman, *Topics in Catalysis*, 2011, **54**, 349-362.
205. N. Nilius, T. Risse, S. Schauermaun, S. Shaikhutdinov, M. Sterrer and H.-J. Freund, *Topics in Catalysis*, 2011, **54**, 4-12.
206. J. Nakamura, J. A. Rodriguez and C. T. Campbell, *Journal of Physics: Condensed Matter*, 1989, **1**, SB149-SB160.
207. Z. M. Zhang and V. E. Henrich, *Surface Science*, 1992, **277**, 263-272.
208. J. M. Pan, B. L. Maschhoff, U. Diebold and T. E. Madey, *Surface Science*, 1993, **291**, 381-394.
209. J. M. Pan and T. E. Madey, *Catalysis Letters*, 1993, **20**, 269-274.
210. J. M. Pan and T. E. Madey, *Journal of Vacuum Science & Technology A: Vacuum Surfaces and Films*, 1993, **11**, 1667-1674.
211. J. M. Pan, U. Diebold, L. Z. Zhang and T. E. Madey, *Surface Science*, 1993, **295**, 411-426.
212. L. S. Dake and R. J. Lad, *Journal of Vacuum Science & Technology A: Vacuum Surfaces and Films*, 1995, **13**, 122-126.
213. X. A. Zhao, E. Kolawa and M. A. Nicolet, *Journal of Vacuum Science & Technology A: Vacuum Surfaces and Films*, 1986, **4**, 3139-3141.
214. F. S. Ohuchi and M. Kohyama, *Journal of the American Ceramic Society*, 1991, **74**, 1163-1187.
215. S. Imaduddin and R. J. Lad, *Surface Science*, 1993, **290**, 35-44.
216. S. K. Saxena, N. Chatterjee, Y. Fei and G. Shen, *Thermodynamic Data on Oxides and Silicates* Springer-Verlag, New York, 1993.
217. M. Schick, in *Les Houches, Session XLVIII, Liquids at Interfaces*, eds. J. Charvolin, J.-F. Joanny and J. Zinn-Justin, Elsevier, Amsterdam, 1988.
218. A. W. Adamson, *Physical Chemistry of Surfaces*, Wiley and Sons, New York, 1990.
219. S. H. Overbury, P. A. Bertrand and G. A. Somorjai, *Chemical Reviews*, 1975, **75**, 547-560.
220. D. Chatain, L. Coudurier and N. Eustathopoulos, *Revue De Physique Appliquee*, 1988, **23**, 1055-1064.
221. A. M. Stoneham, *Applications of Surface Science*, 1983, **14**, 249-259.

222. D. Chatain, I. Rivollet and N. Eustathopoulos, *Journal De Chimie Physique Et De Physico-Chimie Biologique*, 1986, **83**, 561-567.
223. D. Chatain, I. Rivollet and N. Eustathopoulos, *Journal De Chimie Physique Et De Physico-Chimie Biologique*, 1987, **84**, 201-203.
224. I. Rivollet, D. Chatain and N. Eustathopoulos, *Acta Metallurgica*, 1987, **35**, 835-844.
225. R. Sangiorgi, M. L. Muolo, D. Chatain and N. Eustathopoulos, *Journal of the American Ceramic Society*, 1988, **71**, 742-748.
226. F. Didier and J. Jupille, *Surface Science*, 1994, **314**, 378-384.
227. J. V. Naidich, *Progress in Surface and Membrane Science*, 1981, **14**, 354-484.
228. W. R. Tyson and W. A. Miller, *Surface Science*, 1977, **62**, 267-276.
229. J. H. Larsen, D. E. Starr and C. T. Campbell, *Journal of Chemical Thermodynamics*, 2001, **33**, 333-345.
230. D. E. Starr, S. F. Diaz, J. E. Musgrove, J. T. Ranney, D. J. Bald, L. Nelen, H. Ihm and C. T. Campbell, *Surface Science*, 2002, **515**, 13-20.
231. C. T. Campbell and D. E. Starr, *Journal of the American Chemical Society*, 2002, **124**, 9212-9218.
232. J. A. Farmer, N. Ruzycki, J. F. Zhu and C. T. Campbell, *Physical Review B*, 2009, **80**, 035418.
233. J. A. Farmer, C. T. Campbell, L. Xu and G. Henkelman, *Journal of the American Chemical Society*, 2009, **131**, 3098-3103.
234. S. Benedetti, H. M. Benia, N. Nilius, S. Valeri and H.-J. Freund, *Chemical Physics Letters*, 2006, **430**, 330-335.
235. J. A. Snyder, J. E. Jaffe, M. Gutowski, Z. J. Lin and A. C. Hess, *Journal of Chemical Physics*, 2000, **112**, 3014-3022.
236. Y. F. Zhukovskii, E. A. Kotomin and G. Borstel, *Vacuum*, 2004, **74**, 235-240.
237. V. Musolino, A. Selloni and R. Car, *Surface Science*, 1998, **402**, 413-417.
238. G. Henkelman, private communication.
239. L. Giordano, M. Baistrocchi and G. Pacchioni, *Physical Review B*, 2005, **72**, 115403.
240. Y.-L. Hu, W.-B. Zhang, Y.-H. Deng and B.-Y. Tang, *Computational Materials Science*, 2008, **42**, 43-49.
241. L. Xu and G. Henkelman, *Physical Review B*, 2008, **77**, 205404.
242. L. Xu and G. Henkelman, *Physical Review B*, 2010, **82**, 115407.
243. L. Giordano, C. Di Valentin, J. Goniakowski and G. Pacchioni, *Physical Review Letters*, 2004, **92**, 096105.
244. C. R. Henry, C. Chapon, C. Duriez and S. Giorgio, *Surface Science*, 1991, **253**, 177-189.
245. J. A. Venables, *Surface Science*, 1994, **299**, 798-817.
246. J. A. Venables, *Introduction to Surface and Thin Film Processes*, Cambridge University Press, Cambridge, 2000.
247. J. A. Venables, *Philosophical Magazine*, 1973, **27**, 697-738.
248. J. A. Venables and J. H. Harding, *Journal of Crystal Growth*, 2000, **211**, 27-33.
249. M. Hu, S. Noda and H. Komiyama, *Surface Science*, 2002, **513**, 530-538.
250. P. Wynblatt and N. A. Gjostein, *Acta Metallurgica*, 1976, **24**, 1165-1174.
251. I. Galanakis, N. Papanikolaou and P. H. Dederichs, *Surface Science*, 2002, **511**, 1-12.
252. S. C. Parker and C. T. Campbell, *Physical Review B*, 2007, **75**, 035430.
253. M. Methfessel, D. Hennig and M. Scheffler, *Applied Physics A: Materials Science & Processing*, 1992, **55**, 442-448.

254. L. Q. Yang and A. E. Depristo, *Journal of Catalysis*, 1994, **149**, 223-228.
255. P. Wynblatt and N. A. Gjostein, *Progress in Solid State Chemistry*, 1975, **9**, 21-58.
256. P. Wynblatt, R. A. Dalla Betta and N. A. Gjostein, in *The Physical Basis for Heterogeneous Catalysis*, ed. R. I. Jaffee, Plenum Press, New York, 1975.
257. G. B. McVicker, R. L. Garten and R. T. K. Baker, *Journal of Catalysis*, 1978, **54**, 129-142.
258. T. M. Ahn, P. Wynblatt and J. K. Tien, *Acta Metallurgica*, 1981, **29**, 921-929.
259. E. Ruckenstein and D. B. Dadyburjor, *Reviews in Chemical Engineering*, 1983, **1**, 251-282.
260. G. A. Fuentes and E. D. Gamas, in *Catalyst Deactivation*, eds. C. H. Bartholomew and J. B. Butt, Elsevier Science, Evanston, IL, 1991, vol. 68, pp. 637-644.
261. C. H. Bartholomew, in *Catalyst Deactivation*, eds. B. Delmon and G. F. Froment, Elsevier Science, Ostend, Belgium, 1994, vol. 88, pp. 1-18.
262. C. H. Bartholomew, in *Catalyst Deactivation*, eds. C. H. Bartholomew and G. A. Fuentes, Elsevier Science, Cancun, Mexico, 1997, vol. 111, pp. 585-592.
263. G. A. Fuentes and E. Salinas-Rodriguez, in *Catalyst Deactivation*, eds. C. H. Bartholomew and G. A. Fuentes, Elsevier Science, Cancun, Mexico, 1997, vol. 111, pp. 573-583.
264. A. Imre, E. Gontier-Moya, D. L. Beke, I. A. Szabo and G. Erdelyi, *Surface Science*, 1999, **441**, 133-139.
265. X. F. Lai and D. W. Goodman, *Journal of Molecular Catalysis A: Chemical*, 2000, **162**, 33-50.
266. M. J. J. Jak, C. Konstapel, A. van Kreuningen, J. Verhoeven and J. W. M. Frenken, *Surface Science*, 2000, **457**, 295-310.
267. M. J. J. Jak, C. Konstapel, A. van Kreuningen, J. Chrost, J. Verhoeven and J. W. M. Frenken, *Surface Science*, 2001, **474**, 28-36.
268. F. Cosandey and T. E. Madey, *Surface Review and Letters*, 2001, **8**, 73-93.
269. A. G. Sault and V. Tikare, *Journal of Catalysis*, 2002, **211**, 19-32.
270. J. Sehested, *Journal of Catalysis*, 2003, **217**, 417-426.
271. S. C. Parker and C. T. Campbell, *Topics in Catalysis*, 2007, **44**, 3-13.
272. D. Ricci, A. Bongiorno, G. Pacchioni and U. Landman, *Physical Review Letters*, 2006, **97**, 036106.
273. M. Haruta, S. Tsubota, T. Kobayashi, H. Kageyama, M. J. Genet and B. Delmon, *Journal of Catalysis*, 1993, **144**, 175-192.
274. M. Valden, X. Lai and D. W. Goodman, *Science*, 1998, **281**, 1647-1650.
275. M. Valden, S. Pak, X. Lai and D. W. Goodman, *Catalysis Letters*, 1998, **56**, 7-10.
276. M. Haruta and M. Date, *Applied Catalysis A: General*, 2001, **222**, 427-437.
277. M. Haruta, *Cattech*, 2002, **6**, 102-115.
278. D. Kalakkad, A. K. Datye and H. Robota, *Applied Catalysis B: Environmental*, 1992, **1**, 191-219.
279. J. M. Schwartz and L. D. Schmidt, *Journal of Catalysis*, 1992, **138**, 283-293.
280. J. H. Wang, M. L. Liu and M. C. Lin, *Solid State Ionics*, 2006, **177**, 939-947.
281. H. Graoui, S. Giorgio and C. R. Henry, *Philosophical Magazine B: Physics of Condensed Matter Statistical Mechanics Electronic Optical and Magnetic Properties*, 2001, **81**, 1649-1658.

282. L. V. Koplitz, O. Dulub and U. Diebold, *Journal of Physical Chemistry B*, 2003, **107**, 10583-10590.
283. X. P. Xu, J. Szanyi, Q. Xu and D. W. Goodman, *Catalysis Today*, 1994, **21**, 57-69.
284. X. P. Xu, J. W. He and D. W. Goodman, *Surface Science*, 1993, **284**, 103-108.
285. C. Xu, W. S. Oh, G. Liu, D. Y. Kim and D. W. Goodman, *Journal of Vacuum Science & Technology A: Vacuum Surfaces and Films*, 1997, **15**, 1261-1268.
286. D. W. Goodman, *Surface Review and Letters*, 1995, **2**, 9-24.
287. C. L. Liu, J. M. Cohen, J. B. Adams and A. F. Voter, *Surface Science*, 1991, **253**, 334-344.
288. J. A. Rodriguez, M. Kuhn and J. Hrbek, *Journal of Physical Chemistry*, 1996, **100**, 18240-18248.
289. R. J. Lad and L. S. Dake, *Materials Research Society Proceedings*, 1991, **238**, 823.
290. S. Kennou, M. Kamaratos and C. A. Papageorgopoulos, *Vacuum*, 1990, **41**, 22-24.
291. S. Kennou, M. Kamaratos and C. A. Papageorgopoulos, *Surface Science*, 1991, **256**, 312-316.
292. G. Chen, M. D. Weisel, J. H. Hardenbergh, F. M. Hoffmann, C. A. Mims and R. B. Hall, *Journal of Vacuum Science & Technology A: Vacuum Surfaces and Films*, 1991, **9**, 1684-1687.
293. K. A. Fichthorn and R. A. Miron, *Physical Review Letters*, 2002, **89**, 196103.
294. J. C. Hamilton, *Physical Review Letters*, 1996, **77**, 885-888.
295. M. A. N. Santiago, M. A. Sanchez-Castillo, R. D. Cortright and J. A. Dumesic, *Journal of Catalysis*, 2000, **193**, 16-28.
296. C. F. Goldsmith, *Topics in Catalysis*, 2012, **55**, 366-375.
297. K. R. Paserba, N. Vaidyanathan and A. J. Gellman, *Langmuir*, 2002, **18**, 9799-9809.
298. K. Reuter, D. Frenkel and M. Scheffler, *Physical Review Letters*, 2004, **93**, 116105.
299. C. T. Campbell, *Nature*, 2004, **432**, 282-283.
300. K. Honkala, A. Hellman, I. N. Remediakis, A. Logadottir, A. Carlsson, S. Dahl, C. H. Christensen and J. K. Nørskov, *Science*, 2005, **307**, 555-558.
301. K. Reuter and M. Scheffler, *Physical Review B*, 2006, **73**, 045433.
302. A. A. Gokhale, J. A. Dumesic and M. Mavrikakis, *Journal of the American Chemical Society*, 2008, **130**, 1402-1414.
303. H. Eyring and M. Polanyi, *Zeitschrift für Physikalische Chemie, Abteilung B: Chemie Der Elementarprozesse, Aufbau Der Materie*, 1931, **12**, 279-311.
304. G. Henkelman, B. P. Uberuaga and H. Jonsson, *Journal of Chemical Physics*, 2000, **113**, 9901-9904.
305. A. Heyden, A. T. Bell and F. J. Keil, *Journal of Chemical Physics*, 2005, **123**, 224101.
306. G. Henkelman and H. Jonsson, *Journal of Chemical Physics*, 2001, **115**, 9657-9666.
307. K. J. Wu and S. D. Kevan, *Journal of Chemical Physics*, 1991, **95**, 5355-5363.
308. L. D. Peterson and S. D. Kevan, *Physical Review Letters*, 1990, **65**, 2563-2566.
309. S. H. Payne, J. S. McEwen, H. J. Kreuzer and D. Menzel, *Surface Science*, 2005, **594**, 240-262.
310. H. Pfnur, P. Feulner, H. A. Engelhardt and D. Menzel, *Chemical Physics Letters*, 1978, **59**, 481-486.
311. K. J. Laidler, *Chemical Kinetics*, McGraw-Hill, New York, 1965.
312. G. Kresse and J. Hafner, *Physical Review B*, 1993, **47**, 558-561.
313. G. Kresse and J. Hafner, *Physical Review B*, 1994, **49**, 14251-14269.

314. G. Kresse and J. Furthmuller, *Computational Materials Science*, 1996, **6**, 15-50.
315. P. E. Blochl, *Physical Review B*, 1994, **50**, 17953-17979.
316. G. Kresse and D. Joubert, *Physical Review B*, 1999, **59**, 1758-1775.
317. J. P. Perdew, J. A. Chevary, S. H. Vosko, K. A. Jackson, M. R. Pederson, D. J. Singh and C. Fiolhais, *Physical Review B*, 1992, **46**, 6671-6687.
318. J. P. Perdew, K. Burke and M. Ernzerhof, *Physical Review Letters*, 1996, **77**, 3865-3868.
319. J. P. Perdew, K. Burke and M. Ernzerhof, *Physical Review Letters*, 1997, **78**, 1396-1396.
320. J. Greeley and M. Mavrikakis, *Journal of the American Chemical Society*, 2002, **124**, 7193-7201.
321. M. W. Chase, Jr., *Journal of Physical and Chemical Reference Data*, 1998, **Monograph 9**, 1-1951.
322. A. Antony, A. Asthagiri and J. F. Weaver, *Physical Chemistry Chemical Physics*, 2012, **14**, 12202-12212.
323. R. B. McClurg, R. C. Flagan and W. A. Goddard, *Journal of Chemical Physics*, 1997, **106**, 6675-6680.
324. A. Ghysels, T. Verstraelen, K. Hemelsoet, M. Waroquier and V. Van Speybroeck, *Journal of Chemical Information and Modeling*, 2010, **50**, 1736-1750.
325. E. M. Karp, C. T. Campbell, F. Studt, F. Abild-Pedersen and J. K. Norskov, *Journal of Physical Chemistry C*, 2012, **116**, 25772-25776.
326. C. R. Helms and R. J. Madix, *Surface Science*, 1975, **52**, 677-680.
327. J. L. Falconer and R. J. Madix, *Surface Science*, 1975, **48**, 393-405.
328. J. S. McEwen, S. H. Payne, H. J. Kreuzer, M. Kinne, R. Denecke and H. P. Steinruck, *Surface Science*, 2003, **545**, 47-69.
329. C. T. Campbell, G. Ertl, H. Kuipers and J. Segner, *Surface Science*, 1981, **107**, 207-219.
330. C. T. Campbell, G. Ertl and J. Segner, *Surface Science*, 1982, **115**, 309-322.
331. L. C. Grabow and M. Mavrikakis, *ACS Catalysis*, 2011, **1**, 365-384.
332. U. Kürpick, A. Kara and T. S. Rahman, *Physical Review Letters*, 1997, **78**, 1086-1089.
333. L. Xu, G. Henkelman, C. T. Campbell and H. Jonsson, *Physical Review Letters*, 2005, **95**, 146103.
334. D. G. Truhlar, A. D. Isaacson and B. C. Garrett, in *Theory of Chemical Reaction Dynamics*, ed. M. Baer, CRC Press, Boca Raton, FL, 1985, vol. 4, ch. 2, pp. 65-137.
335. J. M. Gottfried, E. K. Vestergaard, P. Bera and C. T. Campbell, *Journal of Physical Chemistry B*, 2006, **110**, 17539-17545.
336. K. Coulter, X. P. Xu and D. W. Goodman, *Journal of Physical Chemistry*, 1994, **98**, 1245-1249.
337. W. Eberhardt, *Surface Science*, 2002, **500**, 242-270.
338. C. E. Gigola, H. R. Aduriz and P. Bodnariuk, *Applied Catalysis*, 1986, **27**, 133-144.
339. J. R. Engstrom, D. W. Goodman and W. H. Weinberg, *Journal of the American Chemical Society*, 1986, **108**, 4653-4655.
340. A. Wolf and F. Schuth, *Applied Catalysis A: General*, 2002, **226**, 1-13.
341. A. L. de Oliveira, A. Wolf and F. Schuth, *Catalysis Letters*, 2001, **73**, 157-160.
342. W. J. Shen, Y. Ichihashi and Y. Matsumura, *Catalysis Letters*, 2002, **79**, 125-127.
343. W. J. Shen, A. Kobayashi, Y. Ichihashi, Y. Matsumura and M. Haruta, *Catalysis Letters*, 2001, **73**, 161-165.
344. Y. Matsumura, W. J. Shen and Y. Ichihashi, Okumura, M., *J. Catal.*, 2001, **197**, 267-272.

345. M. Vaarkamp, J. T. Miller, F. S. Modica and D. C. Koningsberger, *Journal of Catalysis*, 1996, **163**, 294-305.
346. J. A. Rodriguez, G. Liu, T. Jirsak, J. Hrbek, Z. P. Chang, J. Dvorak and A. Maiti, *Journal of the American Chemical Society*, 2002, **124**, 5242-5250.
347. S. Guerin, B. E. Hayden, C. E. Lee, C. Mormiche, J. R. Owen, A. E. Russell, B. Theobald and D. Thompsett, *Journal of Combinatorial Chemistry*, 2004, **6**, 149-158.
348. B. E. Hayden, D. Pletcher, M. E. Rendall and J. P. Suchsland, *Journal of Physical Chemistry C*, 2007, **111**, 17044-17051.
349. B. E. Hayden, D. Pletcher, J. P. Suchsland and L. J. Williams, *Physical Chemistry Chemical Physics*, 2009, **11**, 9141-9148.
350. U. Heiz and E. L. Bullock, *Journal of Materials Chemistry*, 2004, **14**, 564-577.
351. K. Judai, S. Abbet, A. S. Worz, U. Heiz and C. R. Henry, *Journal of the American Chemical Society*, 2004, **126**, 2732-2737.
352. K. Judai, S. Abbet, A. S. Worz, A. M. Ferrari, L. Giordano, G. Pacchioni and U. Heiz, *Journal of Molecular Catalysis A: Chemical*, 2003, **199**, 103-113.
353. S. S. Lee, C. Y. Fan, T. P. Wu and S. L. Anderson, *Journal of the American Chemical Society*, 2004, **126**, 5682-5683.
354. P. Liu and J. A. Rodriguez, *Journal of Chemical Physics*, 2007, **126**, 164705.
355. J. A. Rodriguez, P. Liu, J. Hrbek, J. Evans and M. Perez, *Angewante Chemie*, 2007, **46**, 1329-1332.
356. J. L. Lu, H. J. Gao, S. Shaikhutdinov and H.-J. Freund, *Catalysis Letters*, 2007, **114**, 8-16.
357. J. A. Rodriguez, P. Liu, X. Wang, W. Wen, J. Hanson, J. Hrbek, M. Perez and J. Evans, *Catalysis Today*, 2009, **143**, 45-50.
358. S. Mostafa, F. Behafarid, J. R. Croy, L. K. Ono, L. Li, J. C. Yang, A. I. Frenkel and B. Roldan Cuenya, *Journal of the American Chemical Society*, 2010, **132**, 15714-15719.
359. A. Goguet, F. Meunier, J. P. Breen, R. Burch, M. I. Petch and A. F. Ghenciu, *Journal of Catalysis*, 2004, **226**, 382-392.
360. D. Tibiletti, A. Goguet, F. C. Meunier, J. P. Breen and R. Burch, *Chemical Communications*, 2004, 1636-1637.
361. G. A. Deluga, J. R. Salge, L. D. Schmidt and X. E. Verykios, *Science*, 2004, **303**, 993-997.
362. D. Andreeva, V. Idakiev, T. Tabakova, L. Ilieva, P. Falaras, A. Bourlinos and A. Travlos, *Catalysis Today*, 2002, **72**, 51-57.
363. X. S. Liu, O. Korotkikh and R. Farrauto, *Applied Catalysis A: General*, 2002, **226**, 293-303.
364. Q. Fu, A. Weber and M. Flytzani-Stephanopoulos, *Catalysis Letters*, 2001, **77**, 87-95.
365. M. Flytzani-Stephanopoulos, *Mrs Bulletin*, 2001, **26**, 885-889.
366. S. Hilaire, X. Wang, T. Luo, R. J. Gorte and J. Wagner, *Applied Catalysis A: General*, 2001, **215**, 271-278.
367. T. Bunluesin, R. J. Gorte and G. W. Graham, *Applied Catalysis B: Environmental*, 1998, **15**, 107-114.
368. M. L. Toebes, J. A. van Dillen and Y. P. de Jong, *Journal of Molecular Catalysis A: Chemical*, 2001, **173**, 75-98.
369. F. Charreteur, F. Jaouen, S. Ruggeri and J. P. Dodelet, *Electrochimica Acta*, 2008, **53**, 2925-2938.

370. J. Graciani, J. J. Plata, J. F. Sanz, P. Liu and J. A. Rodriguez, *Journal of Chemical Physics*, 2010, **132**, 104703.
371. J. A. Rodriguez, J. Graciani, J. Evans, J. B. Park, F. Yang, D. Stacchiola, S. D. Senanayake, S. G. Ma, M. Perez, P. Liu, J. F. Sanz and J. Hrbek, *Angewandte Chemie International Edition*, 2009, **48**, 8047-8050.
372. J. A. Rodriguez, X. Wang, P. Liu, W. Wen, J. C. Hanson, J. Hrbek, M. Perez and J. Evans, *Topics in Catalysis*, 2007, **44**, 73-81.
373. Z. Yan, S. Chinta, A. A. Mohamed, J. P. Fackler and D. W. Goodman, *Journal of the American Chemical Society*, 2005, **127**, 1604-1605.
374. A. Vijay, G. Mills and H. Metiu, *Journal of Chemical Physics*, 2003, **118**, 6536-6551.
375. E. Wahlstrom, N. Lopez, R. Schaub, P. Thostrup, A. Ronnau, C. Africh, E. Laegsgaard, J. K. Norskov and F. Besenbacher, *Physical Review Letters*, 2003, **90**, 026101.
376. Y. H. Zhang, M. L. Toebes, A. van der Eerden, W. E. O'Grady, K. P. de Jong and D. C. Koningsberger, *Journal of Physical Chemistry B*, 2004, **108**, 18509-18519.
377. R. J. Lad, *Surface Review and Letters*, 1995, **2**, 109-126.
378. V. Johanek, M. Laurin, J. Hoffmann, S. Schaueremann, A. W. Grant, B. Kasemo, J. Libuda and H.-J. Freund, *Surface Science*, 2004, **561**, L218-L224.
379. S. Bertarione, D. Scarano, A. Zecchina, V. Johanek, J. Hoffmann, S. Schaueremann, J. Libuda, G. Rupprechter and H.-J. Freund, *Journal of Catalysis*, 2004, **223**, 64-73.
380. A. M. Doyle, S. K. Shaikhutdinov and H.-J. Freund, *Journal of Catalysis*, 2004, **223**, 444-453.
381. C. Lemire, R. Meyer, S. Shaikhutdinov and H.-J. Freund, *Angewandte Chemie International Edition*, 2004, **43**, 118-121.
382. R. Meyer, M. Bäumer, S. K. Shaikhutdinov and H.-J. Freund, *Surface Science*, 2003, **546**, L813-L819.
383. A. M. Doyle, S. K. Shaikhutdinov, S. D. Jackson and H.-J. Freund, *Angewandte Chemie International Edition*, 2003, **42**, 5240-5243.
384. A. Kolmakov and D. W. Goodman, *Chemical Record*, 2002, **2**, 446-457.
385. A. K. Santra and D. W. Goodman, *Journal of Physics-Condensed Matter*, 2003, **15**, R31-R62.
386. J. Oh, T. Kondo, D. Hatake, Y. Iwasaki, Y. Honma, Y. Suda, D. Sekiba, H. Kudo and J. Nakamura, *Journal of Physical Chemistry Letters*, 2010, **1**, 463-466.
387. S. H. Lee, S. S. Han, J. K. Kang, J. H. Ryu and H. M. Lee, *Surface Science*, 2008, **602**, 1433-1439.
388. J. P. Jalkanen, M. Halonen, D. Fernandez-Torre, K. Laasonen and L. Halonen, *Journal of Physical Chemistry A*, 2007, **111**, 12317-12326.
389. S. Nemsak, K. Masek and V. Matolin, *Surface Science*, 2007, **601**, 4475-4478.
390. J. Akola and H. Hakkinen, *Physical Review B*, 2006, **74**, 165404.
391. Z. Song, T. H. Cai, J. C. Hanson, J. A. Rodriguez and J. Hrbek, *Journal of the American Chemical Society*, 2004, **126**, 8576-8584.
392. M. R. C. Hunt and R. E. Palmer, *Philosophical Transactions of the Royal Society of London Series A: Mathematical Physical and Engineering Sciences*, 1998, **356**, 231-247.
393. J. C. Parlebas, P. Kruger, M. Taguchi, C. Demangeat and A. Kotani, *Surface Science*, 1997, **377**, 177-180.
394. H. Xu, H. Permana, Y. Lu and K. Y. S. Ng, *Surface Science*, 1995, **325**, 285-293.

395. F. J. C. S. Aires, P. Sautet, J. L. Rousset, G. Fuchs and P. Melinon, *Journal of Vacuum Science & Technology B*, 1994, **12**, 1776-1779.
396. G. W. Clark and L. L. Kesmodel, *Journal of Vacuum Science & Technology B*, 1993, **11**, 131-136.
397. U. Muller, K. Sattler, J. Xhie, N. Venkateswaran and G. Raina, *Journal of Vacuum Science & Technology B*, 1991, **9**, 829-832.
398. M. Bowker, P. Stone, R. Bennett and N. Perkins, *Surface Science*, 2002, **511**, 435-448.
399. M. Bowker, P. Stone, P. Morrall, R. Smith, R. Bennett, N. Perkins, R. Kvon, C. Pang, E. Fourre and M. Hall, *Journal of Catalysis*, 2005, **234**, 172-181.
400. M. Bowker, *Surface Science*, 2009, **603**, 2359-2362.
401. M. Bowker, M. Broughton, A. Carley, P. Davies, D. Morgan, J. Crouch, G. Lalev, S. Dimov and D. T. Pham, *Langmuir*, 2010, **26**, 16261-16266.
402. J. B. Park, J. Graciani, J. Evans, D. Stacchiola, S. G. Ma, P. Liu, A. Nambu, J. F. Sanz, J. Hrbek and J. A. Rodriguez, *Proceedings of the National Academy of Sciences of the United States of America*, 2009, **106**, 4975-4980.
403. M. A. Brown, E. Carrasco, M. Sterrer and H.-J. Freund, *Journal of the American Chemical Society*, 2010, **132**, 4064-4065.
404. M. A. Brown, Y. Fujimori, F. Ringleb, X. Shao, F. Stavale, N. Nilius, M. Sterrer and H.-J. Freund, *Journal of the American Chemical Society*, 2011, **133**, 10668-10676.
405. S. M. McClure, M. Lundwall, Z. Zhou, F. Yang and D. W. Goodman, *Catalysis Letters*, 2009, **133**, 298-306.
406. S. M. McClure, M. J. Lundwall and D. W. Goodman, *Proceedings of the National Academy of Sciences of the United States of America*, 2011, **108**, 931-936.
407. S. Shaikhutdinov and H.-J. Freund, *ChemPhysChem*, 2013, **14**, 71-77.
408. A. Bruix, J. A. Rodriguez, P. J. Ramirez, S. D. Senanayake, J. Evans, J. B. Park, D. Stacchiola, P. Liu, J. Hrbek and F. Illas, *Journal of the American Chemical Society*, 2012, **134**, 8968-8974.
409. B. Roldan Cuenya, *Thin Solid Films*, 2010, **518**, 3127-3150.
410. F. Behafarid and B. Roldan Cuenya, *Surface Science*, 2012, **606**, 908-918.
411. W. L. Winterbottom, *Acta Metallurgica*, 1967, **15**, 303-310.
412. C. Bombis, A. Emundts, M. Nowicki and H. P. Bonzel, *Surface Science*, 2002, **511**, 83-96.
413. S. Giorgio, C. Chapon, C. R. Henry, G. Nihoul and J. M. Penisson, *Philosophical Magazine A: Physics of Condensed Matter Structure Defects and Mechanical Properties*, 1991, **64**, 87-96.
414. R. Lazzari, G. Renaud, J. Jupille and F. Leroy, *Physical Review B*, 2007, **76**.
415. L. Zhang, F. Cosandey, R. Persaud and T. E. Madey, *Surface Science*, 1999, **439**, 73-85.
416. H. Graoui, S. Giorgio and C. R. Henry, *Surface Science*, 1998, **417**, 350-360.
417. C. Revenant, F. Leroy, R. Lazzari, G. Renaud and C. R. Henry, *Physical Review B*, 2004, **69**, 035411.
418. J. Olander, R. Lazzari, J. Jupille, B. Mangili, J. Goniakowski and G. Renaud, *Physical Review B*, 2007, **76**, 075409.
419. C. T. Campbell, *Accounts of Chemical Research*, 2013, **46**, 1712-1719.
420. M. M. Branda, N. C. Hernandez, J. F. Sanz and F. Illas, *Journal of Physical Chemistry C*, 2010, **114**, 1934-1941.

421. C. J. Zhang, A. Michaelides and S. J. Jenkins, *Physical Chemistry Chemical Physics*, 2011, **13**, 22-33.
422. G. Pacchioni, *Physical Chemistry Chemical Physics*, 2013, **15**, 1737-1757.
423. S. L. Tait, L. T. Ngo, Q. M. Yu, S. C. Fain and C. T. Campbell, *Journal of Chemical Physics*, 2005, **122**, 064712.
424. NIST Chemistry Webbook, NIST Standard Reference Database Number 69, <http://webbook.nist.gov/chemistry/>.
425. H. S. Johnston and C. Parr, *Journal of the American Chemical Society*, 1963, **85**, 2544-2551.
426. W. H. Weinberg and R. P. Merrill, *Surface Science*, 1972, **33**, 493-515.
427. W. H. Weinberg, *Journal of Vacuum Science & Technology*, 1973, **10**, 89-94.
428. C. T. Campbell, in *Handbook of Heterogeneous Catalysis*, eds. G. Ertl, H. Knözinger and J. Weitkamp, VCH, Weinheim, Germany, 1997, ch. 4.5, pp. 814-826.
429. V. Bondzie, S. C. Parker and C. T. Campbell, *Catalysis Letters*, 2011, **141**, 1721-1721.
430. J.-H. Fischer-Wolfarth, J. A. Farmer, J. M. Flores-Camacho, A. Genest, I. V. Yudanov, N. Rosch, C. T. Campbell, S. Schauermaann and H.-J. Freund, *Physical Review B*, 2010, **81**, 241416(R).
431. J. M. Flores-Camacho, J.-H. Fischer-Wolfarth, M. Peter, C. T. Campbell, S. Schauermaann and H.-J. Freund, *Physical Chemistry Chemical Physics*, 2011, **13**, 16800-16810.
432. C. Duriez, C. R. Henry and C. Chapon, *Surface Science*, 1991, **253**, 190-204.
433. L. Li, A. H. Larsen, N. A. Romero, V. A. Morozov, C. Glinsvad, F. Abild-Pedersen, J. Greeley, K. W. Jacobsen and J. K. Nørskov, *Journal of Physical Chemistry Letters*, 2013, **4**, 222-226.
434. K. Watanabe, Y. Matsumoto, M. Kamplung, K. Al-Shamery and H.-J. Freund, *Angewandte Chemie International Edition*, 1999, **38**, 2192-2194.
435. D. E. Starr, J. T. Ranney, J. H. Larsen, J. E. Musgrove and C. T. Campbell, *Physical Review Letters*, 2001, **87**, 106102.
436. J. M. Howe, *International Materials Reviews*, 1993, **38**, 233-256.
437. G. A. Somorjai and J. Y. Park, *Surface Science*, 2009, **603**, 1293-1300.
438. J. T. Stuckless, D. E. Starr, D. J. Bald and C. T. Campbell, *Physical Review B*, 1997, **56**, 13496-13502.
439. T. L. Silbaugh, E. M. Karp and C. T. Campbell, *Journal of Catalysis*, 2013, **308**, 114-121.
440. D. A. King and M. G. Wells, *Proceedings of the Royal Society of London Series A: Mathematical and Physical Sciences*, 1974, **339**, 245-269.
441. *Barium Fluoride (BaF₂) Specifications*, ISP Optics, <http://store.ispoptics.com/pdfs/pdfCatalog/page08.pdf>, accessed June 25, 2013.
442. T. Jones, J. Sawler and D. Venus, *Review of Scientific Instruments*, 1993, **64**, 2008-2012.
443. A. Band and J. A. Stroschio, *Review of Scientific Instruments*, 1996, **67**, 2366-2369.
444. C. Lu and Y. Guan, *Journal of Vacuum Science & Technology A*, 1995, **13**, 1797-1801.
445. K. H. Behrndt and R. W. Love, *Vacuum*, 1962, **12**, 1-9.
446. S. Schiller, G. Jaesch and M. Neumann, *Thin Solid Films*, 1983, **110**, 149-164.
447. J. H. Weaver, D. W. Lynch and C. G. Olson, *Physical Review B*, 1974, **10**, 501-516.
448. J. D. McIntyre and D. E. Aspnes, *Surface Science*, 1971, **24**, 417-434.
449. K. C. Lin, R. G. Tobin and P. Dumas, *Physical Review B*, 1994, **49**, 17273-17278.

450. J. Dvorak and H. L. Dai, *Journal of Chemical Physics*, 2000, **112**, 923-934.
451. H. E. Bennett, *Journal of the Optical Society of America*, 1963, **53**, 1389-1393.
452. A. Mandelis and M. M. Zver, *Journal of Applied Physics*, 1985, **57**, 4421-4430.
453. R. J. Batt, D. M. Calcutt and J. M. Hackett, *Journal of Physics-Condensed Matter*, 1989, **1**, SB249-SB250.
454. M. T. Paffett, C. T. Campbell, T. N. Taylor and S. Srinivasan, *Surface Science*, 1985, **154**, 284-302.
455. M. L. Shek, P. M. Stefan, I. Lindau and W. E. Spicer, *Physical Review B*, 1983, **27**, 7277-7287.
456. R. C. Yeates and G. A. Somorjai, *Surface Science*, 1983, **134**, 729-744.
457. L.-W. H. Leung, T. W. Gregg and D. W. Goodman, *Langmuir*, 1991, **7**, 3205-3210.
458. Y. T. Wu, E. Garfunkel and T. E. Madey, *Journal of Vacuum Science & Technology A: Vacuum Surfaces and Films*, 1996, **14**, 1662-1667.

Curriculum Vitae

Jason R. V. Sellers, PhD
Campbell Research Group
University of Washington

EDUCATION

- University of Washington – Seattle, WA – Dual PhD in Chemistry and Nanotechnology
 - Thesis title: “Adsorption and Thin-Film Adhesion on Single-Crystalline Surfaces: Enthalpies, Entropies, and Kinetic Prefactors for Surface Reactions”
 - Research advisor: Charles T. Campbell
 - Graduate courses GPA: 3.47
- Old Dominion University – Norfolk, VA – BS in Chemistry, minor in Music History
 - Undergraduate core chemistry GPA: 3.80
 - Overall undergraduate GPA: 3.75
- First Colonial High School – Virginia Beach, VA – Advanced Studies Diploma

RESEARCH EXPERIENCE

- University of Washington – graduate student/PhD candidate: 6/2007 to present
 - Charles T. Campbell Research Group: 1/2008 to present
 - UHV adsorption microcalorimetry of metal atoms on single crystalline oxide supports
 - Trends in the physical properties of adsorbates on single-crystalline surfaces
 - Markus Raschke Research Group (in collaboration with Daniel Gamelin): 6 to 12/2007
 - Semiconductor nanoparticle synthesis and characterization using ultrafast nonlinear spectroscopy
- Old Dominion University Research Foundation – research assistant: 9/2006 to 5/2007
 - Research and development scientist at Morphix Technologies
 - Synthesis and analysis of hazardous chemical detection methods

PROFESSIONAL EXPERIENCE

- Frame ‘N’ Art – Virginia Beach, VA – picture framer / manager: 3/2001 to 5/2007
 - PPFa professionally certified picture framer (CPF)
 - Customer service
 - Management duties
- Wilkinson Business Services – Virginia Beach, VA – warehouse staff: 3/2000 to 3/2001

SKILLS

- Six years of graduate level research
 - UHV chamber design and usage
 - Surface characterization: AES, XPS, ISS, LEED
 - Sample preparation: ALD, single crystalline oxide film growth
 - Residual gas analysis (MS)
 - ICP-AES
 - Ultrafast laser, optics, spectrophotometry
 - Semiconductor nanoparticle growth and spin-coated film preparation
 - Machining and construction of high precision scientific equipment

- Electrical circuit design, construction, and troubleshooting
- Data analysis: IGOR, Origin, Excel, CasaXPS, XPSpeak, AugerScan
- One year of research and development lab experience
 - ¹H NMR
 - IR microscopy
 - Inorganic synthesis
 - Time resolved UV/Vis spectroscopy
- Four years of ACS accredited undergraduate level lab experience
 - HPLC
 - AAS
 - GC
 - Electrochemistry
 - IR and UV/Vis spectroscopy
 - ¹H and ¹³C NMR
 - Organic and inorganic synthesis
- Two years of college level computer science courses
- Basic knowledge of Turbo Pascal and C++
- Six years of customer service experience

AWARDS AND HONORS

- GSFEI Graduate Student Travel Award: October 2012
- Pacific Coast Catalysis Society Student Presentation Award, 2nd Prize: May 2010
- Shain Graduate Fellowship from the University of Washington: September 2007
- Old Dominion University Dean's List: Awarded 4 times from Spring 2005 to Fall 2006
- Phi Kappa Phi Honor Society
- Governor's Technology Scholarship from Old Dominion University
- Professional Picture Framers Association Certified Picture Framer
- Arkansas All-State Contrabass Clarinetist: 1996
- Enrollment at Old Donation Center for the Gifted and Talented in Virginia Beach, VA

PUBLICATIONS

- Charles T. Campbell and Jason R. V. Sellers. The entropies of adsorbed molecules. *J. Am. Chem. Soc.* **134(43)**, 18109-18115 (2012).
- Charles T. Campbell and Jason R. V. Sellers. Enthalpies and entropies of adsorption on well-defined oxide surfaces: Experimental measurements. *Chem. Rev.* **113(6)**, 4106-4135 (2013).
- Charles T. Campbell and Jason R. V. Sellers. Anchored metal nanoparticles: Effects of support and size on their energy, sintering resistance and reactivity. *Faraday Discuss.* **162**, 9-30 (2013).
- Charles T. Campbell, L. Árnadóttir, and Jason R. V. Sellers. Kinetic prefactors of reactions on solid surfaces. *Z. Phys. Chem.* **227(11)**, 1435-1454 (2013).
- Jason R. V. Sellers, Trevor E. James, Stephanie L. Hemmingson, Jason A. Farmer, and Charles T. Campbell. Adsorption calorimetry during metal vapor deposition on single crystal surfaces: Increased flux, reduced optical radiation, and real-time flux and reflectivity measurements. *Rev. Sci. Instrum.* **84**, 123901 (2013).